



# Étude des neutrinos de réacteur : expériences STEREO et NUCLEUS

Vladimir-George Savu

## ► To cite this version:

Vladimir-George Savu. Étude des neutrinos de réacteur : expériences STEREO et NUCLEUS. Nuclear Experiment [nucl-ex]. Université Paris-Saclay, 2021. English. NNT : 2021UPASP120 . tel-03563659

**HAL Id: tel-03563659**

**<https://theses.hal.science/tel-03563659>**

Submitted on 9 Feb 2022

**HAL** is a multi-disciplinary open access archive for the deposit and dissemination of scientific research documents, whether they are published or not. The documents may come from teaching and research institutions in France or abroad, or from public or private research centers.

L'archive ouverte pluridisciplinaire **HAL**, est destinée au dépôt et à la diffusion de documents scientifiques de niveau recherche, publiés ou non, émanant des établissements d'enseignement et de recherche français ou étrangers, des laboratoires publics ou privés.

# Reactor neutrino studies: STEREO and NUCLEUS experiments

*Étude des neutrinos de réacteur :  
expériences STEREO et NUCLEUS*

Thèse de doctorat de l'université Paris-Saclay

École doctorale n° 576: Particules, hadrons, énergie et noyau :  
instrumentation, imagerie, cosmos et simulation (PHENIICS)

Spécialité de doctorat : Physique des particules

Unité de recherche: Université Paris-Saclay, CEA, Département de Physique Nucléaire,  
91191, Gif-sur-Yvette, France.

Référent: Faculté des sciences d'Orsay

Thèse présentée et soutenue à Paris-Saclay,  
le 26 novembre 2021, par

**Vladimir-George Savu**

Thèse de doctorat

NNT: 2021UPASP120

## Composition du Jury

### **Guillaume MENTION**

Directeur de recherche, IRFU, CEA, Université Paris-Saclay

### **Fabrice PIQUEMAL**

Directeur de recherche, CENBG de Bordeaux-Gradignan

### **Antonin VACHERET**

Professeur des universités, Imperial College London

### **Marco MARTINI**

Professeur, IPSA d'Ivry-sur-Seine

### **Amanda PORTA**

Enseignante-Chercheuse, SUBATECH de Nantes

### **Alain LETOURNEAU**

Directeur de recherche, IRFU, CEA, Université Paris-Saclay

### **David LHUILLIER**

Directeur de recherche, IRFU, CEA, Université Paris-Saclay

Président

Rapporteur & Examineur

Rapporteur & Examineur

Examineur

Examinatrice

Directeur de thèse

Invité

# Acknowledgements

The purpose of this section is to thank the people who have contributed, directly or indirectly, to my training and my development on both a professional and human level, and without whom the accomplishment of this thesis would not have been possible.

I would first like to sincerely thank my thesis supervisor, Alain Letourneau, firstly for offering me the opportunity to work under his supervision, and secondly for always being supportive and encouraging during this turbulent yet enriching three-year journey. I had a lot to learn from the passionate discussions with him on both physics and other subjects and it was his great patience and understanding that helped me overcome many difficult moments and eventually conclude this research work. I am grateful for his advice and suggestions during the writing phase, which resulted in a well-structured and easier to read manuscript.

I would also like to thank David Lhuillier, with whom I collaborated a lot on both STEREO and NUCLEUS, and whose enthusiasm and passion for physics are contagious. I had a lot to learn from the discussions with him and from his impressive physical intuition that has often been crucial in the advancement of the work related to my thesis. I am grateful that he gave me the opportunity to do some hands-on experimental work on NUCLEUS when I was feeling overwhelmed by the arduous coding-related tasks.

I would also like to express my thanks to the two referees of this thesis, Fabrice Piquemal and Antonin Vacheret, for their careful reading of the manuscript and their valuable comments, and to Marco Martini, Guillaume Mention and Amanda Porta for accepting to be part of my jury and for the insightful discussions we had after the defence.

I wish to thank the director of the DPhN department, Franck Sabatié, for making this thesis work possible in excellent conditions and for the useful and empathetic discussions we had during the annual advancement interviews. A big thank you also goes towards all the scientific, technical and administrative staff of DPhN: Danielle Coret and Isabelle Richard, for their help with the administrative procedures and for their constant cheerfulness, Nicolas Pailley for his help with the frequent and annoying hardware problems. A big thank you also goes towards Loïc Thulliez, with whom I had interesting exchanges about art exhibitions and who selflessly accepted to be the "garant technique" for my defence, thus helping me relieve some of the stress related to the D-day.

I would also like to express my sincere gratitude to Marine Vandebrouck, for agreeing to be my tutor and for offering me the opportunity to supervise the NPAC master's experimental projects (TLs), which have allowed me to nourish my pleasure for teaching. Her kindness and the numerous discussions we had helped me see the difficulties that I encountered during the thesis under a different perspective and motivated me to pursue the thesis journey to its end.

I also want to thank all the members of the STEREO collaboration, and particularly those from DPhN for always being available when I had questions about the physics or when I was having a hard time with the codes of STEREO. Among them, Thomas Materna, with whom I collaborated occasionally, was always available to help me with joy and good humour.

I cannot forget my fellow PhD student and good friend, Rudolf Rogly, with whom I shared both the office and the ups and downs of the PhD life for half of my thesis. I will always remember with joy the good time we had together and the funny yet sometimes absurd jokes that we exchanged on a daily basis, be it at the "labo F", in the office or during the several joint missions at the ILL Grenoble. I always admired his optimistic and uplifting nature and I greatly thank him for always being supportive and for listening to me nonjudgmentally when I needed to vent. Finally, I wish him the best of luck in his last year of PhD and I hope he will experience it in an enjoyable way.

I would also like to thank the PhD students that worked on STEREO before me and whom I had the opportunity to meet: Aurélie Bonhomme, who handed me down her work related to the STEREO analysis and who was always ready to answer my eager questions about the details of the codes, and Adrien Blanchet, with whom I had a lot of interesting discussions about literature and politics and who often helped me understand why the STEREO code was not compiling.

In addition, I would also like to thank my fellow PhD students with whom I had the occasion to exchange about the thesis or other interesting subjects during a coffee break or around a beer: Zoé, Robin, Brian, Charles, Aude, Borana ... and I certainly forgot some, but I hope they won't hold it against me.

Many thanks also go to the members of the NUCLEUS collaboration. I am thankful to Victoria Wagner for welcoming me in the Muon Veto group and for her useful suggestions during the weekly online meetings. In the context of NUCLEUS, I also had the pleasure to meet and work with two friendly interns and later PhD students: Andreas Erhart, to whom I am grateful for all the rich discussions we had about the simulations and for his collaboration, and Chloé Goupy, with whom I had the opportunity to work a little on the muon veto prototype, and who I thank for her kindness and for the comic strip featuring Vladimir-kun that she offered me at the end of the thesis and which made me very happy. I wish both of them to have a very successful PhD and to find happiness in their lives and careers.

I am very grateful to my family and friends, who were always by my side and who helped me become the person I am today.

Le sunt foarte recunoscător părinților mei, care au făcut posibil ca eu să cresc într-un mediu plin de dragoste și să urmez calea pe care am ales-o. Vă mulțumesc pentru tot sprijinul pe care mi l-ați acordat și pentru faptul că ați crezut în mine până la capăt.

De asemenea, vreau să-i mulțumesc foarte mult verișoarei mele, Clara, care a fost poarta mea de intrare în Franța și care m-a ajutat foarte mult în primul meu an aici, când am sosit pentru a-mi începe studiile de licență.



There is one particular person, whom I met during the challenging time spent at ENS, and who became a very dear friend since, that I want to greatly thank for all his support, listening and caring: Clément. The almost weekly burger and beer nights spent together before COVID and between its different annoying waves, spiced with amusing and intriguing discussions and jokes, were always a breath of fresh air.

I also want to thank a lot Julian, a cherished friend met during my master's degree. The several videocalls we had were always full of profound exchanges sprinkled with "bêterie"-like amusing jokes. The visit I made to him in Geneva in the middle of the writing phase was great, both because I got the occasion to see him after a long period of time and because it recharged my batteries and helped me conclude the writing of the manuscript.

I want to say a big thank you from my heart to all the close friends who were supportive during all this challenging period and with whom I could share my feelings freely more than once around a glass of wine or through a telephone call: Ana, Lavinia, Giulliana, Mihnea, Matei, Valeriu ...

Last, but not least, I would like to thank from my heart Mariana, who was by my side during all this journey. There are many things for which I could thank her, but I am the most grateful for the fact that she knew how to listen to me without judgment, how to support me with love and how to believe in me even when I didn't believe anymore.



# Contents

<b>Introduction</b>	<b>1</b>
<b>1 Scientific context</b>	<b>3</b>
1.1 Historical context and experimental status . . . . .	4
1.1.1 Beta decay spectrum . . . . .	4
1.1.2 First neutrino detection . . . . .	4
1.2 Neutrino anomalies and neutrino oscillations . . . . .	5
1.2.1 Solar neutrinos and flux anomalies . . . . .	5
1.2.2 Neutrino oscillations formalism . . . . .	11
1.3 Reactor antineutrino anomalies . . . . .	14
1.3.1 Antineutrino production process in a nuclear reactor . . . . .	14
1.3.2 Antineutrino energy spectra prediction . . . . .	17
1.3.3 Reevaluation of the antineutrino spectra . . . . .	20
1.3.4 Reactor antineutrino anomaly (RAA) . . . . .	21
1.3.5 The shape anomaly . . . . .	22
1.4 Current state on the origin of the anomalies . . . . .	23
1.4.1 Sterile neutrino hypothesis . . . . .	23
1.4.2 Kilometre-baseline reactor experiments . . . . .	24
1.4.3 Very short baseline reactor experiments . . . . .	25
1.5 Coherent elastic neutrino-nucleus scattering . . . . .	27
<b>2 Stereo experiment</b>	<b>31</b>
2.1 Experimental site . . . . .	32
2.1.1 The research reactor from ILL . . . . .	32
2.1.2 STEREO positioning inside the reactor hall . . . . .	34
2.2 Neutrino detection . . . . .	35
2.2.1 Inverse beta decay . . . . .	35

---

2.2.2	Scintillation process . . . . .	37
2.2.3	Pulse shape discrimination . . . . .	39
2.3	Detector description . . . . .	41
2.3.1	Inner detector . . . . .	41
2.3.2	Shielding and Muon Veto . . . . .	44
2.3.3	Electronics and acquisition system . . . . .	47
2.3.4	Calibration systems . . . . .	48
2.4	Experiment status . . . . .	51
<b>3</b>	<b>Detector response</b>	<b>53</b>
3.1	Monte Carlo simulation . . . . .	54
3.1.1	Geometry of the detector in Geant 4 . . . . .	54
3.1.2	Particle propagation . . . . .	56
3.1.3	Light generation and collection . . . . .	56
3.1.4	The optical model for the separative plates . . . . .	58
3.1.5	The status of the MC simulation before the fine tuning . . . . .	62
3.2	Fine tuning of the optical parameters of the Monte Carlo . . . . .	64
3.2.1	The gain method . . . . .	65
3.2.2	The global strategy of the fine tuning . . . . .	70
3.2.3	Sensitivity studies . . . . .	72
3.2.4	Results of the fine tuning process . . . . .	78
3.2.5	Cross checks on $^{54}\text{Mn}$ . . . . .	80
3.3	Energy scale . . . . .	85
3.3.1	Energy reconstruction . . . . .	85
3.3.2	Nonlinearities of the energy scale . . . . .	90
3.3.3	Tests and systematics of the energy scale . . . . .	93
3.4	Conclusion . . . . .	102
<b>4</b>	<b>Neutrino signal extraction</b>	<b>103</b>
4.1	Selection cuts for the IBD candidates . . . . .	104

---

4.1.1	Muon tagging . . . . .	105
4.1.2	Energy and topology related cuts . . . . .	106
4.1.3	Time related cuts . . . . .	108
4.1.4	Acceptance of the IBD selection cuts . . . . .	109
4.1.5	Correlated pair search algorithm . . . . .	111
4.1.6	Delayed neutron detection efficiency . . . . .	112
4.2	Background sources . . . . .	116
4.2.1	Pulse shape discrimination . . . . .	116
4.2.2	Accidental and correlated background . . . . .	116
4.2.3	Background correlation with environmental parameters . . . . .	119
4.2.4	Summary of the background sources studies . . . . .	122
4.3	Neutrino extraction methods . . . . .	123
4.3.1	The Saclay method . . . . .	123
4.3.2	The LPSC method . . . . .	131
4.4	Comparison between the LPSC and Saclay methods . . . . .	134
4.4.1	Modified Saclay method . . . . .	135
4.4.2	Comparison between the two neutrino extraction methods . . . . .	139
4.5	Conclusion . . . . .	142
<b>5</b>	<b>Stereo results</b>	<b>143</b>
5.1	Absolute rate . . . . .	144
5.2	Oscillation analysis . . . . .	148
5.3	Unfolded $^{235}\text{U}$ spectrum . . . . .	152
5.3.1	Response matrix . . . . .	152
5.3.2	Systematic uncertainties . . . . .	153
5.3.3	Unfolding procedure . . . . .	155
5.3.4	Unfolded spectrum and bump parameters . . . . .	157
5.4	On the possible origin of the reactor anti-neutrino anomalies . . . . .	159
5.4.1	The summation method . . . . .	159
5.4.2	An empirical beta strength model . . . . .	162

5.4.3	Comparison with STEREO results . . . . .	167
5.5	Conclusion . . . . .	172
<b>6</b>	<b>NUCLEUS experiment</b>	<b>173</b>
6.1	Experimental site . . . . .	174
6.2	Expected background . . . . .	175
6.3	Target detector and shielding . . . . .	175
6.4	Prototype design and performance . . . . .	178
6.5	Conclusion . . . . .	183
<b>7</b>	<b>Muon tracks simulations</b>	<b>185</b>
7.1	Simulation framework . . . . .	186
7.1.1	Geometry . . . . .	186
7.1.2	Simulation algorithm . . . . .	190
7.1.3	Energy loss implementation . . . . .	192
7.2	Observables of interest: efficiency & stopping muons . . . . .	198
7.2.1	Efficiency . . . . .	198
7.2.2	Normalization of the simulation . . . . .	204
7.2.3	Veto muon rate . . . . .	205
7.2.4	Stopping muons . . . . .	207
7.3	Sensitivity studies . . . . .	208
7.3.1	Cryogenic Muon Veto . . . . .	208
7.3.2	Hollow Cylindrical Muon Veto . . . . .	209
7.3.3	Further improvements of the geometry of the Muon Veto . . . . .	211
7.4	Conclusion . . . . .	213
	<b>Conclusion</b>	<b>215</b>
	<b>Appendices</b>	<b>217</b>
	<b>Résumé en français</b>	<b>227</b>
	<b>Bibliography</b>	<b>232</b>

# Introduction

*"En travaux pratiques de physique, n'importe quel collégien peut faire des expériences pour vérifier l'exactitude d'une hypothèse scientifique. Mais l'homme, parce qu'il n'a qu'une seule vie, n'a aucune possibilité de vérifier l'hypothèse par l'expérience de sorte qu'il ne saura jamais s'il a eu tort ou raison d'obéir à son sentiment."*

L'Insoutenable Légèreté de l'être, *Milan Kundera*

Since it was first postulated in 1930 and then detected in 1955, the neutrino has never ceased to amaze physicists with its unexpected behaviour and to drive experimental progress aimed at exploring its properties. Neutrinos interact through the weak force and are always created along with a charged lepton ( $e$ ,  $\mu$ ,  $\tau$ ) that determines their flavour. One of the most fascinating properties of neutrinos is that they can "oscillate" between flavours, which translates as the fact that there is a non-zero probability that an initially created  $\nu_\alpha$  is detected as a  $\nu_\beta$  during its propagation. The oscillation phenomenon implies that at least two out of the three neutrinos are massive, representing the first evidence of physics beyond the Standard Model, in which the neutrinos are considered massless. Even though plenty of progress has been done in the field of neutrino physics, a series of questions still needs to be answered: is the neutrino its own antiparticle? What is the mechanism at the origin of the neutrino mass? What is the neutrino absolute mass scale and mass hierarchy? Is the CP symmetry violated in the leptonic sector?

Since the beginning, reactor neutrino experiments have played an important role in the understanding of neutrino properties: from their discovery to the precise study of their propagation, leading to the discovery of short baseline neutrino oscillations. Nuclear reactors are very powerful sources of pure electron antineutrinos, with a quite well known energy distribution, which allow high statistics measurements. They could help solve burning questions related to the neutrino propagation at short baselines and its interactions on nuclei, thus being able to search for potential deviations from the Standard Model.

On the one hand, a recent reevaluation of the reactor antineutrino spectra performed in 2011 highlighted a  $\sim 6\%$  deficit in the measured antineutrino absolute rate with respect to the prediction, which became known as the Reactor Antineutrino Anomaly (RAA). One possible solution to the RAA could be provided by the existence of a sterile neutrino that doesn't interact with any of the fundamental interactions of the Standard Model. In this context, the observed deficit would be explained by an oscillation of the reactor antineutrinos towards this new sterile neutrino.

On the other hand, neutrinos can scatter off atomic nuclei through the exchange of neutral Z bosons. For small neutrino energies ( $<30$  MeV), the scattering is coherent over all the nucleons found in a nucleus and is denoted coherent elastic neutrino nucleus scattering (CE $\nu$ NS). The CE $\nu$ NS cross-section is more than two orders of magnitude bigger than the IBD cross-section, but its detection is made difficult by the small energy of the induced nuclear recoils, which represent the only measurable observable. The first detection of CE $\nu$ NS was reported by the COHERENT collaboration in September 2017 using accelerator neutrinos with energies up to 50 MeV.

The work performed during this thesis covers both sterile neutrino searches and CE $\nu$ NS interactions by contributing to the analysis and interpretation of results for the STEREO experiment and to the definition of the NUCLEUS experiment.

The STEREO experiment is aimed at testing the hypothesis that an oscillation towards a sterile neutrino with a mass of  $\sim 1$  eV/ $c^2$  could explain the RAA. It uses a segmented detector, placed at  $\sim 10$  m from the quasi-pure  $^{235}\text{U}$  core of the research reactor of ILL in Grenoble, to detect antineutrinos through the inverse beta decay (IBD) reaction. A prediction-independent relative comparison between the spectra measured in the different cells is then performed in order to test the appearance of an oscillation pattern.

The NUCLEUS experiment is aimed at measuring CE $\nu$ NS induced by reactor antineutrinos, thus probing nuclear-recoil energies down to 10 eV. It will be placed near the Chooz nuclear power plant in France and will employ cryogenic detectors with an unequaled low energy threshold to detect the nuclear recoils induced by the antineutrinos.

After a general introduction to the oscillation mechanism of neutrinos, the CE $\nu$ NS interactions and the reactor antineutrino anomalies in chapter 1, the work performed in this thesis is described in the following chapters.

The STEREO-related work focuses on two aspects of the STEREO analysis : the fine-tuning of the Monte Carlo simulation of the detector and the extraction of the  $\bar{\nu}_e$  signal using a modelization of the reactor-off and reactor-on Pulse Shape Discrimination (PSD) distributions.

The simulation fine-tuning, along with the energy scale stability and systematics are presented in chapter 3, after a description of the STEREO experiment in chapter 2.

The work on the  $\bar{\nu}_e$  signal extraction, along with the IBD selection cuts and the background characterization for STEREO are presented in chapter 4.

The results of the STEREO experiment, along with an improvement of the prediction developed in this work to test the origin of the anomalies are presented in chapter 5.

The NUCLEUS-related work is centered on the construction of a muon veto with a simulation-based study aimed at estimating its efficiency and finding its optimal configuration, presented in chapter 7. The NUCLEUS experiment, along with the description of the muon veto prototype tested in this work are presented in chapter 6.



# Chapter 1

## Scientific context

*" Neutrinos, they are very small. They have no charge and have no mass And do not interact at all. The earth is just a silly ball To them, through which they simply pass, Like dustmaids down a drafty hall Or photons through a sheet of glass. They snub the most exquisite gas, Ignore the most substantial wall, Cold-shoulder steel and sounding brass, Insult the stallion in his stall, And, scorning barriers of class, Infiltrate you and me! Like tall And painless guillotines, they fall Down through our heads into the grass. At night, they enter at Nepal And pierce the lover and his lass From underneath the bed - you call It wonderful; I call it crass."*

Cosmic gall, John Updike

## Sommaire

---

<b>1.1</b>	<b>Historical context and experimental status . . . . .</b>	<b>4</b>
1.1.1	Beta decay spectrum . . . . .	4
1.1.2	First neutrino detection . . . . .	4
<b>1.2</b>	<b>Neutrino anomalies and neutrino oscillations . . . . .</b>	<b>5</b>
1.2.1	Solar neutrinos and flux anomalies . . . . .	5
1.2.2	Neutrino oscillations formalism . . . . .	11
<b>1.3</b>	<b>Reactor antineutrino anomalies . . . . .</b>	<b>14</b>
1.3.1	Antineutrino production process in a nuclear reactor . . . . .	14
1.3.2	Antineutrino energy spectra prediction . . . . .	17
1.3.3	Reevaluation of the antineutrino spectra . . . . .	20
1.3.4	Reactor antineutrino anomaly (RAA) . . . . .	21
1.3.5	The shape anomaly . . . . .	22
<b>1.4</b>	<b>Current state on the origin of the anomalies . . . . .</b>	<b>23</b>
1.4.1	Sterile neutrino hypothesis . . . . .	23
1.4.2	Kilometre-baseline reactor experiments . . . . .	24
1.4.3	Very short baseline reactor experiments . . . . .	25
<b>1.5</b>	<b>Coherent elastic neutrino-nucleus scattering . . . . .</b>	<b>27</b>

---

## 1.1 Historical context and experimental status

### 1.1.1 Beta decay spectrum

In 1914 James Chadwick observed experimentally, using a Geiger counter, that the  $\beta$  spectrum of a decay of a radioactive element is continuous [1]. At the time it was known that the  $\gamma$  and  $\alpha$  spectra were discrete and it was thought that the  $\beta$  spectrum should be discrete as well, as expected in the case of a two body decay. Thus, the continuous aspect of the  $\beta$  spectrum raised an important question: *is energy conservation violated at the atomic level?*<sup>1</sup> In 1930, Wolfgang Pauli postulated in an open letter that there must be another electrically neutral, spin 1/2, low mass fermion, that must be emitted along with the electron during a  $\beta$  decay, and proposed that it is named *neutron*, in analogy to the proton [4]. However, the name was changed soon after Chadwick's discovery in 1932 [5] of a new electrically neutral, strong interacting particle, with the mass similar to the proton's mass, for which the name *neutron* was more suitable. The name *neutrino* was proposed by Enrico Fermi and it meant "little neutral one", as he supposed that it has a very small mass. It was Fermi who, in 1932, developed the first theory that describes the  $\beta$  decay using a pointlike interaction between a neutron, a proton, an electron and an antineutrino:  $n \rightarrow p + e^- + \bar{\nu}_e$  [6].

### 1.1.2 First neutrino detection

Pauli did not think that the neutrino could be observed experimentally because of its low interaction probability: "I have done a terrible thing. I have postulated a particle that cannot be detected". Nonetheless, in the beginning of the 1950's F. Reines and C.L. Cowan Jr did an experiment at the Savannah River nuclear reactor in South Carolina during which they observed interactions between antineutrinos produced in the reactor and protons from the liquid scintillator detector [7]. The reaction in question is called inverse beta decay (IBD) and gives rise to a positron and a neutron:  $\bar{\nu}_e + p \rightarrow e^+ + n$ . The positron loses its energy through electromagnetic interactions and then annihilates with an electron to create two gamma rays of 511 keV. Then, after a few microseconds, a new gamma ray is emitted following the deexcitation of a nucleus that captured the neutron. This "delayed coincidence" of two signals separated by a time lapse helped reducing the background signal and thus allowed the experiment to be done near a reactor<sup>2</sup>. With a signal over background ratio of 3 to 1, the experiment measured a rate of  $2.88 \pm 0.22$  antineutrinos per hour [8] and thus confirmed experimentally the existence

<sup>1</sup>In 1924, Niels Bohr published a phenomenological interpretation of  $\beta$  radioactivity in which he proposed that the energy is only statistically conserved [2]. Even though this theory was invalidated quickly, the idea of a local violation of the energy conservation principle remained as a possible explanation for about 10 years [3].

<sup>2</sup>Initially, the experiment was designed to take place near the explosion of an atomic bomb, which presented a real technical challenge. Fortunately, the measurement of the "delayed coincidence" of the two signals produced by an inverse beta decay made possible the use of the less intense neutrino flux from a reactor.

of (anti)neutrinos. Moreover, the experiment provided the most precise estimation of the IBD cross section at that time:  $\sigma_{IBD} = 6.3 \times 10^{-44} \text{ cm}^2$ . The IBD reaction is the most used interaction channel for the detection of reactor antineutrinos and will also be the one used by STEREO.

## 1.2 Neutrino anomalies and neutrino oscillations

Today, we know that there are 3 active species of neutrinos, corresponding to the 3 Standard Model charged leptons, the electron, the muon and the tau, denoted by  $\nu_e$ ,  $\nu_\mu$  and  $\nu_\tau$ . The  $\nu_\mu$  was postulated by Bruno Pontecorvo and detected in 1962 at Brookhaven [9], while the  $\nu_\tau$  was detected more recently, in 2000, at the DONUT experiment from Fermilab [10]. Moreover, we know that the neutrinos created along with a charged lepton during a charged-current process are not eigenstates of the time evolution Hamiltonian, but linear combinations of mass eigenstates. This explains the phenomenon of neutrino oscillations, which makes possible, for example, to detect an initially created electron neutrino as a muon neutrino. This phenomenon, confirmed experimentally by the Super-Kamiokande experiment in 1998, provides a solution to the Solar Neutrino Problem, i.e. the fact that the solar neutrino experiments detected less electron neutrinos than the number predicted by the Standard Solar Model [11]. The experimental "anomalies" that led to the discovery of the neutrino oscillations will be presented in the first part of this section, while the formalism used to describe the oscillations will be introduced in the second part.

### 1.2.1 Solar neutrinos and flux anomalies

#### Solar neutrinos

The total flux of solar electron neutrinos is of  $\sim 2 \times 10^{38} \nu_e \text{ s}^{-1}$  and is due to the nuclear fusion that takes place in the Sun. The proton-proton (pp) cycle showed in figure 1.1 produces around 99% of the energy of the Sun and is also the most important source of solar electron neutrinos  $\nu_e$ . The other source of electron neutrinos in the Sun is the CNO (carbon-nitrogen-oxygen) cycle, which produces around 1% of the energy of the Sun.

The neutrino generating reactions that take place in the Sun can be summarized by the following reaction, which describes the combination of 4 protons and 2 electrons to produce a Helium-4 nucleus and 2 electron neutrinos:  $4p + 2e^- \rightarrow {}^4\text{He} + 2\nu_e$ . The total energy released by such a reaction is equal to  $Q = 4m_p + 2m_e - m_{\text{He}} = 26.73 \text{ MeV}$  and represents the kinetic energy of the final state particles. A part of the energy is taken by the neutrinos that escape from the Sun, while the remaining part represents the thermal energy of the Sun. Using the solar luminosity  $L$ , the flux of solar neutrinos that reach the Earth can be expressed as:

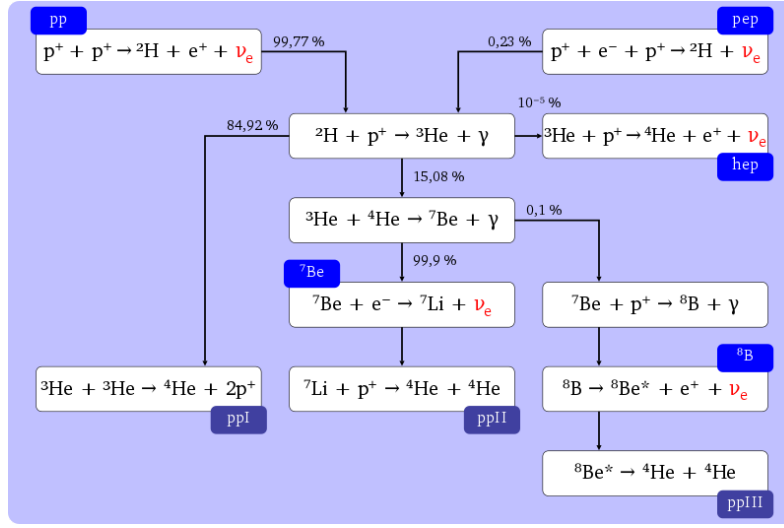


Figure 1.1 – The pp chain with the theoretical branching percentages which define the relative rates of the competing reactions.

$$\Phi_{\nu_e} \sim \frac{1}{4\pi d^2} \frac{2L}{(Q - \langle E_\nu \rangle)} \quad (1.2.1)$$

with the luminosity  $L = 3.842 \times 10^{26}$  J/s, the distance between the Sun and the Earth  $d \sim 1.495 \times 10^{13}$  cm and the average energy of a neutrino in a fusion cycle  $\langle E_\nu \rangle \sim 0.3$  MeV. The flux of neutrinos that reach the Earth<sup>3</sup> is  $\Phi_{\nu_e} \sim 6 \times 10^{10} \text{ cm}^{-2}\text{s}^{-1}$ .

## Homestake

The experiment took place in the Homestake Mine in South Dakota, USA, and its detection system was based on the inverse  $\beta$ -decay reaction  $\nu_e + {}^{37}_{17}\text{Cl} \rightarrow {}^{37}_{18}\text{Ar} + e^-$ . This reaction has a threshold energy of 0.814 MeV and thus the experiment is essentially sensitive to the neutrinos created in the decay of  ${}^8\text{B}$  inside the Sun, as seen in figure 1.2, which shows the Standard Solar Model predictions for the neutrino fluxes.

The final average value of the solar neutrino rate obtained by Homestake was published in 1998 [13], after more than 25 years of activity, and was of  $2.56 \pm 0.25 \text{ SNU}^4$ , while the Standard solar models of the time predicted that Homestake should have seen about  $8.1 \pm 1.2 \text{ SNU}$ . The neutrino rate measured by the Homestake experiment was three times smaller than the prediction of the Standard Solar Model of the time and this difference

<sup>3</sup>The main contribution for this calculation comes from the pp and pep reactions, but it's a good approximation for the total neutrino flux because the other reactions that create neutrinos in the Sun give rise to a much smaller flux.

<sup>4</sup>1 SNU =  $10^{-36}$  neutrino interactions per target atom per second.

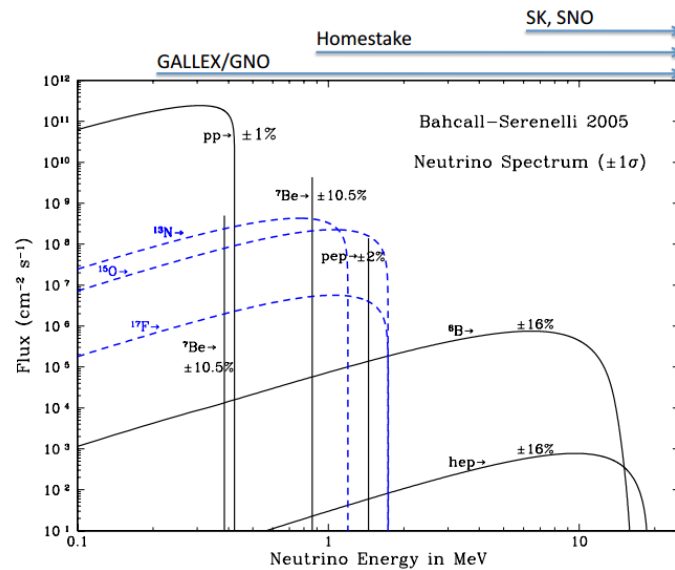


Figure 1.2 – The Standard Solar Model predictions for the neutrino fluxes. In the upper part of the figure we can see the thresholds for some solar experiments. Source: [12].

became known as the Solar Neutrino Problem<sup>5</sup>.

## Kamiokande

The Kamioka Nucleon Decay Experiment (Kamiokande) was built initially to search for nucleon decay but was also capable to measure the solar neutrino flux from  ${}^8\text{B}$  through the elastic scattering reaction<sup>6</sup>  $\nu_x + e^- \rightarrow \nu_x + e^-$  inside a water Cerenkov detector. It was the first detector able to observe in real time the flux of  ${}^8\text{B}$  solar neutrinos and to give information about the arrival time, the direction, and the energy spectrum of the incoming neutrinos.

The measured value of the  ${}^8\text{B}$  neutrino flux was found to be around 46% of the value predicted by the Standard Solar Model [16]. Moreover, Super Kamiokande [17], the next-generation detector that followed Kamiokande, was also able to reconstruct the incoming direction of the neutrinos and prove that there is a peak in the Sun's direction, which showed that the neutrinos that were measured came indeed from the Sun.

<sup>5</sup>The Nobel Prize in Physics 2002 was divided, one half jointly to Raymond Davis Jr.(Homestake) and Masatoshi Koshiba (Kamiokande-II) "for pioneering contributions to astrophysics, in particular for the detection of cosmic neutrinos" (see [14],[15]) and the other half to Riccardo Giacconi "for pioneering contributions to astrophysics, which have led to the discovery of cosmic X-ray sources".

<sup>6</sup>The x stands for e,  $\mu$  and  $\tau$  because the reaction is possible for all the three neutrino flavours through neutral current processes. However, the cross section for  $\nu_e$  is 6 times bigger than the cross section for  $\nu_\mu$  and  $\nu_\tau$  because of the additional contribution from charged current processes.

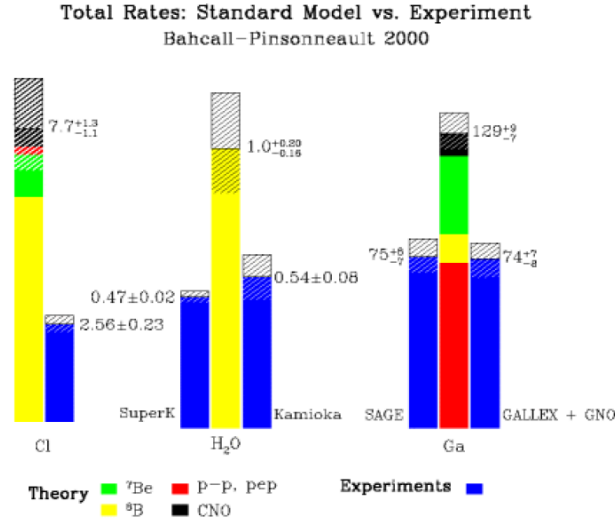


Figure 1.3 – Results of the solar neutrino experiments that preceded SNO: Chlorine on the left, water in the middle and Gallium on the right. The blue bar represents the experimental results in SNU, while the middle bar represents the prediction of the Standard Solar Model. We see that all experiments reported a smaller flux than predicted by the Standard Solar Model.

### SAGE and GALLEX

We have seen that Homestake and Kamiokande experiments were essentially sensitive to the  $^8\text{B}$  neutrinos (with a small contribution from the hep neutrinos, see Figure 1.2). SAGE [18] and GALLEX [19] were two experiments that used Gallium as a target and were able to observe a part of the low-energy pp neutrinos, since the reaction  $\nu_e + {}^{71}\text{Ga} \rightarrow {}^{71}\text{Ge} + e^-$  has an energy threshold of 0.233 MeV.

SAGE observed a flux of  $(75 \pm 6)$  SNU, while the Standard Solar Model predicted value was of  $(129 \pm 9)$  SNU. GALLEX observed a flux of  $(74 \pm 7)$  SNU. This time, the observations were lower than the prediction by about 40%. The importance of these two experiments lies in the fact that they confirmed the energy dependence of the deficit of solar neutrinos observed on Earth. Thus, the Solar Neutrino Problem can be fully defined as the energy dependent deficit of solar neutrinos observed on Earth with respect to the Standard Solar Model predictions.

All the experiments presented until now showed a clear deficit of solar neutrinos, as summarized in figure 1.3. Moreover, it has been observed that the lower the energy threshold, the smaller the difference with respect to the Standard Solar Model. This problem could have had two possible origins: either the Standard Solar Model was not accurate or there was something happening with the neutrinos on their way to the Earth. It turned out that the second alternative was the right one, i.e. neutrinos can "change" flavours during their propagation between their source, the Sun, and the detection point on Earth. This was confirmed exactly by the Super Kamiokande experiment, which gave solid evidence for the oscillation of atmospheric neutrinos [20] and by the SNO (Sudbury

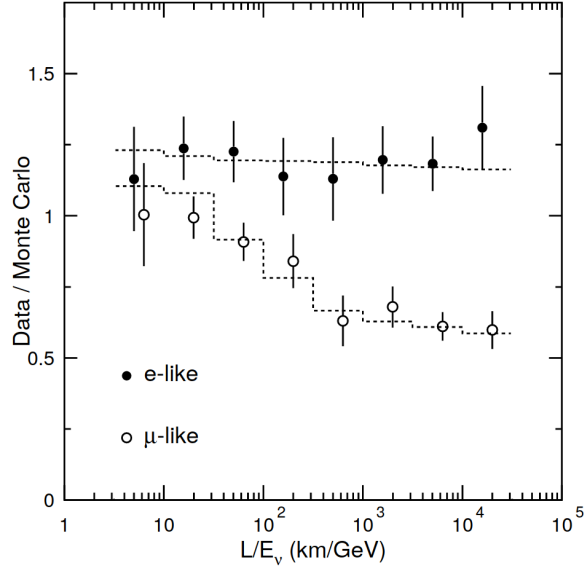


Figure 1.4 – Ratio between observed and predicted fluxes of electron and muon neutrinos (without taking into account oscillations) as a function of the  $L/E_\nu$  ratio. The dotted lines show the ratio including a  $\nu_\mu \leftrightarrow \nu_\tau$  oscillation. Source: [20].

Neutrino Observatory) experiment, which was able to probe the solar neutrino flux in a way that is independent from the flavour of the incoming neutrino, i.e. it was also able to measure the fluxes of  $\nu_\mu$  and  $\nu_\tau$ <sup>7</sup>.

### Super Kamiokande

Super Kamiokande used a Cerenkov detector filled with 55000 tons of water to detect atmospheric neutrinos<sup>8</sup>. It was capable to differentiate between electron and muon neutrinos through the interaction

$$\nu_\alpha + N \rightarrow \alpha + X \quad (1.2.2)$$

by detecting the outgoing lepton  $\alpha = e, \mu$  via the form of the Cerenkov ring it created. Furthermore, the inclination of the Cerenkov ring also gave access to the direction of the incoming neutrino, thus allowing to deduce the propagation distance between its creation point in the atmosphere and the detector. To get rid of the theoretical and experimental uncertainties, the ratio

<sup>7</sup>The Nobel prize in Physics for 2015 was awarded to Takaaki Kajita (Super-Kamiokande Collaboration) from University of Tokyo, Kashiwa, Japan and to Arthur B. McDonald (Sudbury Neutrino Observatory Collaboration) from Queen's University, Kingston, Canada "for the discovery of neutrino oscillations, which shows that neutrinos have mass".

<sup>8</sup>The creation of atmospheric electron and muon neutrinos is essentially dominated by the reactions  $\pi^+ \rightarrow \mu^+ + \nu_\mu$  and  $\mu^+ \rightarrow e^+ + \bar{\nu}_\mu + \nu_e$ .

$$R_{\mu/e} = \frac{(N_{\mu}/N_e)_{exp}}{(N_{\mu}/N_e)_{pred}} \quad (1.2.3)$$

was computed and it turned out to be inferior to 1, which meant that there was a deficit of muon neutrinos with respect to the prediction. Figure 1.4 shows the data/predicted flux of electron and muon neutrinos as a function of the  $L/E_{\nu}$  ratio, where  $L$  is the propagation distance of the neutrino and  $E_{\nu}$  is its energy. While the  $\nu_e$  flux respects the prediction, the  $\nu_{\mu}$  flux decreases with  $L/E_{\nu}$ , which represents the first "real" observation of neutrino oscillations. In section 1.2.2, where the neutrino oscillation formalism will be presented, we will see how oscillation probability depends on the  $L/E_{\nu}$  ratio.

## SNO

All the solar experiments presented in the previous sections used charged current interactions of the form  $\nu_e + X \rightarrow e^- + Y$  to detect solar neutrinos. However, the energies of the solar neutrinos have a maximum value of about 20 MeV, while the muon mass, for example, is of 105 MeV. Hence, the charged current (CC) interactions can only be used to observe electron neutrinos because the muon and tau neutrinos do not have a sufficient energy to interact via CC and create the charged leptons  $\mu$  and  $\tau$ .

The SNO detector [21], based in Canada, finally provided a way to detect all flavours of neutrinos. It used a tank of heavy water (1000 tons) as its target and was viewed by 9600 photo-multiplier tubes. Heavy water,  $D_2O$ , contains deuterium, which is a very fragile nucleus with a binding energy of just 2.2 MeV. This allows any of the three neutrino flavours to break apart the deuteron in a neutral current (NC) interaction. The three different channels that SNO used to detect neutrinos are the following:

1. The elastic scattering  $\nu + e^- \rightarrow \nu + e^-$ , in which the electron neutrinos  $\nu_e$  can interact via CC and NC interactions, while muon and tau neutrinos,  $\nu_{\mu}$  and  $\nu_{\tau}$  can only interact via NC interactions. The neutrino flux probed by this relation is

$$\Phi_{ES} = \Phi(\nu_e) + 0.154(\Phi(\nu_{\mu}) + \Phi(\nu_{\tau})) \quad (1.2.4)$$

2. The charged current channel  $\nu_e + D \rightarrow p + p + e^-$ , in which only electron neutrinos  $\nu_e$  take part and thus can only measure  $\Phi(\nu_e)$

$$\Phi_{CC} = \Phi(\nu_e) \quad (1.2.5)$$

3. The neutral current channel  $\nu + D \rightarrow n + p + \nu$ , which is equally sensitive to all neutrino flavours and allows thus to measure the flux

$$\Phi_{NC} = \Phi(\nu_e) + \Phi(\nu_{\mu}) + \Phi(\nu_{\tau}) \quad (1.2.6)$$

The measurement of neutrino fluxes, given in  $10^6 \text{ cm}^{-2}\text{s}^{-1}$  were [22]



$$\Phi_{CC} = 1.76 \pm 0.1 \quad (1.2.7)$$

$$\Phi_{ES} = 2.39 \pm 0.26 \quad (1.2.8)$$

$$\Phi_{NC} = 5.09 \pm 0.63 \quad (1.2.9)$$

The total flux of muon and tau neutrinos from the Sun is thus 3 times larger than the flux of electron neutrinos. Since the Sun only produces  $\nu_e$ , neutrinos must change flavour between the Sun and the Earth. Moreover, the Standard Solar Model predicts a flux of electron neutrinos created in the Sun of  $\Phi_{e,pred} = 5.1 \pm 0.9 \times 10^6 \text{ cm}^{-2}\text{s}^{-1}$  which agrees very well with  $\Phi_{NC}$  measured by SNO.

A summary of the results obtained by the experiments detecting solar neutrinos is shown in figure 1.5, where the results from the Borexino experiment [23] are also included. The prediction taking into account the vacuum oscillation mechanism and the MSW effect<sup>9</sup> is plotted along with the survival probability for the electron neutrinos, i.e. the ratio between the detected and predicted flux of electron neutrinos without taking into account any oscillation. The low-energy ( $<2 \text{ MeV}$ ) solar neutrinos are suppressed by averaged vacuum oscillations ( $P(\nu_e \rightarrow \nu_e) \sim 1 - \frac{1}{2} \sin^2 2\theta_{Sun} \sim 0.57$ ), while neutrinos which have an energy bigger than 4 MeV are suppressed due to the MSW effect. In fact, the neutrinos of high energy ( $>4 \text{ MeV}$ ) leaving the Sun are in the mass eigenstate  $\nu_2$ , which remains unchanged until they reach the Earth, and the probability to detect a  $\nu_e$  on Earth is thus given by the projection  $|\langle \nu_e | \nu_2 \rangle|^2 \sim \sin^2(2\theta_{Sun}) \sim 0.3$ .

The experimental results presented in this section proved that neutrinos can change their flavour as they propagate through vacuum or matter and represented one of the first proofs of physics beyond the Standard Model. This is because neutrinos are considered to be massless in the Standard Model and, as will be discussed in the next section, one of the requirements that make the oscillation mechanism possible is that the neutrinos have non zero masses.

### 1.2.2 Neutrino oscillations formalism

Neutrino oscillations are due to the fact that the flavour eigenstates, i.e. the states in which neutrinos are created along with a charged lepton at a weak interaction vertex, do not coincide with the mass eigenstates. A flavour eigenstate can be written as a linear superposition of mass eigenstates. In the 3-neutrino case, the relation between the flavour and mass eigenstates is the following

---

<sup>9</sup>The MSW (Mikheyev-Smirnov-Wolfenstein) [24] effect is the adiabatic or partially adiabatic neutrino flavor conversion in a medium with varying density and is due to the neutrino interactions with the electrons from the medium (it becomes important for media with a very high density, such as the Sun).

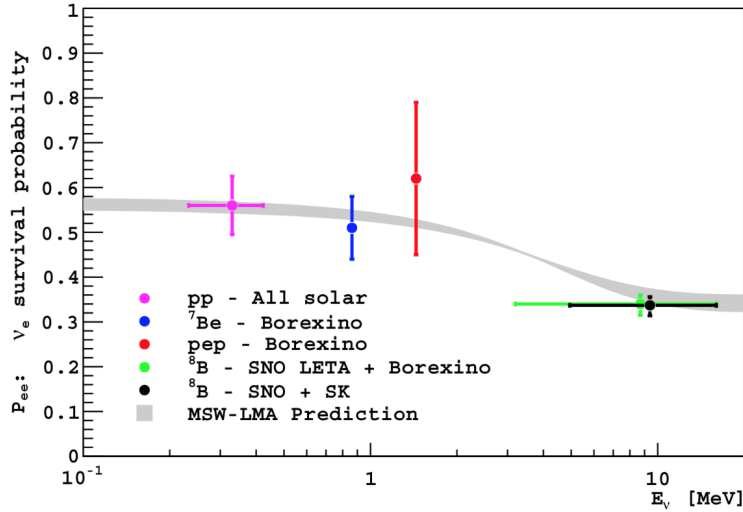


Figure 1.5 –  $\nu_e$  survival probability as a function of the neutrino energy  $E_\nu$ . The grey band represents the prediction, which takes into account both the vacuum oscillations and the MSW matter effect. Source: [25].

$$\begin{pmatrix} \nu_e \\ \nu_\mu \\ \nu_\tau \end{pmatrix} = \underbrace{\begin{pmatrix} U_{e1} & U_{e2} & U_{e3} \\ U_{\mu1} & U_{\mu2} & U_{\mu3} \\ U_{\tau1} & U_{\tau2} & U_{\tau3} \end{pmatrix}}_{U_{PMNS}} \begin{pmatrix} \nu_1 \\ \nu_2 \\ \nu_3 \end{pmatrix} \quad (1.2.10)$$

where  $U_{PMNS}$ , the Pontecorvo-Maki-Nakagawa-Sakata mixing matrix, is unitary and complex. From these properties it follows that  $U_{PMNS}$  can be parametrized using 3 real mixing angles:  $\theta_{12}$ ,  $\theta_{13}$ ,  $\theta_{23}$ , and one CP violating phase,  $\delta_{CP}$ , which gives rise to a complex term of the form  $e^{-i\delta_{CP}}$  in the mixing matrix<sup>10</sup>.

Supposing that a neutrino of flavour  $\alpha$ , where  $\alpha = e, \mu, \tau$ , is created at a weak interaction vertex, we can write its state as the following linear combination of mass eigenstates

$$|\nu_\alpha\rangle = U_{\alpha1}^* |\nu_1\rangle + U_{\alpha2}^* |\nu_2\rangle + U_{\alpha3}^* |\nu_3\rangle \quad (1.2.11)$$

During the propagation, each of the mass eigenstates will develop a phase<sup>11</sup> that will change with time. If the masses of the neutrinos are different, then the relative phases between the mass eigenstates will change with the propagation distance, thus giving rise to the oscillation phenomenon. The probability that an initially created  $\nu_\alpha$  is detected

<sup>10</sup>If neutrinos are Majorana fermions, i.e. they are their own antiparticles, then we should add two more phases in the mixing matrix. However, these two new phases do not affect the oscillation phenomenon and thus will not be taken into account during the present discussion.

<sup>11</sup>That is because the mass eigenstates are the eigenstates of the free-particle Hamiltonian  $\hat{H}\psi = i\frac{d\psi}{dt} = E\psi$ , whose solutions are of the form  $\psi(\mathbf{x}, t) = \phi(\mathbf{x})e^{-iEt}$ .

at a distance  $L$  from the source as a  $\nu_\beta$  is obtained by the projection  $|\langle \nu_\beta | \nu_\alpha(t) \rangle|^2$  and is given by the following expression

$$P(\nu_\alpha \rightarrow \nu_\beta; L) = \delta_{\alpha\beta} - 4 \sum_{i>j} \text{Re}(U_{\alpha i} U_{\beta i}^* U_{\alpha j}^* U_{\beta j}) \sin^2 \left( \frac{\Delta m_{ji}^2 L}{4E} \right) + 2 \sum_{i>j} \text{Im}(U_{\alpha i} U_{\beta i}^* U_{\alpha j}^* U_{\beta j}) \sin \left( \frac{\Delta m_{ji}^2 L}{2E} \right) \quad (1.2.12)$$

where  $i, j = 1, 2, 3$ ,  $m_i$  is the mass of the state  $|\nu_i\rangle$ ,  $\Delta m_{ji}^2 = m_j^2 - m_i^2$  and  $E$  is the energy of the neutrino. For antineutrino oscillations, the last term in equation 1.2.12 gets a minus sign.

It is worth discussing the implications of equation 1.2.12. First of all, we observe that in order to have oscillations  $\Delta m_{ji}^2 \neq 0$  at least for some  $j$  and  $i$  and that  $U = U_{PMNS} \neq 1$ . Moreover, the oscillation probability depends on two independent oscillation frequencies, since we can always express one squared mass difference as a function of the two others, i.e. we can write  $\Delta m_{32}^2 = \Delta m_{31}^2 - \Delta m_{21}^2$  for instance. Looking at expression 1.2.12, we can also conclude that neutrino oscillation experiments can give information about the mass squared differences  $\Delta m_{ji}^2$ , but not about the absolute values of the masses or about which of the masses is bigger (because the probability  $P(\nu_\alpha \rightarrow \nu_\beta; L)$  remains the same under the transformation  $\Delta m_{ji}^2 \rightarrow -\Delta m_{ji}^2$ ).

Each mixing angle dominates the oscillation process in a certain region defined by the ratio between the energy of the neutrino  $E$  and the distance between the source and the detector  $L$ . This is the reason why in the literature we call  $\theta_{12}$  the solar mixing angle,  $\theta_{13}$  the reactor mixing angle and  $\theta_{23}$  the atmospheric mixing angle. Moreover, the squared mass differences are sufficiently different that in practice most of the experiments are only sensitive to a certain pair of parameters  $(\Delta m^2, \theta)$ , which allows us to work in a 2-flavour approximation, where the mixing matrix depends on a single parameter, denoted by  $\theta$

$$U = \begin{pmatrix} \cos(\theta) & \sin(\theta) \\ -\sin(\theta) & \cos(\theta) \end{pmatrix} \quad (1.2.13)$$

The expression of the survival probability in units adapted to reactor antineutrinos that interest us is the following

$$P(\nu_\alpha \rightarrow \nu_\alpha) = 1 - \sin^2(2\theta) \sin^2 \left( 1.27 \frac{\Delta m^2 [eV^2] L [m]}{E [MeV]} \right) \quad (1.2.14)$$

In this approximation, the oscillation probability for neutrinos is the same as that for antineutrinos, since there is no phase in the mixing matrix. It can be deduced from equation 1.2.14 that, for a fixed neutrino energy, the oscillation probability varies periodically as a function of the source-detector distance. In order to reach the maximum of

sensitivity, an experiment should be placed at a distance  $L$  such that the phase of the second sine in equation 1.2.14 is close to  $\pi/2$ , i.e.  $L \sim L_{osc}/2$ , where  $L_{osc} = 4\pi E/\Delta m^2$ . For  $L/E \ll \Delta m^2$  the oscillation does not have the time to develop yet, while for  $L/E \gg \Delta m^2$  the oscillation will be averaged due to the limited resolution in energy and position of the detector.

Currently, all the mixing angles of the PMNS mixing matrix and the squared mass differences of the mass eigenstates are well known [26]<sup>12</sup>, the only remaining parameter to be determined being the CP violating phase  $\delta_{CP}$ . There are hints that  $\delta_{CP} \neq 0, \pi$  from T2K experiment [27], with a preference for values of  $\delta_{CP}$  that are near maximal CP violation.

Even though a lot of progress has been done in neutrino physics lately, it still remains one of the most prolific research domains, with a number of questions that have not been answered yet. The main current goals of neutrino physics are the determination of the mass hierarchy and of the absolute mass scale, the measurement of the degree of CP violation in the leptonic sector, which could provide an explanation for the excess of matter over anti-matter in the Universe, and the search for the neutrinoless double beta decay, which could be evidence of physics beyond the Standard Model of particle physics, since it would imply that the lepton number is not conserved. Furthermore, the observation of the neutrinoless double beta decay reaction would also prove that neutrinos are Majorana particles.

## 1.3 Reactor antineutrino anomalies

### 1.3.1 Antineutrino production process in a nuclear reactor

A nuclear reactor works by exploiting the energy released during nuclear fission reactions. During these reactions, a nucleus splits into two smaller nuclei, called fission fragments. There are two types of fission reactions: spontaneous, which is possible for a few rare heavy isotopes, and induced, in which case the additional energy brought by an incident neutron allows the nucleus to overpass the fission barrier. The isotopes that can undergo nuclear fission are said to be fissile. The share of nucleons between the two daughter nuclei is not symmetrical and is illustrated in figure 1.6 for a  $^{235}\text{U}$  nucleus. The energy released during a fission reaction mainly corresponds to the difference in binding energy between the initial nucleus and the two daughter nuclei and is transmitted as kinetic energy to the fission fragments. Since the fission fragments are rich in neutrons (see figure 1.6), they return to the stability valley by successive beta decays, which are the main source of reactor antineutrinos. The mean number of beta decays that a fission fragment undergoes is equal to 3, which means that there are 6 antineutrinos emitted on average for every

<sup>12</sup>The squared mass difference  $\Delta m_{31}^2$  is known only as an absolute value. Its sign would establish the hierarchy of neutrino masses, i.e. normal hierarchy for  $m_1 < m_2 < m_3$  ( $\Delta m_{31}^2 > 0$ ) or inverted hierarchy for  $m_3 < m_1 < m_2$  ( $\Delta m_{31}^2 < 0$ ). Solar neutrino experiments were able to conclude that  $\Delta m_{21}^2 > 0$ , since the rate of solar neutrinos detected on Earth depends on the sign of  $\Delta m_{21}^2$ .

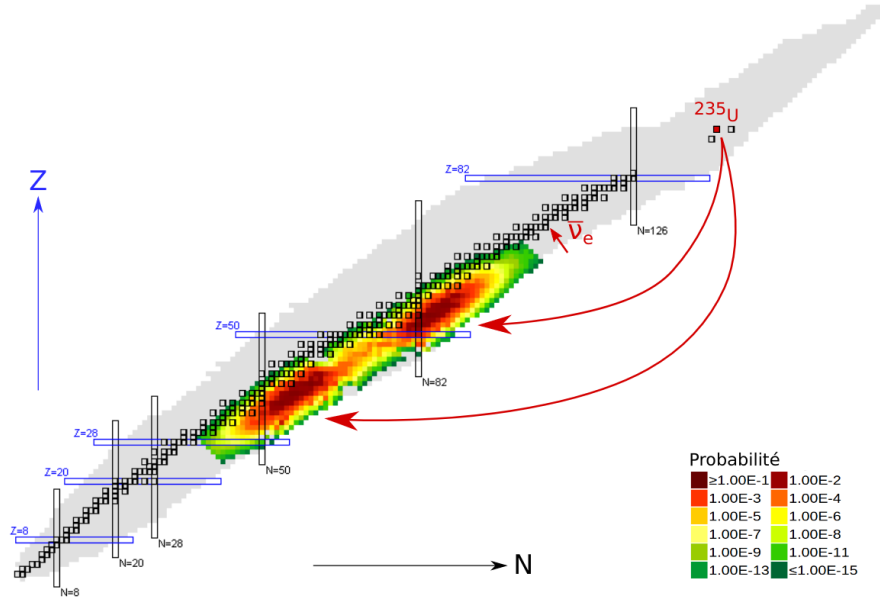
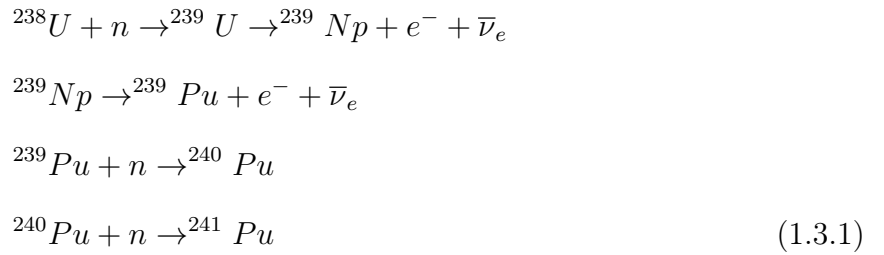


Figure 1.6 – (N,Z) distribution of fission fragments for  $^{235}\text{U}$ . The color scheme represents the 2D probability distribution for the daughter nuclei. Source: [28]. The adapted figure is taken from [29].

fission.

The only fissile isotope that exists in nature is  $^{235}\text{U}$ , with an isotopic fraction of 0.7%. Commercial nuclear reactors use fuels enriched at 3-5% in  $^{235}\text{U}$ , the rest of the fuel being composed of  $^{238}\text{U}$ , whereas research reactors use fuels enriched at 20% or 93% in  $^{235}\text{U}$ . During a reactor cycle, radiative neutron captures on  $^{238}\text{U}$  lead to the formation of  $^{239}\text{Pu}$  and  $^{241}\text{Pu}$  via the following reactions



The two isotopes  $^{239}\text{Pu}$  and  $^{241}\text{Pu}$  are also fissile and thus contribute to the flux of antineutrinos. However,  $^{238}\text{U}$  contributes to the antineutrino flux in a smaller proportion, since it can only undergo fission by interacting with fast neutrons, while the three other isotopes can undergo fission by interacting with the more abundant thermal neutrons. As an example, the evolution of the fraction of the four fissile isotopes for a commercial reactor is shown in figure 1.7. It can be deduced that the antineutrinos coming from  $^{235}\text{U}$  fissions dominate at the beginning of the cycle, but, as the fuel is consumed, the

contribution of  $^{239}\text{Pu}$  to the total flux becomes non-negligible.

The total antineutrino flux at a time  $t$  and energy  $E_\nu$  emitted by a nuclear reactor is thus obtained by summing over all the contributions of the  $^{235}\text{U}$ ,  $^{238}\text{U}$ ,  $^{239}\text{Pu}$  and  $^{241}\text{Pu}$  fission fragments and over all isotopes undergoing beta-decay as activated pieces or spent-fuel. From a general point of view it writes:

$$\Phi_{\bar{\nu}_e}(E_\nu, t) = \sum_f A_f(t) S_f(E_\nu) \quad (1.3.2)$$

where the index  $f$  runs over all the beta-emitters in the reactor,  $A_f(t)$  is their activity at a time  $t$  and  $S_f(E_\nu)$  their associated antineutrino energy spectra.

Usually, it is more convenient to write equation 1.3.2 in the following form:

$$\Phi_{\bar{\nu}_e}(E_\nu, t) = \frac{P_{th}}{\sum_k \alpha_k(t) E_k} \sum_k \alpha_k(t) S_k(E_\nu) + \Phi_{\bar{\nu}_e}^{activation}(E_\nu, t) + \Phi_{\bar{\nu}_e}^{spent fuel}(E_\nu) \quad (1.3.3)$$

where  $P_{th}$  is the thermal power of the reactor,  $E_k$  is the energy released in the fission of isotope  $k$ ,  $\alpha_k$  is the fraction of fissions coming from isotope  $k$ ,  $S_k(E_\nu)$  is the total antineutrino energy spectrum associated to the fission of isotope  $k$  and  $E_\nu$  the energy of

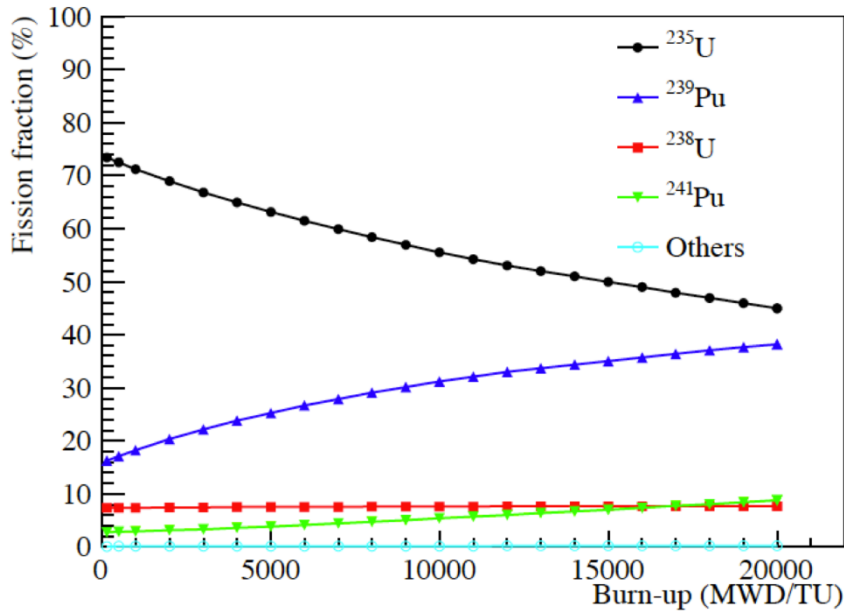


Figure 1.7 – Relative contribution of the four fissile isotopes to the total number of fissions as a function of the burn up. The initial conditions are those of a commercial reactor, enriched at 3.5% in  $^{235}\text{U}$ , at the beginning of a cycle, after the replacement of 1/3 of its fuel. Source: [30].

the antineutrinos.  $\Phi_{\bar{\nu}_e}^{activation}(E_\nu, t)$  and  $\Phi_{\bar{\nu}_e}^{spentfuel}(E_\nu)$  are the antineutrino fluxes coming from activated materials and spent-fuel if present. Usually the spent-fuel term is negligible and the activation term depends on the structure materials, but it generally has a small contribution. The time dependence is apparent in the thermal power and fraction of fissions coming from isotope  $k$  terms. While the thermal power is continuously monitored,  $E_k$  is found in the nuclear databases. The evolution of  $\alpha_k$  is obtained from simulations that take into account the nuclear transmutation inside reactor cores. Finally, the antineutrino spectra  $S_k(E_\nu)$  are determined theoretically and represent the main uncertainty source in the computation of  $\Phi_{\bar{\nu}_e}$ . Reactor antineutrinos have energies of a few MeV and a total flux of  $\sim 10^{20} \bar{\nu}_e \text{ s}^{-1} \text{ GW}_{th}^{-1}$ .

### 1.3.2 Antineutrino energy spectra prediction

The computation of the antineutrino energy spectra  $S_k(E_\nu)$  for the four fissile isotopes is an important ingredient for the reactor energy spectra prediction. This section will present the two methods that are used to calculate these energy spectra: the summation method and the conversion method.

#### Summation method

This method consists of first calculating the energy spectra at the beta branch level and then adding up the contributions coming from all the beta branches of all the different fission fragments. Therefore, several observables need to be well known to reconstruct the antineutrino spectrum using this method: the activities of the fission products, the branching ratios, the endpoint energies of the different beta branches for a given fission fragment, and, most importantly, the shape of the antineutrino spectrum corresponding to each beta branch.

In the summation method, the beta energy spectrum for a fissioning isotope can be written as :

$$S_k(E) = \sum_f A_f S_f(E) = \sum_f A_f \sum_b BR_f^b \times S_f^b(Z_f, A_f, E_{0,f}^b, E) \quad (1.3.4)$$

where the  $f$  index runs over the fission fragments and the  $b$  index runs over the different beta branches of a given fission fragment.  $A_f$  is the activity of a fission fragment,  $BR_f^b$  is the branching ratio of a given beta branch,  $S_f^b$  is the beta spectrum associated to the branch  $b$  of the fission fragment  $f$ , and  $E_{0,f}^b$  is its endpoint energy.  $S_f^b$  is obtained from theoretical calculations based on the Fermi theory, which take into account nucleon and nuclear form factors and Coulomb correction factors. When available, input data on beta-transitions are taken from evaluated nuclear structure databases, such as ENSDF [31] (see 5.4 for more details).

Finally, the antineutrino spectrum is obtained by replacing the electron's energy,  $E$ , with the antineutrino's energy,  $E_\nu$ , in equation 1.3.4

$$E_\nu = E_{0,f}^b - E \quad (1.3.5)$$

One should note that this one-to-one relation is valid only at the single beta branch level and it allows to predict the electron and antineutrino spectra with the same precision.

Unfortunately, as we will see in the following, this method is complex as it involves a huge number of beta-transitions. For example, the fission of  $^{235}\text{U}$  involves  $\sim 6000$   $S_f^b$  spectra. In consequence, it suffers from several drawbacks.

### Pandemonium effect

The main drawback is the so-called *Pandemonium* effect [32]. This effect was observed in the work of Mueller et al. [33] when they compared the beta spectra obtained using the summation method, including all the data available in the ENSDF nuclear database [31], with the ones measured at the ILL for the three isotopes  $^{235}\text{U}$ ,  $^{239}\text{Pu}$  and  $^{241}\text{Pu}$  (see discussion in the **Conversion method** section). They observed a high overestimation in the summation spectra at energies higher than 7.5 MeV, pointing to the well known *Pandemonium* effect.

In fact, branching ratios and endpoints are determined by measuring the intensity and energy of the gamma rays emitted following a beta transition using high resolution but low efficiency Ge detectors. For a transition with a high  $Q_\beta$ , there is a number of beta branches that connect the parent nucleus to very excited levels of the daughter nucleus, in a region with a huge level density. In this case, the daughter nucleus deexcites by emitting multiple low energy gamma rays (with a small gamma intensity, since the density of levels in this region is huge) or a single high energy gamma ray. In both cases, part or all the gamma energy will be missed due to the low efficiency of the Ge detectors. Therefore, high endpoint transitions' weights are overestimated as a consequence of missing some of the low endpoint transitions.

This effect is illustrated in figure 1.8, where the intensities of the transitions for the beta-decay of  $^{88}\text{Br}$  are plotted as a function of the excitation energy of the daughter nucleus, for high resolution measurements (ENSDF) and recent low resolution Total Absorption Gamma-ray Spectroscopy (TAGS) measurements [34]. We clearly see that the density of the ENSDF high excitation energy transitions is lower than that of the TAGS data. As a consequence, the normalisation of the ENSDF low energy transitions is overestimated, as observed on the cumulative intensities shown on the right hand side plot from figure 1.8.

Another drawback of the summation method, not illustrated in this section, is the lack of information for a number of nuclei. In particular, very neutron rich fragments with high  $Q_\beta$  and low half-life are difficult to measure and no beta-transition information exists for them. The contribution of these nuclei to the total fission fragment activity for



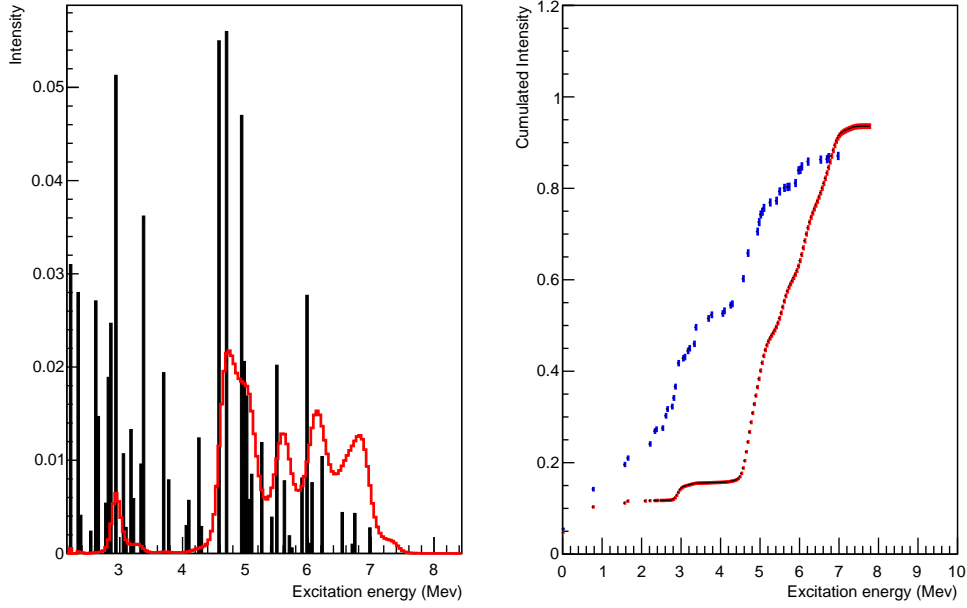


Figure 1.8 – Comparison of the beta-transition intensities (left), and their cumulative (right), as a function of the excitation energy, for data taken from ENSDF (release 2020) nuclear data base (in black/blue) and for TAGS data [34] (in red), for  $^{88}\text{Br}$ .

$^{235}\text{U}$  amounts to about 5%.

For all these reasons, since the beginning, the conversion method was preferred to compute the reactor antineutrino spectra and was used as a reference by reactor neutrino experiments. In section 5.4 we will present a new prediction model developed in this work and based on the summation method, attempting to correct for the *Pandemonium* effect and account for unknown nuclei.

### Conversion method

The conversion method consists of obtaining the antineutrino energy spectra for each fissioning isotope  $S_k(E_\nu)$  directly from the corresponding measured total electron energy spectra  $S_k(E)$ .

The beta energy spectra for  $^{235}\text{U}$ ,  $^{239}\text{Pu}$  and  $^{241}\text{Pu}$  were measured in the 80s at the High Flux Reactor of the Institut Laue-Langevin with the magnetic spectrometer BILL [35]. Target foils containing the isotope of interest were irradiated for a period between 12 hours and 2 days with thermal neutrons and the cumulative beta spectra of the fission fragments were measured with high precision. The beta spectrum associated with  $^{235}\text{U}$  was measured two times, in 1981 and 1985 ([36] and [37]), while those associated with  $^{239}\text{Pu}$  and  $^{241}\text{Pu}$  were measured in 1982 and 1989 ([38] and [39]). The spectra normalization was performed with calibration reactions of the type  $(n, e^-)$ , whose cross sections were

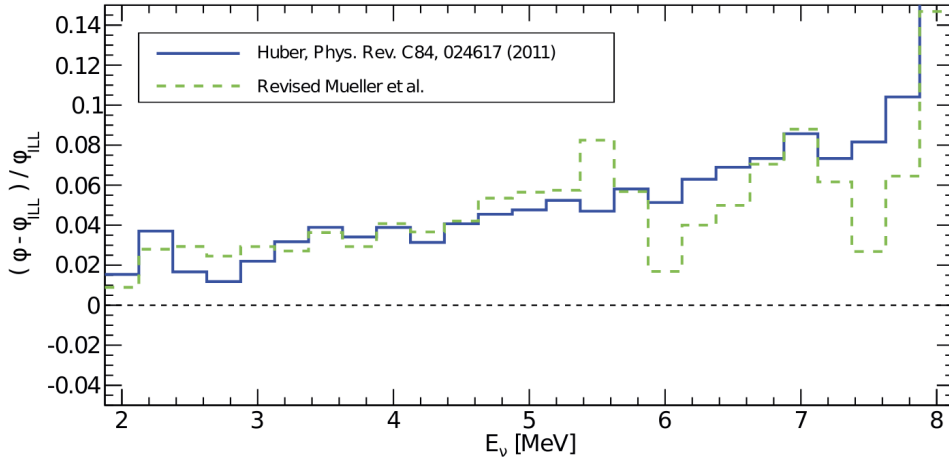


Figure 1.9 – Relative difference of the MUELLER et al. and HUBER revisited predictions with respect to the previous reference antineutrino spectra. Source: [40].

considered to be well known.

The procedure consists in fitting each electron spectrum with 30 virtual beta branches. In practice, the spectrum is divided into 30 slices and the first beta branch is fitted by exploiting the data points from the highest energy slice, thus allowing to obtain its branching ratio and endpoint energy. Then, the full contribution of the previously fitted beta branch is subtracted from the total experimental spectrum and the procedure continues for the next, lower energy, slice. In the end, the antineutrino spectrum is obtained by first converting the fitted virtual beta branches into antineutrino branches by using equation 1.3.5, and then summing them up.

The antineutrino experiments performed in the 90s were compatible with the spectra predicted with the conversion method, which was the official method used at that time, at the 1% level, validating these predictions.

### 1.3.3 Reevaluation of the antineutrino spectra

In the 2010s, the precision required for the measurement of  $\theta_{13}$  led to a regain of interest with regard to the prediction of reactor antineutrino spectra. Mueller et al. [33] reevaluated the antineutrino spectra using a hybrid procedure that combines the summation and the conversion methods. Using the available nuclear data ( $\sim 10000$  beta branches)<sup>13</sup>, it was possible to reconstruct  $\sim 90\%$  of the total electron spectrum, from which the antineutrino associated spectrum could be deduced using equation 1.3.5. The remaining contribution to the antineutrino spectrum, coming from the unknown nuclei and the systematic uncertainties of the nuclear databases, was modelled using five virtual beta branches. In this

<sup>13</sup>The transitions for which the endpoint, spin and parity were well known were used. Moreover, the *Pandemonium* effect was partly accounted for (where data was available) by using data obtained using other experimental techniques than the  $\beta - \gamma$  coincidence used for ENSDF data: Tengblad et al. [41].

way, the systematic uncertainties associated with the conversion method are limited only to the  $\sim 10\%$  of the spectrum that couldn't be obtained using the summation method. This study led to an increase of  $\sim +3\%$  in the normalization of the total reactor antineutrino spectrum. This effect was mainly due to an improved implementation of the finite size corrections to the Fermi theory directly at the branch level<sup>14</sup> and to the use of data corrected for the *Pandemonium* effect.

Following the work of Mueller et al., Huber [42] confirmed the  $\sim +3\%$  excess by correcting the conversion method for the effects highlighted by Mueller et al. The correction brought by the two independent methods with respect to the ILL spectra is illustrated in figure 1.9. Today, the reference reactor antineutrino spectra are called "Huber-Mueller" spectra. In fact, the spectra of the three isotopes that undergo fission by interacting with thermal neutrons come from the revisited conversion method of Huber, while the  $^{238}\text{U}$  spectrum, which undergoes fission by interacting with fast neutrons, comes from a theoretical computation based on the summation method done by Mueller et al.

### 1.3.4 Reactor antineutrino anomaly (RAA)

In addition to the reevaluation of the antineutrino spectra that revealed a  $\sim +3\%$  shift with respect to the previous reference spectra, two more corrections had to be taken into account. Firstly, the target foils containing the fissile isotopes were irradiated for a period between 12 hours and 2 days with thermal neutrons, while the reactor fuels are normally exposed to thermal neutrons for a few tens of days in the case of experimental reactors, or a few hundred days in the case of commercial reactors. Therefore, the reactor spectra contain antineutrinos coming from decays of fission fragments with half-lives bigger than one day. Such off-equilibrium effects were not taken into account before, and they were shown to increase the normalization of the antineutrino spectrum by  $\sim +1\%$ . Secondly, the IBD cross section is inversely proportional to the neutron's lifetime, whose average measured value evolved over time [43]. Accounting for this conducted to an additional shift of  $\sim +1.5\%$  to the normalization of the antineutrino spectrum.

After taking into account all the relevant corrections, the normalization of the reactor antineutrino spectrum was shifted with  $\sim +6.5\%$ , thus highlighting a strong disagreement between the prediction and the existing short baseline reactor antineutrino measurements. The deficit observed in the data with respect to the new prediction is what we now call the "Reactor Antineutrino Anomaly" (RAA) [44].

A global analysis from 2017 [45], taking into account the recent data from Double Chooz, Daya Bay and RENO experiments, which confirm with high precision the mean antineutrino rate detected at short baselines, showed that the ratio between the data and the prediction was of  $(93.4 \pm 2.4)\%$ , as shown in figure 1.10. An updated value for this ratio will be presented in section 5.1, where the rate of antineutrinos measured by STEREO will also be taken into account.

<sup>14</sup>For the conversion method, the corrections to the Fermi theory are implemented at the whole spectrum level, which leads to significant biases.

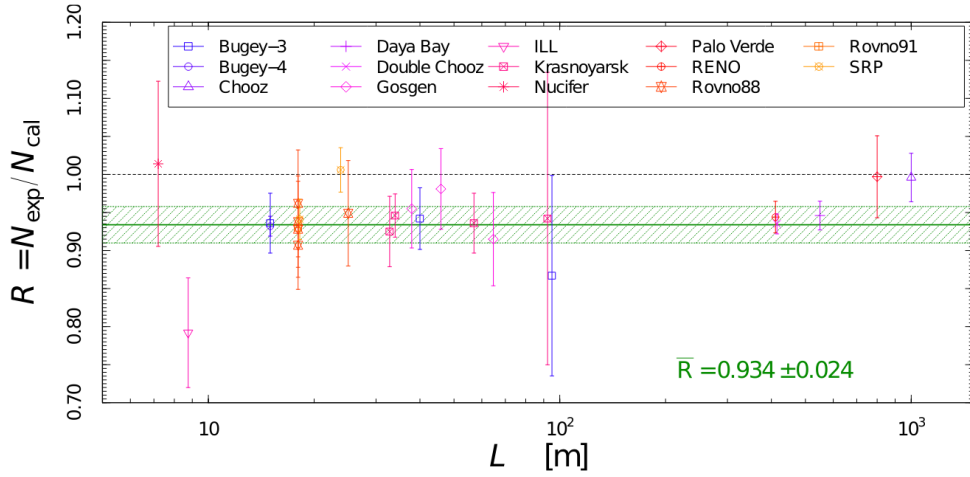


Figure 1.10 – Ratio between the measured and predicted antineutrino rate for different reactor experiments. The green hatched band represents the uncertainty on the anomaly. Source: [45].

### 1.3.5 The shape anomaly

The antineutrino spectra measured by Daya Bay [30], Double Chooz [46], NEOS [47], and RENO [48] highlighted a deviation with respect to the Huber-Mueller prediction in the 5 MeV region. At first order, the mean deviation, illustrated on the left-hand-side of figure 1.11, can be fitted with a Gaussian with an amplitude of  $\sim 10\%$ , a standard deviation of  $\sim 0.5$  MeV and a mean of  $\sim 5$  MeV, which motivated the community to name it the "bump at 5 MeV". It is worth noting that this deviation doesn't impact the RAA, since the bump only accounts for  $\sim 1\%$  of the total antineutrino flux.

Since at the time, Bugey 3 [49] did not observe any deviation, several possible explanations for the origin of the bump were proposed. The fact that the amplitude of the bump was observed to be proportional to the reactor power excluded the hypothesis that uncorrelated background could be at its origin. The bump could also be explained by an incorrect modelization of the emitted antineutrino spectra. Thus, comparing the spectra obtained from Low Enriched Uranium (LEU) and High Enriched Uranium (HEU) reactors, as shown on the right-hand-side of figure 1.11, one could test if the 5 MeV excess is only due to the  $^{235}\text{U}$  contribution or is similar for all isotopes.

Furthermore, a study performed by Mention et al. [50] shown that a  $\sim 1\%$  deviation of the energy scale, which is contained in the calibration uncertainties, could reproduce the distortion observed in the spectrum.

At the moment, the origin of the bump is not known and the information from STEREO and other short baseline reactor experiments could be crucial in understanding this shape anomaly.

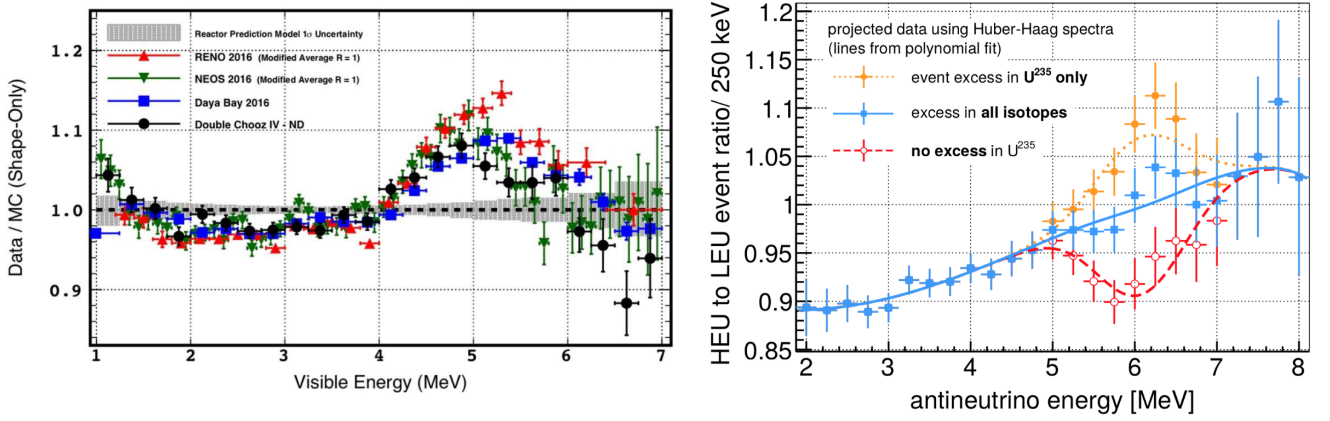


Figure 1.11 – Left: Ratio between the measured and predicted (Huber-Mueller) antineutrino spectra for Daya Bay , Double Chooz, NEOS, and RENO experiments. Source: [51]. Right: ratio of HEU to LEU antineutrino spectra for three hypotheses. Source: [52]

## 1.4 Current state on the origin of the anomalies

### 1.4.1 Sterile neutrino hypothesis

In order to explain the RAA discussed in the previous section, a new hypothesis that explores the existence of sterile neutrino states with  $\sim 1$  eV mass has been introduced. These sterile states cannot interact via the weak interaction but can interact gravitationally. This can be deduced from the measurement of the width of the Z boson, which constrains the number of active neutrino flavours to  $N_\nu = (2.9841 \pm 0.0083)$  [53]. However, they can mix with the three active flavours,  $\nu_e, \nu_\mu$  and  $\nu_\tau$ , and thus generate distance dependent oscillations in the detected neutrino rate.

In the scenario where we consider only one additional sterile neutrino, the PMNS mixing matrix becomes

$$U = \begin{pmatrix} U_{e1} & U_{e2} & U_{e3} & U_{e4} \\ U_{\mu1} & U_{\mu2} & U_{\mu3} & U_{\mu4} \\ U_{\tau1} & U_{\tau2} & U_{\tau3} & U_{\tau4} \\ U_{s1} & U_{s2} & U_{s3} & U_{s4} \end{pmatrix} \quad (1.4.1)$$

where, from the current values of the parameters of the PMNS matrix we know that  $|U_{e4}|^2 \ll 1$ ,  $|U_{\mu4}|^2 \ll 1$ ,  $|U_{\tau4}|^2 \ll 1$  and  $|U_{s4}|^2 \approx 1$ .

As short baseline experiments (less than 100 m) are used to test the existence of a sterile neutrino state, the 2-flavour approximation introduced in equation 1.2.14 can be used. This is justified by the fact that the oscillations governed by the solar, atmospheric and reactor parameters are not yet developed at this distance. In this context, we can write the survival probability for (anti)neutrinos as

$$P(\nu_e \rightarrow \nu_e) = 1 - \sin^2(2\theta_{ee}) \sin^2\left(\frac{\Delta m_{41}^2 L}{4E}\right) \quad (1.4.2)$$

where  $\sin^2(2\theta_{ee}) = 4|U_{e4}|^2(1 - |U_{e4}|^2)$ .

The combined oscillation analysis of reactor data only performed by Mention et al. [44] led to the possible existence of a sterile neutrino state with  $\Delta m_{41}^2 = 2.4 \text{ eV}^2$  and  $\sin^2(2\theta_{ee}) = 0.14 \pm 0.08$  that could explain the RAA. The analysis was based on the first-generation short-baseline experiments, for which only the absolute antineutrino rates were used, with the exception of Bugey-3 and ILL experiments, from which shape information could also be extracted (see [44] for details).

The antineutrino rate only information from a detector placed at a given position is not sufficient to conclude on the existence of sterile neutrinos, since it suffers from non-negligible uncertainties coming from the absolute normalisation of the detected antineutrino rate and the reactor power (see equation 1.3.3). Meanwhile, important information can be extracted from high statistics experiments as it will be seen in the next section. Moreover, next generation short-baseline experiments integrate the possibility to explore the development of an oscillation pattern in the antineutrino spectrum by performing relative comparisons between the spectra measured at different distances.

### 1.4.2 Kilometre-baseline reactor experiments

Kilometre-baseline reactor experiments (Daya Bay, Double Chooz and RENO) use similar experimental setups with far detectors at a 1 km baseline and near detectors at a few hundred metres. The detectors are unsegmented and the distance from the source is too big to see oscillations associated to eV mass scale sterile antineutrinos. Nonetheless, the oscillations could manifest in deviations from the predictions.

Daya Bay found no evidence of sterile neutrinos in the region of  $2 \times 10^{-4} \text{ eV}^2 \leq \Delta m_{41}^2 \leq 0.3 \text{ eV}^2$  [54]. Double Chooz also did not find any indication for sterile neutrinos in the  $5 \times 10^{-3} \text{ eV}^2 \leq \Delta m_{41}^2 \leq 0.3 \text{ eV}^2$  region [55]. Similarly, RENO reports no evidence for sterile neutrinos in the range of  $10^{-4} \text{ eV}^2 \leq \Delta m_{41}^2 \leq 0.5 \text{ eV}^2$  [56].

In 2017, the Daya Bay collaboration was able to use its large amount of detected antineutrinos to decorrelate the contribution of the two most relevant isotopes,  $^{235}\text{U}$  and  $^{239}\text{Pu}$  to the total antineutrino flux [57], by analysing the evolution of the detected flux over time. The reconstructed IBD yield per fission for the two isotopes is shown in figure 1.12. The study suggested that  $^{235}\text{U}$  was virtually the only isotope responsible for the RAA, with an IBD yield per fission deficit of 7.8% with respect to the Huber-Mueller prediction, while the  $^{239}\text{Pu}$  contribution was compatible with the prediction.

Moreover, results from Daya Bay with improved statistics (2019) and an independent study performed by the RENO [58] collaboration confirmed the deficit observed for  $^{235}\text{U}$ .

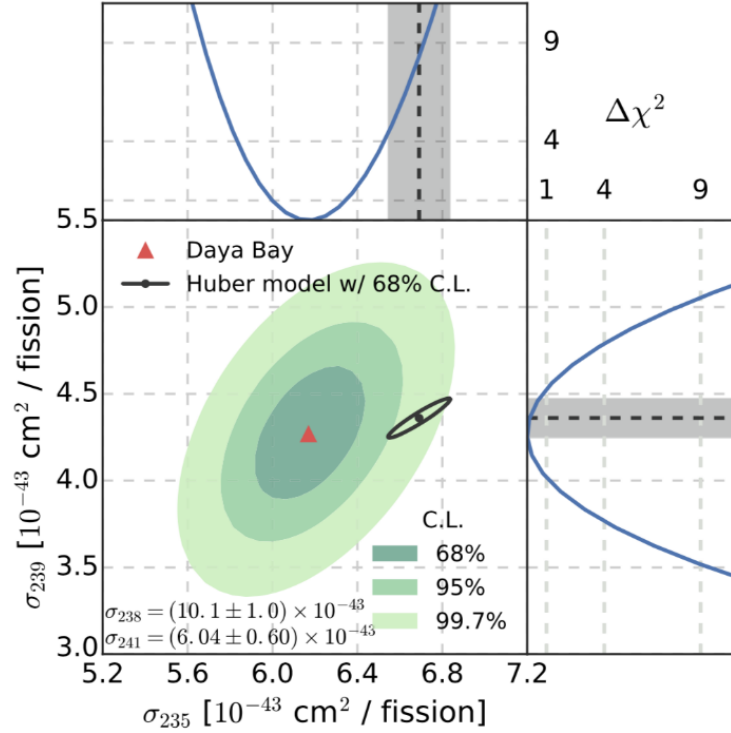


Figure 1.12 – IBD yields per fission for  $^{235}\text{U}$  and  $^{239}\text{Pu}$ . The best fit of Daya Bay is shown by the red triangle, while the region allowed by the Huber-Mueller prediction is shown in black. Source: [57].

These results seem to disfavor the hypothesis that an oscillation towards a sterile neutrino could explain the RAA, since this would impact equally the antineutrinos coming from all the fissile isotopes. Instead, they seem to point out potential normalisation biases on the  $^{235}\text{U}$  electron energy spectrum measured at ILL, used as a reference in the conversion method (see the previous section 1.3).

A recent measurement of the ratio between the cumulative electron energy spectra associated to  $^{235}\text{U}$  and  $^{239}\text{Pu}$  performed by Kopeikin et al. [59] revealed a 5% deviation to the same ratio obtained when using the ILL data. The conclusion goes in the same direction as the Daya Bay's one, *i.e.* the RAA may come from an overestimation of the normalisation of the electron energy spectrum measured at ILL for  $^{235}\text{U}$ .

### 1.4.3 Very short baseline reactor experiments

The RAA led to the appearance of several experiments measuring antineutrinos at a distance of the order of  $\sim 10$  m. These "Very Short Baseline" (VSBL) experiments aim at testing the appearance of an oscillation pattern in the antineutrino spectra independently of any theoretical prediction. To do so, a relative comparison between the spectra measured at different distances must be possible and thus the VSBL experiments have

either segmented (STEREO [60], PROSPECT [61], SOLID [62]) or movable (DANSS [63], Neutrino-4 [64]) detectors, with the exception of NEOS [47], which compares its spectrum with a reference spectrum taken at a different baseline by Daya Bay.

Table 1.1 shows a summary of the most important characteristics of VSBL experiments. Besides the detector type (segmented or movable), there are two more factors that define the differences between these experiments: the type of reactor that generates the antineutrinos and the way in which the delayed neutron coming from the IBD is detected.

Some of the experiments are placed near HEU reactors (research reactors), while others are placed near LEU reactors (commercial reactors). On the one hand, LEU reactors generate a huge antineutrino flux, which allows the experiments placed in their vicinity to acquire fast a big sample of antineutrinos and have an excellent signal-to-background ratio. However, the size of their core impacts negatively the spatial resolution of the experiment. On the other hand, the HEU reactors have the advantage of having a small core ( $\sim 50$  cm), which ensures a good spatial resolution, and the disadvantage of having an antineutrino flux almost 10 times smaller than that of the commercial reactors. Moreover, since they are highly enriched in  $^{235}\text{U}$ , the experiments placed near research reactors can measure the antineutrino spectrum associated to this isotope alone and thus conclude whether or not the RAA is only caused by an imprecise modelization of the  $^{235}\text{U}$  contribution to the total  $\bar{\nu}_e$  flux (they can also examine if the bump has the same characteristics as that of the one observed in the case of commercial reactors).

All VSBL experiments use liquid or plastic scintillator (LS or PS) materials to detect antineutrinos. However, some of them are doped with Gd, while others are doped with Li. The Gd isotopes emit a gamma cascade of  $\sim 8$  MeV following the capture of a neutron. This has the advantage of being in a region where no natural radioactivity is present. However, the fact that most of the VSBL detectors are compact results in an important Compton plateau and the possibility for the gammas to exit the target volume. The Li nucleus emits a  $^3\text{H}$  and an  $\alpha$  following the capture of a neutron through the interaction:  $n + ^6\text{Li} \rightarrow ^3\text{H} + \alpha + 4.78$  MeV. The tritium and the alpha particle deposit their energy in a localised space region, which ensures a good detection efficiency. However, since these particles are heavy and charged, the signal they create is heavily quenched (see section 3.3.2 for a discussion on the quenching effect) and appears in the 500 keV energy region. Thus, the identification of the delayed neutron strongly relies on the PSD capabilities of the scintillator.

The VSBL experiments are running since a few years and are already excluding most of the sterile oscillation parameter space favoured by the RAA [65]. NEOS [47] excludes the parameter space below  $\sin^2(2\theta_{ee}) = 0.1$  for  $0.2 \text{ eV}^2 < \Delta m_{41}^2 < 2.3 \text{ eV}^2$  at 90% confidence level (CL), by comparing its spectrum to Daya Bay's unfolded spectrum [30], while DANSS [63],[66] excludes the parameter space region defined by  $0.01 < \sin^2(2\theta_{ee}) < 0.1$  and  $0.5 \text{ eV}^2 < \Delta m_{41}^2 < 2.5 \text{ eV}^2$  at 95% CL. As for PROSPECT [67], it excludes oscillations characterized by  $\sin^2(2\theta_{ee}) > 0.09$  and  $0.8 \text{ eV}^2 < \Delta m_{41}^2 < 4 \text{ eV}^2$  at 95% CL. SoLid [68] estimates its signal-to-background ratio to be 0.33, but have not yet reported any oscillation results. One of the VSBL experiment, Neutrino-4 [69], reports a  $2.9 \sigma$  significance oscillation signal with  $\sin^2(2\theta_{ee}) = 0.36 \pm 0.12$  [stat] and  $\Delta m_{41}^2 = (7.3 \pm 1.17)$



	STEREO	PROSPECT	SOLID	Neutrino-4	NEOS	DANSS
Site	France	USA	Belgium	Russia	Korea	Russia
Reactor type	HEU	HEU	HEU	HEU	LEU	LEU
Reactor power [ $MW_{th}$ ]	58	85	50-80	100	2800	3100
Baseline [ $m$ ]	9-11	7-9	6-9	6-12	24	11-13
Detector	LS	LS	PS	LS	LS	PS
Dopped with	Gd	Li	Li	Gd	Gd	Gd
IBD rate [ $d^{-1}$ ]	400	750	450	200	2000	5000

Table 1.1 – Characteristics of the reactor experiments searching for a sterile neutrino with the mass of the order of 1 eV.

eV<sup>2</sup>. This results is, however, in conflict with the previous VSBL results and is partly excluded by them. Moreover, it is also in strong tension with cosmological constraints [70],[71], and several critiques, mainly regarding its statistical treatment, have been issued [72],[73].

The STEREO experiment, whose goal is to test the sterile neutrino hypothesis and to measure the reactor antineutrino energy spectrum associated to <sup>235</sup>U, uses a segmented detector based on the Gd-loaded liquid scintillator technology to detect reactor antineutrinos. It will be presented in chapter 2 and the part of the work of this thesis related to STEREO will be detailed in the following chapters. The recent results from STEREO will be presented in chapter 5.

## 1.5 Coherent elastic neutrino-nucleus scattering

Within the Standard Model of particle physics, neutrinos can undergo neutral-current interactions through the exchange of neutral Z bosons. It was in 1974 that Daniel Z. Freedman proposed the existence of elastic neutrino-nucleus scattering. For a nucleus at rest with Z protons and N neutrons, the elastic neutrino-nucleus cross section [74] is given by

$$\frac{d\sigma}{dE_r} = \frac{G_F^2}{4\pi} Q_W^2 F^2(q^2) \cdot m_{(Z,N)} \left( 1 - \frac{E_R}{E_R^{max}} \right) \quad (1.5.1)$$

where  $G_F$  is the Fermi constant,  $Q_W$  is the nuclear weak charge,  $m_{(Z,N)}$  is the total mass of the nucleus,  $E_R$  is the nuclear-recoil energy and  $F(q^2)$  is the nuclear form factor as a function of the momentum transfer  $q$ . The nuclear weak charge has the following expression:  $Q_W = N - Z(1 - 4 \cdot \sin^2(\theta_W)) \sim N$ , where  $\theta_W$  is the Weinberg angle, with  $\sin^2(\theta_W) \sim 1/4$ . The maximum nuclear recoil energy is given by

$E_R^{max} = 2E_\nu^2/(m_{(Z,N)} + 2E_\nu)$ , with  $E_\nu$  being the incident neutrino energy. For small momentum transfers, corresponding to neutrino energies smaller than 30 MeV<sup>15</sup>, the form factor is close to unity. In this case, the scattering is coherent over all the nucleons found in a nucleus and is denoted coherent elastic neutrino nucleus scattering (CE $\nu$ NS).

The CE $\nu$ NS cross section is more than two orders of magnitude bigger than the IBD cross section [75]. This is explained by the fact that the CE $\nu$ NS cross section is proportional to  $N^2$  (due to the cross section dependence on  $Q_W^2$ , see equation 1.5.1). However, the detection of such a process is made difficult by the small energy of the nuclear recoil  $E_R$  (suppressed by the nucleus mass  $m_{(Z,N)}$ ), which represents the only measurable observable of CE $\nu$ NS. An important feature of CE $\nu$ NS is that it does not imply any threshold on the incident neutrino energy, unlike IBD, which is only possible for  $E_\nu > 1.8$  MeV. Since NUCLEUS is an absolute-rate experiment which aims at studying the CE $\nu$ NS cross section, it is dependent on the reactor antineutrino flux predictions (see section 1.3), which will induce an important systematic uncertainty on the measurement. Moreover, the low threshold of the experiment will allow NUCLEUS to be sensitive to the as yet unobserved low-energy part of the reactor antineutrino spectrum. Consequently, this justifies the need of new sophisticated studies aimed at accurately predicting the reactor antineutrino spectrum below the IBD threshold in order to be able to interpret the NUCLEUS data in the low recoil-energy region<sup>16</sup>.

### First CE $\nu$ NS detection

It took more than four decades between the theoretical prediction of CE $\nu$ NS and its detection. Its first detection was reported by the COHERENT collaboration in September 2017 [75], which measured the process at a  $6.7\sigma$  confidence level using a 14.6 kg CsI[Na] scintillating crystal target. The experiment took place at the Oak Ridge National Laboratory and it used the neutrinos emitted by the Spallation Neutron Source (SNS), which acts as a stopped-pion source. The neutrino spectrum of SNS is well defined and it spans energies up to 50 MeV, with a total neutrino flux of  $4.3 \cdot 10^7 \nu \text{ s}^{-1} \text{ cm}^{-2}$ . At these energies, the CE $\nu$ NS cross section value compensates for the small neutrino flux. Moreover, COHERENT made use of the pulsed nature of the stopped-pion source to greatly suppress the background by implementing a beam-on/beam-off comparison method.

The first detection of coherent elastic neutrino-nucleus scattering on argon, using a 22 kg, single-phase liquid argon detector, was reported in 2020 by the COHERENT collaboration [76]. Argon is the lightest nucleus for which CE $\nu$ NS has been observed until now. Moreover, this measurement confirmed the expected neutron-number dependence of the CE $\nu$ NS cross section.

The NUCLEUS experiment, whose goal is to measure CE $\nu$ NS induced by reactor

<sup>15</sup>In fact, the energy for which the elastic scattering of neutrinos becomes coherent depends on the size of the nucleus the neutrino is scattering off.

<sup>16</sup>One should note that in the case of NUCLEUS, most of the details about the measured antineutrino spectrum are washed out, since the experiment is only sensitive to the nuclei recoils and doesn't have access to the energy or diffusion angle of the incident antineutrino.

---

neutrinos (thus probing nuclear-recoil energies down to the 10 eV regime) coming from the Chooz nuclear power plant in France, will use cryogenic detectors which feature an unequalled low energy threshold and a time response fast enough to be operated in above-ground conditions. The NUCLEUS experiment and the muon veto prototype built and tested at CEA Saclay will be presented in chapter 6, whereas the part of the work of this thesis related to the NUCLEUS experiment will be presented in chapter 7.



# Chapter 2

## Stereo experiment

*"The worth of a new idea is invariably determined, not by the degree of its intuitiveness—which incidentally, is to a major extent a matter of experience and habit—but by the scope and accuracy of the individual laws to the discovery of which it eventually leads."*

*Max Planck*

### Sommaire

---

<b>2.1</b>	<b>Experimental site . . . . .</b>	<b>32</b>
2.1.1	The research reactor from ILL . . . . .	32
2.1.2	STEREO positioning inside the reactor hall . . . . .	34
<b>2.2</b>	<b>Neutrino detection . . . . .</b>	<b>35</b>
2.2.1	Inverse beta decay . . . . .	35
2.2.2	Scintillation process . . . . .	37
2.2.3	Pulse shape discrimination . . . . .	39
<b>2.3</b>	<b>Detector description . . . . .</b>	<b>41</b>
2.3.1	Inner detector . . . . .	41
2.3.2	Shielding and Muon Veto . . . . .	44
2.3.3	Electronics and acquisition system . . . . .	47
2.3.4	Calibration systems . . . . .	48
<b>2.4</b>	<b>Experiment status . . . . .</b>	<b>51</b>

---

The STEREO experiment is designed to detect antineutrinos emitted by a compact reactor with highly enriched  $^{235}\text{U}$  fuel at different baselines. Its scientific goal is multiple. Firstly, it aims at testing a low baseline oscillation pattern induced by a hypothetical sterile neutrino that could explain the Reactor Antineutrino Anomaly. Secondly, it can provide a precise measurement of the antineutrino spectrum associated to the fission of  $^{235}\text{U}$ , as well as an absolute value for the total rate of antineutrinos. STEREO is the product of a collaboration of five European research institutes, four of which are found in France: the "Institut de recherche sur les lois fondamentales de l'univers" (IRFU) of CEA Paris-Saclay, the "Laboratoire de Physique Subatomique et de Cosmologie" (LPSC) and "Institut Laue-Langevin" (ILL) from Grenoble and the "Laboratoire d'Annecy-le-Vieux de Physique des Particules" (LAPP) from Annecy, and one in Germany: the "Max Planck Institute fur Kernel physics" (MPIK) from Heidelberg.

The first section of this chapter will describe the experimental site, while the second one will treat the inverse beta decay (IBD) reaction by which the neutrinos are detected, as well as the liquid scintillator's pulse shape discrimination power. The next section provides a description of the detector and the shielding used to mitigate the environmental background. The last section summarizes the current status of the data taking and the problems encountered during the first phase of the data taking.

## 2.1 Experimental site

### 2.1.1 The research reactor from ILL

The "Institut Laue Langevin" (ILL) is an European research institute based in Grenoble, France. Its nuclear reactor, the RHF (Réacteur à Haut Flux) provides a high flux of neutrons<sup>1</sup> that is used by about 40 instruments to explore various topics from different fields: particle physics, nuclear physics, medical physics, biology or materials science.

Since the goal of the ILL reactor is to provide a high flux of thermal neutrons, its functioning principle is different from the one used for commercial reactors. The fuel ( $\sim 8$  kg) is 93% enriched in  $^{235}\text{U}$  and is contained in 280 curved Aluminum plates arranged in a hollow cylinder of 41 cm outer and 26 cm inner diameter by 81 cm height. In the cylinder's center there is a nickel rod that allows to control the power emitted by the reactor. The cylinder is placed in an Aluminum tank filled with heavy water ( $\text{D}_2\text{O}$ ), whose role is to dissipate the thermal power and to moderate the neutron flux, while minimizing the captures. The Aluminum tank is at his turn placed in a pool of light water ( $\text{H}_2\text{O}$ ) of 6 m diameter by 8 m height, whose role is to absorb the residual neutron flux. The thermal neutrons are collected close to the reactor core by Aluminum beams and the measurement instruments are placed at the end of these beams in the experimental hall, on level C of the reactor building, at the same height with the fuel element.

---

<sup>1</sup>The flux of neutrons in the moderator is estimated at  $\sim 1.5 \cdot 10^{15} \text{ cm}^{-2}\text{s}^{-1}$  at nominal power.

The previously presented particularities of the ILL reactor represent both advantages and disadvantages for STEREO. One of the advantages is that the  $^{235}\text{U}$  enrichment of the reactor renders the contribution of  $^{239}\text{Pu}$  to the total number of fissions negligible (the mean fission fraction of  $^{239}\text{Pu}$  was found to be 0.7% only for one reactor cycle). This allows to measure a virtually pure  $^{235}\text{U}$  antineutrino spectrum and to test whether the Reactor Antineutrino Anomaly is mainly due to a misevaluation of the  $^{235}\text{U}$  IBD yield per fission. Furthermore, we could also examine the excess of antineutrinos in the 5 MeV region obtained with an almost pure  $^{235}\text{U}$  source and see how it compares to the excess measured by other experiments. Another advantage is represented by the compactness of the reactor core, which ensures a good precision on the antineutrino propagation distance ( $\pm 20$  cm) and allows to measure oscillations developing over a few meters. Finally, the frequent renewal of the fuel guarantees a quasi-constant antineutrino energy spectrum.

The main disadvantage comes from the big quantity of Aluminum present in the reactor core, since the  $^{28}\text{Al}$ , formed by neutron captures on  $^{27}\text{Al}$ , can beta decay and thus participate to the antineutrino flux up to energies of 2.86 MeV. The predicted antineutrino flux thus needs to be corrected for this effect, which has been shown to mainly impact the first energy bin used in the analysis. For a complete summary of the different corrections that have to be applied to the predicted spectrum, which include off-equilibrium effects and residual antineutrinos from spent fuel, the reader should refer to section IV of [77].

The emitted antineutrino flux can be estimated starting from the thermal power of the reactor as

$$\Phi_{\bar{\nu}_e} \simeq \frac{\langle P_{th} \rangle}{\langle E_{th}^{fission}(^{235}\text{U}) \rangle} N_{\bar{\nu}_e/fission}(^{235}\text{U}) \quad (2.1.1)$$

where  $\langle P_{th} \rangle$  is the thermal power, measured in real time while the reactor is functioning,  $\langle E_{th}^{fission}(^{235}\text{U}) \rangle$  is the energy released per fission and  $N_{\bar{\nu}_e/fission}(^{235}\text{U})$  is the number of antineutrinos emitted per fission. Considering the nominal reactor power of 58 MW and the energy released per fission of  $^{235}\text{U}$  of 200 MeV and taking into account only the antineutrinos whose energies are bigger than the IBD threshold,  $N_{\bar{\nu}_e/fission}(^{235}\text{U}) \simeq 2$ , the order of magnitude of the antineutrino flux is estimated to be

$$\Phi_{\bar{\nu}_e} \simeq 10^{18} \bar{\nu}_e s^{-1} \quad (2.1.2)$$

Even though the emitted number of antineutrinos is huge, when taking into account the IBD cross section, the solid angle and the dimensions of the detector, the expected detected number of antineutrinos drops to  $\sim 400$  per day. The main component of the systematic uncertainty on the predicted antineutrino flux comes from the measurement of the thermal power  $\langle P_{th} \rangle$ , which is monitored by observing the balance of enthalpy at the primary cooling circuit. However, it has been shown that the relative uncertainty on the total thermal power is well constrained and has a value of 1.4% [78].

The operation of STEREO coincided with a period of high reactor maintenance,

resulting in having 2 to 3 reactor-on cycles of  $\sim 50$  days per year. Reactor-off periods allow the change of the fuel and maintenance work for the instruments operating at ILL. Moreover, they are essential for STEREO, since they allow the precise measurement of the background spectrum, which is crucial for the extraction of the antineutrino rates.

### 2.1.2 STEREO positioning inside the reactor hall

The STEREO detector is located on level C of the reactor building, which is at the same height with the fuel element. Its neighbouring instruments, D19 [79] and IN20 [80], constrain the dimensions of the detector and its shielding and induce a background of gamma rays and neutrons in varying rates. Moreover, they also induce stray magnetic fields of up to  $\sim 1$  mT [81] at the detector level. All these led us to reinforce the shielding of the STEREO site before installing the detector, as shown in figure 2.1 and to enclose the detector in several layers of shielding, which will be discussed in section 2.3.2. The detector is placed under the transfer channel of the reactor, which is filled with light water and serves for the storage of used fuel elements. This has the advantage of providing an inclination angle dependent shielding of about 15 metre water equivalent (m.w.e) on average. The detector is thus aligned with the transfer channel, which results in an angle of  $(17.9 \pm 0.2)^\circ$  between the detection axis and the direction to the core. The center of the active detector volume is found to be  $(10.298 \pm 0.028)$  m away from the center of the reactor core, including the fact that the center of the active detector is lower than the center of the reactor core by 0.21 m.

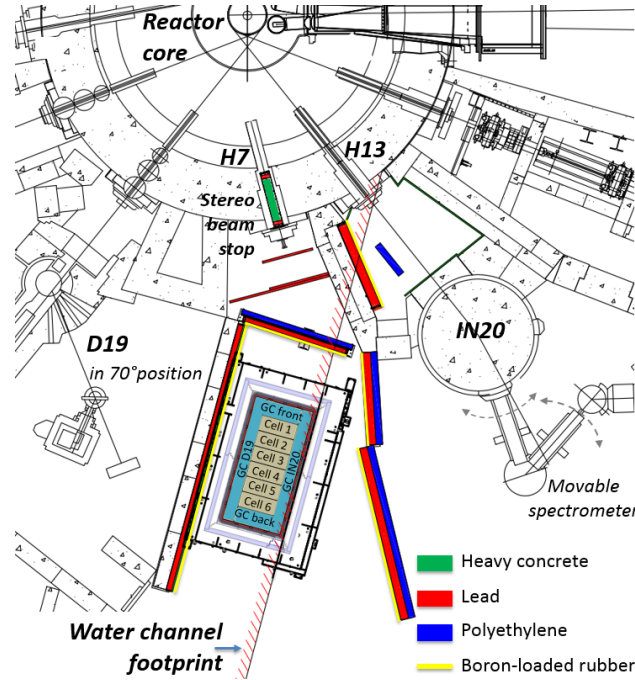


Figure 2.1 – Top view of the experimental site at level C of the ILL reactor building. The reinforced shielding of the STEREO site is shown in color. Source: [77].



## 2.2 Neutrino detection

### 2.2.1 Inverse beta decay

The antineutrinos are detected by the inverse beta decay (IBD) reactions they undergo inside the liquid scintillator

$$\bar{\nu}_e + p \rightarrow e^+ + n \quad (2.2.1)$$

where an incident antineutrino interacts with a proton from the liquid scintillator and gives rise to a positron and a neutron. The antineutrino needs to have a minimum kinetic energy (called the threshold energy) for the reaction to be possible. This is due to the fact that the mass of the proton is inferior to the sum of the masses of the positron and neutron. The threshold energy can thus be approximated by

$$E_{\bar{\nu}_e} > 1.806 \text{ MeV} \simeq m(n) + m(e^+) - m(p) \quad (2.2.2)$$

The IBD reaction is the most used detection mode for the antineutrinos and it has been first employed more than sixty years ago. This is due to its great advantages

- It has a well-known, bigger than that of the neutral current reactions, cross section, which varies quadratically with the antineutrino energy ( $\sigma_{IBD} \propto G_F^2 E_{\bar{\nu}_e}^2$ ).
- The liquid scintillators used for the detection of the antineutrinos have a big concentration of free protons.
- The positron and neutron signals are correlated in time, which allows us to apply selection cuts that help reducing the background.
- The positron carries the information about the incident antineutrino energy.

The antineutrino detection principle is based on the identification of the time-correlated IBD reaction products, the positron and the neutron and is illustrated in figure 2.2. The next subsections will treat the detection of what will be called the Prompt signal (the positron) and the Delayed signal (the neutron).

#### Positron detection (Prompt)

The positron loses its energy by interacting with the liquid in multiple ways: through ionisation, Bremsstrahlung (if it has a sufficiently high energy) and molecular excitation (this type of interaction is responsible for the emission of the scintillation light). After

losing all its kinetic energy, it annihilates with an electron from the medium and gives rise to two 511 keV gamma rays, which transmit their energy to electrons through Compton scattering and photoelectric effect. In turn, these electrons interact with the liquid similarly to the positrons. All these processes take place in a time window of a few hundreds picoseconds and can thus be considered instantaneous with respect to the acquisition system. This is why the detection of the positron is designated as the Prompt event.

Most of the kinetic energy of the antineutrino is transmitted to the positron [82], since its mass is significantly smaller than that of the neutron. In turn, the neutron recovers the direction of the momentum from the incident antineutrino. Finally, the energy of the antineutrino can be directly deduced from the total visible energy deposited by the positron,  $E_{visible} = E_{e^+}^{kin} + 2m_e = E_{e^+} + m_e$ , as

$$\begin{aligned} E_{\bar{\nu}_e} &= E_{visible} - m_e + \Delta \\ &= E_{visible} + 0.782\text{MeV} \end{aligned} \quad (2.2.3)$$

where  $\Delta = m(n) - m(p)$  and the kinetic energy of the neutron has been neglected.

### Neutron detection (Delayed)

The neutron thermalizes in the scintillator until it reaches an energy of about 0.025 eV. This phase usually takes a few hundreds of nanoseconds. Afterwards, the neutron undergoes several elastic scatterings until it is captured by a nucleus, leaving it in an excited

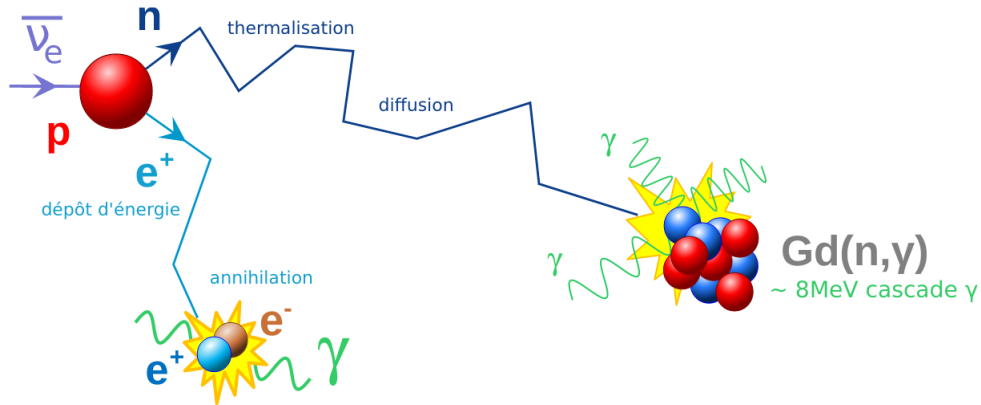


Figure 2.2 – Illustration of the IBD reaction 2.2.1. The Prompt signal consists of the energy deposited by the positron through ionisation and the two 511 keV gamma rays created following its annihilation with an electron from the medium. The Delayed signal consists of a gamma cascade with an energy of  $\sim 8$  MeV, created by the deexcitation of a Gd nucleus following a neutron capture. Source: [29].

state. STEREO detects the gamma rays that are emitted following the deexcitation of the excited nucleus.

Hydrogen is the most abundant element capable of neutron captures naturally found in a liquid scintillator. However, the liquid scintillator used by STEREO was doped with Gadolinium in order to increase the background rejection capabilities of the experiment. While the Hydrogen has a neutron capture cross section of the barn order, the ones for the Gadolinium nuclei used by STEREO ( $^{155}\text{Gd}$  and  $^{157}\text{Gd}$ ) reach a few hundreds of thousands of barns. Thus, with only 0.2% of the liquid's mass represented by Gadolinium, the characteristic capture time is reduced from 230  $\mu\text{s}$ , for the non-doped liquid, to 16  $\mu\text{s}$ <sup>2</sup>. This leads to the reduction of the accidental coincidences rate by a factor of  $\sim 10$  by imposing a cut on the time distance between the detection of the positron and neutron signals.

A second advantage of doping the liquid scintillator with Gadolinium concerns the total energy carried by the gamma rays emitted during its deexcitation following a neutron capture. While the Hydrogen only emits one gamma ray with 2.2 MeV energy, the Gadolinium emits a cascade of gamma rays with a total energy of  $\sim 8$  MeV, making it easier to identify the neutron capture. The detection of these gamma rays represents the Delayed event. Since the gamma rays coming from the natural radioactivity have energies inferior to 2.6 MeV, imposing selection cuts on the energy of the Delayed event further helps mitigating the background.

### 2.2.2 Scintillation process

Scintillator materials emit light through fluorescence when they are traversed by ionizing radiation. There are several types of scintillator materials which have different characteristics: response time, light yield, fabrication constraints, etc. Liquid scintillators, as the one used by STEREO, have the advantage of being fast, rich in protons and having a good light yield.

The scintillation process results from radiative transitions from the first singlet excited states  $S_1$  to the ground states  $S_0$  of aromatic  $\pi$ -electron systems, formed from the hybridization of the s and p orbitals of the H and C atoms composing the organic molecules of the scintillator [83]. The energy level diagram of the scintillator molecules is shown in figure 2.3. It can be seen that in addition to the singlet states  $S_x$ , the molecule can also be excited in the triplet states  $T_x$ . Moreover, there is a fine structure of vibrational states corresponding to every singlet and triplet state. The typical energy that separates two singlet or triplet states between them is of the order of some tens of eV, while there are only a few eV between the vibrational states.

---

<sup>2</sup>The total capture time that includes the thermalization phase is of the order of 18  $\mu\text{s}$ .

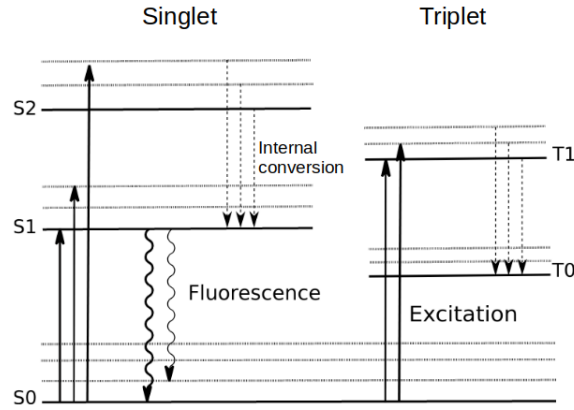


Figure 2.3 – Illustration of the scintillator molecules' energy levels relevant for explaining the light emission. The singlet and triplet states are shown in solid lines, while the corresponding vibrational states are shown in dotted lines. The  $S_x \rightarrow S_1$  and  $T_x \rightarrow S_0$  transitions are non-radiative. The light emission corresponds to the  $S_1 \rightarrow S_0$  transitions.

The light response of a liquid scintillator can be described quite accurately with a model consisting of a sum of two exponential functions

$$S(t) = A_f \cdot \exp\left(\frac{-t}{\tau_f}\right) + A_d \cdot \exp\left(\frac{-t}{\tau_d}\right) \quad (2.2.4)$$

where the first component is denoted as the fast principal component and the second one is a delayed component, such that  $\tau_f < \tau_d$ .

As said earlier, the scintillation light originates from the transitions between the first excited level  $S_1$  and the ground state  $S_0$ , passing through the intermediate vibrational states. It is precisely the presence of these vibrational states that renders the scintillation process possible by making the liquid scintillator transparent to its own radiation. Indeed, the energy of the photons emitted between  $S_1$  and a vibrational state  $S_0 + \delta$  is not sufficient to induce again a  $S_0 \rightarrow S_1$  transition.

The fast scintillation component arises from the excitation of the liquid molecules by charged particles in high energy singlet states  $S_x$ , which undergo several fast non-radiative transitions ( $10^{-11}$  to  $10^{-10}$  s) to return to the  $S_1$  state, from which scintillation light can be emitted. However, the complete dissipation of the  $S_x$  energy can be induced by interactions with other excited or ionized molecules, resulting in a loss of scintillation. This effect is called the "ionization quenching" and it becomes more important for bigger stopping powers ( $dE/dx$ ). The way in which we account for this effect for the STEREO simulation will be presented in section 3.3.1.

The delayed scintillation component involves the triplet states  $T_1$ , which are formed by non-radiative transitions from high energy  $T_x$  states excited by charged particles. Even though  $T_1 \rightarrow S_0$  transitions are suppressed by the multiplicity selection rule, the molecules

found in the triplet state  $T_1$  can interact between them through Triplet-Triplet Annihilation and give rise to a singlet state  $S_1$ , which decays as described previously, by  $T_1 + T_1 \rightarrow S_1 + S_0 + \text{phonons}$ . The characteristic time for the delayed scintillation component is of a few hundreds of nanoseconds, significantly bigger than that of the fast principal component. This component becomes important for a high density of deposited energies, which induces a high density of  $T_1$  states. This is the case for fast neutrons that induce proton recoils, which have a high  $(dE/dx)$  at the end of their paths, thus depositing a lot of energy in a very localised area.

### 2.2.3 Pulse shape discrimination

The fact that the distribution of light between the two components of the light response (equation 2.2.4), the fast one and the delayed one, depends on the  $(dE/dx)$  of the interacting charged particle, can be exploited to discriminate between electronic recoils (induced by antineutrinos or electrons) and proton recoils (induced by neutrons). Indeed, as seen in the previous section, a high  $(dE/dx)$  induces a high density of excited molecules, which favors inter-molecular interactions and non-radiative transitions and thus lowers the weight of the fast scintillation component,  $A_r$ , with respect to the delayed one,  $A_d$ . This implies that the form of the signals characterizing electronic recoils and proton recoils are slightly different, with the proton recoil signal having a longer tail. We can thus define an observable to distinguish between the two types of signals

$$PSD = \frac{Q_{tail}}{Q_{tot}} = \frac{\sum_{i=0}^{n_{PM}} Q_{tail}^i}{\sum_{i=0}^{n_{PM}} Q_{tot}^i} \quad (2.2.5)$$

where  $Q_{tail}$  and  $Q_{tot}$  are the tail and total charge of the signal, defined using the charges registered in the vertex cell, i.e. the cell in which the interaction took place. The pulse shape discrimination principle is illustrated in figure 2.4.

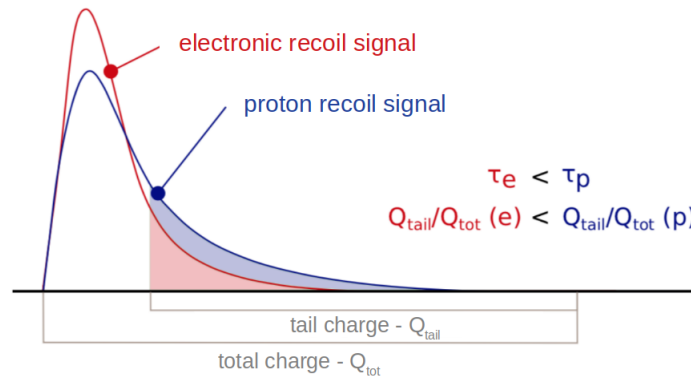


Figure 2.4 – Illustration of the pulse shape discrimination principle. The signals induced by electronic recoils (red) have a smaller  $Q_{tail}/Q_{tot}$  ratio than those induced by proton recoils (blue).

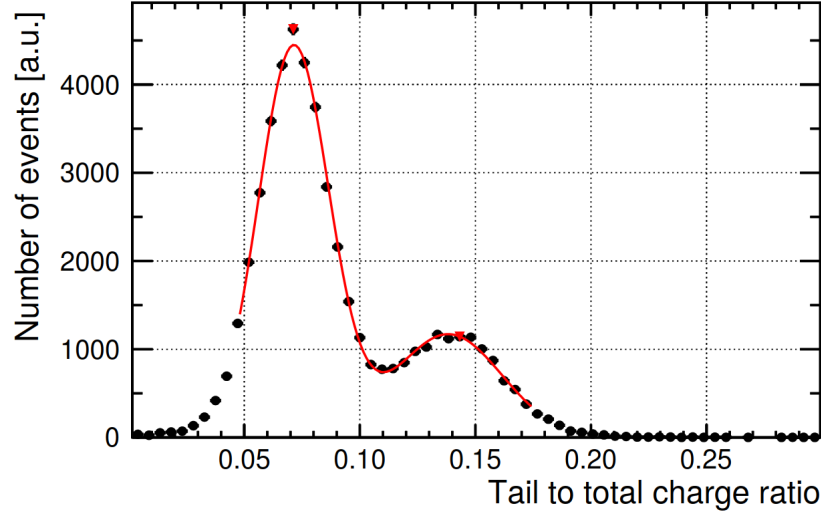


Figure 2.5 – PSD distribution at 2.2 MeV obtained with an AmBe source. The  $Q_{tail}/Q_{tot}$  ratio is used to discriminate electronic recoils (left peak) and proton recoils (right peak). Source: [60].

During the data taking, the form of the signals is not registered in the memory. In fact, only the time that marks the beginning of the pulse,  $t_{CFD}$ , defined using a constant fraction discriminator, the total charge of the signal,  $Q_{tot}$ , and the tail charge of the signal,  $Q_{tail}$ , are registered. This constrains us to fix the integration interval for  $Q_{tail}$  before registering any data. The optimisation of the integration interval was performed by maximizing an observable called Figure Of Merit (FOM), computed from runs performed with a calibration source of AmBe<sup>3</sup>

$$FOM = \frac{\mu_p - \mu_\gamma}{2.35 \cdot (\sigma_p + \sigma_\gamma)} \quad (2.2.6)$$

where  $\mu_p$  and  $\mu_\gamma$  are the mean values of the PSD distributions of proton recoils and electronic recoils and  $\sigma_p$  and  $\sigma_\gamma$  are their standard deviations. These parameters are obtained by fitting the PSD distribution measured with the AmBe source with two Gaussians, as illustrated in figure 2.5. Specifically, the FOM measures the distance between the electronic recoils and proton recoils populations in standard deviation units.

The integration interval for  $Q_{tail}$  was optimised for every cell. Its optimal value was found to be of 0.7 in phase II at 2.2 MeV<sub>ee</sub><sup>4</sup> (the energy released by a Hydrogen nucleus following a neutron capture) and of 0.6 in phase I.

<sup>3</sup>The AmBe source was chosen because it emits both gamma rays and neutrons, thus allowing to compute the FOM for a wide range of energies.

<sup>4</sup>"ee" stands for electron equivalent. The detector is calibrated using gamma rays, which transmit their energy to electrons that subsequently lose their energy through electromagnetic interactions with the liquid scintillator. However, this energy scale is arbitrary for neutrons, which deposit their energy through proton recoils. In other words, the light produced by a proton that loses 1 MeV of energy is different than the light produced by an electron that loses 1 MeV of energy.

## 2.3 Detector description

### 2.3.1 Inner detector

The inner part of the detector, designated as the Target (TG), consists of an acrylic aquarium with 12 mm thick walls, of inner dimensions  $L \times l \times h = 2.223m \times 0.889m \times 1.230m$ , which is divided into six identical and optically separated cells. Each cell is 369 mm thick, 892 mm wide, and 918 mm high. The Target volume is enclosed within a larger double walled stainless steel vessel, defining an outer crown around the central aquarium: the Gamma Catcher (GC). This crown is designed to contain  $\gamma$  rays escaping from events generated in the TG (511 keV gamma rays from  $e^+e^-$  annihilation or gamma rays from the n-Gd cascade) and it also serves as an active veto against external background entering the TG. The GC is divided into four cells, two cells in prolongation of the TG cells, with the same geometry, in order to suppress edge effects in the detector response, and two 30 cm thick cells covering the full length at both sides. The walls and the bottom of every TG and GC cell are made highly reflective using a specular reflective film (ESR film - new denomination of VM2000 films). An illustration of the STEREO detector is given in figure 2.6, where one can see both the different components of the detector and the spatial conventions that will be used in this manuscript. The TG liquid scintillator is doped with Gadolinium to increase the efficiency of neutron captures, to reduce the lifetime and the diffusion length of the IBD neutrons, and to take advantage of the high energy gammas emitted following a neutron capture. In turn, the GC liquid scintillator is not doped with Gadolinium.

The scintillation light readout is done by 48 photomultiplier tubes (PMTs) on top of the cells. There are 4 PMTs for each TG and short GC cell and 8 for each long GC cell. They are located on top of each cell and separated from the scintillator by thick acrylics blocks (20 cm) designated as buffers. The optical coupling between the PMTs and the acrylics is provided by a bath of mineral oil.

### Separating walls

The separating walls between the cells were built such that they assure the optical separation between the cells while maximising the collected light and minimising the light collection inhomogeneities. For that, an ESR<sup>5</sup> film allowing for a specular reflection was chosen. This choice was motivated by the fact that the ESR film has a reflectivity bigger than 98% in air for all the incident angles in the wavelength region of interest for STEREO and it has a negligible light absorption probability. However, once submerged in a liquid, its reflectivity properties drop abruptly for incident angles bigger than  $\sim 60^\circ$  depending on the light's polarisation.

---

<sup>5</sup>ESR comes from Enhanced Specular Reflection; the film used by STEREO is produced by 3M and is constituted of multilayer polymer mirrors [84].

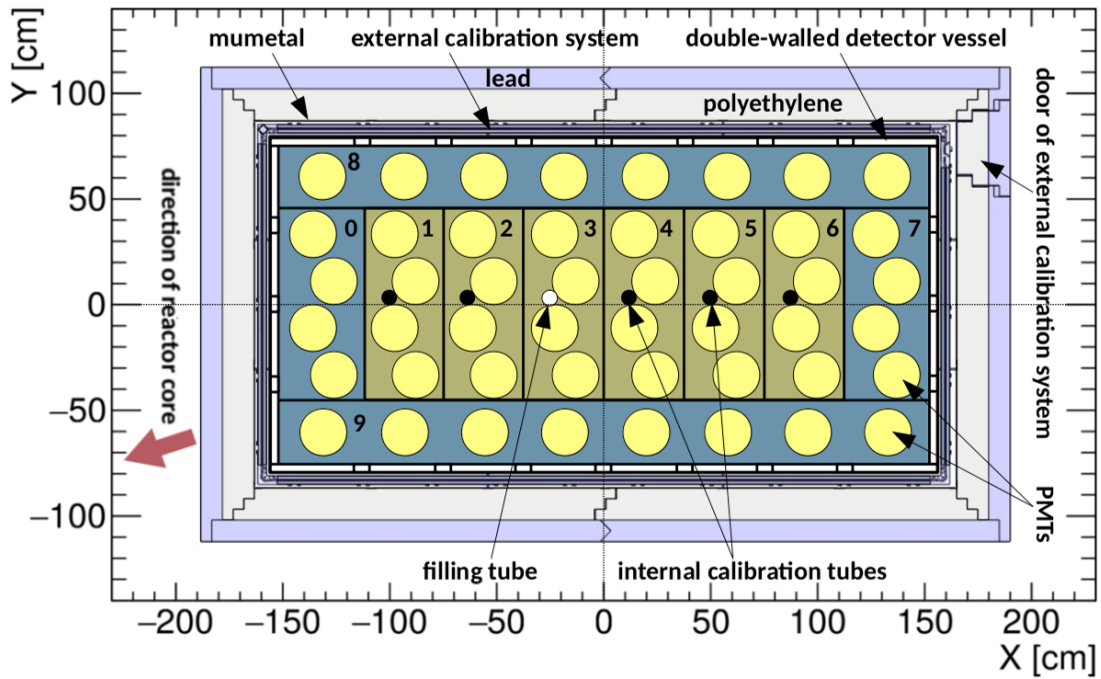
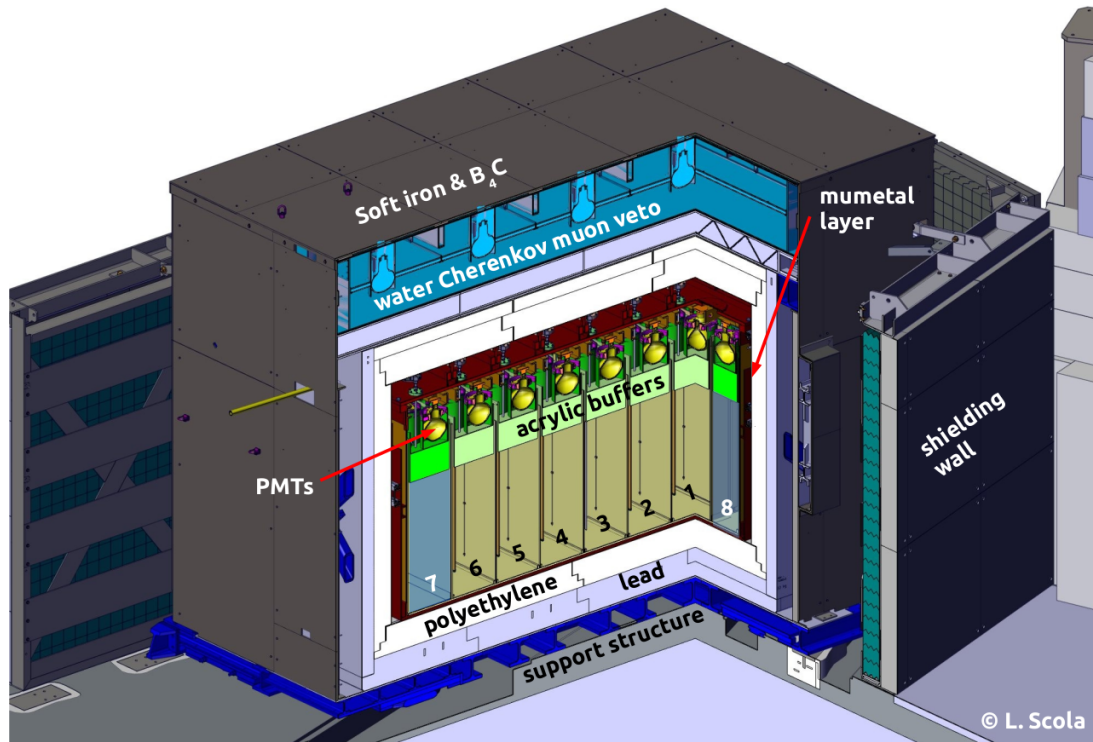


Figure 2.6 – Top: sectional view of the detector setup. Bottom: top view of the detector setup. Legend: 1 – 6: Target cells (baselines from reactor core: 9.4 – 11.2 m); 0 and 7 – 9: Gamma Catcher cells. The z-axis starts at the bottom of the cells and points upwards, i.e. towards the Muon Veto. Source: [77].



In order to avoid the direct contact between the liquid and the ESR film, the latter is enclosed in an air-filled gap between two thin acrylic plates (2 mm)<sup>6</sup>. The air gap between the ESR film and the acrylic plates is ensured by placing a very thin nylon net ( $\sim 100 \mu\text{m}$ ) between them, as seen in figure 2.7. Since the acrylic has the same optical index as the liquid scintillator, the light passes unperturbed the liquid-acrylic interface and can undergo a total reflection at the level of the acrylic-air interface for angles bigger than  $42^\circ$ . Otherwise, the light will most likely be reflected on the reflective film, thus guaranteeing an almost perfect mirror. An illustration of this ideal scenario can be seen in figure 2.7.

Unfortunately, the ideal scenario presented above did not coincide with the reality of the detector's functioning. In fact, shortly after the beginning of the data taking for phase I, the air gap of most of the separating walls was filled with liquid scintillator due to sealing problems, thus leading to the progressive degradation of their reflectivity properties, which in turn lead to a time evolution of the light leaks between the cells. In order to describe more accurately the light leaks between the cells, a versatile model of the separating walls was implemented and will be discussed in section 3.1 of the next chapter. Moreover, the time evolution of the light leaks between the cells complicates the energy reconstruction. Thus, in order to take into account the evolving reflectivity of the separating walls and the evolution of the liquid scintillator's properties, an energy reconstruction method based on a weekly calibration with a  $^{54}\text{Mn}$  source was developed and is presented in section 3.3 of the next chapter.

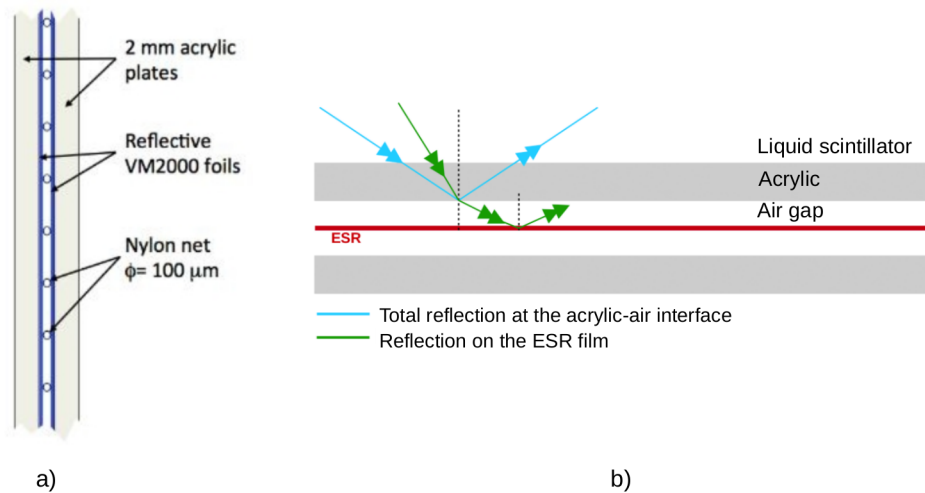


Figure 2.7 – a) Schematic of the separating wall structure showing the nylon net introduced in order to benefit from the optimal reflective properties of the ESR film. b) Schematic showing the expected behaviour of the separating wall if the air gap is ensured. The light can either undergo total reflection at the interface acrylic-air or reflection at the air-ESR interface (with  $\sim 98\%$  probability). Source: a) [60], b) [29].

<sup>6</sup>There are two types of separating walls, one that has a single ESR film enclosed between the two acrylic plates and another one that has two ESR films enclosed between the two acrylic plates. The former one is used for the walls between the detector cells and the stainless steel aquarium (there is no need to have a perfect mirror on the stainless steel side), while the latter one is used between the detector cells themselves.

## Liquid scintillator

The liquid scintillator is mainly composed of LAB (Linear Alkyl Benzene), which accounts for  $\sim 75\%$  of the total mass. In addition, it is also composed of  $\sim 20\%$  PXE (ortho-phenyl-xylyl-ethane) and  $\sim 5\%$  DIN (di-isopropyl-naphtalene). The choice of these constituents was driven by the specificities of STEREO: good transparency, high light yield, pulse shape discrimination capabilities and radiopurity. Moreover, the liquid also had to be compatible with the detector materials and meet multiple safety aspects, like a high flash point, since the experiment operates in the building of a nuclear reactor.

While the main component, the LAB, is chemically inert and has a high transparency above 400 nm wavelength, the PXE and DIN were added to increase the light yield and the pulse shape discrimination capabilities of the liquid. The doping is done by dissolving Gd (thd)<sub>3</sub> molecules in the liquid scintillator. This procedure ensures that the transparency of the liquid remains virtually unmodified. The molecules diphenyloxazole (PPO) and bis-methylstyrylbenzene (bis-MSB) are additionally used as wavelength shifters to maximize the PMTs light collection efficiency.

The obtained liquid has a light yield of  $\sim 7000$  photons/MeV with wavelengths between 375 and 450 nm and a measured attenuation length of  $\sim 7$  m. Finally, to maintain the scintillation properties over time, an atmosphere of slightly overpressured Nitrogen is constantly maintained above the liquid to limit its Oxygen absorption.

The number of protons in the Target  $N_p$  mainly depends on the absolute liquid mass,  $M_L$ , and the relative Hydrogen fraction  $f_H$

$$N_p = \frac{f_H M_L}{m_H} \quad (2.3.1)$$

where  $m_H = 1.673533 \cdot 10^{-27}$  g is the Hydrogen mass. The liquid mass, derived by comparing the masses of full and emptied scintillator barrels during the detector filling, has a value of  $M_L = (1602 \pm 2)$  kg. The Hydrogen fraction was accurately measured at TUM (Technical University of Munchen) by CHN element analysis (combustion analysis) of a scintillator sample [85]:  $f_H = (11.45 \pm 0.11)\%$ . Finally, the number of Target protons is estimated at  $(1.090 \pm 0.011) \cdot 10^{29}$ . This is considered to be a cell-to-cell correlated uncertainty and thus it is relevant for the absolute rate measurement. However, since the oscillation analysis that will be presented in chapter 5 does not use a comparison with an absolute spectrum, the uncertainty on the proton number is not relevant to it.

### 2.3.2 Shielding and Muon Veto

An important concern during the implementation of the experiment was that at the STEREO site there are several factors for which a shielding must be constructed. Firstly, a high flux of thermal and high energy neutrons (energy of about 25 meV and of several

MeV, respectively) is present due to the intense beams of neutrons that are extracted from the reactor moderator in order to perform neutron scattering experiments. These neutrons can also give rise to neutron capture gamma rays with an energy of up to 9 MeV. Secondly, the experiment is not underground and the shielding against cosmic radiation is limited to about 15 m.w.e, represented by the transfer channel of the reactor that is just above the detector. Lastly, nearby experiments use magnetic fields of up to 15 T and the stray field at the STEREO site can reach values of  $\sim 1$  mT.

The correlations between the positron and the neutron resulting from the IBD reactions allows us to reject most of the background. However, we can distinguish two types of residual background that can mimic the signature of an IBD process

- accidental background, which consists of random coincidences between independent events. Their rate depends directly on the environmental background rate.
- correlated background, which consists of coincidences between events that have a common origin.

Natural radioactivity is responsible for gammas that can reach energies of up to 2.6 MeV. While these gammas cannot be mistaken for a Delayed signal, which in our case has an energy of 8 MeV, they can very well mimic a Prompt signal. Atmospheric muons do not represent a problem by themselves, because they have a sufficiently high energy to saturate the detector and thus they can be easily recognized and eliminated. However, the muons can give rise to fast neutrons through spallation on the nuclei of the materials surrounding the detector, which can afterwards be captured on Gadolinium. The gamma rays emitted by the excited Gadolinium could then mimic the Delayed signal. Thus, a Prompt signal coming from a natural radioactivity gamma coupled with a Delayed signal coming from a fast neutron has the same signature as the antineutrino signal and represents one example of accidental background. It is worth mentioning that even though all this accidental background can be subtracted online, it is important to reduce it as efficiently as possible in order to keep to a minimum the statistical fluctuations coming from its subtraction.

The fast neutrons created by muon spallation or produced in the cosmic-ray showers are also the most important source of correlated background. In fact, a neutron will scatter in the liquid scintillator and induce the proton recoils that will at their turn be responsible for the scintillation light, which represents a Prompt signal of some MeV. After being thermalized, the neutron will be captured on a Gadolinium nucleus that will subsequently deexcite and mimic the Delayed signal. Moreover, a single muon can create multiple fast neutrons that can be captured, for example, on Hydrogen, giving a 2.2 MeV signal and on Gadolinium, giving a 8 MeV signal, which again reproduces the antineutrino signature.

Several types of shielding were used in order to reduce the contribution of the earlier mentioned particles to the background relevant for the extraction of the antineutrino rates. Besides the supplementary shielding added around the detector at the STEREO site (see

figure 2.1), the experimental setup is enclosed in a passive shielding of about 65 tons (see figure 2.6), composed of borated polyethylene (29.7 cm on top, 14.7 cm on sides, and 20 cm below) and lead (15 cm on top, 10 cm on sides, and 20 cm below). To protect the detector from the magnetic fields generated by the nearby experiments, several layers of magnetic shielding have been installed: a soft iron layer that surrounds the lead shielding and the Muon Veto, a mu-metal layer inserted between the polyethylene and the detector and cylinders of mu-metal placed around the PMTs. Additionally, the soft iron layer is covered by boron-loaded rubber to help absorbing the ambient thermal neutrons present in the reactor hall.

Even though the reactor building and the transfer channel above the detector provide a shielding of 15 m.w.e., whose effects are visible at the muon flux level, as seen in figure 2.8, the muon-induced neutrons still represent the most important source of background for STEREO. Thus, a water Cherenkov detector was placed on top of the detector, as shown in figure 2.6, and is used as an active Muon Veto. It is filled with 25 cm of demineralized water and the Cherenkov light is read by 20 PMTs placed on top of the water surface. Moreover, a small quantity of 4-methylumbeliferone is added to convert the Cherenkov light in visible light corresponding to the optimal efficiency of the PMTs, and the walls of the detector are covered with a reflective film (Tyvek). The Muon Veto has a detection efficiency for vertical muons greater than 99.5% and exhibits a very good stability.

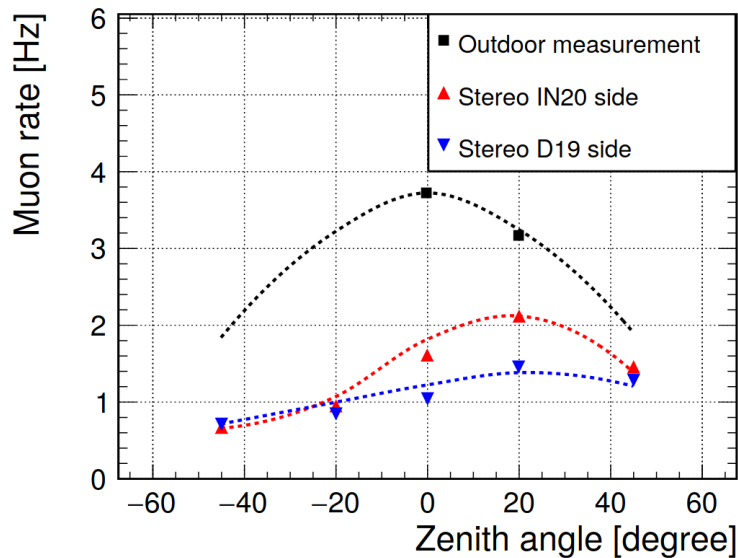


Figure 2.8 – Muon fluxes at the ILL for different locations and zenith angles. The measurements are plotted with markers, while the simulation results are plotted with dashed lines. The simulation is normalized on the outdoor measurement at  $0^\circ$  zenith angle. Source: [60].

### 2.3.3 Electronics and acquisition system

The signals registered by the PMTs are digitized with a 250 MHz frequency, which corresponds to a sample every 4 ns. The STEREO experiment benefits of a dedicated system [86] for the triggering, processing and readout of the PMT signals. If a signal passes the first level trigger ( $\sim 300$  keV energy deposition in one cell), then the processing of the event begins

- the start time of the pulse  $t_{CDF}$  of each individual PMT is determined using a constant fraction discriminator algorithm (CFD).
- the total pulse integral (total charge)  $Q_{tot}$  detected by each PMT is computed by a Riemann-integration over  $N_{tot}$  samples, starting a few  $\mu s$  before  $t_{CDF}$  in order not to lose the signal's rise; 60 samples (240 ns) are enough to fully contain a pulse.
- the tail pulse integral (tail charge)  $Q_{tail}$  detected by each PMT is computed by a Riemann-integration over  $N_{tail}$  samples, starting from  $t_{CDF} + N_{tot} - N_{tail}$ . It is the  $N_{tail}$  parameter that is varied in order to reach the best Figure of Merit for the separation between the electronic recoils and the proton recoils.

The previously discussed processing is summarized in figure 2.9. After the first level trigger, a second level trigger intervenes, which imposes an inferior threshold on the total charge registered by all the Target PMTs and on the total charge detected by the Muon Veto. This allows to already eliminate part of the environmental gamma background that passes the first level trigger. In standard acquisition mode, for the events that pass the two trigger levels, only the observables of interest,  $t_{CDF}$ ,  $Q_{tot}$  and  $Q_{tail}$ , are saved to disk. This allows for a high instantaneous trigger rate ( $\sim 2\text{-}3$  kHz) and a negligible fraction of dead time (less than 0.02%).

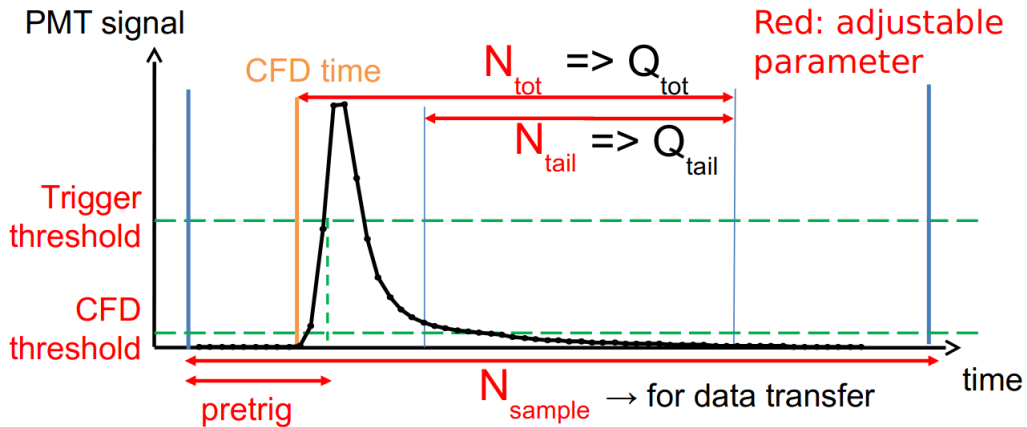


Figure 2.9 – Illustration of the signal processing by the acquisition system. The integration windows for  $Q_{tot}$  and  $Q_{tail}$  are fixed with respect to  $t_{CDF}$ . The adjustable parameters are shown in red. Source: [87].

### 2.3.4 Calibration systems

#### ADC to PE calibration

The calibration of the PMTs at the photo-electron (PE) level and the monitoring of the linearity of the electronics are performed using a LED-based light injection system. In order to get rid of the arbitrariness of the charge units (ADC) given by the acquisition system, we want to convert it into a physically meaningful observable. This observable is the number of photo-electrons that were generated by the photocathode.

An acquisition with an amplification factor 20 times bigger than the one normally used, performed to register the signal coming from low intensity LED light sources, allows to measure charge distributions like the one in figure 2.10. We distinguish the pedestal, reflecting the electronic noise, and a succession of PE peaks corresponding to the conversion of one, two or more photons in photo-electrons at the photocathode. Their relative amplitudes depend on the LED intensity and on the efficiency of the photocathode. By fitting this distribution with a sum of functions that parametrize the noise and the PMT response, we can determine the ADC charge that corresponds to the detection of a single photo-electron,  $Q_{PE}$ . Then, to convert a charge expressed in ADC,  $Q_{ADC}$  into a charge expressed in photo-electrons,  $Q$  during standard acquisition runs we use

$$Q = \frac{Q_{ADC}}{Q_{PE}^{\times 20}} \cdot \frac{A^{\times 20}}{A^{\times 1}} [PE] \quad (2.3.2)$$

where  $A^{\times 20}/A^{\times 1}$  is the ratio between the amplification factors used for the PE calibration and for standard acquisition conditions and  $Q_{PE}^{\times 20}$  is the ADC charge associated to a single photo-electron extracted from the fit.

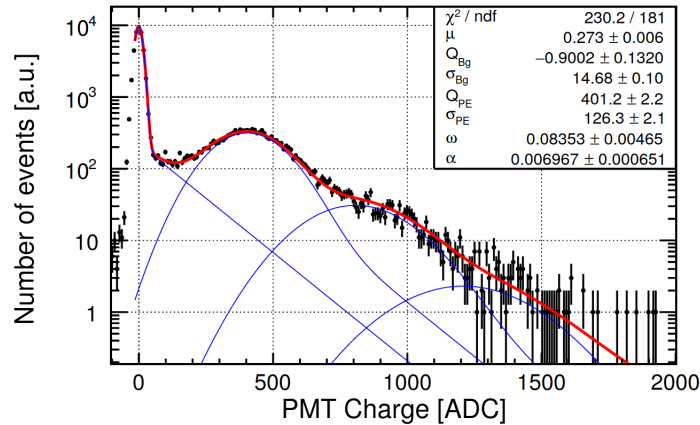


Figure 2.10 – Typical PE spectrum of a Target cell fitted with a sum of functions that parametrize the noise and the PMT response in order to extract the  $Q_{PE}$  parameter. Source: [60].

This type of measurement is carried every 2 hours during short periods of 30 s. Since the charge of the electronic noise is an order of magnitude smaller than that of a single PE, the collected charge expressed in photo-electrons has an uncertainty smaller than  $\pm 1$  PE.

The linearity of the Target PMTs is tested by comparing PMT signals registered while several LEDs are simultaneously switched on, with the sum of PMT signals registered while only one LED is switched on. In the case of a perfect linearity, the two values should be equal. The range of interest for the analysis (up to 1500 PE  $\sim 10$  MeV) is tested by varying the LED amplitudes. The PMTs and the electronics are assumed to be perfectly linear below 200 PE in order to assure the convergence of the method. Figure 2.11 shows that the deviations from linearity are lower than 1% for all Target PMTs, thus satisfying the experimental requirements.

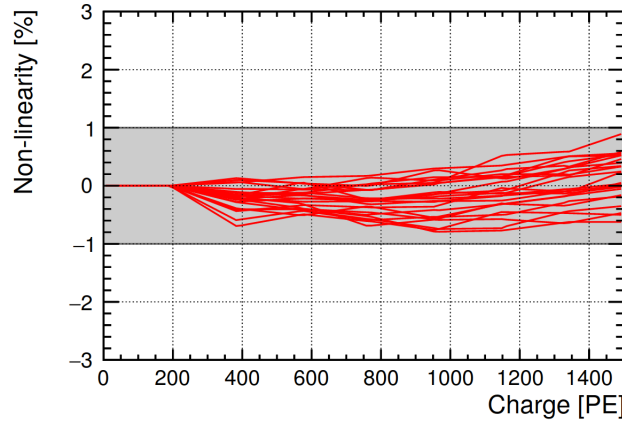


Figure 2.11 – Deviation from linearity for all the Target PMTs. In grey is shown a  $\pm 1\%$  band containing all the non-linearities up to energies of 10 MeV corresponding to 1500 PE. Source: [60].

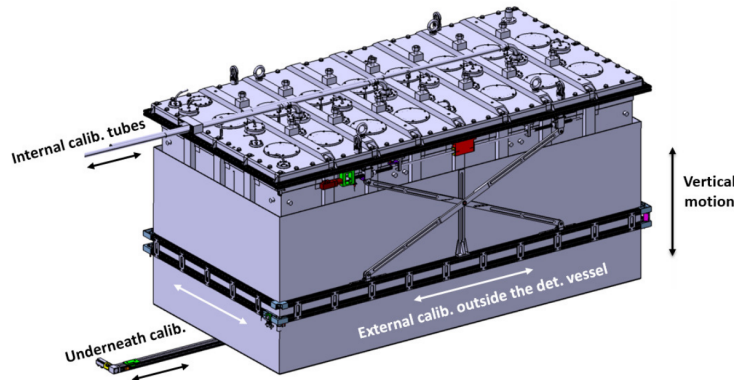


Figure 2.12 – Calibration systems used for STEREO. Source: [60].

### Detector calibration with radioactive sources

The stability of the detector's response and the energy scale determination rely on the deployment of a set of radioactive gamma and neutron sources ( $^{68}\text{Ge}$ ,  $^{137}\text{Cs}$ ,  $^{54}\text{Mn}$ ,  $^{65}\text{Zn}$ ,  $^{42}\text{K}$ ,  $^{60}\text{Co}$ ,  $^{24}\text{Na}$ ,  $^{241}\text{Am}/^9\text{Be}$ ) inside and around the detector. The sources can be deployed via three calibration systems illustrated in figures 2.6 and 2.12: 1) through vertical, Teflon-coated steel tubes spanning the full height of the Target, positioned approximately at the center of each Target cell (slightly shifted towards the reactor direction, see figure 2.6), with the exception of cell 3 where a pure Teflon filling tube is installed, 2) in a semiautomated positioning system, called the "pantograph", which spans over all the perimeter of the detector and is installed between the detector vessel and the shielding, 3) on a rail placed below the detector along its central long axis. The range of possible coordinates for the source deployment positions is shown in table 2.1.

Table 2.1 – Coordinates of source deployment positions in the internal calibration tubes (top) and selected calibration positions along the  $X$ -axis for the external (middle) and underneath (bottom) systems.  $\Delta Z$  is the distance between the calibration position and the bottom of the tube. The bottom of each tube has a distance of 2.5 cm to the bottom of the cells. Marked with an asterisk (\*) are coordinates that can be chosen freely, the others being fixed by the detector geometry. See figure 2.6 for the definition of the cell numbers and coordinate system. Source: [77]

Internal Calibration Tubes					
Cell	$X/\text{cm}$	$Y/\text{cm}$		$Z$ -position	$\Delta Z^*/\text{cm}$
1	-100	3		top	80
2	-63	3		mid-top	60
3	–	–		middle	45
4	12	3		mid-bottom	30
5	49	3		bottom	10
6	87	3			

External Calibration System					
Cell	$X^*/\text{cm}$	$Y/\text{cm}$		$Z$ -position	$Z^*/\text{cm}$
1	-93	$\pm 82$		top	87
2	-56	$\pm 82$		middle	45
3	-19	$\pm 82$		bottom	17
4	19	$\pm 82$			
5	56	$\pm 82$			
6	93	$\pm 82$			

Underneath Calibration System			
Cell	$X^*/\text{cm}$	$Y/\text{cm}$	$Z/\text{cm}$
1	-93	3	-10
2	-56	3	-10
3	-19	3	-10
4	19	3	-10
5	56	3	-10
6	93	3	-10



## Detector monitoring

The monitoring of the experimental conditions and the control of the data acquisition stability are simplified by the presence of a variety of sensors inside and outside the detector. Observables such as temperature, absolute and relative pressures, liquid levels and magnetic fields are continuously monitored. Moreover, besides allowing to perform the ADC to PE calibration, the ultraviolet LEDs are used to monitor the liquid's attenuation length. In addition, the trigger rates, high voltages and currents of the PMTs are also monitored. Finally, neutron counters installed outside the shielding allow to keep track of the fluxes of ambient neutrons. All this information is saved every minute in a database that is accessible online.

## 2.4 Experiment status

The STEREO detector was installed at ILL in November 2016. The first data taking phase lasted until March 2017 and consisted of 84 reactor-on data and 32 reactor-off data. The analysis of these data was made difficult by several deficiencies of the acrylics that impacted the response of the detector. Firstly, the oil bath on top of two buffers (the ones in cell 4 and in the front Gamma Catcher cell) was lost due to leaks in the buffer aquariums. As a result, the collected light in these cells dropped by a factor of 2.5 compared to the other cells. Moreover, most of the separating walls lost their tightness, which resulted in the liquid scintillator filling the air gap around the ESR film. This caused the optical cross-talks between cells to increase from  $\sim 5\%$  to  $\sim 15\%$  (see figure 2.14) and made it necessary to develop a complex energy reconstruction method, which will be presented in section 3.3.1. However, the STEREO collaboration took advantage of the long reactor shut-down between phases I and II of the data taking (March 2017  $\rightarrow$  October 2017) to repair the defective acrylics and perform maintenance work on the detector.

After solving the problems encountered in phase I, the detector response became much more stable. Data was registered for two more periods, called phase II (from October 2017 to April 2019), and phase III (from April 2019 to November 2020). Since light collection, cross-talks and potentially reactor background are different for the three phases, they were analyzed separately (this includes a specific fine-tuning of the simulation for each phase, as it will be explained in section 3.2). STEREO detected its last antineutrino on the 27<sup>th</sup> of September 2020 and it continued to register reactor-off data until November 2020, when its dismantling has started.

In total, the detector registered 387 days of reactor-on data and 750 days of reactor-off data. A summary of the number of reactor-on and reactor-off days for every data taking phase is shown in table 2.2, while a plot showing the variation of the reactor power over time, where one could see the different reactor-on and reactor-off periods, is shown in figure 2.13.

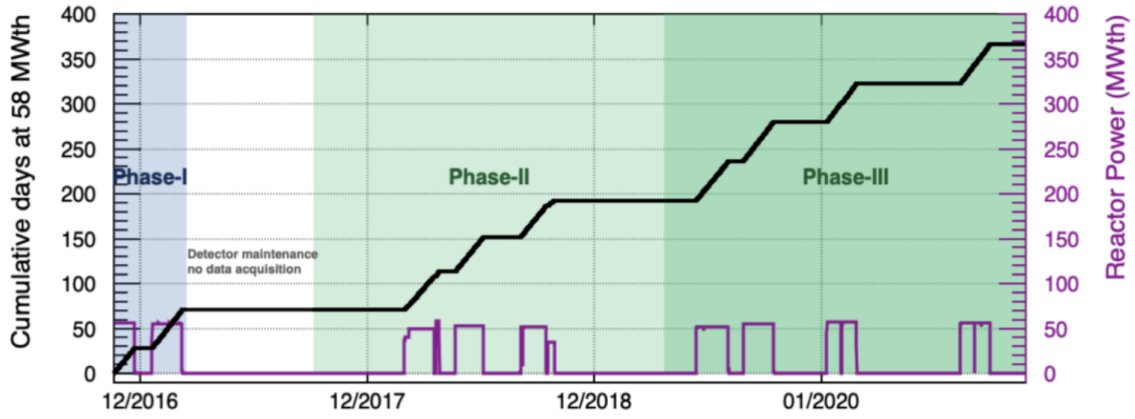


Figure 2.13 – Cumulative (black) and daily (purple) variation of the reactor power over time. The different reactor-off and reactor-on periods are depicted, as well as the long reactor shut-down phase used for detector maintenance. Source: [88].

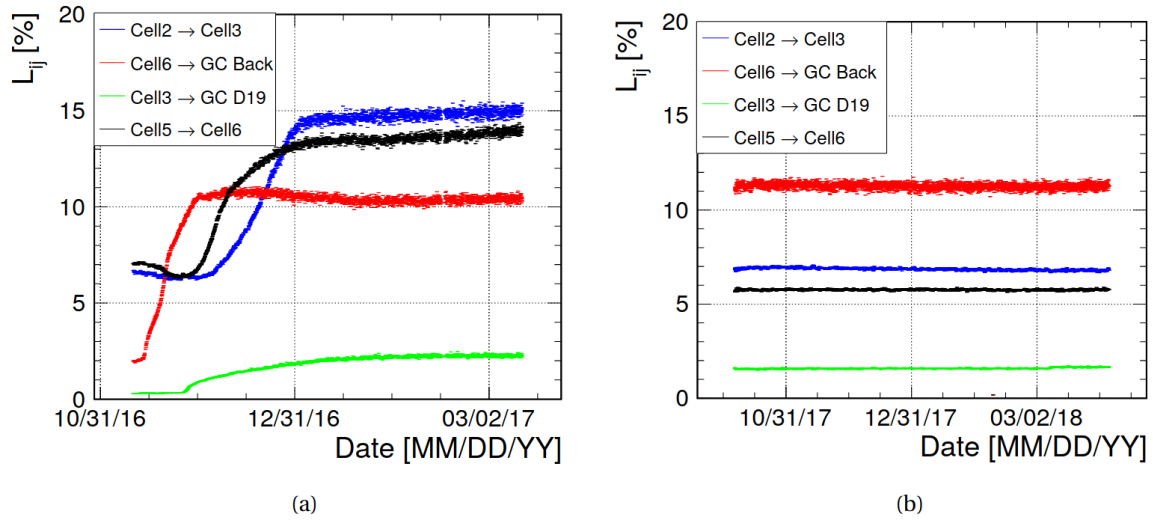


Figure 2.14 – Light leaks evolution with time for some selected cells during Phase I(a) and Phase II of the data taking. This coefficients are measured using cosmic muons, as it will be explained in section 3.3.1. Source: [29].

Table 2.2 – The different data taking periods of STEREO. The time for each period is expressed in days. The number of reactor-on days for an equivalent reactor power of 58 MW is also shown.

	Period	Reactor-on	Reactor-on (58 MW)	Reactor-off
Phase I	Nov. 2016 → Mar. 2017	71	70	28
Phase II	Oct. 2017 → April 2019	137	122	377
Phase III	April 2019 → November 2020	179	174	345
Total	Nov. 2016 → November 2020	387	366	750

# Chapter 3

## Detector response

*"An expert is a person who has made all the mistakes that can be made in a very narrow field."*

*Niels Bohr*

### Sommaire

---

<b>3.1</b>	<b>Monte Carlo simulation . . . . .</b>	<b>54</b>
3.1.1	Geometry of the detector in Geant 4 . . . . .	54
3.1.2	Particle propagation . . . . .	56
3.1.3	Light generation and collection . . . . .	56
3.1.4	The optical model for the separative plates . . . . .	58
3.1.5	The status of the MC simulation before the fine tuning . . . . .	62
<b>3.2</b>	<b>Fine tuning of the optical parameters of the Monte Carlo . .</b>	<b>64</b>
3.2.1	The gain method . . . . .	65
3.2.2	The global strategy of the fine tuning . . . . .	70
3.2.3	Sensitivity studies . . . . .	72
3.2.4	Results of the fine tuning process . . . . .	78
3.2.5	Cross checks on $^{54}\text{Mn}$ . . . . .	80
<b>3.3</b>	<b>Energy scale . . . . .</b>	<b>85</b>
3.3.1	Energy reconstruction . . . . .	85
3.3.2	Nonlinearities of the energy scale . . . . .	90
3.3.3	Tests and systematics of the energy scale . . . . .	93
<b>3.4</b>	<b>Conclusion . . . . .</b>	<b>102</b>

---

The observable of interest for Stereo is the energy spectrum of the detected electron antineutrino candidates. Thanks to the good performances of the liquid scintillator, energy resolutions of the order of 6% at 1 MeV can be reached for an ideal detector, i.e. if all the deposited light is collected. However, the detector does not behave as a perfect calorimeter and the response of the detector has to be simulated as realistically as possible in order to reproduce the volume effects, the imperfect reflectivity of the separating walls between the cells, the light cross-talks between cells and to control the efficiencies of the selection cuts used when extracting the correlated pairs, while optimising the signal-over-background ratio. Moreover, the simulation is of a crucial importance since it is used to generate the positron spectra that are subsequently compared with the data.

The Monte-Carlo model of the detector developed by the collaboration will be presented in the first section where the parameters to fine tune are introduced. The fine tuning of the optical properties of the detector, which represents an important work done during this thesis, will be presented in the second section. The third section will treat the energy reconstruction technique and the systematic uncertainties on the energy scale. The impact of the precise Monte-Carlo fine tuning on the reconstructed energy spectra is also illustrated.

## 3.1 Monte Carlo simulation

The Monte Carlo simulation of the STEREO detector is based on the C++ libraries of GEANT4 [89] responsible for simulating the passage of particles through matter. These libraries allow the simulation of physical processes of different types, such as electromagnetic or optical processes, on an energy range from several hundreds of eV to the TeV, while taking into account the particular geometry of the detector involved as well as the materials constituting it. Actually, the simulation code used by STEREO has been developed starting from Double Chooz's experiment code [46], itself based on the simulation code dedicated to KamLAND, called GLG4sim [90]. This allowed us to take advantage of all the progress done during the last 20 years concerning the simulation of detectors using liquid scintillators. In fact, phenomena such as the light emission by the scintillation process, its propagation and conversion to the sensitivity domain of the PM's, the quenching effect, light emission by Cherenkov effect or the deexcitation cascade of the excited Gadolinium nuclei are implemented and ready to use. Moreover, even the geometry and the properties of the photomultipliers are included and only small changes of some physical parameters had to be made in order to adapt their use for the STEREO detector. The simulation is implemented such that its output has the same format as real data, thus allowing us to analyse it in parallel with the data.

### 3.1.1 Geometry of the detector in Geant 4

The STEREO energy response depends on the detector's details implemented in the simulation, as it has been shown by previous studies carried out on a prototype consisting

of half of a Target cell [29]. Thus, a detailed description of the geometry of the detector and acrylics has been implemented in the simulation from the technical drawings in [29]. A particular attention has been paid to the details at the edges of the acrylic plates, where wedges and tabs containing reflective sheets have been added to assure the optical junctions when glue joints are present. Moreover, the acrylic buffers, the photomultipliers and the calibration tubes are also implemented in the simulation. The source holders were also implemented in order to take into account the possible absorption of a part of the particles emitted by the calibration sources. An illustration of the level of detail implemented in the simulation can be seen in figure 3.1.

In addition to the detector's internal structure, the stainless steel tank holding the acrylic structure is also included in the simulation, along with the different shielding layers surrounding the detector. Also implemented are the muon veto on top of the detector, the transfer channel above the detector and the exterior shielding layers installed along the walls separating the STEREO room from the neighbouring experiments. These elements allow us to study the level of background at the STEREO site and especially to simulate the cosmic background using the CRY libraries [91], which represents the main source of background in the neutrino expected region.

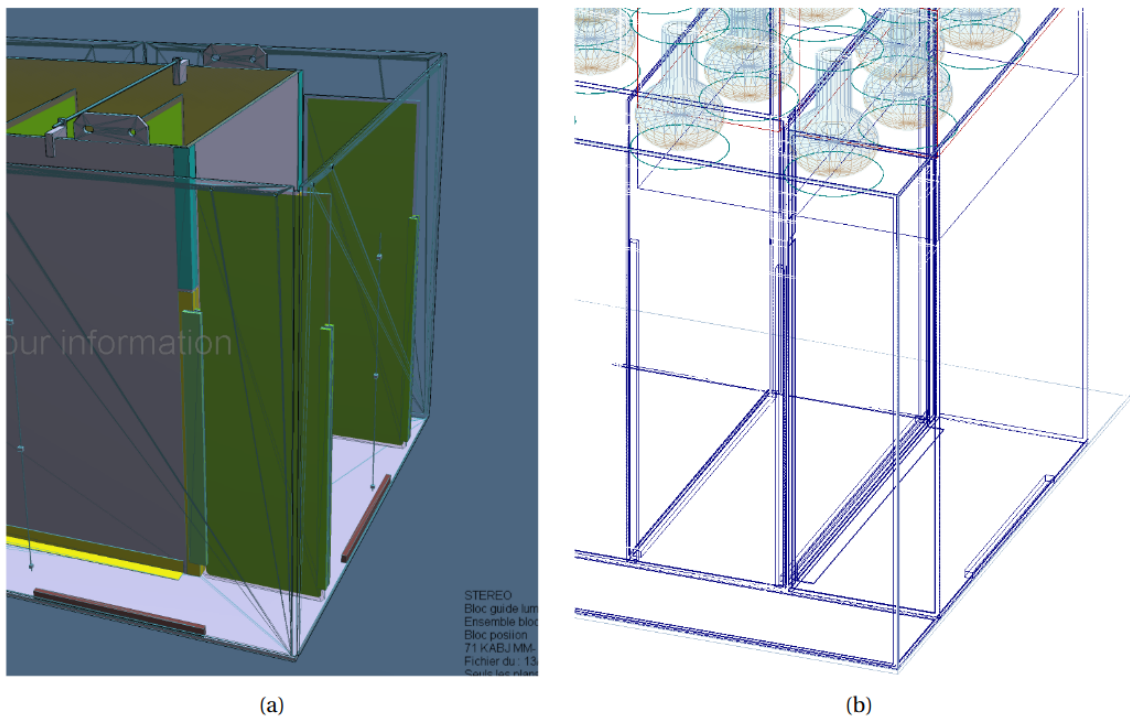


Figure 3.1 – Internal geometry of STEREO detector a) in the technical drawings and b) as implemented in GEANT4. Source: [92].

### 3.1.2 Particle propagation

The propagation and interactions of the simulated particles are done in regular steps that are automatically adapted in GEANT4 such that a compromise is found between the precision of the simulation and the computation time. At every step, a MC technique is used to decide what physical interaction the particle will undergo. After the interaction is chosen, the state of the particle is updated and eventual daughter particles are registered to the memory in order to be subsequently simulated. The scintillation light is generated (see section 3.1.3) and tracked until it reaches the PMs, where it is converted in an electric signal by making use of the simulated electronic chain.

A simulated event has a well defined time window, chosen to correspond with the integration window of a PM pulse. This allows us to separate the Prompt and Delayed signals and to analyse the simulated events in the same way in which the real events are analysed. The simulated events are registered in a ROOT file as entries of a tree of data (TTree). Every entry contains all the information of the respective simulated event, from the initial state of the particle to the propagation of all the daughter particles. From the tree of data we can extract all the relevant information for the analysis, such as the total deposited energy in the liquid scintillator  $E^{dep}$ , which is of crucial importance for the energy reconstruction technique that will be described in section 3.3.1.

### 3.1.3 Light generation and collection

The scintillation light is emitted photon by photon, at every step in GEANT4, by converting the deposited energy in light using an emission spectrum that takes into account the presence of the PPO and Bis-MSB wavelength shifters, as illustrated in figure 3.2. Once emitted, a photon can undergo a series of absorptions and re-emissions until it eventually disappears, for example by being absorbed by the photocathode of a PM or by a molecule that will subsequently deexcite without emitting light. The probability that a photon is absorbed by the liquid is driven by the value of the attenuation length, while the probability that a photon reaching the photocathode of a PM is converted into a photo-electron is driven by the value of the quantum efficiency. The quantum efficiency's dependence on the wavelength and the incidence angle of the incoming light on the photocathode was measured by WANG et al. [93] and is implemented in the simulation code.

A special attention was put into replicating the parameters driving the light transport and absorption in the simulation. The properties of the liquid scintillator were measured in dedicated laboratory tests [85]. These measurements, along with information coming from the comparison between data coming from the calibration campaigns and the simulation, were used to fine tune the values of the parameters governing the scintillation and light-propagation processes. The parameters with the biggest impact on the simulation that can be adjusted during the fine tuning campaigns are the attenuation length of the liquid and the light yield of the Target liquid and of the Gamma Catcher liquid. The way in which these parameters were fine tuned in practice will be presented in section 3.2.

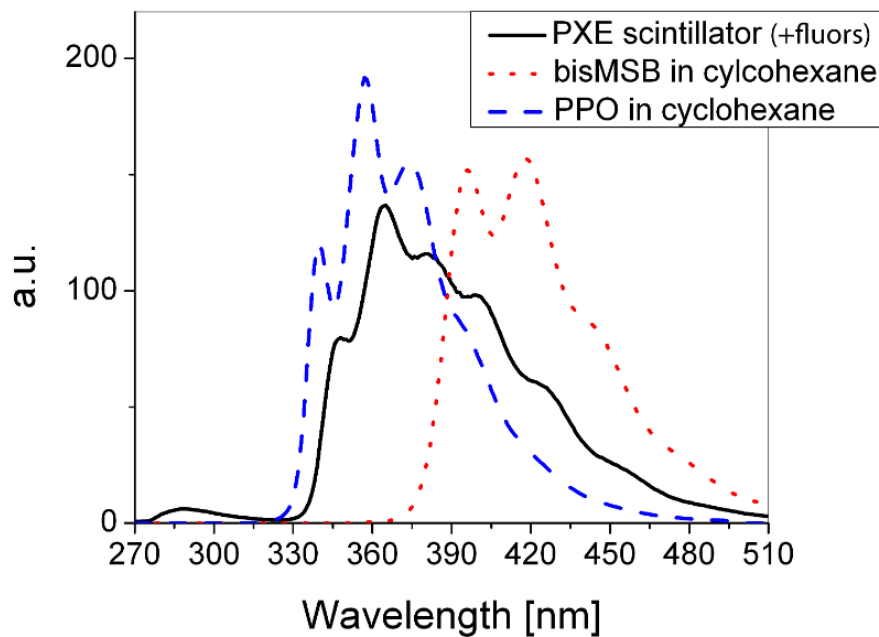


Figure 3.2 – Combined emission spectrum for the fluors used inside the STEREO liquid scintillator (black solid line). The blue dashed line represents the emission spectrum of the PPO fluor, while the red dotted line represents the emission spectrum of the bis-MSB fluor. Source: [94].

To be able to compute the Target proton number, the chemical composition and the densities of all the scintillator components are implemented in the simulation. This is also important in order to correctly estimate the detection efficiency, which depends on the fraction of neutron captures by Gd isotopes. The main component of the liquid scintillator, accounting for 73% of the total mass, is the linear alkyl benzene (LAB) which does not have a well-defined molecular formula, since it is a mixture with hydrocarbon chains of different lengths. In order to surpass this difficulty, we have used the average molecular mass specified by the supplier to estimate the number of hydrogen and carbon atoms per molecule in the simulation. The wavelength shifters and the Gd-complex are not taken into account when computing the Target proton number. This could introduce a small bias on the computed Target proton number in the simulation, since the scintillator density is calculated from the individual densities of the solvents composing it. Since the calculated Target proton number is less accurate than the one obtained from the mass and hydrogen fraction measurements described in section 2.3.1, a correction factor of  $(0.983 \pm 0.010)$  has to be applied on the normalization of the anineutrino events that interact in the scintillator below the acrylic buffers. However, in section 4.1 we will see that the fraction of selected IBD candidate events outside of the Target volume is much smaller than 1%, thus allowing us to neglect volumes other than the Target in the calculation of the proton number.

### 3.1.4 The optical model for the separative plates

Due to the liquid scintillator's leaking inside the separating walls (see section 2.4), their reflectivity properties degraded, since the air gap between the ESR film and the acrylic plates that was ensuring the optimal properties of the reflective film has disappeared. In order to account for this scenario, a versatile modelization of the separating walls, that accounts for both the different individual liquid filling levels for the acrylic walls and the effect of the liquid's presence on the reflectivity properties of the ESR film, was implemented in the Monte Carlo [29]. Moreover, absorption due to the presence of the nylon net was also introduced in the simulation. This section will firstly present the measurements that show the behaviour of the ESR film inside the liquid scintillator and secondly explain the optical model that was implemented to take into account the complex behaviour of the ESR film's reflectivity properties. It introduces the parameters that will be fine-tuned in the next section 3.2.3.

#### ESR film properties

The ESR film used for STEREO is designed to have a high reflectivity in a large range of wavelengths at any incident angle in air. Indeed, the reflectivity of the film used by STEREO was measured with a spectrophotometer to be above 98% in the 400-950 nm range in air, at an incidence angle of  $7^\circ$ .

The real-life conditions of the experiment made that the ESR film was submerged in liquid scintillator. In this situation, a strong decrease in reflectivity is expected at large angles [95],[96]. For example, the transmission was measured with a spectrophotometer to have a value of  $\sim 50\%$  for angles of incidence larger than  $75^\circ$ , at a wavelength of 450 nm, when the ESR film was placed in liquid scintillator. Thus, the reflectivity of the ESR film depends both on the wavelength of the incoming light and on its incident angle, when placed in liquid scintillator. In fact, the critical angle starting from which there is an abrupt drop in reflectivity for the ESR film placed in liquid scintillator depends on the polarization of the incident light. The critical angle for p-polarized light,  $\theta_p$ , is smaller than the critical angle for s-polarized light,  $\theta_s$ , for most of the wavelengths of interest for STEREO. This leads to a split in three regions of different reflectivity. The first one, for  $\theta < \theta_p$ , has a high reflectivity. The second one, for  $\theta_p < \theta < \theta_s$ , has a reflectivity of the order of 50%. The third one, for  $\theta > \theta_s$ , has a reflectivity virtually equal to zero. Thus, most of the light in this third region is transmitted through the ESR film. Part of this transmitted light can also be absorbed due to the presence of the nylon net. The practical implementation of the optical model which takes into account all the aspects discussed here is presented in the next part of this section.



### Model of the separating walls

In the STEREO simulation, the separating walls are considered as a black box, in the sense that the real physical effects taking place inside the walls are not simulated directly. Instead, a photon arriving on the surface of the separating wall can be reflected, transmitted or absorbed with different probabilities, depending on its incident angle, its wavelength, and the presence or absence of the liquid scintillator inside the separating wall.

Every separating wall is characterized by a parameter  $p$  that represents the proportion of the wall's height that is filled with liquid scintillator. For example, the parameter  $p\_c3\_c4$  represents the proportion of the height of the wall between cells 3 and 4 that is filled with liquid scintillator (see figure 3.3). A value of  $p=1$  means that the respective separating wall is filled with liquid scintillator, while a value of  $p=0$  means that the respective separating wall has no liquid scintillator inside.

The way in which the  $p$  parameters are fine tuned is presented in section 3.2.3.

Since the optical properties of the separating walls depend on whether the air gap between the ESR film and the acrylic walls is present or not, the reflection, transmission and absorption probabilities for a photon reaching the surface of the separating wall vary accordingly to the two possible scenarios. In any case, if the wavelength of the light is smaller than 378 nm, it is absorbed.

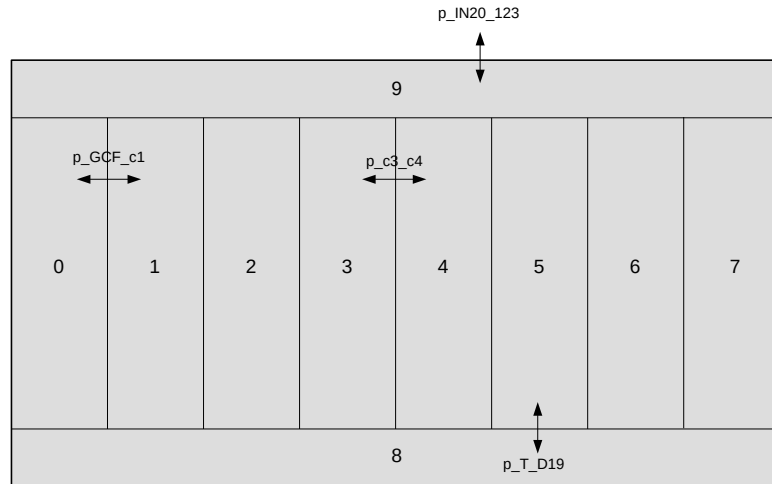


Figure 3.3 – Illustration of the liquid height parameters  $p$  that describe the proportion of a separating wall's height that is filled with liquid scintillator. The cells 1-6 are the Target cells, while cells 0,7,8 and 9 are the Gamma Catcher cells. See figure 2.6 for a complete detector scheme.

### Air gap maintained

In the case in which the air gap is maintained, the probability that the light arriving on a separating wall with a single ESR film (see footnote 6) is reflected is determined following the formula:

$$R(\theta) = r(\theta) = \begin{cases} 100\% & , \text{ if } \theta > \theta_c = \arcsin(n_{air}/n_{acrylic}) \simeq 42^\circ \\ 98.5\% & , \text{ otherwise} \end{cases} \quad (3.1.1)$$

where  $R(\theta)$  is the reflection probability of the entire separating wall and  $r(\theta)$  is the reflection probability of a single ESR film. For the separating walls containing two ESR films  $R(\theta) \neq r(\theta)$ . This case will be briefly treated at the end of this section.

If the angle of incidence is bigger than the critical angle  $\theta_c = \arcsin(n_{air}/n_{acrylic}) \simeq 42^\circ$  the light will be reflected with a 100% probability. This is due to the total reflection on the acrylic-air interface. Otherwise, the light is reflected with a 98.5% probability. This is due to the reflection on the ESR film, whose properties are optimal if kept in air.

Since we account for the probability that the light is absorbed, the transmission probability, denoted by  $T$ , won't simply be of 1.5% as one would expect if there was no absorption, but it will be slightly modified. The absorption probability, denoted by  $A$ , is due to the fact that the transmitted light can be absorbed by the nylon net while it traverses the separating wall. The expressions for the absorption and the transmission probabilities for a separating wall with a single ESR film are

$$\begin{cases} A = (1 - r)a \\ T = (1 - r)(1 - a) \end{cases} \quad (3.1.2)$$

where  $a$  is the probability that the light traversing the nylon net is absorbed by it.

Equation 3.1.2 makes it clear that for the case of a separating wall containing a single ESR treated here, the light that is not reflected is either transmitted or absorbed. As expected, we find that  $R + T + A = 1$ . For example, for  $r=98.5\%$  and  $a=10\%$  we find that  $R=98.5\%$ ,  $T=1.35\%$  and  $A=0.15\%$ , which demonstrates the low impact of the absorption term for the single ESR film separating walls. An illustration of the angle dependent reflection and transmission processes on the part of a separating wall that maintained an intact air gap can be seen on the upper part of figure 3.4.

### Air gap filled with liquid scintillator

In the case in which the air gap is filled with liquid scintillator, the probability that the light arriving on a separating wall with a single ESR film is reflected is determined following the formula

$$R(\theta) = r(\theta) = \begin{cases} 0\% & , \text{ if } \theta > \theta_s \\ r_{inband} & , \text{ if } \theta_p < \theta < \theta_s \\ 97\% & , \text{ if } \theta < \theta_p \end{cases} \quad (3.1.3)$$

where  $r_{inband}$  is the probability that the light is reflected if the incidence angle is in the band defined by the critical angles for s and p-polarized light<sup>1</sup>. The transmission and absorption coefficients are computed with the formulas from equation 3.1.2. An illustration of the angle dependent reflection and transmission processes on the part of a separating wall that is filled with liquid scintillator can be seen on the lower part of figure 3.4.

In the case of a separating wall with two ESR films enclosed between the acrylic plates (see figure 2.7), the expression of the reflection, transmission and absorption probabilities of the wall are more complex. This is due to the fact that the light that is transmitted by the first ESR film encountered could be reflected by the second ESR film and thus has a probability to return to the cell from which it was coming. Moreover, since the light can bounce between the two ESR films multiple times, it passes the nylon net multiple times, thus having a larger probability of being absorbed. In this case, the reflection, transmission and absorption probabilities of the separating wall have the following expressions:

$$\begin{cases} R = r + \frac{rt^2(1-a)^2}{1-r^2(1-a)^2} \\ T = \frac{t^2(1-a)}{1-r^2(1-a)^2} \\ A = 1 - R - T \end{cases} \quad (3.1.4)$$

where  $r$  is the reflection probability of a single ESR film defined in 3.1.1 and 3.1.3,  $t = 1 - r$  and  $a$  is the absorption probability when the light traverses a single time the nylon net.

As an illustration, for  $r=98.5\%$  and  $a=10\%$ , we find that  $R=98.6\%$ ,  $T=0.1\%$  and  $A=1.3\%$ , which demonstrates the sizeable impact of the absorption term for the double ESR film separating walls. Compared to the single ESR film separating walls, the absorption and transmission probabilities are now inverted while the reflection probability remains virtually the same.

The parameters describing the optical properties of the separating walls that can be adjusted during the fine tuning are the inband reflectivity of the ESR film,  $r_{inband}$ , the  $p$  parameters describing the height of a separating wall filled with liquid and the probability that the light is absorbed when traversing a single time the nylon net,  $a$ . The way in which they were adjusted and their impact on the simulation results and on the agreement between the data and the MC will be presented in section 3.2.

---

<sup>1</sup>These critical angles depend on the wavelength of the incident light and are computed using a model fitted to the experimental measurements of the ESR film's reflectivity properties in a liquid with a similar optical index with the one used by STEREO [95].

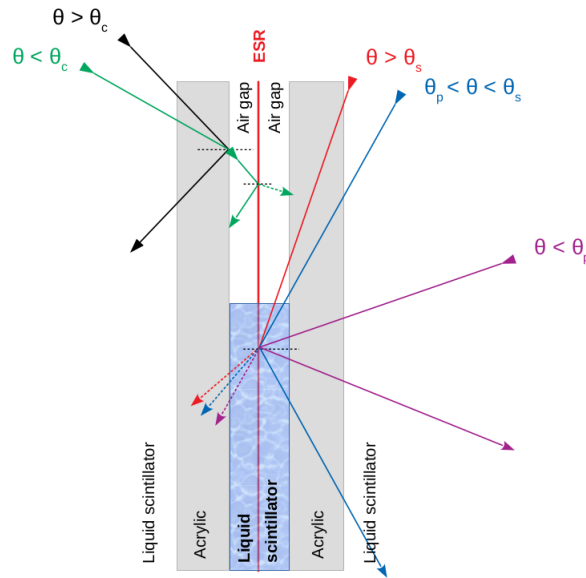


Figure 3.4 – Scheme illustrating the reflectivity and transmission properties of a single ESR separating wall. Illustrated is the case in which part of the separated wall was filled with liquid scintillator (lower part of the scheme) and part of it maintained an intact air gap (upper part of the scheme).

### 3.1.5 The status of the MC simulation before the fine tuning

In the previous sections we have presented the Monte Carlo simulation of the STEREO detector. We have seen that there are several parameters that can be estimated from real measurements, such as the attenuation length and light yield of the liquid scintillator, while other parameters, such as the  $p$  parameters or the absorption parameter  $a$ , need to be fine tuned in order to obtain the best possible agreement between the data and the simulation. While for the phase I of the data taking we tried to stay as close as possible to the real values of the parameters of the simulation, for phases II and III we have preferred to give effective values to certain simulation parameters in order to be able to reproduce at best the data.

If we compare the fine tuned simulation from phase I with the data from a calibration campaign representative for phase II, as shown in figure 3.5 for the  $^{24}\text{Na}$  source, at the raw charge level, we see that the ratio simulation/data is different from 1 for most of the positions of the calibration source. Moreover, another striking feature is that we do not reproduce very well the top-bottom light collection asymmetries, as it can be deduced from the slope of the simulation/data ratio for different source heights inside a given cell.

The next section will be dedicated to a method developed in the present thesis and used to perform the fine tuning of the simulation parameters for phases II and III of the data taking, such that the discrepancies between the data and the simulation illustrated in the previous paragraph are corrected.

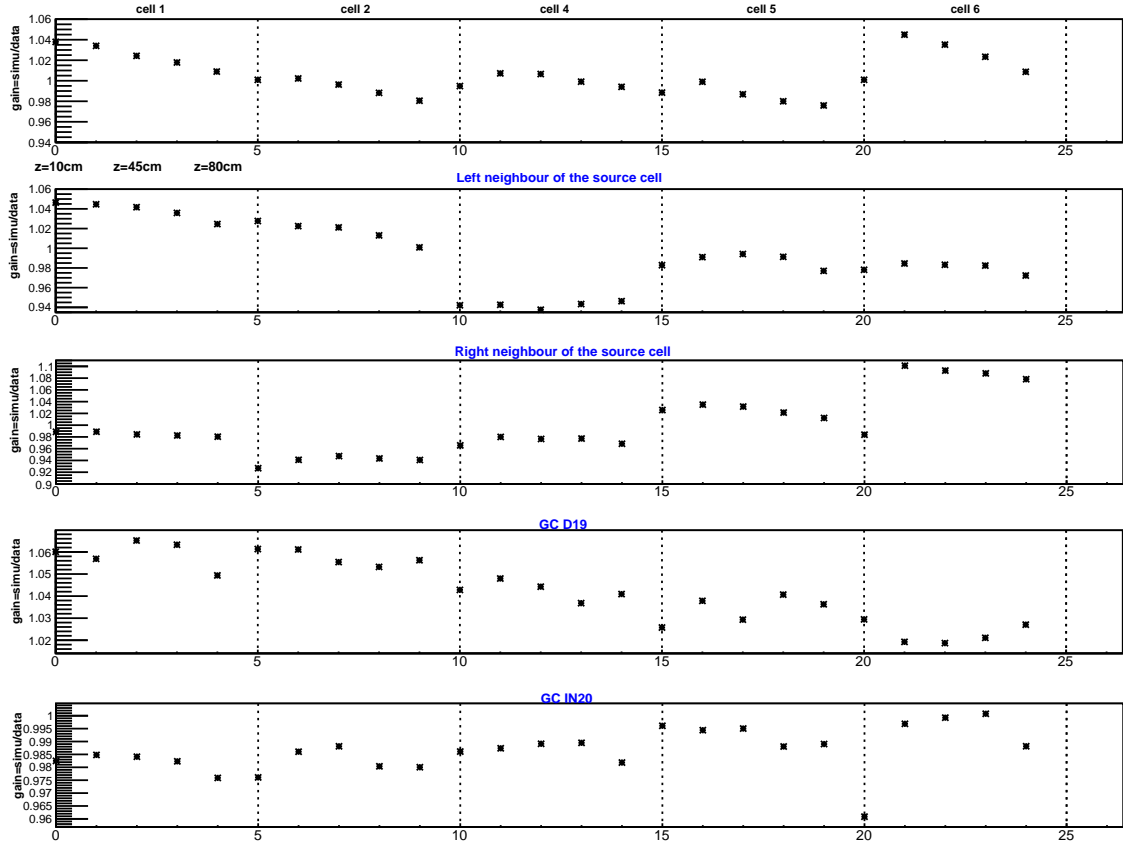


Figure 3.5 – Gain values obtained by comparing the v2r3 version of the Monte Carlo, i.e. before the phase II fine tuning, with the data acquired during the calibration campaign of 26<sup>th</sup> April 2018 (in the middle of phase II), for the  $^{24}\text{Na}$  source. The columns indicate the cell in which the source is deployed as well as its position. The first row shows the gain values obtained by fitting the two gamma peaks of the  $^{24}\text{Na}$  source when looking at the charge spectra inside the cell with the source. The other rows show the gain values obtained when fitting the two gamma peaks of the  $^{24}\text{Na}$  source for gamma particles that interacted in a neighbouring cell; in our case, we look to the left and right cells with respect to the source cell as well as to the two lateral Gamma Catcher cells. The cell placed to the left of cell 1 is the Gamma Catcher Front, while the cell placed to the right of cell 6 is the Gamma Catcher Back.

## 3.2 Fine tuning of the optical parameters of the Monte Carlo

The goal of the fine tuning is to obtain the best possible agreement between the data and the Monte Carlo simulations at the raw charge level, before applying the energy reconstruction algorithm. In order to do so, we compare the simulated charge spectra for a given calibration source with the collected charge spectra obtained during the energy calibration campaigns, at the cell level:

$$Q_i = \sum_{PM_i} Q_{PM_i} \quad (3.2.1)$$

where  $Q_i$  is the total charge collected inside cell  $i$  and  $Q_{PM_i}$  is the charge collected by a PM of cell  $i$ <sup>2</sup>. The comparison is performed for the configurations in which the calibration source is deployed inside the internal calibration tubes at five different  $z$  positions:  $z=10,30,45,60,80$  cm (see table 2.1 and figures 2.12 and 2.6) by applying a homogeneous scaling factor to the simulated spectra such that they match at best the corresponding measured spectra. The obtained scaling factors along with the form of the spectra in the low charge region, called the light-leaks region, when the source is placed in a neighbouring cell to the one that we're looking at, guide us into fine tuning the parameters of the simulation iteratively until obtaining the desired agreement between data and simulation.

In order to perform the fine tuning for phases II and III of the data taking we have used the calibration runs for the  $^{24}\text{Na}$  source as a reference, since its energy spectrum presents a well defined structure, being formed of two gamma rays of energies 1.38 MeV and 2.76 MeV. This structure gives rise to a charge spectrum that presents three distinguishable peaks, two corresponding to the two individual gamma rays of the  $^{24}\text{Na}$  source, and one corresponding to the simultaneous detection of the two gamma rays inside one cell, denoted as the sum peak. Moreover, this structure is also present in the light-leaks region, when the source is placed in a neighbouring cell to the one that we're looking at, giving us precious insight about the needed fine tuning of the liquid level inside the separating walls between the detector's cells.

The fine tuning of the optical parameters is performed once for every phase, by comparing the simulation with the data taken during a given calibration campaign which is chosen to be representative for the entire data taking phase (it is usually chosen to be close to the middle of the phase that we want to fine tune). However, since the detector properties slowly evolve in time during the period of a phase of data taking, the energy reconstruction method discussed in section 3.3.1 is responsible for correcting to first order the remaining time evolution effects.

In this section we will first present the method that is used to compare the simulated

---

<sup>2</sup>The data charge spectra are obtained by subtracting the background spectrum from the spectrum obtained with a calibration source.

and the measured charge spectra in order to assess their agreement. Then, we will present the global strategy that was used to perform the fine tuning based on sensitivity studies to understand the influence of the different parameters. In the end, we will present the final status of the fine tuning for the data taking phases II and III and discuss the remaining discrepancies between data and simulation.

### 3.2.1 The gain method

#### Principle of the gain method

In order to examine the compatibility between the data and the Monte Carlo simulations we need to define a method that allows us to compare them quantitatively. For example, when comparing the charge spectrum of a calibration source in the data with the one obtained in the MC simulation one may look at the position of one particular energy peak and compute the ratio  $\mu_{data}/\mu_{MC}$ , where  $\mu$  is obtained by fitting the peak with a suitable function, usually a Gaussian. In this way, we have the information of how the data compares with the MC simulation at the level of the peak but we ignore the compatibility between the two of them in the rest of the spectrum. Moreover, only the average value  $\mu$  is compared, thus ignoring for example the possible difference in the width of the peaks.

In this section, a method that allows the comparison between the data and the MC simulations at the level of the entire spectrum will be presented. We will refer to this method as the gain method for the rest of the manuscript. The gain method consists of applying a homothetic transformation to the simulated charge spectra in order to best reproduce the data charge spectra, as it is illustrated schematically in figure 3.6. This works as a dilation with respect to a fixed point that is applied on the simulated spectrum. The transformation is characterized by the gain parameter that will be denoted by  $g$ . The spectra with which we are working are stored in the form of binned histograms. It is worth noting that the applied homothetic transformation is not equivalent with a shift in the spectrum. An illustration of what happens at the level of the bin when applying the homothetic transformation to the simulated spectrum is given in figure 3.7. It can be seen that the bin contents of the dilated simulated spectrum ( $h_s$ ) can be obtained as linear combinations of the bin contents of the raw simulated spectrum ( $h$ ).

#### Implementation of the gain method

In order to find the appropriate homothetic transformation (the best gain  $g$ ) that should be applied to the simulation spectrum such that it best reproduces the data spectrum one should define a  $\chi^2$  that has to be minimized:

$$\chi^2(g, \alpha) = \sum_{i=min}^{max} \frac{(h_d[i] - \alpha h_s[i])^2}{\sigma_d^2[i] + \alpha^2 \sigma_s^2[i]} \quad (3.2.2)$$

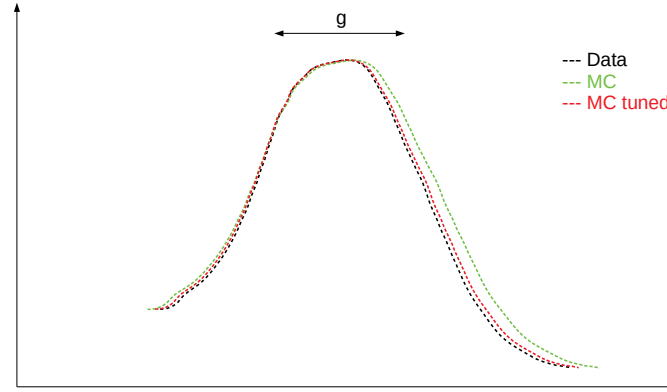


Figure 3.6 – Illustration of the principle of the gain method: the black dotted curve represents the data, the green curve represents the MC simulation and the red curve represents the tuned MC simulation, which is obtained by applying the appropriate homothetic transformation on the green curve, such as to best reproduce the data.

where

- $h_d$  is the data histogram.
- $h_s$  is the tuned simulation histogram that depends on the value of the gain parameter  $g$ .
- $\alpha$  controls the normalization of the tuned simulation histogram, i.e it allows us to compare histograms that have different number of events.
- $\sigma_d$  and  $\sigma_s$  are the uncertainties associated to the data and the tuned simulation histograms, respectively.
- $[min, max]$  is the range in which the fit is performed.

The fit is finally performed by minimizing  $\chi^2(g, \alpha)$  and it provides us the parameters  $g$  and  $\alpha$  that should be applied to the simulation histogram in order to best reproduce the data. It is worth mentioning that we could interpret the parameter  $g$  as a ratio  $\sim$  simulation/data and that it has been verified that it is compatible within the uncertainties with the ratio  $\mu_{MC}/\mu_{data}$  obtained by locally fitting the peaks in the data and the simulation with a Gaussian.

In figure 3.8 we can see an example of fit performed using the gain method presented



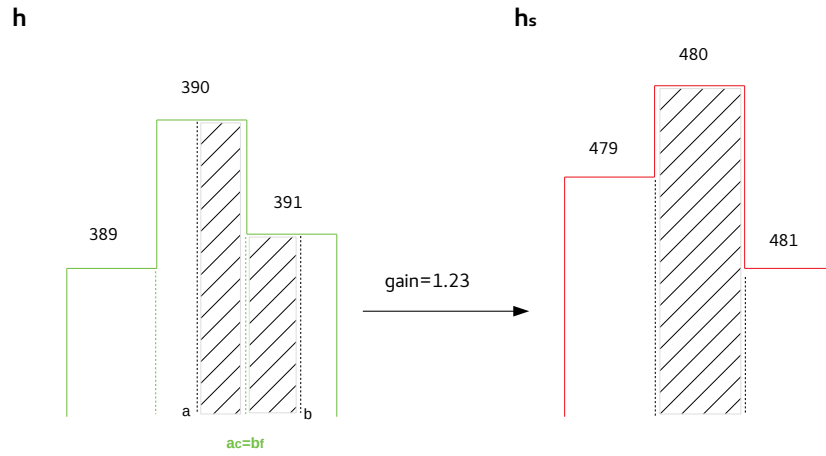


Figure 3.7 – Each bin of the tuned simulation histogram  $h_s$  is computed as a weighted linear combination of the contents of the appropriate bins of the simulation histogram  $h$ , which depends on the value of the gain parameter  $g$  of the transformation. In the given example, for an applied gain of  $g = 1.23$ , the content of bin 480 of the tuned histogram is obtained as a linear combination of the contents of bins 390 and 391 of the simulation histogram  $h$ , as:  $h_s[480] = \alpha h[390] + \beta h[391]$ .

above, for a source of  $^{54}\text{Mn}^3$ , while figure 3.9 presents an example of fit for a source of  $^{24}\text{Na}$ . In both examples the simulation is compared with the data acquired during the calibration campaign of 26<sup>th</sup> April 2018, which is representative for the phase II data.

Finally, it is worth emphasizing that the gain method is used as a way to assess the agreement between the data and the simulation at the raw charge level during the different steps of the fine tuning process. The extracted  $g$  parameters after applying the gain method on a data-simulation couple are used as a guide in the fine tuning of the optical parameters of the STEREO simulation.

---

<sup>3</sup>Even though the fine tuning of the simulation parameters for the phase II and III data sets was performed by looking at the raw charge spectra of the  $^{24}\text{Na}$  source, we used the  $^{54}\text{Mn}$  source in order to perform cross-checks during the fine tuning process.

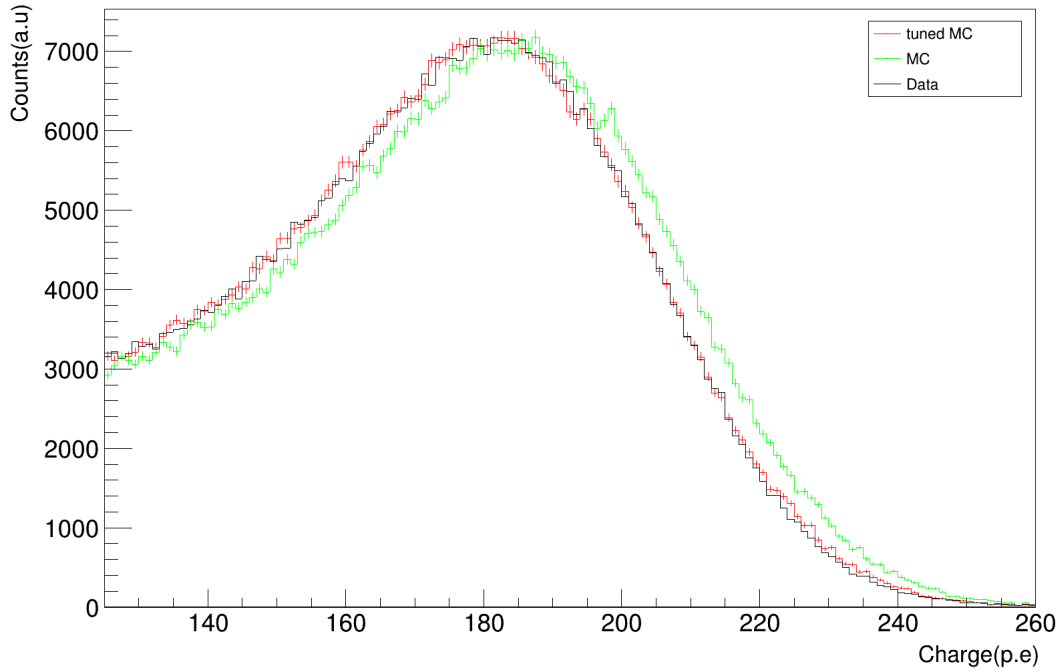


Figure 3.8 – Example of fit using the gain method for a  $^{54}\text{Mn}$  source deployed on top of cell 1 ( $z=80$  cm). The data histogram is plotted in black, while the MC simulation histogram is plotted in green. After applying the gain method, we obtain the tuned MC simulation histogram plotted in red, which best describes the data. The factor  $g$  by which the initial simulation was dilated provides us the wanted information about the compatibility between the data and the MC simulation and guides us into fine tuning the optical parameters of the simulation such that it best describes the data.

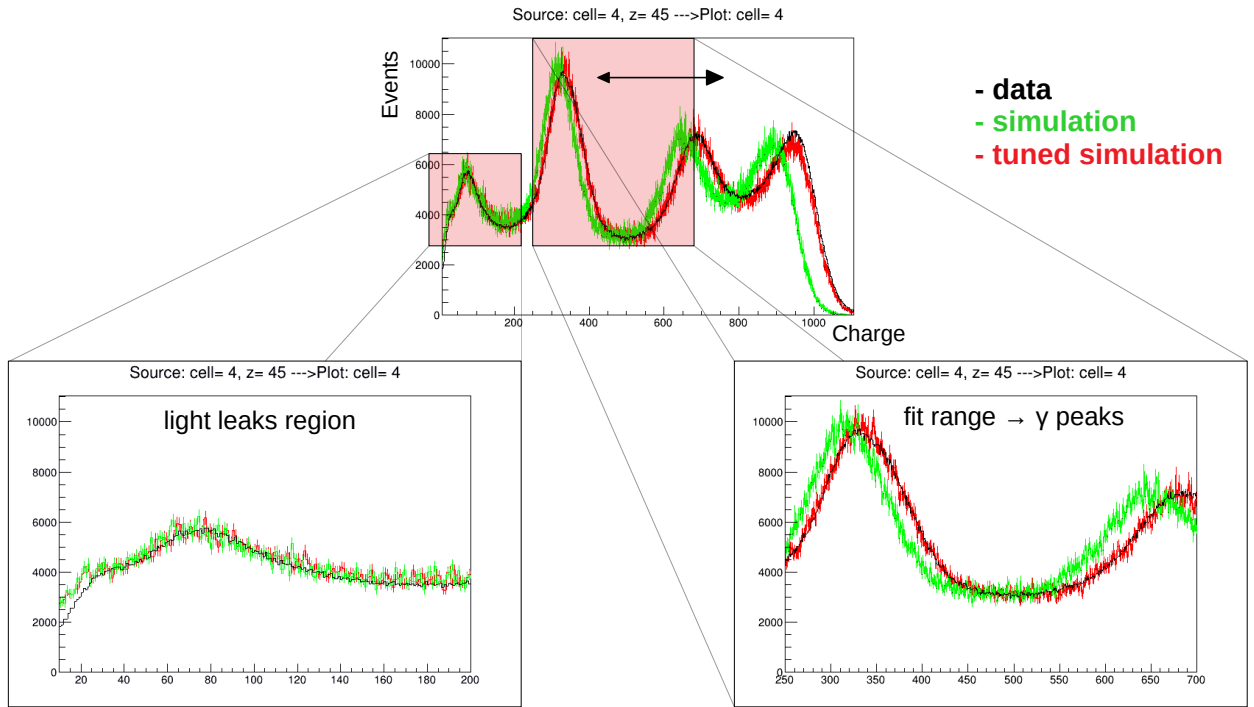


Figure 3.9 – Example of fit using the gain method for a  $^{24}\text{Na}$  source deployed at the center of cell 4 ( $z=45$  cm). The data histogram is plotted in black, while the MC simulation histogram is plotted in green. After applying the gain method, we obtain the tuned MC simulation histogram plotted in red, which best describes the data. The plot also shows the zoomed image on the fit range region and the zoomed image of the light leaks region. This latter region is mainly populated by light from gamma particles that have interacted in the neighbouring cells and has leaked back to the source cell through the separating walls.

### 3.2.2 The global strategy of the fine tuning

It can be seen in figure 3.5, which presents the status of the Monte Carlo simulation before the phase II fine tuning, that the gain values are not always centered at a value of 1, which would mean a perfect agreement between the data and the Monte Carlo simulations. Moreover, there are visible discrepancies in the gain value observed when the source is deployed at different heights within one cell. For example, in cell 1, there is a  $\sim 4\%$  gain variation between the configuration in which the source is placed at the  $z=10$  cm position and the configuration in which the source is placed at  $z=80$  cm position inside the cell. This is due to the fact that the top-bottom light collection effect seen in the data is not well reproduced by the simulation.

The goal of the fine tuning is to obtain the best possible match between the data and the simulation at the raw charge level. In our case, that means reaching a gain close to 1 for every cell and every position of the source inside the cell, thus correcting the top-bottom discrepancies observed at the cell level.

To reach this goal we need to be guided by several observables. First of all, for a given position of the source inside one cell, the gain value is the main observable that guides globally the way in which we need to modify the simulation parameters.

If the gain value for a given position of the source is different from 1, we can correct it by modifying one or more of the following parameters that were presented in section 3.1: the light yield of the liquid scintillator, the attenuation length of the liquid scintillator, the absorption inside the separating walls, the color of the calibration tubes (which is related to their reflectivity), the height of the liquid inside the separating walls between the cells, or the inband reflectivity of the separating walls.

Secondly, a finer information about the changes that are needed in the simulation is given by the light leaks region of the charge spectra registered in the neighbouring cells to the cell in which the source is placed. Figures 3.10 and 3.11 show an example of agreement between the data and the simulation at the raw charge level for the  $^{24}\text{Na}$  source placed in cell 1 at  $z=45$  cm both for the spectrum registered in the source cell and in the neighbouring cells. While figure 3.10 shows the agreement between data and simulation in the gamma rays region for the neighbouring cells, figure 3.11 shows the agreement in the low charge region, which is mainly populated by light leaks from gamma rays that deposited their energy in the neighbouring cells.

It can be seen that the light leaks region of the spectrum has a well-defined structure and that in the neighboring Target cells to the source cell even the two peaks structure is visible. Along with the information provided by the gain value, which quantifies the overall agreement between data and simulation in the gamma peaks region<sup>4</sup>, the information provided by the agreement in form and position between the data and the simulation in the light leaks region helps us in the fine tuning of the  $p$  parameters, *i.e.* the parameters

---

<sup>4</sup>For the purpose of the fine tuning, we chose the range in which we minimize the  $\chi^2$  distribution to correspond to the two individual gamma peaks region of the  $^{24}\text{Na}$  source. Due to this choice, the gain quantifies the overall agreement between data and simulation in the gamma peaks region.

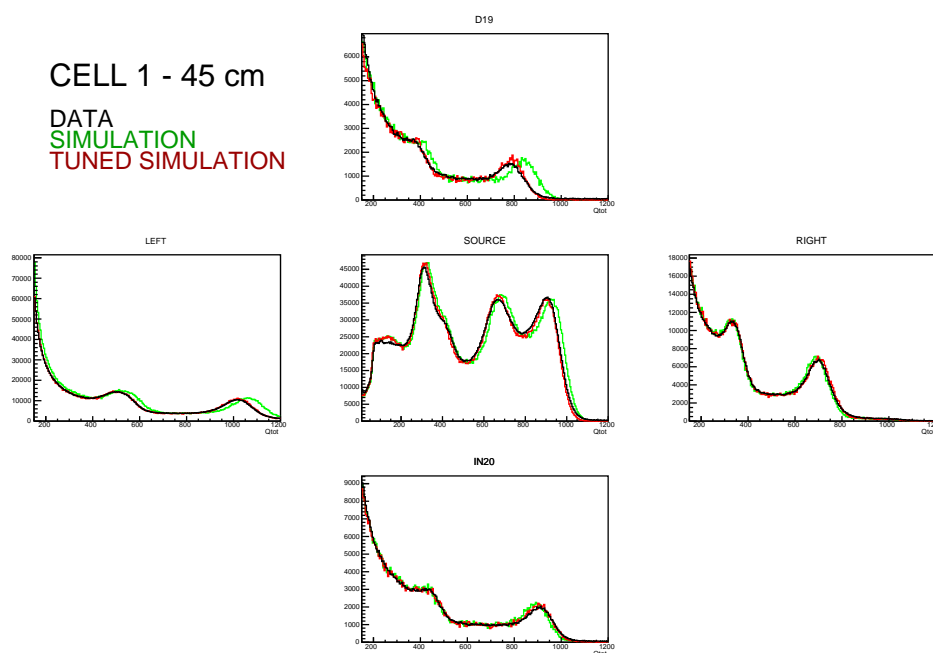


Figure 3.10 – Example of gain fit for the source placed at the center of cell 1 ( $z=45$  cm). The figure shows both the fit performed on the charge spectrum registered by the PM's of the source cell, in the center, and the fit performed on the spectra registered by the neighboring cells. The range of the plots is set in order to make visible the full gamma peaks region of the spectrum, as opposed to the light-leaks region. The fit performed to obtain the optimal gain value is done in the range containing the two single gamma peaks of the  $^{24}\text{Na}$  source.

defining the height of the liquid in the separating walls between the cells, as well as in the fine tuning of the absorption and reflectivity parameters of the separating walls.

Since most of the parameters of the simulation are highly correlated between them and since the modification of one of these parameters may have an impact on both the light leaks between the different cells and on the gain value for the different positions of the source, we have defined a strategy from the beginning in order to be able to easily follow the changes brought by each step of the fine tuning. Moreover, since the simulation of the charge spectra for the  $^{24}\text{Na}$  source takes  $\sim 24$  hours, the fine tuning had to be done "by hand", in a step by step approach. In practice, we modified only a few parameters at each step of the fine tuning in order to be able to disentangle the changes brought to the simulation by every parameter change.

After several steps of the phase II fine tuning we realised that the optimal approach would be to first fine tune the  $p$  parameters, i.e. the parameters defining the height of the liquid in the separating walls between the cells, by looking at the low charge region of the spectrum when the source is in a neighboring cell. Then we could go on and tune the absorption in the separating walls and the reflectivity of the calibration tubes in order to minimize the top-bottom effects. At the end, when the  $p$  parameters are tuned and the top-bottom effects are reduced to a minimum, we look at the gain values for the different

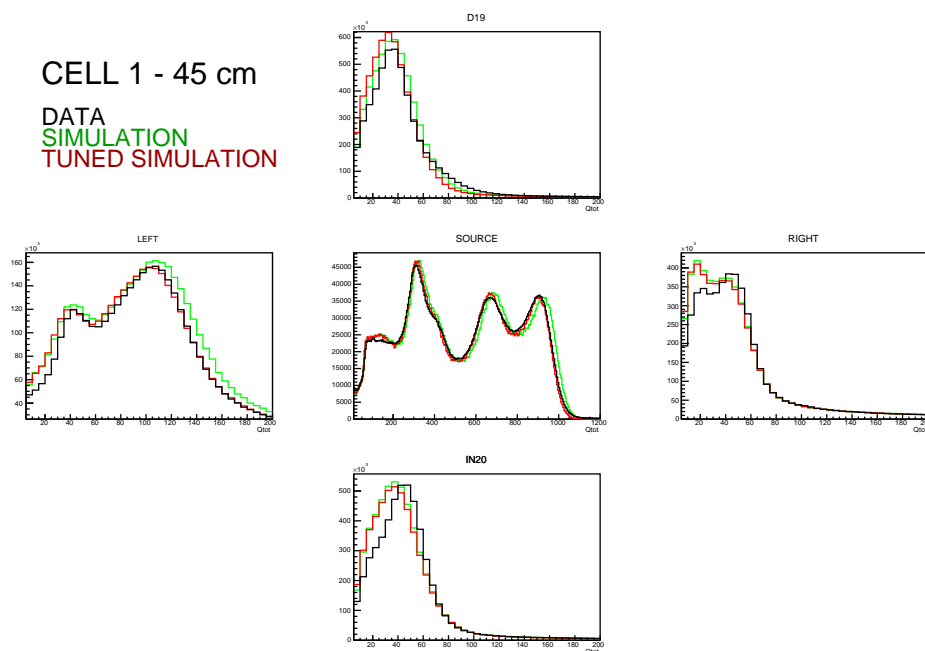


Figure 3.11 – Same as figure 3.10, but the range of the plots is such that the light leaks region of the charge spectra is visible for the neighbouring cells to the source cell.

positions of the  $^{24}\text{Na}$  calibration source, and, if they are different from 1, we change the attenuation length and the light yield of the liquid scintillator in order to bring these values as close to 1 as possible.

When tuning the  $p$  parameters and the absorption in the separating walls we make sure that the mean gain value (mean of the different heights of the source inside the cell) is roughly the same for the different cells, such that we are left with only a common shift to correct in order to reach the best agreement between the simulated and the data raw charge spectra in all the cells. By first tuning the  $p$  parameters and the absorption in the separating walls, we make sure that the light leaks are described as well as possible. Afterwards, when tuning the light yield or the attenuation length in order to reach a gain as close to 1 as possible, the gamma rays region will be mostly affected, while the light leaks region will be scarcely modified. This is because changing the light yield or the attenuation length is equivalent to applying a homothetic transformation, which will influence more the high charge region of the spectrum (gamma rays region) than the low charge region of the spectrum (light leaks region) - see section 3.2.3.

### 3.2.3 Sensitivity studies

This section will present the different sensitivity studies that have been performed in order to understand the influence of the optical model's parameters on the form of the charge spectra. The information gained from these studies guided us towards the fine tuning of the relevant parameters of the simulation.

### Liquid height in the separative plates

The  $p$  parameters describing the percentage of the height of the separating walls that is filled with liquid scintillator are of crucial importance for the present fine tuning. They have an influence both on the gain value at the level of the cell and on the gain value for the neighbouring cells to the source cell. We recall here that the optimal gain is computed by minimizing a  $\chi^2$  value that is computed for a given range. In the case of the  $^{24}\text{Na}$  source we have chosen that range to roughly contain the two gamma peaks.

Increasing the value of the  $p$  parameter for a given separating wall results in an increased transmission and a decreased reflectivity for the given wall. Moreover, since the separating wall's reflection properties are different between the parts of the wall that are not filled with liquid scintillator (since the air gap ensures the optimal reflectivity on the ESR film - see section 3.1.4) and the parts of the wall that are filled with liquid scintillator, the change in the  $p$  parameter may have a different effect depending on the source  $z$  position inside the internal calibration tubes. Added to this is the fact that the light produced by the source placed at a low- $z$  position has to travel a bigger distance and thus has a bigger probability of hitting multiple times the separating walls and being transmitted or absorbed compared to the light produced by the source placed at a high- $z$  position.

We will now analyse a given example, where the source is placed in cell 1 and we look at the charge spectra registered in cell 9 (GC IN20), for two different values of the percentage of the height of the separating wall between cell 1 and cell 9 (GC IN20),  $p\_T\_GCIN20$ , that is filled with liquid scintillator.

The increase of the  $p\_T\_GCIN20$  has both an influence on the spectrum registered inside the source cell, namely cell 1 in our case, and on the spectrum registered inside cell 9 (GC IN20). For example, the spectrum in cell 1 is modified in the following manner

1. At low charge, i.e. in the region of the light leaks coming from the neighbouring cells, we expect the spectrum to be slightly shifted towards bigger values and wider. This is because the spectrum in this region is mainly populated by light emitted following the gamma rays interactions in the neighbouring cells, which then leak inside cell 1.
2. At high charge, in the region of the gamma peaks, the spectrum is shifted towards smaller charge values and it becomes less wide. This is because the light created by the gammas that interacted in cell 1 will be transmitted more to cell 9 due to the increase of  $p\_T\_GCIN20$ .

The spectrum in cell 9 (GC IN20) is expected to change in a similar manner to the one in cell 1. Figure 3.12 shows the charge spectra registered in cell 9 (GC IN20) when the source is placed in cell 1 at  $z=45$  cm for  $p\_T\_GCIN20=0.6$  and  $p\_T\_GCIN20=0.8$  (for the purpose of the comparison and in order to disentangle the effect of the increase in  $p\_T\_GCIN20$ , all the other parameters of the simulation remain constant

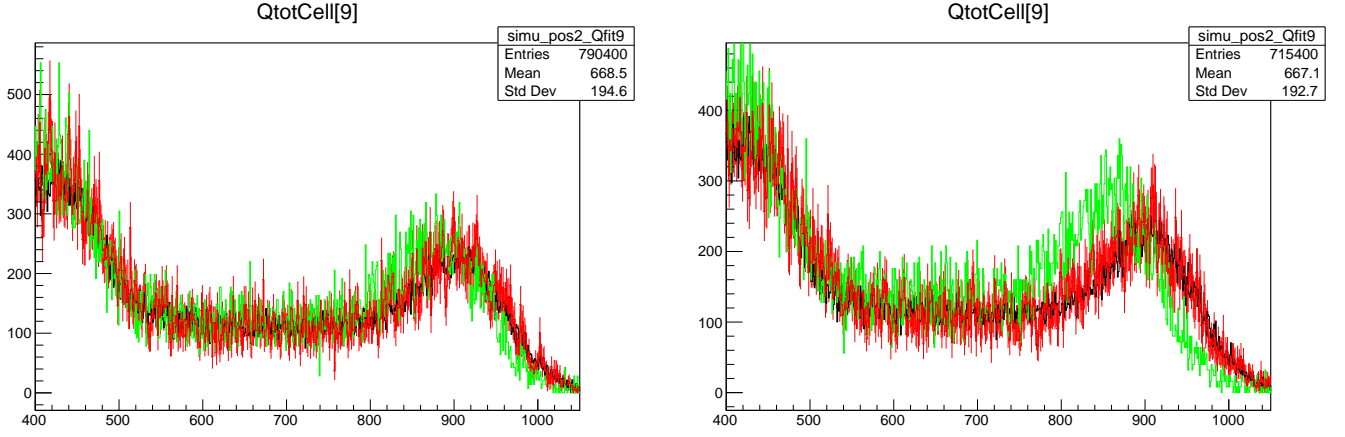


Figure 3.12 – Example of sensitivity of the simulation to the height of the liquid in the walls separating the cells; in this case the source of Na24 is located in cell 1 at  $z=45$  cm and we look at the gamma rays region of the charge spectra in cell 9 (GC IN20). On the left hand side plot we have  $p - T - GCIN20=0.6$  (gain=0.98) and on the right hand side plot we have  $p - T - GCIN20=0.8$  (gain=0.96). The plots are presented in the charge range in which the fit was performed.

between the two simulations). It can be seen that the better agreement between the data and the Monte Carlo simulation in the region of the gamma peaks is obtained for  $p\_T\_GCIN20=0.6$ , since the computed gain for this configuration (gain=0.98) is closer to 1 than the computed gain for the configuration in which  $p\_T\_GCIN20=0.8$  (gain=0.96). However, looking at figure 3.13, which illustrates the low charge region of the spectrum corresponding to the light leaks for cell 9 (GC IN20), we observe that the better agreement between data and simulation is obtained for  $p\_T\_GCIN20=0.8$ . Moreover, it is visible that increasing  $p\_T\_GCIN20$  from 0.6 to 0.8 has a bigger impact on the low- $z$  charge spectrum than on the  $z=80$  cm charge spectrum, which is virtually unchanged. This is a good example to illustrate the strategy employed during the fine tuning since in this case we would prefer to have a better agreement in the light leaks region, i.e. by setting  $p\_T\_GCIN20=0.8$  and to correct later the gain, by tuning the light yield or the attenuation length of the liquid, such that it becomes closer to 1.

In addition to the form of the charge spectra in the light leaks region, the evolution of the light leaks coefficients, defined as  $L_{ij} = Q_j/Q_i$ <sup>5</sup> and computed using the cosmic muons energy depositions inside the Target (see section 3.3.1), are a helpful information when fine tuning the  $p$  parameters. The biggest evolution in the  $L_{ij}$  parameters during the data taking was observed for the walls between cells 2 and 3 and between cells 3 and 4, as it can be seen in figure 3.14. This is likely due to the fact that the liquid continued to gradually fill the air gap in the walls, which led to the degradation of the reflectivity properties of the separating walls.

<sup>5</sup>The light leaks coefficients measure the fraction of the light produced in cell  $i$  that is detected in cell  $j$ .



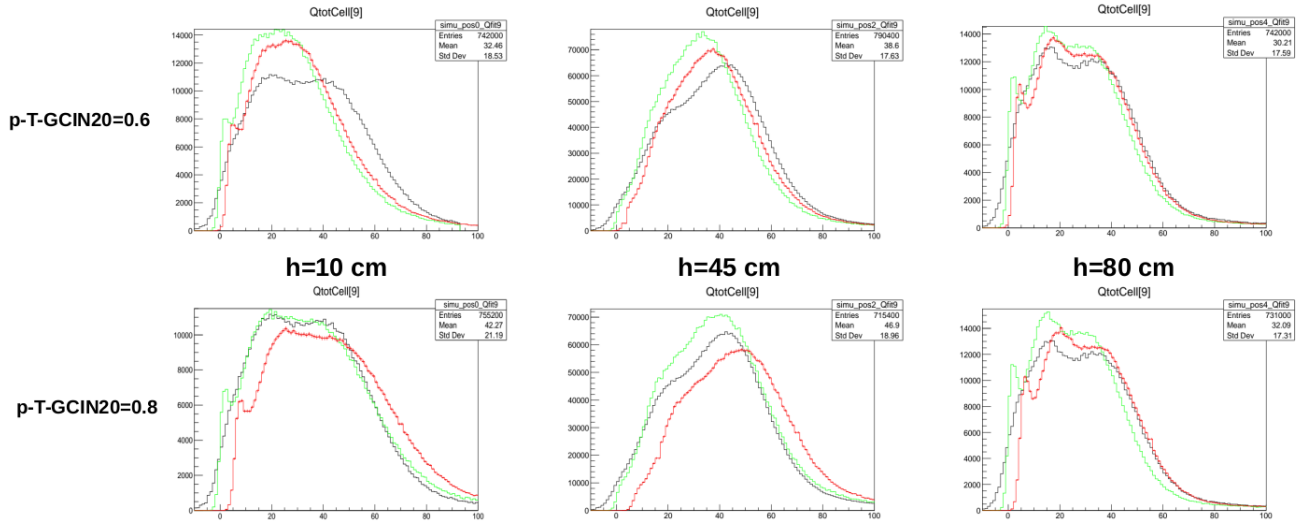


Figure 3.13 – Light leaks region for cell 9 (GC IN20) for the two studied values of  $p - T - GCIN20$ . It can be seen that the high- $z$  positions are less sensitive to a  $p$  parameter change than the low- $z$  positions.

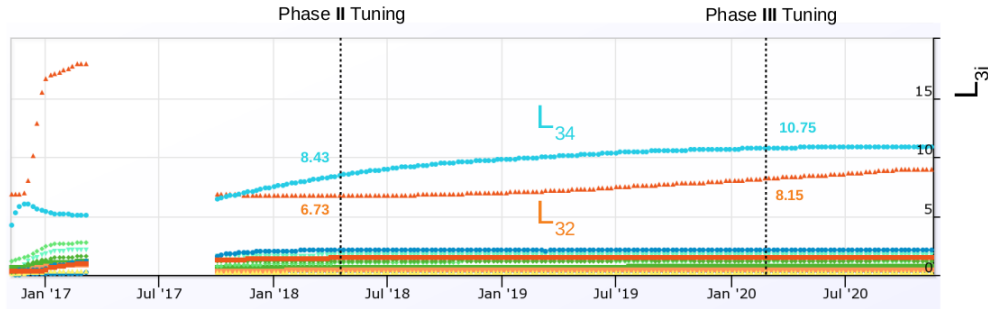


Figure 3.14 – Evolution of the light leaks  $L_{3j}$  from cell 3 to the other cells. On the figure are marked with a dotted line the calibration campaign dates used as a reference for the fine tuning of phases II and III.

### Absorption in the separative walls

The absorption parameter  $a$  translates the probability for the light to be absorbed when passing through the separative walls between the cells. It was introduced to take into account the fact that the light could be absorbed by the nylon net that is placed around the ESR film in order to assure optimal light reflectivity.

An increase of the  $a$  parameter leads to a contraction of the charge spectrum, which, for a given gamma peak, means a decrease in both the mean value and the standard deviation of the peak. Figure 3.15 illustrates an example of a charge spectrum variation for two different values of the  $a$  parameter (for the purpose of the comparison and in order to disentangle the effect of the increase in  $a$ , all the other parameters of the simulation remain constant between the two simulations). By fitting the first gamma peak locally with a Gaussian for the two values of  $a$  we observe a variation of  $\sim 4\%$  in the mean value

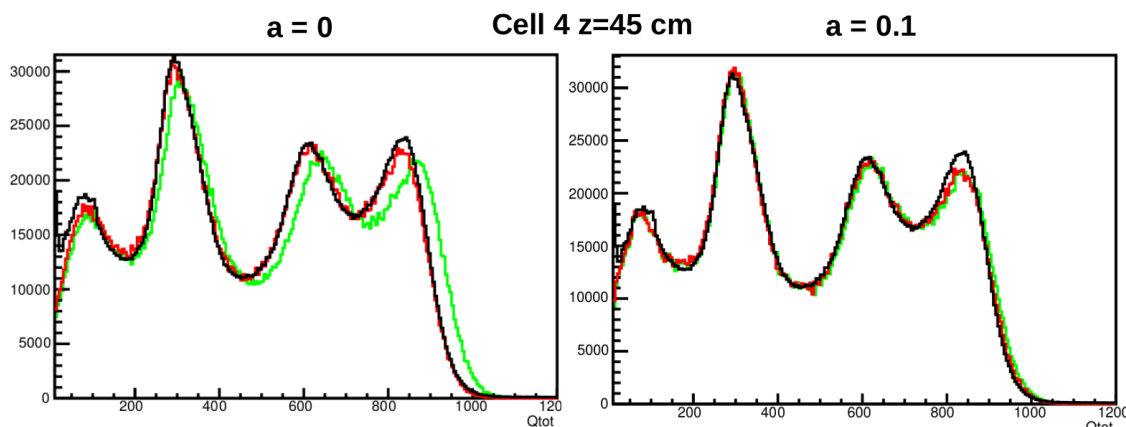


Figure 3.15 – Charge spectrum for the source placed in cell 4 at  $z=45$  cm for two different values of the  $a$  parameter characterizing the absorption inside the separating walls:  $a=0$  and  $a=0.1$ .

and a variation of  $\sim 10\%$  in the standard deviation.

As it was the case for the  $p$  parameters, the absorption parameter  $a$  is expected to have a different impact depending on the source  $z$  position inside the calibration tubes. This is easily understood if we consider the fact that the scintillation light coming from the bottom of the detector undergoes a bigger mean number of interactions with the separating walls, thus having a bigger probability of being absorbed inside them. This is illustrated in figure 3.16 where we plotted the relative gain variation between the two configurations with different values for the  $a$  parameter presented above, for the 5 Target cells containing calibration tubes. A descending trend with  $z$  in the relative gain variation can be observed in most of the cells, confirming the expected behavior.

## Light yield

The light yield of the Target LY(TG) and the Gamma Catcher LY(GC) liquid scintillator can be fine tuned separately. A change in the light yield of the liquid scintillator results in a global shift of the gain value that quantifies the agreement between the data and the simulation and has a negligible impact on the top-bottom asymmetries. Moreover, since the result of an increase of the light yield is equivalent with a dilatation of the charge spectrum, its relative impact is bigger in the gamma-rays region than in the light leaks region. This allows us, as explained in section 3.2.2, to correct the remaining gain difference from 1 after having fine tuned the  $p$  parameters.

## Attenuation length

The attenuation length  $L_{att}$  of the liquid evolved during the different phases of data taking due to the degradation of the liquid properties. This can be seen from the time evolution of

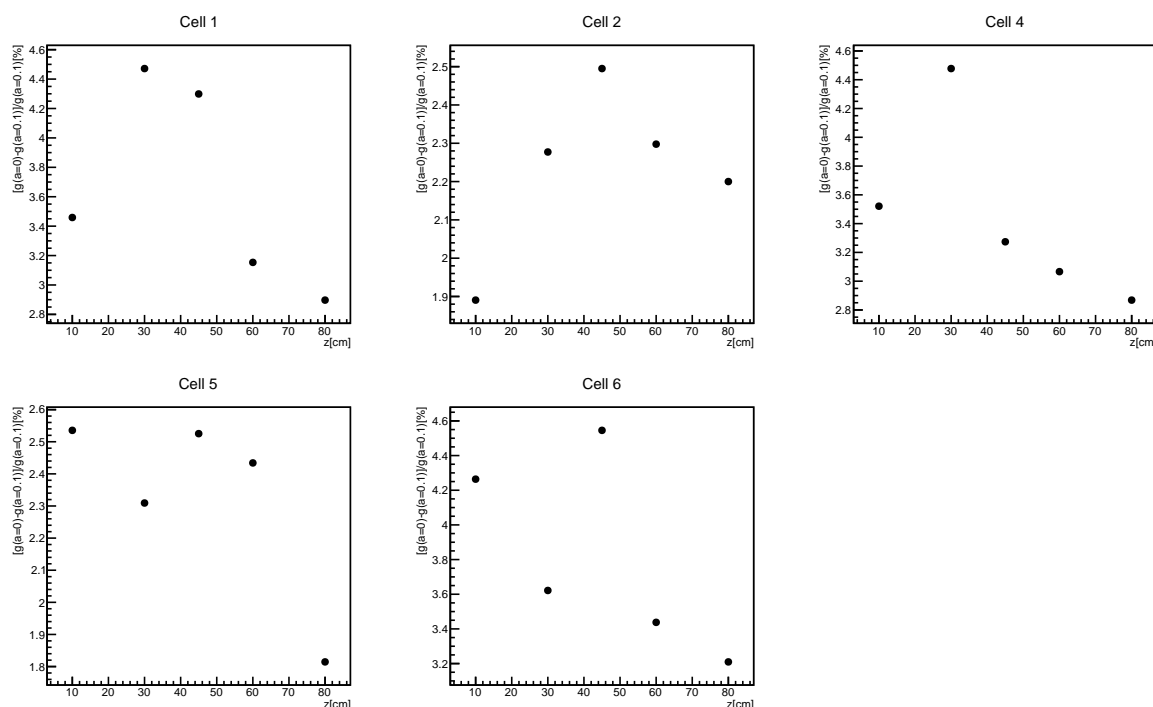


Figure 3.16 – Relative gain variation between the two configurations with different values for the  $a$  parameter characterizing the absorption inside the separating wall:  $a=0$  and  $a=0.1$ . It can be seen that the  $z=80$  cm position is affected less than the other source  $z$  positions.

the calibration coefficients' values presented in figure 3.26. Since the attenuation length plays a different role on the absorption of the scintillation light following its traveled distance, it has a direct impact on the top-bottom asymmetries. Thus, a compromise between the fine tuning of  $L_{att}$  and of the absorption inside the separating walls  $a$  has to be found.

### Calibration tubes' color

The color of the calibration tubes also plays a role in the top-bottom asymmetries. In fact, cell 3 has a white Teflon filling tube while the other cells have grey calibration tubes, which translates into a decreased reflectivity and an increased absorption probability. This aspect has also been taken into account during the fine tuning by artificially reducing the reflectivity of the grey calibration tubes.

### Inband reflectivity

In section 3.1.4 we have presented the optical model of the separating walls that was used for the simulation during the phase II and III fine tuning campaigns. We have seen that, in the case in which the air gap inside the separating walls is filled with liquid, there are three

incident angle regions with different reflectivity properties. The reflection probability in the case in which  $\theta_p < \theta < \theta_s$ ,  $r_{inband}$ , is not very well constrained experimentally and we have to fine tune its value. It has an impact both on the gain and on the top-bottom asymmetries. We have found that a value of  $r_{inband} = 0.4$  works well for both the phase II and the phase III fine tuning. One could note that this value is not very far from the value of  $r_{inband} = 0.5$  that one would have intuitively expected.

### Position of the calibration source

Finally, the z-position of the calibration source inside the internal calibration tubes was also fine tuned in the simulation. In fact, the markers on the calibration cables showing the z-position did not coincide exactly with the values measured initially, since the cables slightly bent over time. This led to a normalization mismatch between the experimental and the simulated peaks that was corrected by fine tuning the z-position of the calibration source in the simulation.

### 3.2.4 Results of the fine tuning process

In this section will be presented the results of the fine tuning for phases II and III of the data taking in terms of gain value and light leaks. The simulation tuning for phase II was anchored on the calibration campaign of 26<sup>th</sup> April 2018, while the simulation tuning for phase III was anchored on the calibration campaign of 28<sup>th</sup> February 2020.

Figure 3.17 shows the agreement between data and simulation at the raw charge level for phases II and III of the data taking, for the cell where the source is placed. It can be seen that for both phases, all the gain values, with the exception of a few points, are contained in a  $\pm 1\%$  band, which illustrates the overall good agreement between data and simulation after the fine tuning campaigns. The points that were outside the  $\pm 1\%$  band for the phase II fine tuning, namely those corresponding to the source placed at  $z=10$  cm in cells 4 and 5, are no longer outliers in phase III. Moreover, if the gain for cell 5 was not aligned on a value of 1 for phase II, this effect is also corrected in phase III. The only observed outlier for phase III is the point corresponding to the source placed at  $z=80$  cm in cell 1. This may be due to an overestimation of the absorption effects, which are responsible for correcting the top-bottom asymmetries.

Before performing the fine tuning of phase II, we have seen in figure 3.5 that top-bottom asymmetries of the order of 4% were present at the cell level. The same behavior was observed before the phase III fine tuning. After the fine tuning, however, the top-bottom light collection asymmetries are well reproduced by the simulation. In fact, at the cell level, all the gain values are contained in a  $\pm 0.5\%$  band, which demonstrates the good capacity of the simulation to replicate complex volume effects present in the data.

Since cell 3 does not have an interior calibration tube, we need to compare the data and the simulation charge spectra registered in cell 3 when the source is placed either in

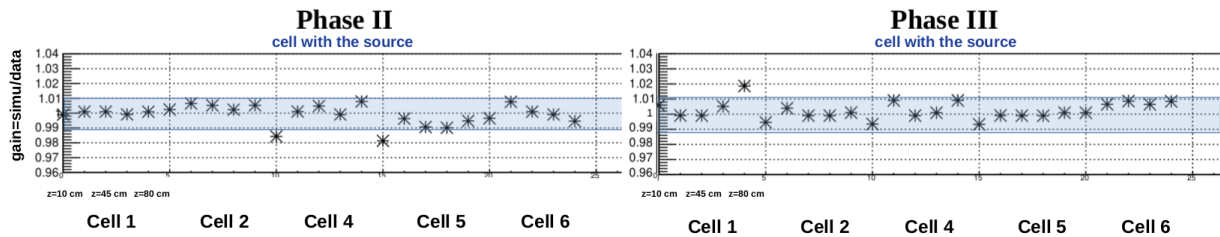


Figure 3.17 – Agreement between data and simulation, for the cell where the source is placed, quantified by the gain value that must be applied to the simulation in order to best reproduce the data, for phases II and III of the data taking, obtained with a  $^{24}\text{Na}$  source. For illustration purposes, a  $\pm 1\%$  band is highlighted in blue around a gain value of 1. Refer to figure 3.5 for more details about the way in which to read this plot.

cell 2 or in cell 4. This comparison can be seen in figure 3.18, when looking to the left neighbour of cell 4 and the right neighbour of cell 2. It can be seen that in this case the gain value lies in the region  $[0.97, 0.98]$ , showing that the simulation does not reproduce the data as well as for the other cells which are equipped with internal calibration tubes.

In figure 3.18 it can also be seen that the simulation reproduces very well the data for the two Short Gamma Catchers, the Gamma Catcher Front (left neighbour of cell 1) and the Gamma Catcher Back (right neighbour of cell 6), with a gain value centered on 1 for both phase II and phase III fine tuning campaigns. Concerning the Long Gamma Catchers, for the phase II fine tuning the gain value is not centered on 1. For the Gamma Catcher D19 it is centered on a value of 1.03, meaning that the simulation is "shifted" to the right of the data, while for the Gamma Catcher IN20, it is centered on a value of 0.97, meaning that the simulation is "shifted" to the left of the data. However, for the phase III fine tuning, this issue was resolved and both the Long Gamma Catchers are centered on a value close to 1.

The agreement between data and Monte Carlo at the raw charge level after the phase III fine tuning campaign is illustrated in figures 3.20 and 3.19. It can be seen that for cell 2 (figure 3.20), which represents an example of a very good agreement between data and simulation, the positions and integrals of the three peaks are very well reproduced. However, looking at cell 4 (figure 3.19), it can be seen that the positions of the three peaks are well reproduced but there are some discrepancies concerning their integrals.

A visual illustration of the agreement between data and simulation in the light leaks region after the phase III fine tuning campaign is presented in figures 3.21 (cell 2,  $z=45\text{cm}$ ) and 3.22 (cell 4,  $z=45\text{cm}$ ), where we can see the agreement in the full range of the spectrum for the source cell and the agreement in the light leaks region for its four neighbouring cells. It can be seen that the light leaks form and approximate position are reproduced quite well by the simulation. This is due to the fine tuning of the  $p$  parameters characterizing the height of the liquid that entered the separating walls.

### 3.2.5 Cross checks on $^{54}\text{Mn}$

The fine tuning of the simulation parameters was mainly done by comparing the data with the simulation at the raw charge level for the  $^{24}\text{Na}$  source. This section aims at testing the agreement between data and simulation for the  $^{54}\text{Mn}$  source which is used to anchor the energy calibration as it will be explained in the next section 3.3.1.

Figure 3.23 shows a summary of the gain values obtained by comparing the phase II fine tuned simulation with the data from 26<sup>th</sup> April 2018 for the  $^{54}\text{Mn}$  source. It can be observed that this plot shows the same characteristics as the ones shown in figures 3.17 and 3.18, where we compared the agreement for the  $^{24}\text{Na}$  source.

Figure 3.24 shows a comparison between the light leaks coefficients  $L_{ij}$  (see 3.3.1 for their definition) obtained from the data and the ones obtained from the simulation for the  $^{54}\text{Mn}$  source. It can be seen that the  $L_{ij}$  evolution with the height of the source within one cell is well reproduced by the simulation. However, there are some global discrepancies in the value of the light leaks coefficients between the Target cells and between the Target cells and the two Long Gamma Catchers. This may be due to the fact that we used the calibration data taken with the  $^{24}\text{Na}$  source to fine tune the  $p$  parameters. In this way, we aimed at reproducing the form and the position of the light leaks but we did not concentrate on reproducing exactly their integral.

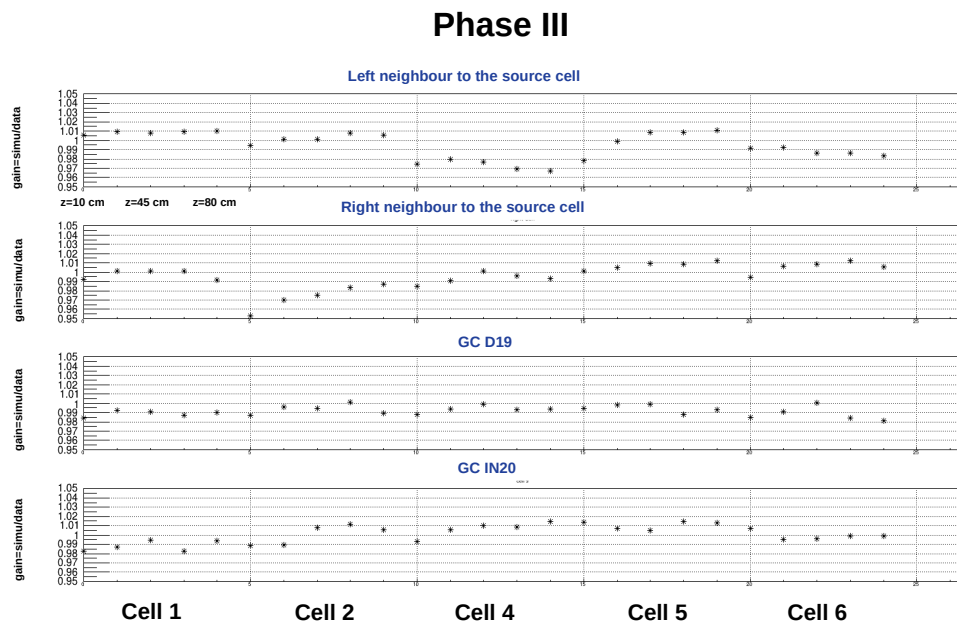
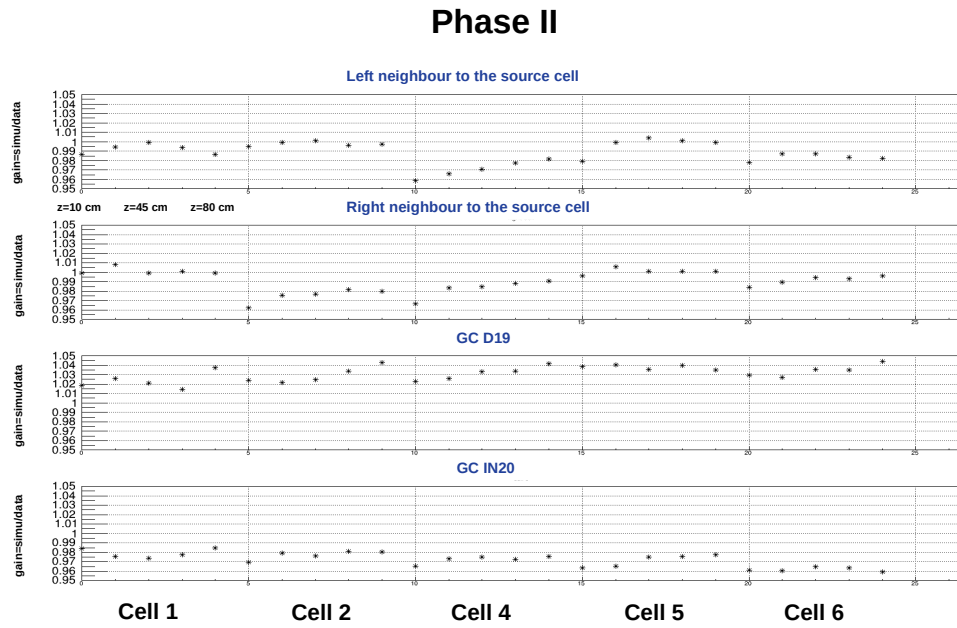


Figure 3.18 – Agreement between data and simulation, for the neighbouring cells to the cell where the source is placed, quantified by the gain value that must be applied to the simulation in order to best reproduce the data, for phases II and III of the data taking. Refer to figure 3.5 for more details about the way in which to read this plot.

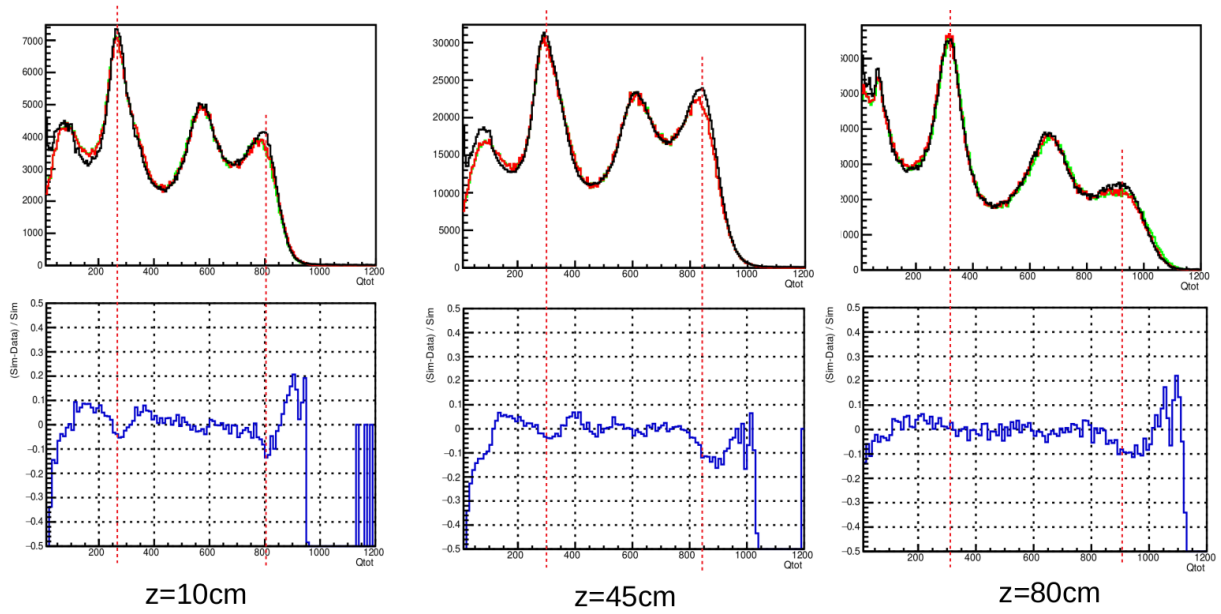


Figure 3.19 – Comparison between data and simulation charge spectra for the  $^{24}\text{Na}$  source placed in cell 4 after phase III fine tuning. The lower plots show the relative difference between the data and simulation spectra.

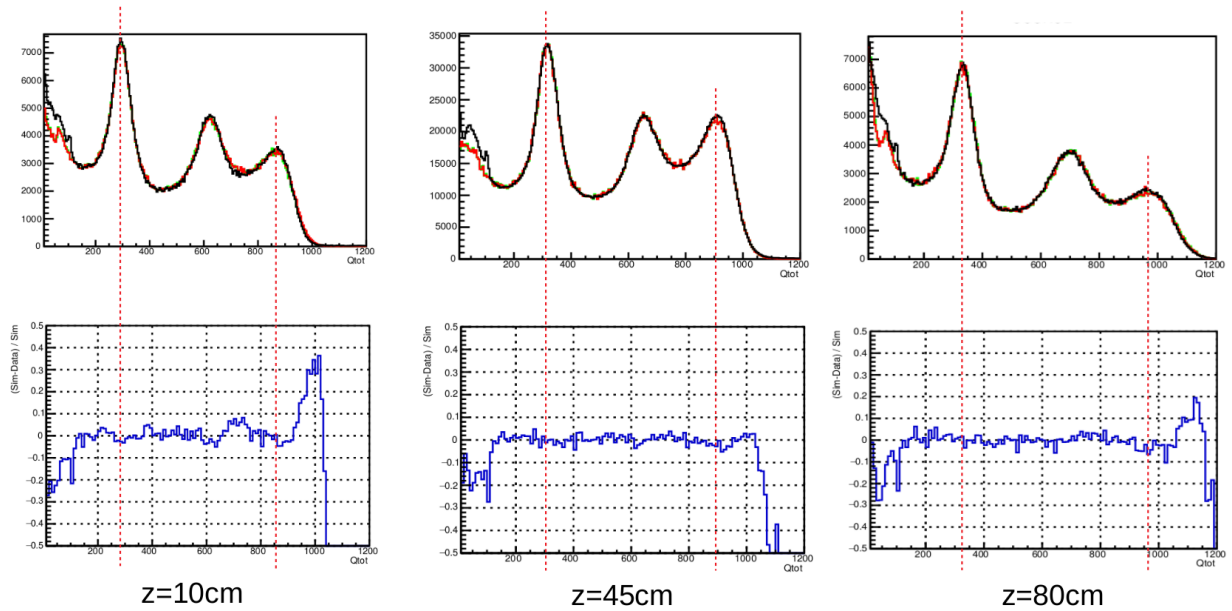


Figure 3.20 – Comparison between data and simulation charge spectra for the  $^{24}\text{Na}$  source placed in cell 2 after phase III fine tuning. The lower plots show the relative difference between the data and simulation spectra.



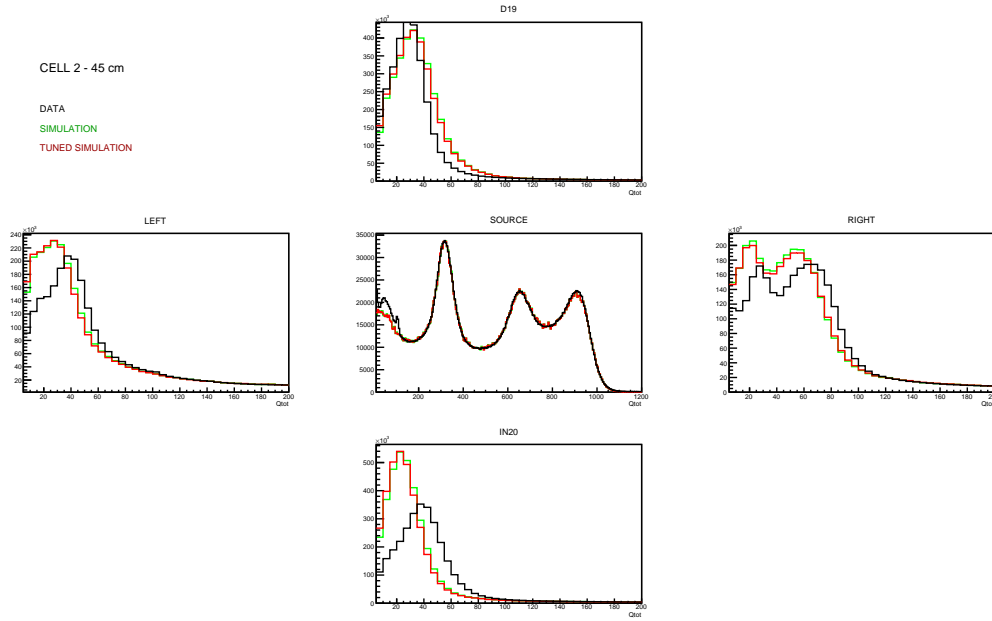


Figure 3.21 – Full data and charge spectra for the source cell and light leaks spectra for the neighbouring cells when the source is placed in cell 2 at  $z=45$  cm after phase III fine tuning.

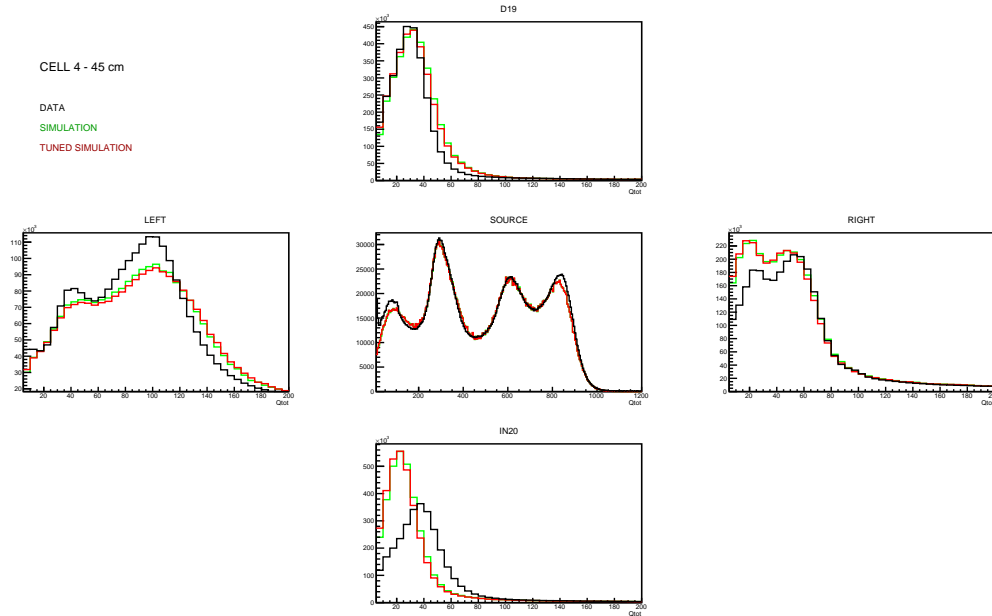


Figure 3.22 – Full data and charge spectra for the source cell and light leaks spectra for the neighbouring cells when the source is placed in cell 4 at  $z=45$  cm .after phase III fine tuning

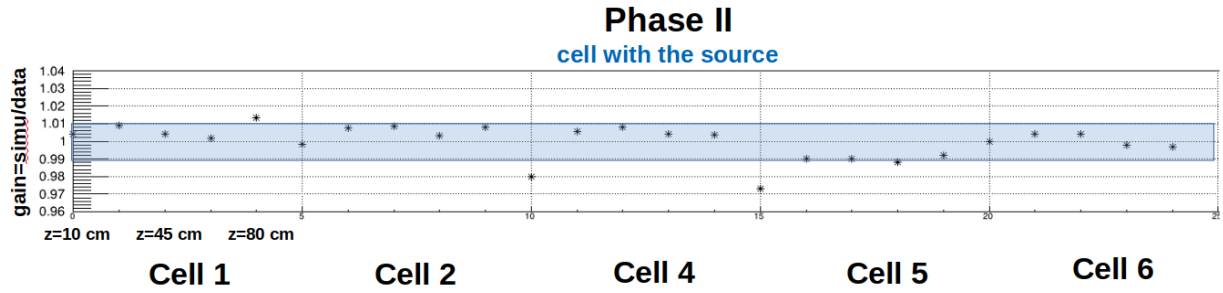


Figure 3.23 – Agreement between data and simulation, for the cell where the source is placed, quantified by the gain value that must be applied to the simulation in order to best reproduce the data, for phases II of the data taking, obtained with a  $^{54}\text{Mn}$  source. For illustration purposes, a  $\pm 1\%$  band is highlighted in blue around a gain value of 1. Refer to figure 3.5 for more details about the way in which to read this plot.

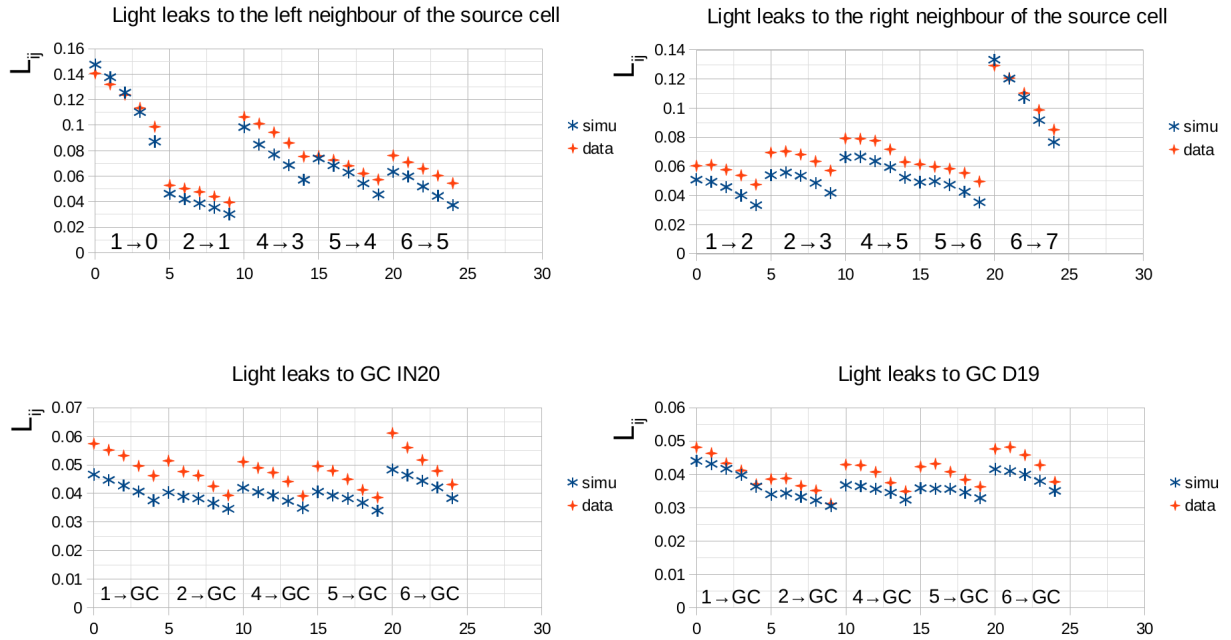


Figure 3.24 – Comparison of the light leaks factors  $L_{ij}$  between data and simulation for a  $^{54}\text{Mn}$  source after phase II fine tuning.

### 3.3 Energy scale

A good comprehension of the energy scale is crucial for the STEREO experiment. Firstly, the study of the IBD detected spectrum shape, which has steep variations with the energy, strongly depends on the good control of the energy scale. Secondly, even though the search for an oscillation signal in the data is based on a relative comparison between identical cells, which allows us to neglect an overall bias in the energy scale at the detector level, we still have to precisely estimate the remaining uncorrelated effects between the cells.

This section will first present the method developed by the collaboration [92] to reconstruct the energy of an event, as well as the method used to control the nonlinearities of the energy scale. Then, the quality of the energy reconstruction, which largely depends on the demonstrated accuracy of the fine tuning previously presented (see section 3.2.4), will be illustrated, as well as the remaining systematic uncertainties for the whole range of the energy scale, tested with radioactive sources, n-capture gamma rays and with the continuous  $^{12}\text{B}$  spectrum.

#### 3.3.1 Energy reconstruction

The light collection efficiency was highly impacted by the loss of the optical contact for the PMs of two cells and the liquid scintillator's leaking inside the separating walls, which led to evolving light leaks between cells during phase I of the data taking. This issues made it impossible for us to directly use the charges collected by the PMs of the different cells in order to reconstruct the energies deposited in those cells, since it was difficult to distinguish between the share of light between the cells and the respective real share of energy. One way to overcome the previously exposed difficulties would be to have an evolving simulation that is adjusted regularly on the data. However, this is impossible, since the fine tuning of the simulation is very time consuming, as it was seen in the previous section, and cannot be done with infinite precision. The chosen solution to this problem was to develop a method of reconstructing the energy that allows for a first order correction of the evolution of the light collection efficiency and of the evolving light leaks between the cells by regularly monitoring the response of every cell with a  $^{54}\text{Mn}$  source deployed in the internal calibration tubes. Finally, this method gives us the possibility to compare the data at every point in time with a unique reference simulation<sup>6</sup>.

#### Principle of the method

Given an event that deposits energy in the detector, the charge  $Q_j$  collected in cell  $j$  is obtained as the sum of two contributions:

1. The charge resulting from the energy deposited in cell  $j$ .

---

<sup>6</sup>A unique reference simulation is used for each of the three phases of data taking.

2. The charge resulting from light leaks coming from energy deposits that take place in the other cells  $i \neq j$ .

Thus, the charge  $Q_j$  can be written as

$$Q_j = E_j C_j + \sum_{i \neq j} E_i C_i L_{ij} = \sum_i E_i C_i L_{ij} \quad (3.3.1)$$

with

$$\begin{aligned} C_i &\doteq LY_i \alpha_i \\ L_{ij} &\doteq \frac{Q_j}{Q_i} \end{aligned} \quad (3.3.2)$$

where  $E_i$  is the energy deposited in cell  $i$ ,  $C_i$  is the calibration coefficient for cell  $i$ , defined as the product between the number of photons produced per MeV ( $LY_i$ ), called the light yield, and the light collection efficiency for the PMs of cell  $i$  ( $\alpha_i$ ), and  $L_{ij}$  are the light leaks coefficients which quantify the proportion of light produced in one cell  $i$  that leaks in the other cells  $i \neq j$ . One should note that the  $C_i$  and  $L_{ij}$  coefficients are treated as constant even though in practice they depend on the position of the interaction vertex, i.e.  $C_i = C_i(x, y, z)$  and  $L_{ij} = L_{ij}(x, y, z)$ . The way in which the mean values for  $C_i$  and  $L_{ij}$ , which are used in the energy reconstruction method, are obtained will be briefly presented later in this section. If by definition we set  $L_{ii} = 1$ , we can write equation 3.3.1 in a matrix form

$$\vec{Q} = M \vec{E}_{rec} \quad (3.3.3)$$

where  $(M)_{ij} = C_i L_{ij}$ . By inverting the matrix  $M$  we can then obtain the reconstructed energies in every cell starting from the respective collected charges:

$$\vec{E}_{rec} = M^{-1} \vec{Q} \quad (3.3.4)$$

### Calibration coefficients estimation

In order to obtain the calibration coefficients, a  $^{54}\text{Mn}$  source is deployed in the internal calibration tubes at five different heights along the  $z$  direction and a value of  $C_i$  representative for a given cell is computed as the mean over the values obtained for the five tested heights. This high activity source, which emits a monoenergetic gamma ray with an energy of 835 keV, allows to calibrate the detector while minimizing the background contribution. The gamma rays emitted by the  $^{54}\text{Mn}$  source interact mainly by Compton scattering and have a mean interaction length of  $\sim 10$  cm, similar in size to the width of

one cell in the x direction ( $\sim 37$  cm). However, the cell volume is not entirely covered by gamma ray vertices in the y direction ( $\sim 90$  cm) when using the  $^{54}\text{Mn}$  source, as it can be seen in figure 3.25, which shows the gamma rays' interaction vertices. The energy response of the detector in this region that remains unexplored by the gammas coming from the  $^{54}\text{Mn}$  source will be tested by using n-capture gammas and will be presented in section 3.3.3.

The calibration coefficients, which are computed in the same way for the simulation and the data, allow for the conversion between the collected charge and the reconstructed energy in MeV. They are computed in the following way

$$C_i = \frac{\langle Q_i \rangle}{\langle E_i^{\text{dep}} \rangle} \quad (3.3.5)$$

where  $\langle Q_i \rangle$  is the mean value of the collected charge distribution for events that deposited all their energy in cell i (this condition is necessary in order to avoid taking into account the light that is produced in a neighbouring cell which subsequently leaks towards cell i) and  $\langle E_i^{\text{dep}} \rangle$  is the mean value of the respective deposited energy distribution and is only available in the simulation. Since  $\langle E_i^{\text{dep}} \rangle$  does not depend on the optical properties of the detector, its value obtained from the simulation is used to obtain the  $C_i$  for both data and MC.

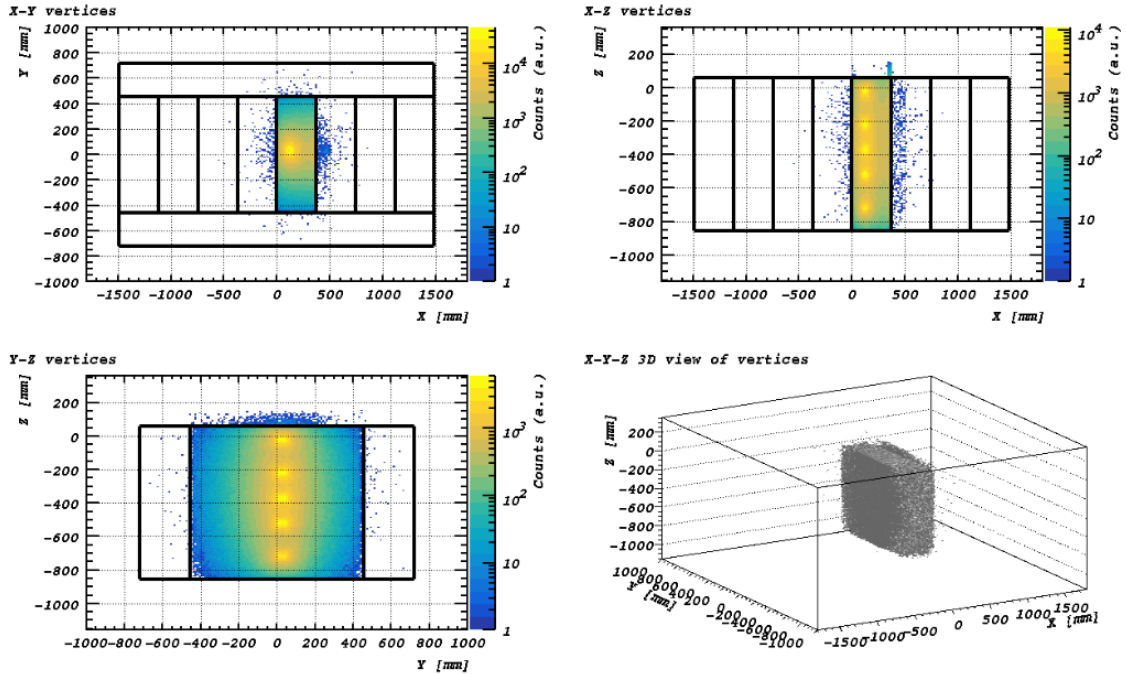


Figure 3.25 – Distribution of first interaction vertices for the gamma rays emitted by the  $^{54}\text{Mn}$  source placed in cell 4. Since the source can be deployed at different heights inside the calibration tube, the energy deposits along the z-axis are homogeneous. However, the corners of the cell in the y-axis direction are not fully populated. Source:[92].

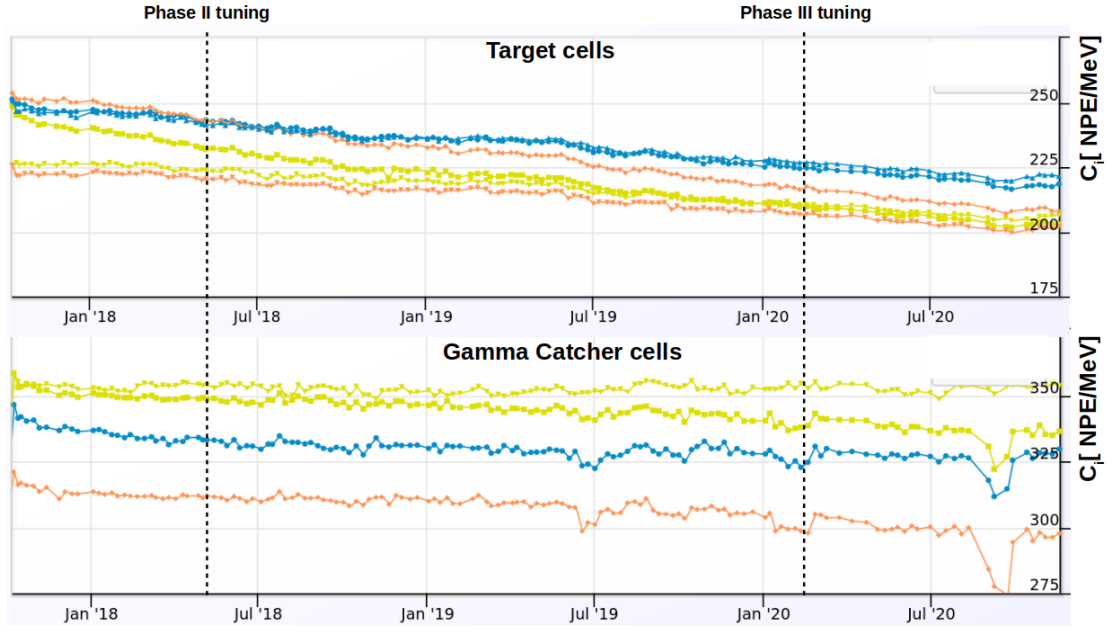


Figure 3.26 – Illustration of the evolution of the calibration coefficients during phases II and III of data taking for the Target cells (upper plot) and the Gamma Catcher cells (lower plot). The reference dates used for the fine tuning of the simulation are marked on the figure with dotted lines.

In order to select events that deposited all their energy in cell  $i$ , a cut on the light leaks coefficients  $L_{ij}$  has to be used

$$\frac{Q_{j \neq i}}{Q_i} < L_{ij} + k\Delta L_{ij} \quad (3.3.6)$$

where  $\Delta L_{ij}$  represents the dispersion of the light leaks coefficients  $L_{ij}$  and the value of  $k$  is chosen to limit at maximum the light leaks towards the neighbouring cells and such that a small change  $\delta k$  has a negligible impact on  $\langle Q_i \rangle$  and  $\langle E_i^{dep} \rangle$ .

The calibration coefficients evolution in time for the target cells and for the Gamma Catcher cells during phases II and III of data taking are presented in figure 3.26. It can be seen that the  $C_i$  for the Target cells decrease in time by  $-10\%/year$  (which justifies the modification of the light yield and attenuation length of the liquid scintillator in the simulation during the fine tuning), while the  $C_i$  for the Gamma Catchers stay roughly constant.

### Light leaks coefficients estimation

The light leaks coefficient  $L_{ij}$  is defined as the ratio between the charge collected in cell  $j$  and the charge collected in cell  $i$  for the case in which the main energy deposit takes place in cell  $i$

$$L_{ij} = \frac{Q_j}{Q_i} \quad (3.3.7)$$

In practice, the  $L_{ij}$  coefficients are computed from the cosmic muons registered during the data taking, by selecting those events that deposited all their energy in a given cell  $i$ . The main advantage of using this type of events is that they deposit their energy uniformly inside the detector's cells, close to the way in which the antineutrinos are expected to deposit their energy. Another advantage of using cosmic muons is that they allow us to monitor the evolution of the light leaks coefficients continuously in time.

Another technique for determining the  $L_{ij}$  coefficients from the  $^{54}\text{Mn}$  runs was developed. As for the cosmic muons, the idea was to select those events that deposited all their energy in a given cell  $i$ . The main difficulty of this method was the determination of the light leaks coefficients for the cells missing an internal calibration tube, due to the small interaction length for the 835 keV gamma rays inside the liquid scintillator, which made it difficult to select full energy events in these cells. Moreover, since the  $x$  and  $y$  positions of the calibration tubes are fixed, we could only compute a mean  $L_{ij}$  value over the  $z$  dimension (see figure 3.25), as for the calibration coefficients  $C_i$ , which should then be used as representative for the entire cell.

Finally, the  $L_{ij}$  coefficients computed from the cosmic muons are used at first order in the energy reconstruction method. The values of the light leaks coefficients are of the order of 5% for the repaired separating walls (no liquid scintillator inside) and can reach values of 10% during phases II and III for the walls that still have liquid inside (during phase I, the  $L_{ij}$  even reached values of 20-30%). An example of evolution in time for the  $L_{ij}$  coefficients was given in figure 3.14, which presented the leaks between cell 3 and the other cells.

### Refinement of the energy reconstruction method

When using the  $C_i$  (equation 3.3.5) and  $L_{ij}$  (equation 3.3.7) coefficients determined as explained in the previous paragraphs directly in the energy reconstruction method (equation 3.3.4), the obtained reconstructed energies for data and simulation,  $E_{rec}^{data}$  and  $E_{rec}^{simu}$ , are different. This is mainly due to the way in which we apply the cuts allowing us to select the full energy deposit events in the data and simulation. In fact, since the light leaks are only reproduced at first order by the simulation, we obtain slightly different efficiencies for the cuts that make use of the light leaks coefficients.

In order to correct for this effect, an iterative method of correcting the  $C_i$  and  $L_{ij}$  was introduced [92]. The goal of this method is to align both  $E_{rec}^{data}$  and  $E_{rec}^{simu}$  on a reference value  $E_{rec}^{ref}$ , which is determined as the most probable value of the deposited energy in the simulation and depends only on the precise description of the physical processes and on the geometry of the detector.

This iterative energy reconstruction method is very effective and allows us to precisely

align the reconstructed energies for the data and simulation on the common reference  $E_{rec}^{ref}$  with an uncertainty of 0.2% on  $E_{rec}^{ref}$ .

### Data vs MC in reconstructed energy for the $^{54}\text{Mn}$

The agreement between the data and simulation reconstructed energy distributions for the  $^{54}\text{Mn}$  source is very good and is illustrated in figure 3.27, which presents the average energy distribution over the five explored heights of the source for cell 5. The residual difference between the data and simulation distributions is of the order of 0.2% for the Target cells and of 0.4% for the Gamma Catcher cells. This accuracy is due to the precise fine tuning at the level of the raw charges spectra presented in section 3.2.

#### 3.3.2 Nonlinearities of the energy scale

As presented in the previous section, the  $^{54}\text{Mn}$  source was chosen as the anchor point<sup>7</sup> of the energy calibration, meaning that the conversion factors between the collected charge and the reconstructed energy,  $C_i$  and  $L_{ij}$ , representative of the average response in the entire volume of a cell, are computed on a weekly basis using an iterative method that aims at aligning both the data and simulation reconstructed energy on a common reference.

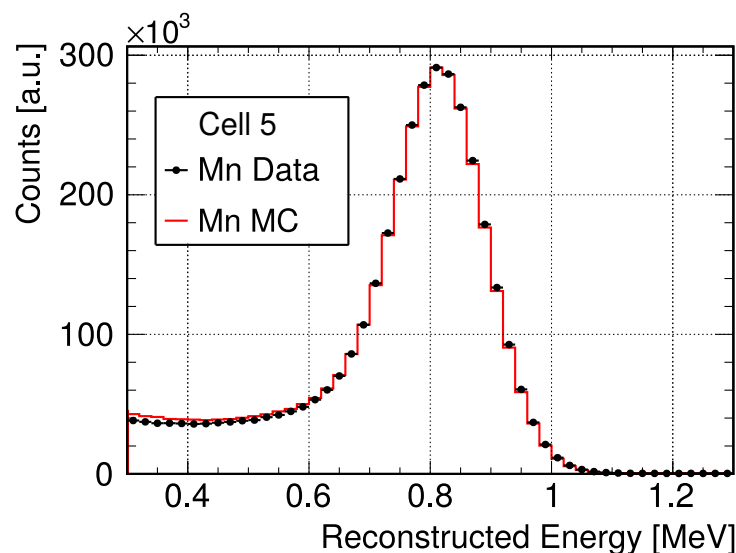


Figure 3.27 – Average data and simulation reconstructed energy distributions for the  $^{54}\text{Mn}$  source deployed at five different heights inside the internal calibration tube of cell 5, after the phase II fine tuning.

<sup>7</sup>The choice of the  $^{54}\text{Mn}$  as the anchor point was justified by the fact that, among the sources with long half-life, it was the only single-gamma source of high energy that can be reliably distinguished from the energy of the gamma rays of  $^{41}\text{Ar}$ , which is present in the reactor building and whose concentrations strongly vary during reactor-on periods.



The energy reconstruction method only corrects the light collection inhomogeneities at first order. Moreover, it does not account for the nonlinearities of the scintillation process, such as the quenching effect. Therefore, the simulation parameters have to be adjusted in order to control the energy response at high energy.

### Quenching effect

The quenching effect translates a nonlinearity of the calibration coefficients for low energy deposits. For the  $^{54}\text{Mn}$  source, the electrons produced by Compton effect are responsible for inducing the scintillation process. As the electrons slow down, they lose energy and their stopping power  $dE/dx$  strongly increases, which leads to very localised energy deposits. In turn, this induces a saturation of the scintillation power of the liquid molecules, which means that part of the energy deposited by the electron is not converted into light. This effect is reproduced in the simulation by using the effective Birks model [97]

$$\frac{dL}{dx} = L_0 \frac{\frac{dE}{dx}}{1 + k_B \frac{dE}{dx}} \quad (3.3.8)$$

where  $\frac{dL}{dx}$  is the light yield per unit length,  $L_0$  is the light yield in the linear regime,  $\frac{dE}{dx}$  is the stopping power of the particle that deposits energy and  $k_B$  is a constant called the Birks coefficient, which depends on the scintillating material.

In order to test the response of the detector at higher energies compared to the  $^{54}\text{Mn}$  835 keV gamma ray and to study the quenching effect, pointlike radioactive gamma sources ( $^{137}\text{Cs}$ ,  $^{54}\text{Mn}$ ,  $^{65}\text{Zn}$ ,  $^{42}\text{K}$ ,  $^{60}\text{Co}$ ,  $^{24}\text{Na}$ ) and the gamma-neutron source  $^{241}\text{Am}/^9\text{Be}$  (see table 3.28) are deployed both in the internal calibration tubes and the external calibration system at all Z-positions (see figure 2.12 and table 2.1). Besides testing the energy response at higher energies, the gammas from the radioactive sources that were used in this study also give us a better insight about the volume effects, since the mean interaction length of a gamma ray increases with its energy, which allows the exploration of a bigger volume of a cell compared to the  $^{54}\text{Mn}$  source alone.

Figure 3.29, which shows the calibration coefficients at  $z=45$  cm averaged over all the Target cells and normalized to the one of the  $^{54}\text{Mn}$  source, for the different gamma ray energies, clearly illustrates the impact of the quenching effect on the energy scale, namely the reduced light yield at low energy. The Birks coefficient is tuned in the simulation in order to reproduce at best the quenching effect observed in the data. With a value of  $k_B = (0.096 \pm 0.007)$ , the agreement between data and simulation reaches sub-% accuracy, as it can be seen in the bottom part of figure 3.29.

It is worth mentioning that the choice of anchoring the calibration on the  $^{54}\text{Mn}$  source (835 keV) leads to a few percent overestimation of the reconstructed energies for the positrons of the IBD candidates in the  $[1.625, 7.125]$  MeV analysed range, with respect to their "true" energies. The reason for this is twofold. Firstly, the energy of the gamma rays from the  $^{54}\text{Mn}$  source lies in a low energy region impacted by quenching effects.

Source	Energy (MeV)	Multiplicity
$^{137}\text{Cs}$	0.6617	1
$^{54}\text{Mn}$	0.8348	1
$^{65}\text{Zn}$	1.116	1
$^{60}\text{Co}$	1.173	2
	1.332	
$^{42}\text{K}$	1.525	1
$^{24}\text{Na}$	1.369	2
	2.754	
AmBe	4.440	1 + neutron
	2.223 (n-H)	1

Figure 3.28 – Radioactive sources used for the calibration. The multiplicity represents the number of emitted gamma rays.

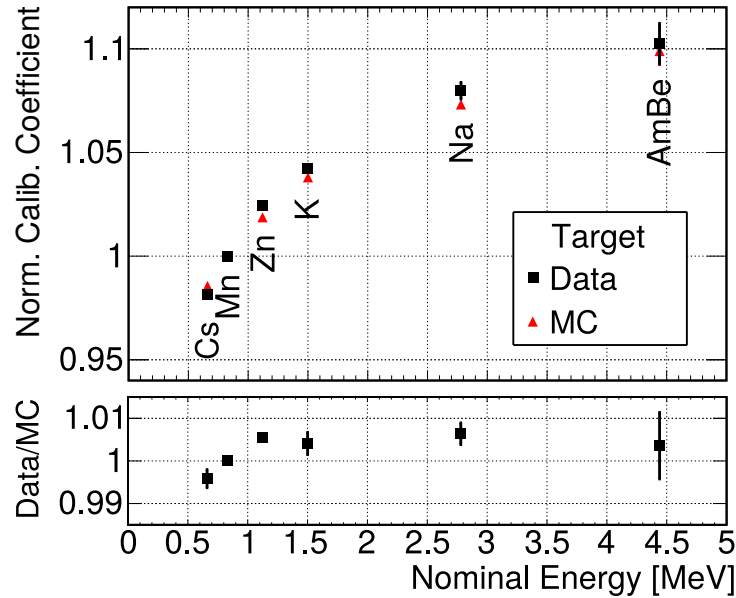


Figure 3.29 – Top: Calibration coefficients for various radioactive sources at mid-height, normalised to the  $^{54}\text{Mn}$  point and averaged over all Target cells, for phase II data. The horizontal axis represents the true deposited energy corresponding to the charge peak value. For  $^{24}\text{Na}$ , only the higher energy gamma ray is used. Bottom: Ratio of data and MC curves, after tuning of the Birks coefficient  $k_B$ . Source:[77].

Secondly, gamma rays mainly interact by Compton effect and transfer only part of their energy to electrons from the liquid, which subsequently deposit their energy by ionisation, while positrons deposit their energy continuously until they lose all their energy and they finally annihilate with an electron and give rise to two gamma rays of 511 keV each. However, we do not correct the data for this effect but rather include all the relevant effects in the simulation. In this way, any model that needs to be compared with the data is forward folded with the simulated detector response.

### 3.3.3 Tests and systematics of the energy scale

After having obtained the relevant parameters necessary for the energy reconstruction by anchoring the calibration on the  $^{54}\text{Mn}$  source and having fitted the effective Birks  $k_B$  coefficient, we can now test the quality of the agreement between the data and the simulation for different energy deposits and different spatial configurations of the gamma ray interaction vertices. Moreover, the systematic uncertainties that are relevant for the oscillation analysis, the rate analysis and the spectrum shape analysis can be determined.

#### $E_{\text{rec}}^{\text{Data}}/E_{\text{rec}}^{\text{MC}}$ and energy resolution

In order to illustrate the agreement between data and simulation in reconstructed energy for a wider range of energies, we have plotted in figure 3.30 the mean ratio  $E_{\text{rec}}^{\text{Data}}/E_{\text{rec}}^{\text{MC}}$  over the five vertical source positions for the different radioactive sources from table 3.28. It can be seen that  $E_{\text{rec}}^{\text{Data}}/E_{\text{rec}}^{\text{MC}}$  is contained in a  $\pm 1\%$  band for all the used sources.

Figure 3.31 shows the agreement between data and MC in reconstructed energy for different dates over the phase III of data taking, using either phase II or phase III simulation fine tuning to obtain  $E_{\text{rec}}^{\text{MC}}$ . It emphasizes the importance of a precise simulation

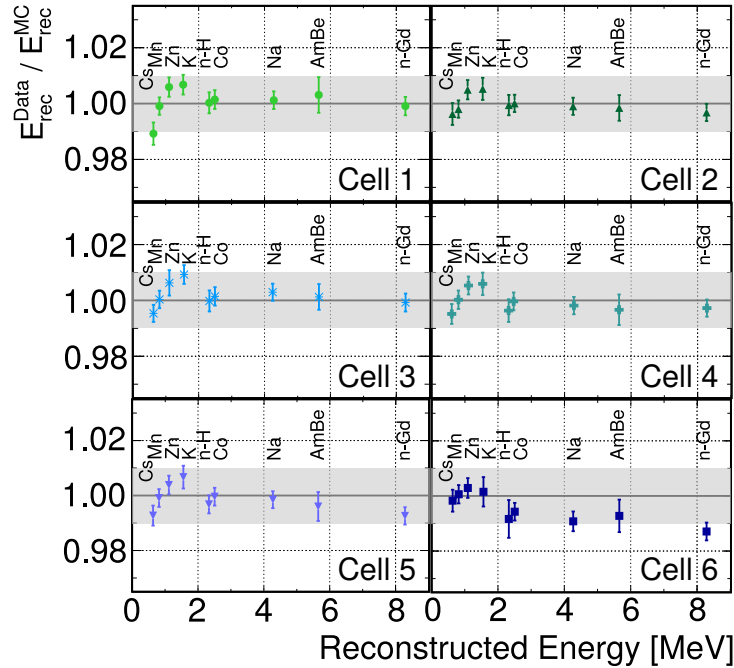


Figure 3.30 – Ratio of reconstructed energy between data and MC as a function of the reconstructed energy of emitted gamma rays for the average of the 5 vertical deployment positions of the sources, for phase II data. If two gamma rays are emitted, we use the sum energy. Shown in grey is a  $\pm 1\%$  uncertainty band. The uncertainties on the points are computed taking into account the data statistics and the fit range and time dependence of the peaks. However, no correlations across sources are taken into account. Source:[77].

fine tuning. It can be seen that when using the phase III simulation fine tuning, the ratio  $E_{rec}^{Data}/E_{rec}^{MC}$  is contained in a  $\pm 1\%$  band for all the three shown dates. However, when using the phase II simulation fine tuning, the ratio  $E_{rec}^{Data}/E_{rec}^{MC}$  is no longer contained in a  $\pm 1\%$  band, with deviations from 1 reaching almost  $\sim 4\%$  for September 2020. This is due to the evolution of the liquid scintillator's optical properties and to the evolving light leaks, proving that the energy reconstruction technique alone cannot correct for these effects and thus emphasizing the need of re-tuning the simulation for every data taking phase.

The relative energy resolution  $\sigma(E_{rec})/E_{rec}$ , with  $\sigma(E_{rec})$  the standard deviation to the right of the energy peak is plotted in figure 3.32. The good agreement between data and simulation is also apparent at the energy resolution level. While the resolution follows a  $1/\sqrt{E}$  law in the low energy region, at higher energy it saturates around a value of 5%. This behaviour is the result of the convolution between the pure statistical resolution and the dependence of the light collection efficiency on the altitude of the energy deposit vertex.

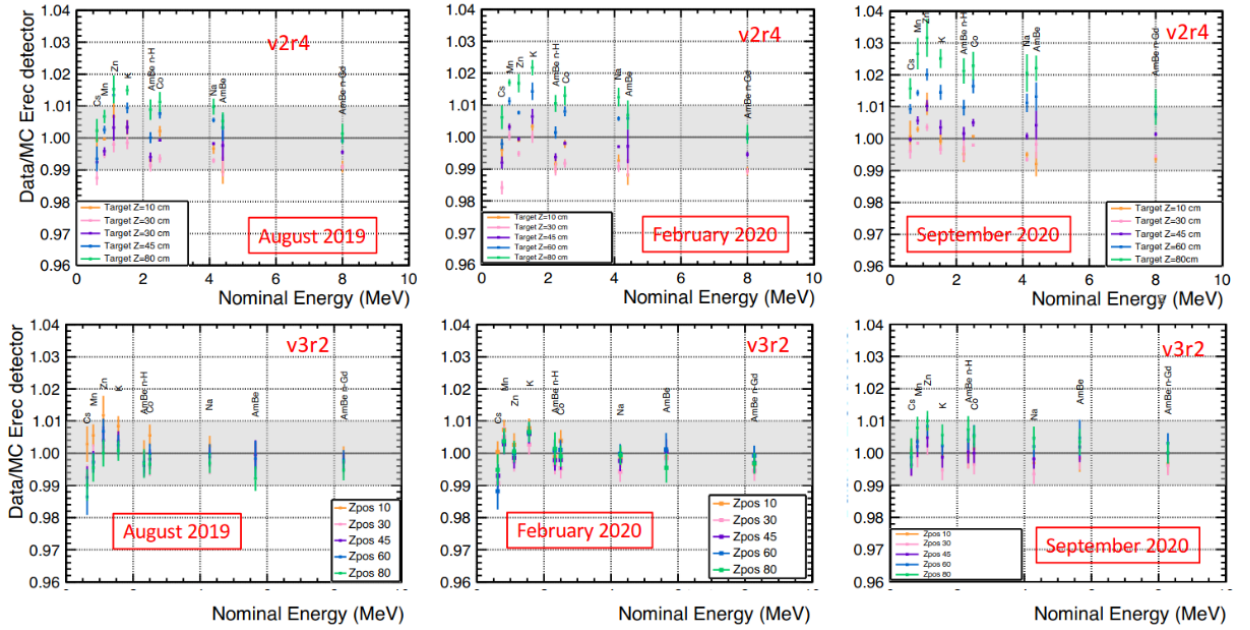


Figure 3.31 – Ratio of reconstructed energy between data and MC as a function of the nominal energy of the emitted gamma rays, averaged over the Target cells, shown for the five vertical source positions at three different dates over the phase III of data taking. For the top plots, the  $E_{rec}^{MC}$  is obtained using the phase II simulation fine tuning (v2r4, anchored on the reference date of 26<sup>th</sup> April 2018), while for the bottom plots, the  $E_{rec}^{MC}$  is obtained using the phase III simulation fine tuning (v3r2, anchored on the reference date of 28<sup>th</sup> February 2020).

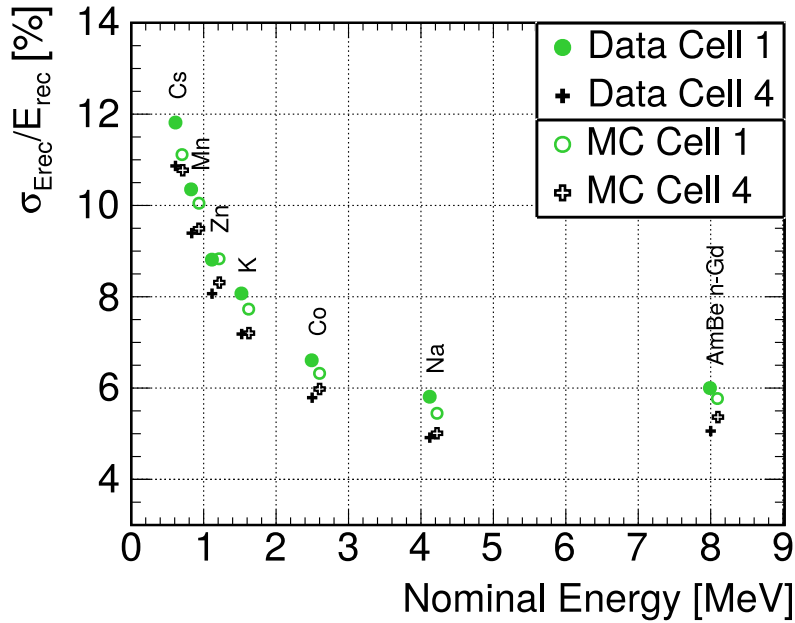


Figure 3.32 – Energy resolution as a function of the nominal energy of emitted gamma rays for the average of the 5 vertical deployment positions of the sources, for phase II data. Data points are plotted with filled markers, while simulation points are plotted with open markers. If two gamma rays are emitted, we use the sum energy. Cell 4 is representative for the four inner Target cells (2,3,4 and 5), while cell 1 is representative for the two outer Target cells (1 and 6). Source:[77].

### Spatial nonuniformity

It has been shown in figure 3.25 that the interaction vertices of gamma rays coming from sources placed inside the internal calibration tubes are concentrated in the central region of each cell and thus allow us to precisely probe the detector response in this region. However, at the cell borders, especially in the y-direction, additional effects could impact the detector response. To investigate these effects, an AmBe source is deployed in the external calibration system (see figure 2.12), which is placed outside the detector vessel, but inside the shielding. The tested points are located at the center of the cell in the x-direction. We then look at the neutrons coming from the AmBe source that are captured on hydrogen. Figure 3.33 shows that the agreement between data and MC in reconstructed energy for the n-H capture peaks is at the 1%-level across all cells, when looking at the average of 3 y-axis deployment positions of the AmBe source at  $z=45$  cm. Thus, we can conclude that there is no need for any additional correction or uncertainty for the reconstructed energy of events close to the cell borders in the y-direction.

### Data vs simulation for the n-H capture peak

In order to further put to test the agreement between data and simulation in reconstructed energy, the MC n-H capture peaks were simulated and compared with the ones obtained

from the data. Figure 3.34 shows such a comparison for cells 5 (representative for cells 2,3,4 and 5) and 6 (representative for cells 1 and 6) using both the phase I (v2r3) and phase II (v2r4) simulation fine tuning. For v2r3, it can be seen that the ascending part of the peak is well reproduced by the simulation but the data have a bigger width  $\sigma$ . However, when comparing the widths of the data and simulation distributions after phase II fine tuning, for the v2r4 MC version, we observe that the width of the data distribution is well reproduced by the simulation. Furthermore, for cell 6, the simulation doesn't reproduce exactly the low energy tail of the n-H capture peak distribution (this is also true for cell 1).

It is worth noting that in order to compare the widths of the two distributions for the v2r4 MC version, the data distribution was rescaled such that its peak is aligned with the one of the simulation. This rescaling was needed because the data and MC peak values are slightly different, with the data peak value being higher with 1-1.5%. This may be due to the fact that the energy deposit distribution for the gammas coming from n-H captures is not homogeneous in the z-direction, with slightly more events at the bottom of the detector, as shown by the simulation (see chapter 3 from [92]). In contrast, the calibration coefficients  $C_i$  used for the energy reconstruction are obtained as an average for the  $^{54}\text{Mn}$  source deployment at five different heights, thus being representative for a homogeneous energy deposit distribution in the z-direction.

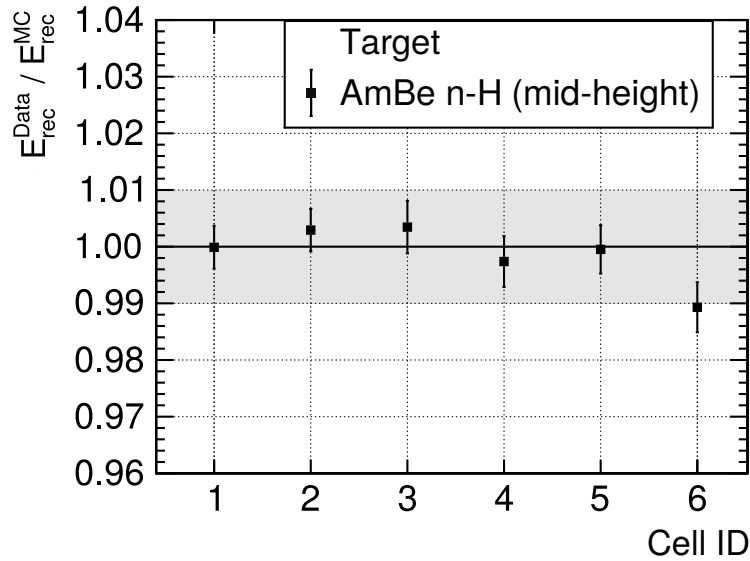
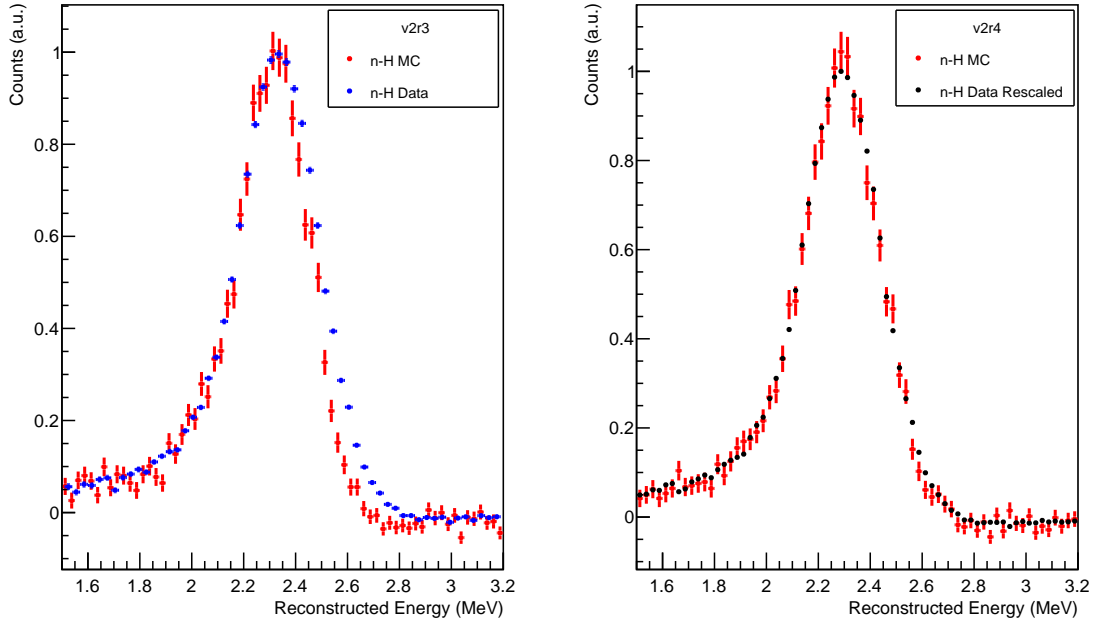
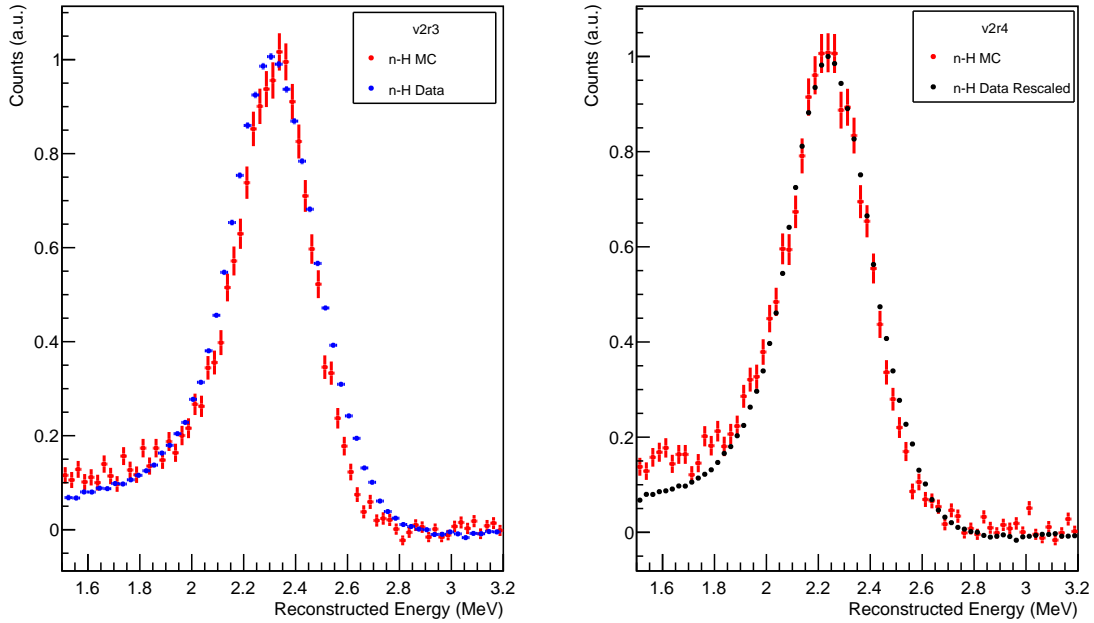


Figure 3.33 – Ratio of reconstructed energy between data and MC of neutron captures by hydrogen for the average of 3 horizontal deployment positions of an AmBe source at  $z=45$  cm (2 external and 1 internal Y-positions). Shown in grey is a  $\pm 1\%$  uncertainty band. Source: [77].



(a)



(b)

Figure 3.34 – Comparison between data and MC n-H capture peaks in reconstructed energy using the phase I simulation fine tuning, i.e. the v2r3 version (left) and using the phase II simulation fine tuning, i.e. the v2r4 version (right) for phase II. Data are shown for cell 5 (a) and cell 6 (b). For the v2r4 MC version (right) the data  $E_{rec}$  distribution is rescaled such that its peak is aligned with the peak of the MC  $E_{rec}$  distribution in order to compare the widths of the two distributions.

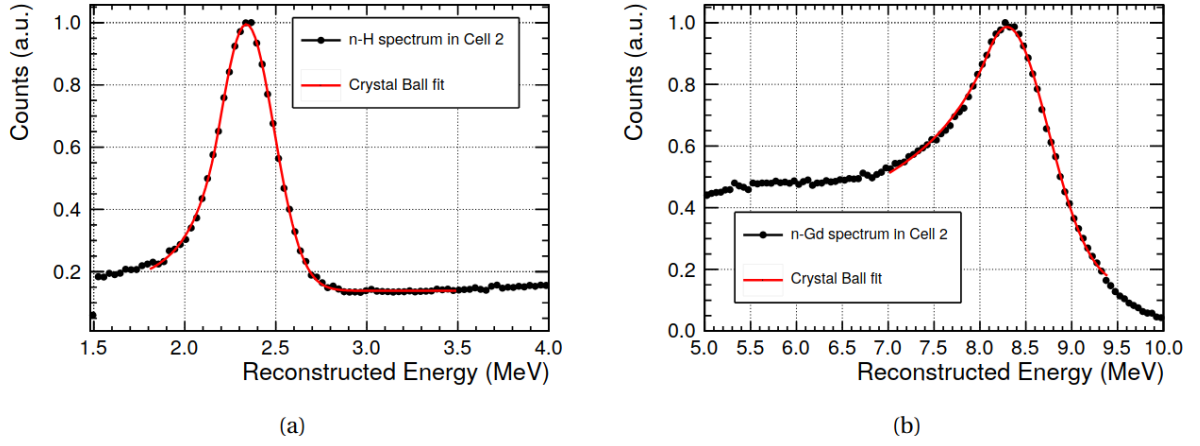


Figure 3.35 – Example of Crystal Ball fit for the n-H (a) and n-Gd (b) neutron capture peaks in cell 2 for phase II data. Source:[92].

### Time stability

In order to evaluate the time stability of the detector response we looked at the n-H and n-Gd capture events, which have the advantage of being spatially distributed similarly to the electron antineutrino searched events. Most of the neutrons that are captured inside the detector are generated by muon spallation reactions inside the lead shielding, as shown by the simulation of cosmic rays in the STEREO detector (see chapter 3 from [92]). The mean and the standard deviation of the n-H and n-Gd reconstructed energy capture peaks are extracted by fitting a Crystal Ball function on the data, as shown in figure 3.35.

The time evolution of the n-H and n-Gd reconstructed energy peak positions and standard deviations are reported in figure 3.36 for phase II of the data taking. It can be seen that the detector response is stable at the 0.3% level for each cell. Moreover, the remaining fluctuations are fully correlated across all cells and, thus, the uncertainty on the time stability is considered an estimate of the cell-to-cell correlated systematic uncertainty.

### Continuous energy spectra

In order to better constrain the energy scale at high energies a complementary source of calibration is used, the  $\beta$ -decay spectrum of the  $^{12}\text{B}$  isotope. Even though the residuals shown in figures 3.32 and 3.33 prove that there is no need to consider any supplementary correlated systematic uncertainty, we still need to study the cell-to-cell fluctuations in order to estimate the uncorrelated systematic uncertainty.

The  $^{12}\text{B}$  is an unstable isotope which undergoes  $\beta$ -decay with a half-life of 20.20 ms and a Q-value of 13.37 MeV, which is sufficient to cover the energy range of interest for STEREO. It is produced in two dominant processes by the interaction of the cosmic rays



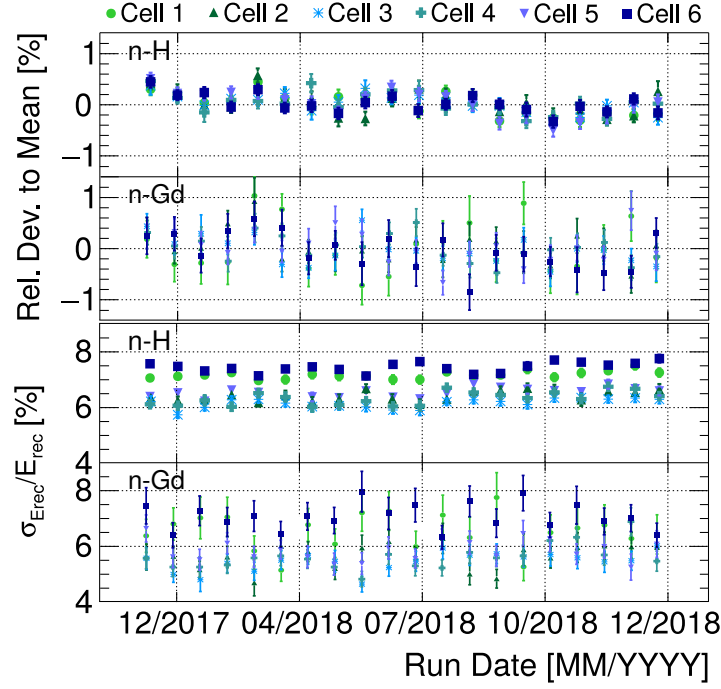


Figure 3.36 – Time evolution of the n-H and n-Gd reconstructed energy peak positions (top) and standard deviations (bottom) extracted using a Crystal Ball fit. The values are given relative to the means of individual cells over time. Source:[77].

with the liquid scintillator. A low energy  $\mu^-$  can stop in the detector and be captured by a  $^{12}\text{C}$  atom. Then, in 1% of the cases [98], the muon cascades down into the 1S orbital state and can be subsequently captured by the nucleus due to the important overlap between the 1S orbital state and the nucleus, thus giving rise to a  $^{12}\text{B}$  isotope. The second process is represented by the transformation of the  $^{12}\text{C}$  nucleus into a  $^{12}\text{B}$  through a (n-p) reaction, with the incoming neutrons being produced by muon spallation on the nuclei found inside or near the detector.

The beta spectrum is extracted by selecting pairs of muon-electron events separated in time by  $2\text{ ms} < \Delta T < 35\text{ ms}$ , with a muon in the Prompt window and an electron coming from the  $\beta$ -decay of the  $^{12}\text{B}$  in the Delayed window. The energy of the muon candidates is selected in the [45, 120] MeV range, which corresponds to a distribution of stopping vertices that cover most of the cell volume but allows to reject crossing muons and cosmic showers. Decaying muon events are tagged by searching for coincidences between a muon candidate and a second event, representing the Michel-electron, whose energy lies in the [5,70] MeV range and is detected less than  $6\text{ }\mu\text{s}$  after the muon. These events are therefore rejected. Moreover, we require that there is no muon event in  $200\text{ }\mu\text{s}$  before the  $^{12}\text{B}$  candidate in order to mitigate the contribution of the spallation neutrons, whose captures in the detector can mimic the behaviour of a  $^{12}\text{B}$  event. Finally, the remaining background is subtracted by looking for accidental coincidences in ten off-time windows (see section 4.1.5). The final counting rate is found to be of  $(793.2 \pm 3.5)$  boron candidates per day for a total of 573.8 days of analyzed data and the signal-to-background ratio varies between 0.1 and 0.8 in the [3.75, 15.50] MeV range.

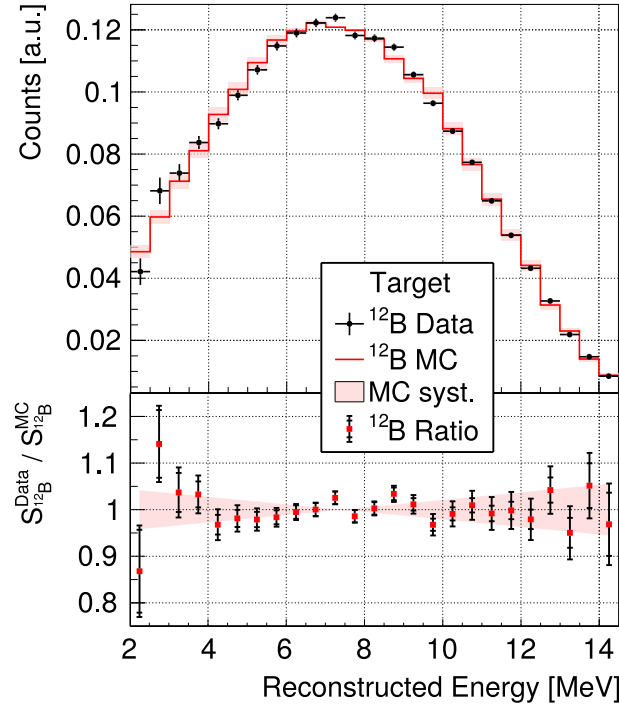


Figure 3.37 – Top: Comparison between the experimental (black circles) and the simulated (red solid line)  $^{12}\text{B}$  beta spectra. The uncertainties of the data are statistic, while the red shaded area shows the systematic uncertainty of the simulation. Bottom: data/MC ratio. The uncertainty on each ratio point show both the statistics-only and total uncertainties. Source: [77].

Having obtained the  $^{12}\text{B}$  beta spectrum, we need to compare it with the simulation in order to probe the accuracy of the energy scale. The dominant uncertainties on the simulated  $^{12}\text{B}$  beta spectrum come from the vertex distribution of stopping muons and radiative corrections and are comparable in magnitude (see [77] for a detailed discussion of the simulated  $^{12}\text{B}$  beta spectrum and its associated uncertainties). The comparison between the experimental and the simulated  $^{12}\text{B}$  beta spectra is shown in figure 3.37. The reached agreement is reasonable, with a  $\chi^2/\text{ndf}=40/25$  corresponding to a p-value of 0.03.

A combined fit of the  $^{12}\text{B}$  beta spectrum and the radioactive source data can now be performed for each cell in order to characterize the distortion of the energy scale. While the residuals of radioactive sources directly probe the discrepancies between the experimental and the simulated reconstructed energies, in the case of the boron spectrum, the impact of a distortion of the energy scale is propagated using the formalism from [50]. The combined data is fitted with polynomial functions of different degrees (between 1 and 4), as it is illustrated in figure 3.38, where is presented an example of combined fit performed by using a second-order polynomial.

Using the formalism from [50], we can then compute the deformations induced on the detected IBD spectra by the fitted distortion of the energy scale. These induced deformations are presented in figure 3.39. It can be seen that fit results for cell 6 is

different than the ones for cells 1 to 5. The deformations on the detected IBD spectra are contained in a region obtained by considering a  $\pm 1\%$  uncertainty on the linear calibration coefficients. This is the case independently of the model that was used to perform the combined fit. Finally, we consider the envelope defined by considering a  $\pm 1\%$  uncertainty on the linear calibration coefficients as a  $1\sigma$  uncertainty with 100% energy-bin-to-energy-bin correlation and no cell-to-cell correlation.

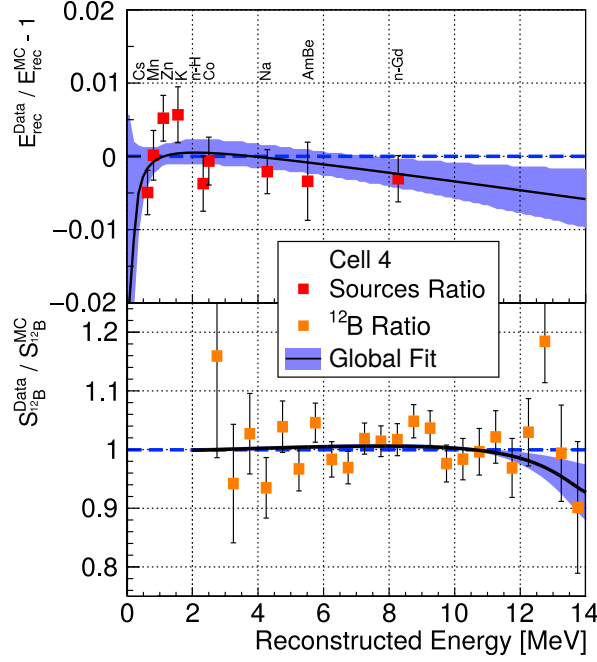


Figure 3.38 – Example of a combined fit of sources (top) and boron data (bottom) in cell 4, where the experimental energy scale is assumed to be a second order polynomial of the simulated energy scale. The blue shaded area represents the uncertainty band of the fit. Source: [77].

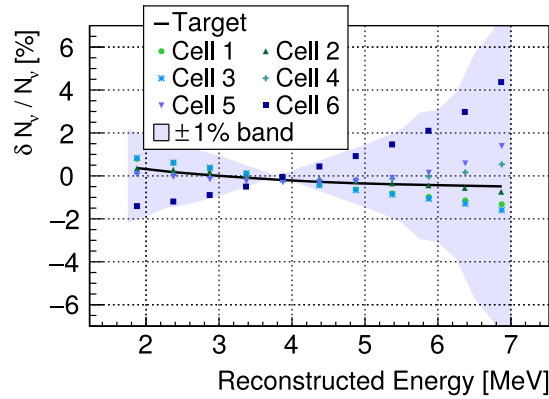


Figure 3.39 – Deformations induced on the detected IBD spectra by a distortion in the energy scale, presented for each cell and for the entire Target. The blue shaded area is obtained by considering a  $\pm 1\%$  uncertainty on the linear calibration coefficients. Source: [77].

## 3.4 Conclusion

This chapter presented the Monte Carlo simulation of the STEREO detector and focused on the fine tuning of the optical parameters of the detector within the simulation for phases II and III of the data taking, which was the main contribution of the present work for the STEREO analysis. We have seen that an accurate agreement between data and simulation at the raw charge level can be reached using the data and simulated spectra of a  $^{24}\text{Na}$  calibration source as a guide. At the cell level, the agreement reaches  $\sim 0.5\%$  accuracy, proving that the simulation reproduces well the top-bottom asymmetries observed in the data.

This fastidious work was very important for a good control of the energy scale and its associated systematic uncertainties, which are crucial for the data analysis results that will be presented in chapter 5.

# Chapter 4

## Neutrino signal extraction

*"La science n'a jamais tout à fait raison, mais elle a rarement tout à fait tort, et, en général, elle a plus de chance d'avoir raison que les théories non scientifiques. Il est donc rationnel de l'accepter à titre d'hypothèse."*

*Bertrand Russell*

### Sommaire

---

<b>4.1</b>	<b>Selection cuts for the IBD candidates . . . . .</b>	<b>104</b>
4.1.1	Muon tagging . . . . .	105
4.1.2	Energy and topology related cuts . . . . .	106
4.1.3	Time related cuts . . . . .	108
4.1.4	Acceptance of the IBD selection cuts . . . . .	109
4.1.5	Correlated pair search algorithm . . . . .	111
4.1.6	Delayed neutron detection efficiency . . . . .	112
<b>4.2</b>	<b>Background sources . . . . .</b>	<b>116</b>
4.2.1	Pulse shape discrimination . . . . .	116
4.2.2	Accidental and correlated background . . . . .	116
4.2.3	Background correlation with environmental parameters . . . . .	119
4.2.4	Summary of the background sources studies . . . . .	122
<b>4.3</b>	<b>Neutrino extraction methods . . . . .</b>	<b>123</b>
4.3.1	The Saclay method . . . . .	123
4.3.2	The LPSC method . . . . .	131
<b>4.4</b>	<b>Comparison between the LPSC and Saclay methods . . . . .</b>	<b>134</b>
4.4.1	Modified Saclay method . . . . .	135
4.4.2	Comparison between the two neutrino extraction methods . . . . .	139
<b>4.5</b>	<b>Conclusion . . . . .</b>	<b>142</b>

---

This chapter is dedicated to the procedure employed to extract the antineutrino rates for every cell of the Target. Firstly, the cuts used to select the IBD candidates as well as the respective induced biases will be presented. Secondly, the background sources will be briefly examined with an emphasis on the stability of the correlated background. Finally, the two methods that were used to extract the antineutrino rates for every cell and energy bin will be exposed and compared in order to determine their compatibility.

The work done within this thesis mainly concerns section 4.4 and focused on adapting an existing neutrino extraction method such that it could be compared with the official method used to extract the IBD rates for phases II and III of the data taking. It allowed to evaluate the potential biases of the official extraction method and to estimate a systematic uncertainty on the extracted absolute antineutrino rate.

## 4.1 Selection cuts for the IBD candidates

The extraction of the antineutrino signal is based on the signature of the IBD reaction, i.e. the time coincidence between a positron (Prompt event) and a neutron (Delayed event). The first level of background reduction consists in applying cuts on the data in order to select the IBD candidates. These cuts are chosen such that an optimal compromise between the detection efficiency and the background rejection is achieved and they aim at reducing both the correlated background, which is due to particles that have a common origin, and the accidental background, which is due to combinations of uncorrelated particles that can pass the selection cuts.

There are four types of events that will be important when discussing the selection cuts

1. **Muon events.** They are identified by charge or energy cuts<sup>1</sup> in the Muon Veto or in the detector.
2. **Single events.** They are all the events which pass the energy cuts relevant for the data analysis and which are not tagged as muons. The Prompt and Delayed events defined below are also contained in this class of events.
3. **Prompt events.** The expected Prompt event is composed of a positron created in the IBD reaction and two annihilation gamma rays.
4. **Delayed events.** The expected Delayed event is composed of a gamma cascade associated to the capture of the neutron created in the IBD reaction on a Gadolinium nucleus.

The set of applied cuts along with their acceptances  $a_{\text{cut}}$  are reported in table 4.1 and will be discussed in the next two sections. The acceptance of a cut is defined as

---

<sup>1</sup>When referring to energy cuts one should understand cuts applied on the reconstructed energy for the rest of this chapter.

Table 4.1 – Selection cuts for IBD candidates and their acceptance  $a_{\text{cut}}$  (equation 4.1.1). Source: [77].

Type	#	Requirement for passing cut	$a_{\text{cut}}/\%$
Energy	1	$1.625 \text{ MeV} < E_{\text{prompt}}^{\text{detector}} < 8.125 \text{ MeV}$	89.2
	2	$4.5 \text{ MeV} < E_{\text{delayed}}^{\text{detector}} < 10.0 \text{ MeV}$	75.9
Coincidence	3	$2 \mu\text{s} < \Delta T_{\text{prompt-delayed}} < 70 \mu\text{s}$	95.5
	4	$\Delta X_{\text{prompt-delayed}} < 600 \text{ mm}$	99.3
Topology	5	$E_{\text{prompt}}^{\text{cell}} < \begin{cases} 1.0 \text{ MeV, neighbour cell} \\ 0.4 \text{ MeV, other cell} \end{cases}$	98.6
	6		99.6
	7	$E_{\text{delayed}}^{\text{Target}} > 1.0 \text{ MeV}$	97.9
Rejection of muon-induced background	8	$\Delta T_{\text{muon-prompt}}^{\text{veto}} > 100 \mu\text{s}$	–
	9	$\Delta T_{\text{muon-prompt}}^{\text{detector}} > 200 \mu\text{s}$	–
	10	$\Delta T_{\text{before prompt}} > 100 \mu\text{s}$ and $\Delta T_{\text{after delayed}} > 100 \mu\text{s}$ for all events with $E_{\text{event}}^{\text{detector}} > 1.5 \text{ MeV}$	–
	11	$\frac{Q_{\text{PMT max, prompt}}}{Q_{\text{cell, prompt}}} < 0.5$	99.3

$$a_{\text{cut}} = \frac{N_{\text{all cuts}}}{N_{\text{all cuts w/o studied cut}}} \quad (4.1.1)$$

#### 4.1.1 Muon tagging

The Muon Veto placed on top of the detector allows the identification of vertical muons by deposited charge criteria with an efficiency  $>99.5\%$ . However, muons with a bigger angle do not pass through the Muon Veto and thus cannot be tagged by it. Since a muon deposits  $\sim 2 \text{ MeV cm}^{-1}$ , it only takes 5-10 cm of traversed length inside the detector to induce nonlinearities in the acquisition, which was not designed to be linear in the high energy region. Thus, to complement the Muon Veto tagging power, we adopt the following arbitrary cut in order to tag as a muon an event that deposits energy inside the detector

$$E^{\text{detector}} > 20 \text{ MeV} \quad (4.1.2)$$

since there are very few background events that can deposit more than 20 MeV.

In what follows we will call a muon any event identified as such by the Muon Veto or/and the detector. The rate of tagged muons is of  $\sim 850 \text{ Hz}$ , from which  $\sim 650 \text{ Hz}$  are detected in the Muon Veto and  $\sim 400 \text{ Hz}$  in the detector, resulting in an overlap of 20%.

### 4.1.2 Energy and topology related cuts

The positron created in the IBD reaction carries the information on the energy of the incident electron antineutrino. The Prompt IBD events are selected with cut #1

$$1.625 \text{ MeV} < E_{\text{prompt}}^{\text{detector}} < 8.125 \text{ MeV} \quad (4.1.3)$$

where the lower cut at 1.625 MeV aims at rejecting background contributions, for the most part coming from the neutron activation of  $^{41}\text{Ar}$ , present during the reactor-on periods, and the upper cut at 8.125 MeV is defined by the end of the antineutrino spectrum emitted by  $^{235}\text{U}$ . The vertex cell of an event is defined as the Target or Gamma Catcher cell with the largest reconstructed prompt energy.

The positron deposits its energy locally in the vertex cell. However, the two 511 keV annihilation gamma rays can travel a bigger distance and deposit all or part of their energy in other cells of the detector. In order to limit the gamma background contribution on the positron spectrum we require that the vertex cell be a Target cell and we put an upper limit on the energy reconstructed in the cells other than the vertex cell using cuts #5 and #6

$$E_{\text{prompt}}^{\text{cell}} < \begin{cases} 1.0 \text{ MeV, neighbour cell} \\ 0.4 \text{ MeV, other cell} \end{cases} \quad (4.1.4)$$

which impose that only one 511 keV gamma ray can be detected in a neighbour cell, since it is very improbable to detect the two 511 keV gamma rays in the same neighbour cell. The difference between 511 keV and the 1 MeV cut allows to take into account the light leaks from the vertex cell to its neighbours.

The expected signature of the neutron created in the IBD reaction is the emission of a  $\sim 8$  MeV gamma cascade following its capture on a Gadolinium nucleus. Thus, the Delayed IBD events are selected with cut #2

$$4.5 \text{ MeV} < E_{\text{delayed}}^{\text{detector}} < 10.0 \text{ MeV} \quad (4.1.5)$$

where the lower cut at 4.5 MeV is chosen such that it includes most of the Gd events found in the tail of the neutron capture gamma rays energy distribution (see figure 4.3), while cutting most of the events coming from neutron captures by Hydrogen, which give rise to a gamma of  $\sim 2.2$  MeV. The upper cut at 10 MeV is defined by the end of the delayed energy spectrum. This energy cut on the Delayed event allows an important reduction of the accidental coincidences, which are mainly due to low energy events.

The fact that only the Target liquid scintillator is doped with Gd allows us to apply a new constraint on the Target energy of the Delayed event by imposing cut #7



$$E_{\text{delayed}}^{\text{Target}} > 1.0 \text{ MeV} \quad (4.1.6)$$

which reduces the high energy background events that enter the detector through the sides and which are mainly creating accidental coincidences.

The fact that the positron and the neutron created in a IBD reaction have a common origin led us to impose cut #4, which puts a limit on the maximal distance between their vertices along the x-axis

$$\Delta X_{\text{prompt-delayed}} < 600 \text{ mm} \quad (4.1.7)$$

where the value of 600 mm represents  $\sim 1.5 \times \text{length of a cell in the x-direction}$ . The value of  $\Delta X_{\text{prompt-delayed}}$  is computed as the difference between the barycenters of the vertices of the Prompt and Delayed events along the x-direction, where the barycenter  $B_x$  for one event is defined as

$$B_x = \frac{\sum_{c=0}^{10} E_c^{\text{rec}} \times b_c}{\sum_{c=0}^{10} b_c} \quad (4.1.8)$$

with  $b_c$  being the charge barycenter for cell  $c$  and  $E_c^{\text{rec}}$  being the reconstructed energy in cell  $c$ . Unlike IBD events, the accidental coincidences are not correlated in space. Thus, this cut helps reducing the number of accidental coincidences.

Even though most of the muons are tagged by the Muon Veto or by depositing more than 20 MeV in the detector (see equation 4.1.2), there are muons that do not pass through the Muon Veto and have a short track length inside the active detector volume before stopping and decaying, such that they deposit less than 20 MeV. The decays of stopping muons can mimic an IBD event if the muon deposits by ionization an energy that falls into the Prompt energy window (equation 4.1.3) and the energy of the Michel-electron produced in its decay falls into the Delayed energy window (equation 4.1.5). These events have a vertex distribution that is very peaked at the top of the detector, which leads to an asymmetric charge distribution between the four PMTs of the cell in which the muon has stopped, with the muon producing most of the scintillation light in the vicinity of just one PMT. Cut #11 exploits this asymmetry by asking that the ratio between the maximal charge collected by a single PMT and the total charge collected by all PMTs of the vertex cell for a Prompt event is smaller than 0.5

$$\frac{Q_{\text{PMT max, prompt}}}{Q_{\text{cell, prompt}}} < 0.5 \quad (4.1.9)$$

The MC studies shown that the charge asymmetry cut allows to reject up to 50% of the decays of stopping muons, while keeping the neutrino detection efficiency at 99%.

### 4.1.3 Time related cuts

The common origin of the positron and neutron created in an IBD reaction results in a time correlation between their respective detection times. The neutron is detected following its capture by a Gd nucleus. The capture time of a neutron inside the liquid is the result of the competition between the thermalization and the diffusion phases. Since the thermalization time scarcely depends on the initial kinetic energy of the neutron<sup>2</sup>, we can study the neutron capture time using an AmBe source (figure 4.1), which emits neutrons with kinetic energies of the order of 1 MeV (to be compared with the neutrons created in the IBD reaction, whose kinetic energies are of the order of some tens of keV).

The neutron capture time probability distribution from figure 4.1 increases up to 6  $\mu\text{s}$  due to the increase of the neutron capture cross section with decreasing neutron energy. After the peak at 6  $\mu\text{s}$ , the distribution follows an exponential law with a time constant  $\tau$  of  $\sim 16 \mu\text{s}$ , which characterises the diffusion of thermal neutrons. The time constant  $\tau$  of the exponential only depends on the capture cross sections of the absorbing nuclei.

To exploit the fact that the Delayed neutron is captured at an interval  $\Delta T$  after the Prompt positron we imposed cut #3

$$2 \mu\text{s} < \Delta T_{\text{prompt-delayed}} < 70 \mu\text{s} \quad (4.1.10)$$

The upper time cut at 70  $\mu\text{s}$  is set in a region where the contribution of accidental coincidences exceeds that of physically correlated events. The lower time cut at 2  $\mu\text{s}$  allows the rejection of the decays of stopping muons that have survived cut #11 (equation 4.1.9), considering the fact that the lifetime of muons is of  $\sim 2.2 \mu\text{s}$ .

The interaction of cosmic muons in the close proximity of the detector can produce multiple particles that can subsequently deposit energy inside the detector. These particles have a common origin and can thus pass the  $\Delta T$  cut #3 (equation 4.1.10). For example, a muon can create several fast neutrons that can enter the detector volume and mimic an IBD event. In this case, the proton recoils or the gamma(s) from the neutron captures on Hydrogen or Gadolinium could be identified as Prompt and Delayed events. To reject these type of events, which are close in time to the incident muon, we reject all the events that arrive in a defined time interval after the detection of a muon in the Muon Veto (cut #8) or in the detector (cut #9)

$$\Delta T_{\text{muon-prompt}}^{\text{veto}} > 100 \mu\text{s} \quad (4.1.11)$$

---

<sup>2</sup>The time between two neutron collisions is proportional to the ratio between the neutron's mean free path  $\lambda_n$  and its speed  $v_n(t)$ , which decreases with time,  $t_{\text{between collisions}} \propto \lambda_n/v_n(t)$ . If we suppose that the neutron's speed is divided by 2 after each collision, then the time between two collisions increases proportionally to the powers of 2, i.e.  $t_{\text{between collisions}} \propto 2^n$ , where n is the number of collisions experienced by the neutron. Thus, it can be seen that the thermalization time is dominated by the time interval of the neutron's last collisions, which allows us to use the AmBe source to study the capture time of the neutron inside the STEREO detector.

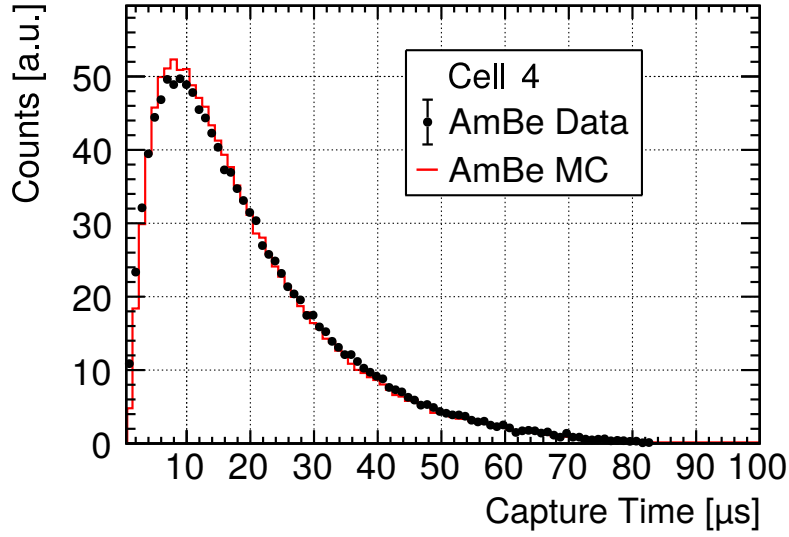


Figure 4.1 – Data and MC distributions of neutron capture times for an AmBe source placed in cell 4, obtained as a sum of 5 measurements at 5 heights along the z-axis. The accidental background has been subtracted from the shown distributions. Source: [77].

$$\Delta T_{\text{muon-prompt}}^{\text{detector}} > 200 \mu\text{s} \quad (4.1.12)$$

To account for the possible correlated background events coming from a multiple neutron cascade who was caused by an undetected primary particle, such as a muon that couldn't be tagged by either the Muon Veto or the detector, the isolation cut #10 was introduced

$$\begin{aligned} \Delta T_{\text{before prompt}} &> 100 \mu\text{s} \text{ and} \\ \Delta T_{\text{after delayed}} &> 100 \mu\text{s} \text{ for all events} \\ \text{with } E_{\text{event}}^{\text{detector}} &> 1.5 \text{ MeV} \end{aligned} \quad (4.1.13)$$

which requires that no event with an energy bigger than 1.5 MeV can happen less than 100  $\mu\text{s}$  before or after an IBD candidate, since the neutrons that we aim to reject are expected to be close in time. The acceptance of cuts #8–#10 is directly corrected via the veto time.

#### 4.1.4 Acceptance of the IBD selection cuts

The impact of the IBD selection cuts on the selection efficiency for the Prompt positron spectra in each cell was studied by the collaboration using simulations. Before applying the selection cuts, the ratio of antineutrino interactions in the simulation was 39:47:14 for Target, Gamma Catcher and acrylic detector components, while after applying the cuts

the ratio becomes better than 99:0:1. The overall acceptance at the entire Target level after applying all the cuts is of 60%, with a  $\sim 4\%$  relative variation across the prompt energy range. The overall cut acceptance as a function of the Prompt energy for each cell is shown in figure 4.2.

It can be seen that the central cells (2-5) have a very similar behaviour with an average acceptance of 63%, while the two lateral cells, 1 and 6, have a smaller acceptance even though they exhibit the same energy distortion shape. This is mainly due to the loss of neutron detection efficiency at the edges of the detector, as it will be seen in section 4.1.6. The smaller cut acceptance seen for cells 1 and 6 is related to the cut imposed on the Target Delayed energy (cut #7 - equation 4.1.6) and the upper cut on the Prompt-Delayed time interval (cut #3 - equation 4.1.10). In fact, since an excited Gd nucleus produces several gamma rays isotropically, some of them can traverse the Target without depositing energy and stop in the Gamma Catcher. Moreover, a neutron produced in cells 1 or 6 has a bigger probability of having part of their trajectory inside the Gamma Catcher, which is unloaded in Gd, and thus it can take them more time to reenter the Target and get captured. The probability for the two previous scenarios is bigger for the edge cells 1 and 6. However, there remains a discrepancy between cells 1 and 6 that needs to be explained, i.e. the fact that cell 6 has a smaller cut acceptance than cell 1. This may be due to the fact that the neutrons are preferentially emitted in the direction of the incident antineutrino, thus have a bigger chance to reach the Gamma Catcher if the interaction has taken place in cell 6.

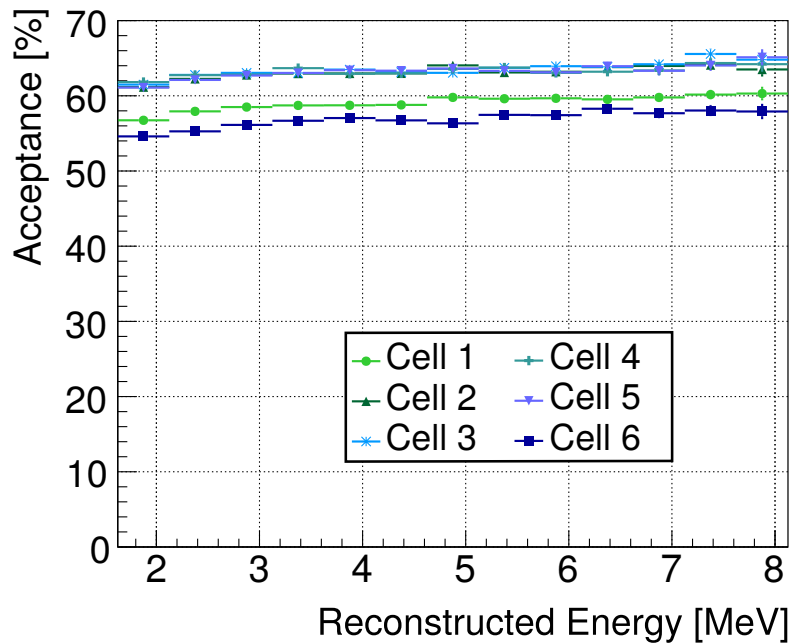


Figure 4.2 – Acceptance of the IBD selection cuts as a function of the Prompt reconstructed energy. Source: [77].

### 4.1.5 Correlated pair search algorithm

#### Principle of the algorithm

The correlated pair search algorithm's scope is to select pairs of events that pass the selection cuts described in the previous sections, as well as to determine the accidental background component, which is due to combinations of uncorrelated particles that can pass the selection cuts and thus be registered as correlated pairs, and eventually subtract this component.

Two independent correlated pair search algorithms were developed within the STEREO collaboration. Even though the philosophy behind the codes was similar, the advantage of having two different frameworks was that we could cross-check their respective results and identify any remaining errors or biases. The method presented in the following paragraphs is the one developed at CEA Saclay [29].

The used algorithm was inspired by the NUCIFER experience [96],[99] and is based on using a sliding memory window that contains the information of four successive events: Pre-Prompt(1), Prompt(2), Delayed(3) and Post-Delayed(4). The neutrino runs are thus read from the beginning to the end by moving the sliding window over each event. At each step, the algorithm tests if the following conditions on a Prompt-Delayed candidate pair are met

- (2) is not too closely preceded by a muon: cuts #8 and #9
- (2) is a valid Prompt candidate: cuts #1, #5, #6 and #11
- (3) is a valid Delayed candidate: cuts #2 and #7
- (2) and (3) are correlated in space and time: cuts #3 and #4
- (2) is sufficiently distant in time from (1) and (3) is sufficiently distant in time from (4): cut #10

and if it is the case, the pair is registered in a database. Thus, the registered pairs can have three different origins: IBD events induced by the electron antineutrinos, correlated background and accidental background.

#### Accidental background estimation

The accidental background due to uncorrelated combinations of events that can pass the selection cuts presented in table 4.1 depends directly on the rates of single Prompt and Delayed events. The rate and spectrum of the accidental coincidences is determined statistically by the method of time shifted gates. In practice, for every pair that passes the selection cuts, the Prompt event is virtually cloned and shifted in time by 1 ms. Then,

all the selection cuts are applied again to test if the shifted Prompt event is associated to a valid Delayed candidate. If it is the case, the newly formed pair is registered in the accidental sample and an accidental counter is increased. The time shift value of 1 ms was chosen such that any residual physical correlation can be negligible. In practice, a valid Prompt events is shifted 100 times in order to have an optimal statistical uncertainty on the accidental pairs distributions.

Since the method used to estimate the accidental background is done offline along with the IBD search, it allows us to track accurately any change in the accidental distributions, for each cell and energy bin, that may be induced for example by changes in the configuration of the neighbouring experiments. Between the reactor-on and reactor-off periods we have observed variations up to a factor 4 in the accidental rate.

### Effective acquisition time

In order to compute the effective acquisition time one has to estimate the dead time accurately. For STEREO, the dead time's main origin is represented by the time isolation selection cuts #8, #9 and #10, while the dead time induced by the electronics is inferior to 0.2%. The procedure allowing to estimate the dead time is presented in detail in [29].

#### 4.1.6 Delayed neutron detection efficiency

Along with the systematic uncertainties on the energy scale, the neutron detection efficiency is an observable that plays an important role in the data analysis. Thus, a method aimed at estimating it was developed by the collaboration [100]. Since the Delayed signal, represented by the detection of the gamma cascade emitted following a neutron capture, has lost all the information about the initial antineutrino particle, we can study the agreement between the neutron detection efficiency extracted from the data and from the simulation using an AmBe source. The final goal of this study is to correct the neutron detection efficiency extracted from the simulation, such that it reproduces the behaviour encountered in the data

$$\epsilon_{\text{neutron}}^{\text{corrected}} = \epsilon_{\text{neutron}} \cdot (c_{\text{Gd}} \cdot c_{\text{IBD}}) \quad (4.1.14)$$

where the neutron detection efficiency  $\epsilon_{\text{neutron}} = \epsilon_{\text{Gd}} \cdot \epsilon_{\text{IBD}}$  depends on the fraction of neutrons captured by Gd with respect to the total number of neutron captures<sup>3</sup>,  $\epsilon_{\text{Gd}}$ , and on the IBD selection cut efficiency,  $\epsilon_{\text{IBD}}$ , defined as the fraction of Gd-capture events passing the IBD cuts #2, #3 and #7 that mainly influence the selection of Delayed events:

---

<sup>3</sup>In the Target volume, neutron captures by Gd and H are dominant.

$$\epsilon_{\text{Gd}} = \frac{N_{\text{Gd}}}{N_{\text{Gd}} + N_{\text{H}}} \quad (4.1.15)$$

$$\epsilon_{\text{IBD}} = \frac{N_{\text{cut}\#2\cap\text{cut}\#3\cap\text{cut}\#7}}{N_{\text{Gd}}} \quad (4.1.16)$$

and  $c_{\text{Gd}}$  and  $c_{\text{IBD}}$  are the correction coefficients that quantify the discrepancy between data and simulation in the fraction of neutrons captured by Gd and in the IBD selection cut efficiency.

$$c_{\text{Gd}} = \frac{\epsilon_{\text{Gd}}^{\text{data}}}{\epsilon_{\text{Gd}}^{\text{MC}}} \quad (4.1.17)$$

$$c_{\text{IBD}} = \frac{\epsilon_{\text{IBD}}^{\text{data}}}{\epsilon_{\text{IBD}}^{\text{MC}}} \quad (4.1.18)$$

The efficiency terms appearing in equations 4.1.17 and 4.1.18 are estimated in the same way for the AmBe calibration data and the MC simulations and are compared to estimate the discrepancies that are due to possible imperfections of the simulation. There is no attempt to fine tune the simulation parameters in order to reach a perfect agreement in terms of neutron detection efficiency, since this could have significant consequences on the optical properties of the liquids and on the neutron capture time. Instead, we chose to let the simulation unchanged and account for these discrepancies later in the analysis by correcting the simulation results.

To compare the data and simulation neutron capture efficiencies, an AmBe source was deployed at five different heights along the z-axis inside the internal calibration tubes of the Target cells. The neutrons are emitted via  ${}^9\text{Be}(\alpha, n){}^{12}\text{C}$  reactions, with the  $\alpha$  particle coming from radioactive decays of  ${}^{241}\text{Am}$ . Moreover, in 60% of the cases, a 4.4 MeV gamma ray is emitted along with a neutron as the carbon nucleus is produced in an excited state [101]. The pair search algorithm is then used in order to select Delayed neutron-capture events in a 100  $\mu\text{s}$  interval after the detection of a 4.4 MeV Prompt event. In addition, the accidental background is estimated and subtracted as explained in section 4.1.5. A neutron capture spectrum extracted in this way can be seen in figure 4.3. The good agreement observed between data and simulation is the result of the implementation of the FIFRELIN code [102] that improves the description of the de-excitation cascade for the relevant Gd isotopes [103].

The H-capture events ( $N_{\text{H}}$ ) are defined as the sum of all the events with energies between 1.5 and 3 MeV. The lower energy cut of 1.5 MeV is chosen to exclude the region with background [100]. The Gd-capture events ( $N_{\text{Gd}}$ ) are defined as the sum of all the events with energies between 3 and 10 MeV, containing the Gd-capture peak and its tail.

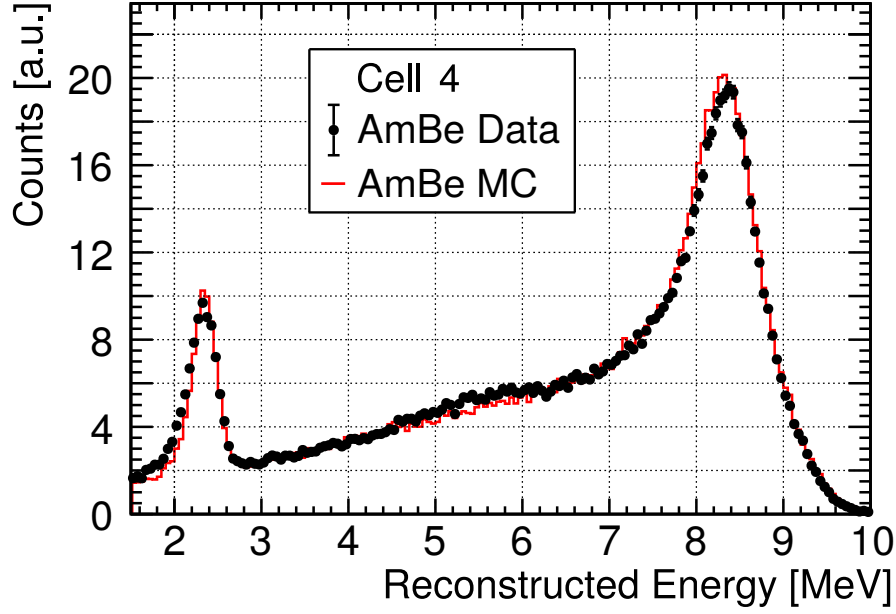


Figure 4.3 – Neutron capture spectrum obtained with an AmBe source deployed in cell 4, as a sum of five spectra measured at five vertical heights along the z-axis. Source: [77].

### IBD selection cut efficiency

The average of all the calibration points inside the detector yields a value of  $c_{\text{IBD}} = 0.9985 \pm 0.0059$  for the correction coefficient related to the IBD selection cut efficiency, which is consistent with unity within one standard deviation. The uncertainty on  $c_{\text{IBD}}$  takes into account time variations of the 25 detector calibration points, inhomogeneities and possible movements of the source position within the deployment accuracy.

### Gd fraction efficiency

The correction coefficient related to the Gd fraction,  $c_{\text{Gd}}$ , is not constant in every place of the Target volume. This is mainly due to the inability of the simulation to describe very accurately the mobility of thermal neutrons. Figure 4.4 shows the  $c_{\text{Gd}}$  coefficients for the five Target cells equipped with internal calibration tubes. It can be seen that there is a 2% difference between the value of  $c_{\text{Gd}}$  at the center of the detector in the x-direction and its value at the borders of cells 1 and 6. The value of  $c_{\text{Gd}}$  is smaller for cell 1 than for cell 6. This is due to the fact that the calibration tube is closer to the border of the cell for cell 1. The points from the left-hand side of figure 4.4 are fitted using a Subbotin distribution, which allows the presence of a plateau in the center of the detector [104]

$$C_{\text{Gd}}(x) = \exp \left[ - \left( \frac{|x - \mu|}{\sigma} \right)^\beta \right] \quad (4.1.19)$$



where  $\mu$  is the mean of the distribution, fixed to zero in our case, and  $\sigma$  and  $\beta$  are parameters that allow to scale and shape the distribution. Since the same behaviour is expected in the y-direction, i.e. towards the long Gamma Catchers, the fit function obtained from fitting the x-axis distribution is extrapolated to the y-direction by adapting the plateau length. The correction coefficients in the x-y plane, obtained by using the two-dimensional fit function recalled earlier, are presented in the right-hand side of figure 4.4. Finally, the  $c_{\text{Gd}}$  coefficients are obtained by weighting the two-dimensional function by the expected distribution of IBD vertices. In this way, we obtain  $c_{\text{Gd}} = 0.9846$  for the central cells and  $c_{\text{Gd}} = 0.9650$  for the border cells.

For completeness, a table containing the total correction coefficients  $c_{\text{tot}} = c_{\text{Gd}} \cdot c_{\text{IBD}}$  is shown in 4.2. For a discussion of the correlated and uncorrelated uncertainties on  $c_{\text{tot}}$ , the reader should refer to [100]. The correction coefficients will be used as factors that correct the normalization of each individual cell in the oscillation analysis.

Table 4.2 – Correction coefficients  $c_{\text{tot}}$  for the delayed neutron efficiency along with their uncertainties.

Cell	$c_{\text{tot}}$	$\delta_{\text{uncorr}}(c_{\text{tot}})$	$\delta_{\text{corr}}(c_{\text{tot}})$
1	0.9635	0.0084	0.0041
2	0.9828		0.0015
3	0.9831		0.0013
4	0.9831		0.0013
5	0.9829		0.0015
6	0.9643		0.0040

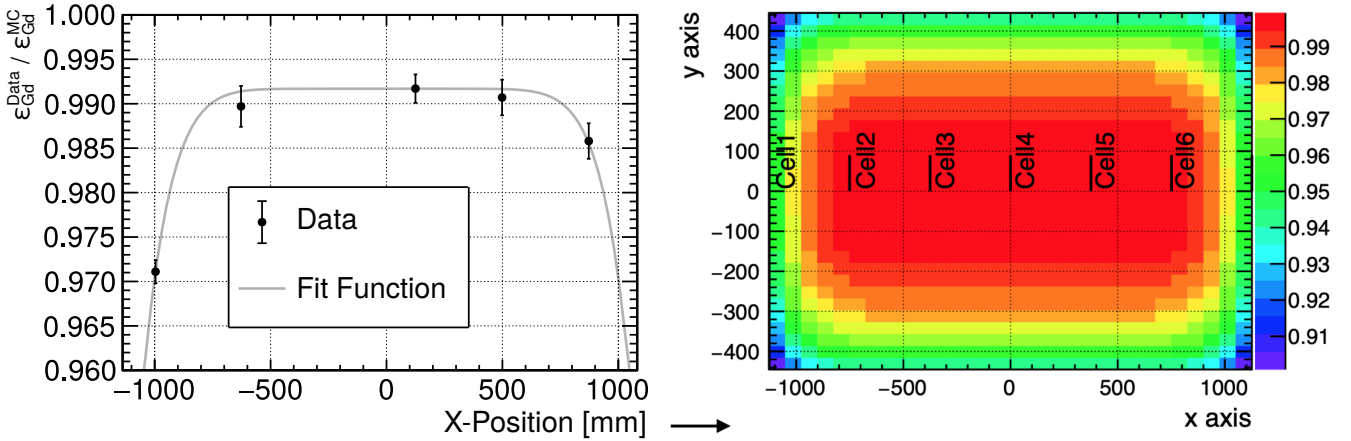


Figure 4.4 – Left: ratio between the Gd efficiency of data and MC simulation events  $c_{\text{Gd}}$  for an AmBe source averaged over five vertical heights in each Target cell. The fit function illustrated in equation 4.1.19 is represented in grey. Right: the 2D extended model for the  $c_{\text{Gd}}$  correction coefficients. Source: [100].

## 4.2 Background sources

This section is devoted to the study of the different types of background and their spectra. Firstly, the pulse shape discrimination (PSD) method will be introduced as an additional way of rejecting the background. Secondly, the accidental and correlated background spectra will be presented and discussed. Lastly, the stability of the background with varying environmental observables will be considered in order to prove that the reactor-off correlated PSD distributions of IBD candidates can be directly used as a model of background in the extraction of the antineutrino signal.

### 4.2.1 Pulse shape discrimination

The PSD capability of the liquid scintillator used by STEREO allows to further reject part of the correlated background that remains after applying the IBD selection cuts. The  $Q_{\text{tail}}/Q_{\text{tot}}$  variable that allows to discriminate the signals depending on their origin, electronic recoils or proton recoils (see section 2.2.3), will be often denoted simply as the "PSD" in the rest of the manuscript.

The prompt energy PSD distribution for one cell and one energy bin is shown in the upper part of figure 4.5, along with the PSD distribution for a sample of single events shown in the lower part of the same figure. The events that populate the low  $Q_{\text{tail}}/Q_{\text{tot}}$  region come from IBD events, correlated electronic background induced by cosmic rays and accidental coincidences, while those that populate the high  $Q_{\text{tail}}/Q_{\text{tot}}$  mainly come from muon-induced fast neutrons<sup>4</sup>. Even though the proton recoil background is dominant, most of it can be rejected using the PSD method, since it is situated in a high  $Q_{\text{tail}}/Q_{\text{tot}}$  region.

The PSD distribution of single events can be monitored continually for each cell and energy bin. It is dominated by electronic recoils, which represent most of the environmental background, and can be fitted with a Gaussian in order to track the changes of its mean position  $\mu_\gamma$  and standard deviation  $\sigma_\gamma$ . For background investigation purposes, the electronic recoils region is defined as the region for which  $Q_{\text{tail}}/Q_{\text{tot}} < \mu_\gamma + 2\sigma_\gamma$ , while the proton recoils region is defined as the region for which  $Q_{\text{tail}}/Q_{\text{tot}} > \mu_\gamma + 2.5\sigma_\gamma$ .

### 4.2.2 Accidental and correlated background

The accidental and correlated coincidence background prompt spectra, obtained by integrating the rate of events for  $Q_{\text{tail}}/Q_{\text{tot}} < \mu_\gamma + 2\sigma_\gamma$  in each energy bin, are shown in the upper part of figure 4.6.

The prompt spectrum of accidental coincidences is mainly populated by low-energy

---

<sup>4</sup>For example, a fast neutron interacting in the liquid can induce a Prompt proton recoil signal that is followed by a valid Delayed signal represented by its capture on a H or Gd nucleus.

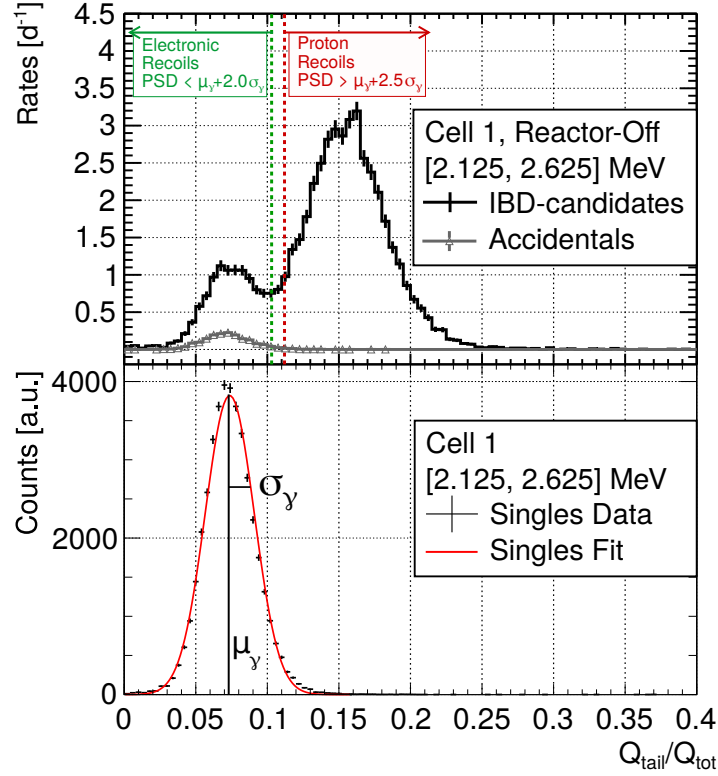


Figure 4.5 – Top: PSD distribution of the IBD candidates in black and accidental background contribution in grey for the reactor-off periods of phase II in the first cell and for prompt energies in [2.125, 2.625] MeV. Bottom: PSD distribution of single events for one day of data taking. The distribution is dominated by electronic recoils. The parameters  $\mu_\gamma$  and  $\sigma_\gamma$  are extracted by fitting the PSD distribution of single events with a Gaussian and they are used to define a PSD cut to separate electronic recoils from proton recoils. Source: [77].

gamma rays and it reflects the single events spectrum. Above the 2.6 MeV energy, corresponding to the highest gamma energy coming from natural radioactivity ( $^{208}\text{Tl}$ ), the main contributions to the accidental spectrum come from gamma cascades following neutron captures on Gd and from high energy gamma rays produced following neutron captures on the surrounding materials (Al, Fe) during reactor-on periods, due to the activity of the neighboring instruments. The contribution of the accidental coincidences to the total background is thus important for the first three energy bins used for the neutrino analysis (for the [1.625, 3.125] MeV interval), but becomes negligible afterwards, where the correlated coincidences dominate.

The correlated background spectrum is mainly of a cosmic-induced origin. Its contribution to the prompt background spectrum features a peak at 2.2 MeV. This is associated to multiple neutron events that survived the time isolation cut #10 and for which the Prompt event consists of a 2.2 MeV gamma ray created following a neutron capture on hydrogen and the Delayed event originates from the capture of a second neutron on a Gd nucleus. The nature of the events populating the 2.2 MeV peak is thus electromagnetic. Another feature of the correlated spectrum is the peaked structure appearing around 5.4

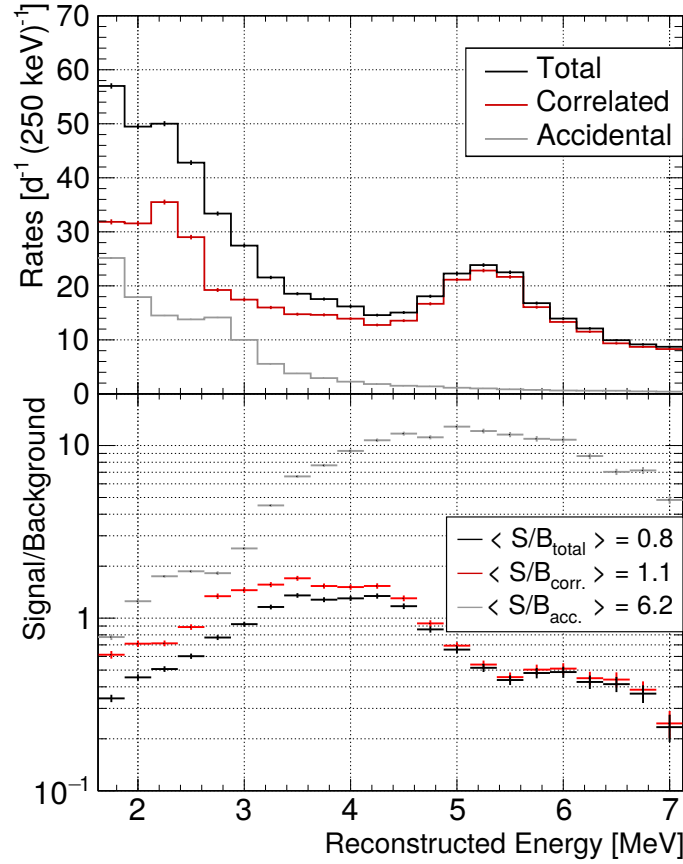


Figure 4.6 – Top: accidental and correlated contributions to the prompt background spectrum obtained as the rate integral of the electronic recoil component ( $Q_{\text{tail}}/Q_{\text{tot}} < \mu_\gamma + 2\sigma_\gamma$ ). Bottom: signal-to-background ratio with respect to the background spectra shown above. The average values given in the legend are calculated from the data points weighted by the signal. Source:[77].

MeV. It is mainly made up of the coincident detection of a neutron-induced proton recoil and a 4.4 MeV gamma ray created during the inelastic scattering of fast neutrons on  $^{12}\text{C}$  nuclei  $^{12}\text{C}(n,n'\gamma)^{12}\text{C}$ . Following this reaction, the  $^{12}\text{C}$  nucleus can be left in an excited state  $^{12}\text{C}^*$  with an energy of 4.4 MeV or 7.7 MeV [28], from which it recovers the ground state by emitting one or two gamma rays. Since this contribution is not purely electromagnetic, due to the neutron-induced proton recoil, its value of  $Q_{\text{tail}}/Q_{\text{tot}}$  is expected to be higher than that for purely electromagnetic events, such as gamma rays or positrons.

In the lower part of figure 4.6 are shown the signal-to-background ratios for the different contributions. These are obtained by making use of the detected IBD spectra that will be presented in section 4.3.

### 4.2.3 Background correlation with environmental parameters

#### PSD variation with temperature

The PSD position was found to be dependent on the temperature of the liquid. This was observed in earlier uses of liquid scintillators for pulse shape discrimination experiments and is probably due to a change in the density of the excited molecules caused by the temperature variation [105]. The maximal liquid temperature variation reaches 3°C and is typically observed over the two months periods in which the reactor is functioning. Indeed, by monitoring the sample of single events over time for the phase II data (see figure 4.5), a linear anticorrelation was found between the PSD position  $\mu_\gamma$  and the temperature of the liquid  $\Delta\mu_\gamma/\Delta T \sim -0.1\sigma_\gamma/\text{K}$  [106]. For the maximal temperature variation of 3°C quoted earlier, this means that the evolution of  $\mu_\gamma$  can reach 30% in units of  $\sigma_\gamma$ . To correct for this temperature variation, a reference temperature, common to every run, is chosen and a mean shift  $\delta\text{PSD}$  is computed for every data run as

$$\delta\text{PSD} = (T_{\text{ref}} - T_{\text{run}})f_{\text{temp}} \quad (4.2.1)$$

where  $f_{\text{temp}}$  is the observed anticorrelation coefficient. Afterwards, this shift is applied for every event of a given run

$$\text{PSD}_{\text{corrected}} = \text{PSD} + \delta\text{PSD}, \quad (4.2.2)$$

which allows to correct at first order the PSD evolution with temperature.

Since the shift in the PSD is computed using the single events, which have  $Q_{\text{tail}}/Q_{\text{tot}}$  values characteristic to electronic recoils, we needed to check if the same PSD-liquid temperature correlation was present for  $Q_{\text{tail}}/Q_{\text{tot}}$  values characteristic of proton recoils. This was examined with dedicated studies of the AmBe source PSD spectrum which prove that a similar correlation is retrieved for the proton recoils part of the PSD spectrum, thus confirming that we can apply the correction from equation 4.2.2 for all the data events.

#### Background dependence on atmospheric pressure and water pool level

The rates of electronic recoils and proton recoils events were found to be correlated to the atmospheric pressure, as shown in figure 4.7. This is due to the fact that the correlated background has a cosmic-induced origin. In fact, the rate at which muons deposit energy in the atmosphere depends on its density. In turn, the atmospheric pressure at the ground level reflects the effective density of the air column traversed by a muon. The rate of cosmic muons detected in the Muon Veto or inside the detector was found to be anticorrelated with the atmospheric pressure measured at the ground level [29], as expected from the consideration that a high atmospheric pressure reflects a high effective air column density and thus a higher  $dE/dx$  for the traversing muons.

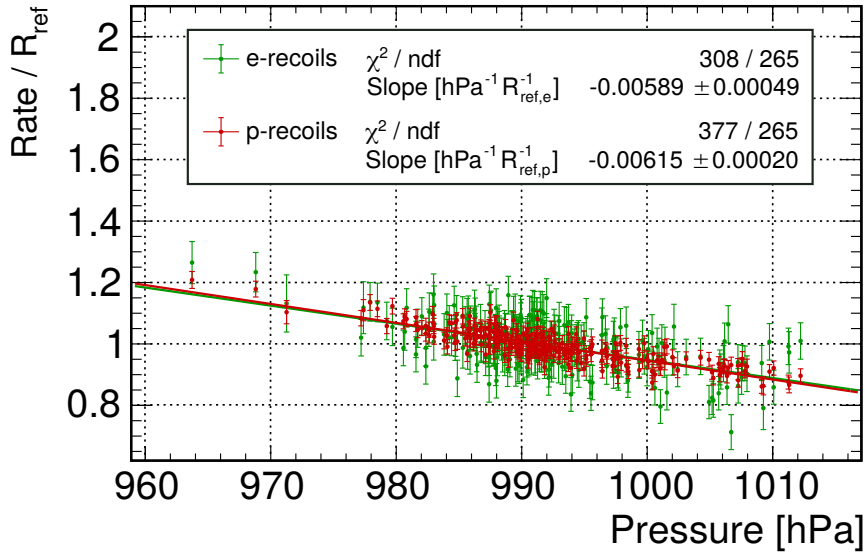


Figure 4.7 – Relative rates of electronic recoils ( $Q_{\text{tail}}/Q_{\text{tot}} < \mu_\gamma + 2\sigma_\gamma$ ) and proton recoils ( $Q_{\text{tail}}/Q_{\text{tot}} > \mu_\gamma + 2.5\sigma_\gamma$ ) candidates from reactor-off periods of phase II as a function of the atmospheric pressure. Source:[77].

The linear correlation coefficient is compatible between the electronic-recoil and the proton-recoil populations. To study the effect of the atmospheric pressure variations on the PSD distribution, the reactor-off dataset was divided into two subsets of high and low mean atmospheric pressure. Then, one of the subsets was rescaled with a normalization factor  $a$  in order to overlap it at best with the other subset and thus take into account the pressure difference between the datasets. It was found that this rescaling was enough to precisely overlap the two subsets with different mean atmospheric pressures, as seen in figure 4.8. Moreover, the fitted  $a$  parameter was found to be compatible with the correlation coefficients from figure 4.7.

The rates of electronic recoils and proton recoils were also observed to be correlated to the filling level of the water pool above the reactor core but, in this case, the greatest effect, due to a 7m change in the water level, was 16 times weaker than the effect due to a 30 hPa atmospheric pressure variation. Again, a single normalization factor  $a$  was sufficient to accurately overlap two subsets of data with opposite values for the filling level of the water pool [77].

### Reactor-induced background

Since STEREO uses the reactor-off periods PSD distribution of correlated events as a model of background for the extraction of the antineutrino rates, we need to make sure that the background does not vary significantly between reactor-on and reactor-off periods. Principally, such a reactor-induced background could be made of fast neutrons that would produce a Prompt proton recoil and a Delayed capture signal.

To test the magnitude of the potential reactor-induced background, all the data runs,

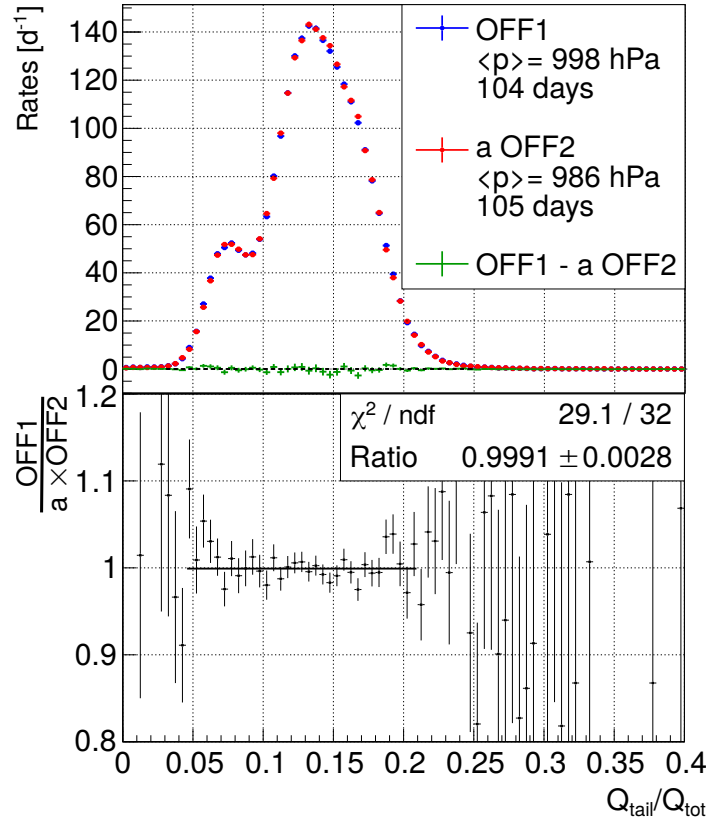


Figure 4.8 – Top: comparison of the two PSD distributions with high and low mean atmospheric pressure using data from the reactor-off periods of phase II. The two distributions were recorded for the same level of the water pool above the reactor and are normalized to their acquisition times. The low mean atmospheric pressure subset OFF2 is scaled with a normalization parameter  $a$  such that it overlaps at best with OFF1. Bottom: ratio between OFF1 and the scaled OFF2 spectra, showing that they are compatible in shape within uncertainties. Source: [77].

reactor-off and reactor-on, were first projected to the same environmental parameters (pressure and water pool level). Then a normalization factor  $a$  was applied to the reactor-off dataset, in the same manner in which it was done for the dependence of the PSD on the atmospheric pressure, in order to overlap it at best with the reactor-on dataset. Figure 4.9 shows the relative difference of proton recoil rates ( $Q_{\text{tail}}/Q_{\text{tot}} > \mu_\gamma + 3.0\sigma_\gamma$ <sup>5</sup>) with respect to the reconstructed energy between reactor-on and reactor-off phases. It can be seen that for the first four energy bins the relative difference is not compatible with zero, while it becomes compatible for the bins above 3.5 MeV. We fitted the relative difference with a power law

$$R(E) = u \cdot E^{-v} + w \quad (4.2.3)$$

where  $E$  is the reconstructed energy and  $u, v$  and  $w$  are free fit parameters. If we

<sup>5</sup>We chose this region for the proton recoils in order to avoid a contribution from the IBDs caused by antineutrino interactions inside the detector while the reactor is on.

suppose that the excess of events between reactor-on and reactor-off periods is present only in the proton recoils region, and is probably due to fast neutrons from the reactor or a neighbouring experiment, it would result in an underestimation of the antineutrino rates, since the extraction method assumes that the shape of the PSD background distribution remains constant between the reactor-on and off phases. Considering this to be the most probable scenario, we correct the antineutrino rates in the first two energy bins by 3.6% and 1.8% respectively, while for the other bins the correction is negligible. These numbers are obtained using the fit of the relative difference from figure 4.9 and taking into account the signal-to-background ratio presented in figure 4.6. However, to take into account the scenario in which the excess of events during reactor-on periods would be shared equally between proton and electronic recoils, an uncertainty equal to the size of the correction is conservatively added in each bin as additional uncorrelated systematic uncertainty on the antineutrino rates, though it remains small compared to the statistical uncertainty.

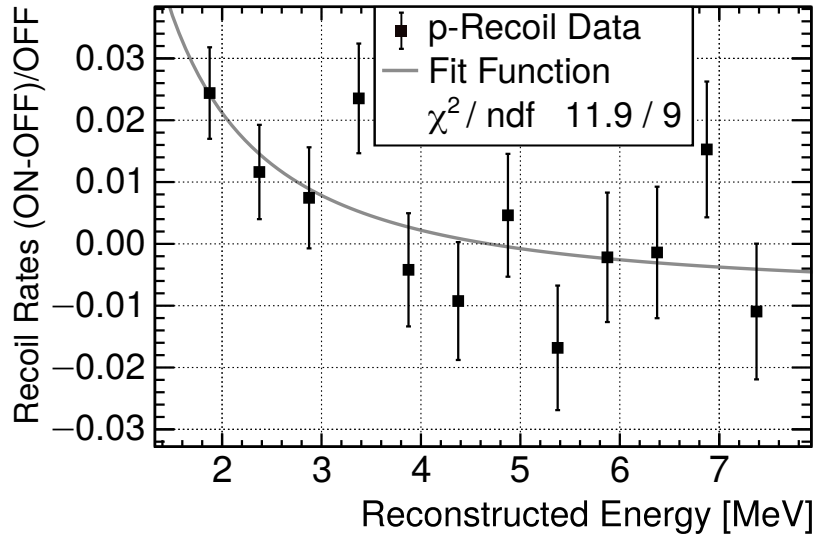


Figure 4.9 – Relative difference of proton recoils rates ( $Q_{\text{tail}}/Q_{\text{tot}} > \mu_\gamma + 3.0\sigma_\gamma$ ) between reactor-on and reactor-off periods. The depicted energy bins are those that are used in the extraction of the antineutrino signal. The fit function from equation 4.2.3 is plotted in grey. Source: [77].

#### 4.2.4 Summary of the background sources studies

We have seen in this section the behaviour of the accidental and correlated background and explained the different types of events that participate to them. In addition, the stability of the correlated background has been studied, and we proved that it is stable in shape under varying environmental parameters and that a normalization factor suffices to overlap subsets with opposite pressures or water level fillings. Moreover, the small excess in the rate of proton recoils present during the reactor-on periods was accounted for by a correction in the first two energy bins of the extracted antineutrino rates. All these proves that it is reasonable to use the PSD distributions of IBD candidates obtained



during reactor-off periods as a model of background for the extraction of the antineutrino signal. The results presented in this section were all obtained using phase II data. The same studies were performed for phase III data, which led to the same level of precision and conclusions. For phase I data, however, the PSD distributions of the correlated background were not so stable in time and a dedicated neutrino extraction method, which splits the data into time bins, was developed and will be briefly presented in the next section.

## 4.3 Neutrino extraction methods

This section is dedicated to the presentation of the two neutrino extraction methods used by the STEREO collaboration. These methods use different pair search algorithms and were developed successively in order to integrate the evolving understanding of the correlated background as more data were recorded. Firstly, the method developed at CEA Saclay [29], which uses a multi-Gaussian function to model the background, will be presented. Secondly, the method developed at LPSC Grenoble [106], which directly uses the PSD distribution of correlated background obtained during reactor-off periods for the neutrino extraction, will be presented. In the next section, a modification to the CEA Saclay method, developed during the present thesis, will be introduced in order to allow for the comparison in norm and form between the two methods.

### 4.3.1 The Saclay method

The Saclay method was initially developed to analyse phase I data. During phase I, the highly evolving light leaks between the detector's cells induced sizeable variations in the PSD distributions for reactor-on and reactor-off data, in addition to the temperature effect (see section 4.2.3), which wasn't yet corrected for. This implied that a simple subtraction method, that would consist in subtracting the reactor-off PSD distribution of correlated pairs from the reactor-on one, using a singles-related cut on the PSD value

$$Q_{\text{tail}}/Q_{\text{tot}} < \mu_{\gamma}(t) + c \cdot \sigma_{\gamma}(t) \quad (4.3.1)$$

would induce important biases, dependent on the position of the cut  $c$ , on the extracted rate of antineutrinos. Moreover, if the position of the electronic recoils peak, illustrative for the neutrino peak position, can be followed using the singles sample, it is not the case for the position of the proton recoils peak, whose evolution was also important during phase I. A scheme illustrating this effect can be seen in figure 4.10.

The solution to the previous issues was to split the data into sufficiently small time bins, for which the PSD evolution is negligible, and to use information derived from the reactor-off data in order to constrain the background during the reactor-on periods. The

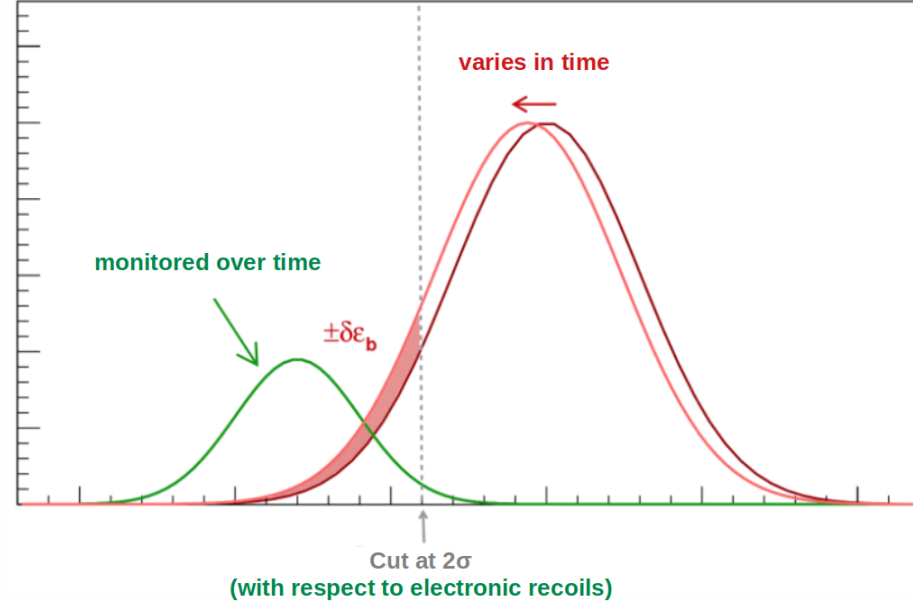


Figure 4.10 – Effect of the relative variations between the PSD distributions of electronic recoils and proton recoils on the extraction of the neutrino rates. Even if the electronic recoils component’s position can be followed in time using the singles sample -and supposing that the neutrino component has the same behaviour- the relative variations of the proton recoils component’s position can induce a bias  $\epsilon_b$  on the neutrino rate extraction. Source: [29].

new method makes use of normalized Gaussian functions  $\mathcal{G}(x; \mu, \sigma)$ <sup>6</sup> to model the different components of the correlated background PSD distributions, which are split into energy, cell and time bins. Reactor-off data is used to adjust the background parameters

$$M_{OFF}(t, PSD) = \mathcal{A}_p^{OFF}(t) \left( \frac{\mathcal{A}_\gamma^{OFF}(t)}{\mathcal{A}_p^{OFF}(t)} \mathcal{M}_\gamma(t, PSD) + \mathcal{M}_p(t, PSD) \right) \quad (4.3.2)$$

where  $\mathcal{M}_\gamma$  and  $\mathcal{M}_p$  are the normalized probability density functions describing the  $PSD \equiv Q_{\text{tail}}/Q_{\text{tot}}$  distributions for electronic recoils and proton recoils, while  $\mathcal{A}_\gamma$  and  $\mathcal{A}_p$  quantify their norm. Since the nature and form of the correlated background is supposed to be the same during reactor-off and reactor-on periods, we impose that the ratio  $\frac{\mathcal{A}_\gamma}{\mathcal{A}_p}$  is a constant. In fact, this ratio is the only parameter that is propagated to the reactor-on correlated background PSD distribution

<sup>6</sup>The Gaussian functions  $\mathcal{G}(x; \mu, \sigma) = \frac{1}{\sqrt{2\pi}\sigma} \exp - \left( \frac{(x-\mu)^2}{2\sigma^2} \right)$  are normalized to 1 and will be used to implement the models  $\mathcal{M}_i$  describing the different components of the background and the signal. Their means and standard deviations will be either fixed, constrained or free to vary during the fit.

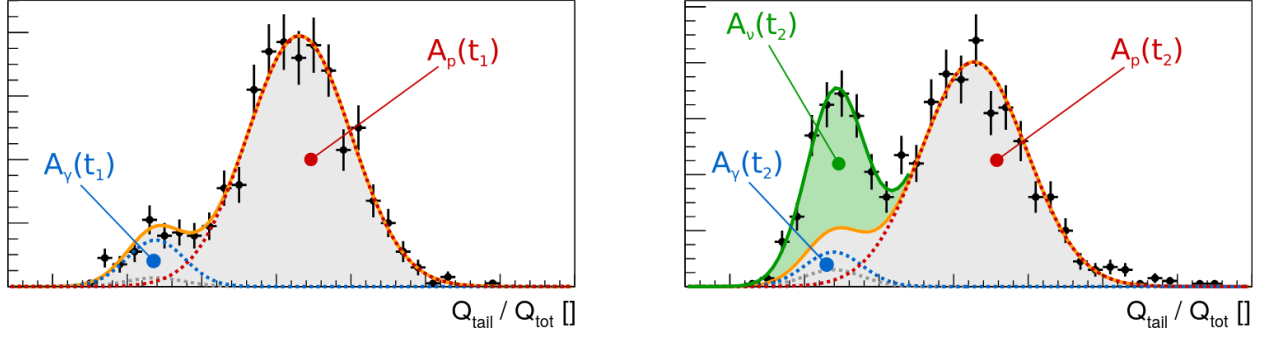


Figure 4.11 – Illustration of the Saclay neutrino rate extraction method starting from the  $Q_{\text{tail}}/Q_{\text{tot}}$  distributions of the Prompt signal. On the left is depicted the reactor-off data, fitted with the model from equation 4.3.2, which allows to model the correlated background (in grey) and to extract the  $\frac{\mathcal{A}_\gamma}{\mathcal{A}_p}$  ratio that will be propagated to the model from equation 4.3.3 in order to fit the reactor-on data, shown on the right. This model has an additional component that models the neutrino signal shown in green.

$$M_{ON}(t, PSD) = \mathcal{A}_p^{ON}(t) \left( \frac{\mathcal{A}_\gamma^{OFF}(t)}{\mathcal{A}_p^{OFF}(t)} \mathcal{M}_\gamma(t, PSD) + \mathcal{M}_p(t, PSD) \right) + \mathcal{A}_\nu(t) \mathcal{M}_\nu(t, PSD) \quad (4.3.3)$$

where  $\mathcal{A}_\nu$  and  $\mathcal{M}_\nu$  are the norm and probability density function of the neutrino component, which is added to the correlated background component to obtain the model describing the reactor-on PSD distributions. The principle of the method is illustrated in figure 4.11.

### Background and neutrino models

In the subsequent paragraphs we will briefly present the functions used to model the probability density functions  $\mathcal{M}_i$  of the different components from equations 4.3.2 and 4.3.3.

For the first phase I analysis, whose results are presented in [107], the model of background consisted of a sum of three Gaussian functions:

1.  $\mathcal{M}_{\text{acc}}(t) = \mathcal{G}(\mu_\gamma(t), \sigma_\gamma(t))$ , which describes the accidental pairs component and whose mean  $\mu_\gamma$  and standard deviation  $\sigma_\gamma$  are fixed on those of the singles. This is an approximation and it is not very precise at low energy, probably because the vertex distributions of the two classes of events are not identical [29]. However, it has been verified that the integrals obtained using this simple model agreed with the real accidental rates.

2.  $\mathcal{M}_\gamma(t) = \mathcal{G}(\mu_\gamma(t), \sigma_\gamma(t))$ , which describes the correlated electronic recoils component of the background and whose mean  $\mu_\gamma$  and standard deviation  $\sigma_\gamma$  are also fixed on those of the singles.
3.  $\mathcal{M}_p(t) = \mathcal{G}(\mu_p(t), \sigma_p(t))$ , which describes the correlated proton recoils component of the background and whose mean  $\mu_p$  and standard deviation  $\sigma_p$  are free parameters that are directly determined from the fit, which represents an advantage with respect to the brute subtraction method that didn't allow to track the  $\mu_p$  variations.

To fit the reactor-on PSD distributions, an additional Gaussian function allowing to fit the neutrino signal was added

$$\mathcal{M}_\nu(t) = \mathcal{G}(\mu_\gamma(t) + \Delta\mu_\nu \cdot \sigma_\gamma(t), \Delta\sigma_\nu \cdot \sigma_\gamma(t)) \quad (4.3.4)$$

where  $\Delta\mu_\nu = (\mu_\nu - \mu_\gamma)/\sigma_\gamma$  and  $\Delta\sigma_\nu = \sigma_\nu/\sigma_\gamma$  are parameters that allow the mean and standard deviation of the neutrino Gaussian to deviate from the ones characterizing the single events. They are common for all cells and energy bins and were determined using phase I data [29]. Their values are allowed to vary within their uncertainties, as it will be shown later in this section when the likelihood of the fit will be presented.

The higher statistics of phase II imposed two main modifications to the background model. Firstly, one should account for the fact that the correlated electronic recoils component of the background can deviate from the single events distribution, which is mainly composed of gammas. This is principally due to the fact that in the 5-6 MeV region, part of the Prompt signals are not of a purely electromagnetic origin, being composed of the coincident detection of neutron-induced proton recoils and a 4.4 MeV gamma ray created in a  $^{12}\text{C}(n,n'\gamma)^{12}\text{C}$  reaction, as it has been explained in section 4.2.2. Thus, the

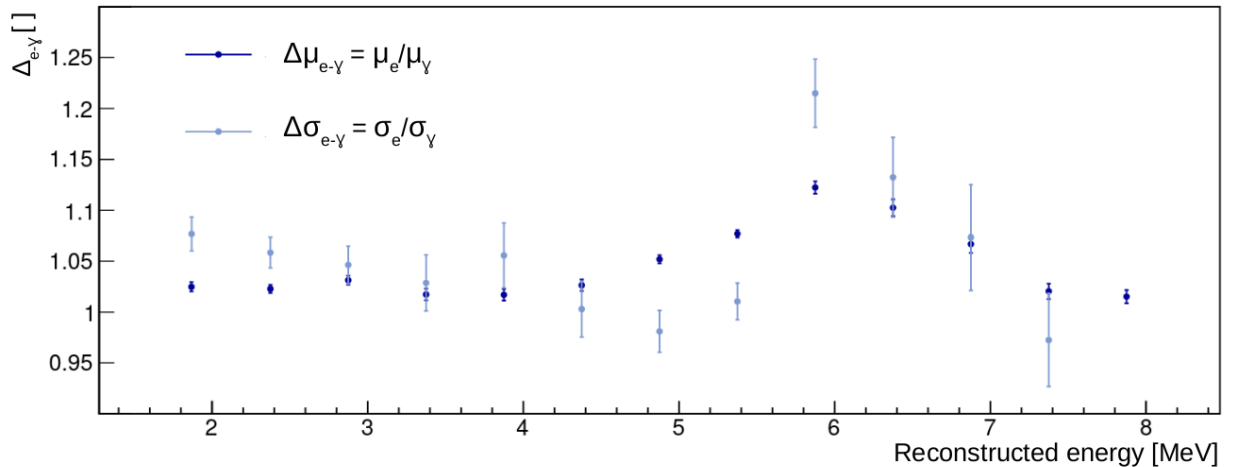


Figure 4.12 – Mean and standard deviation departures from the ones determined from the single events sample, obtained using data from the reactor-off periods of phase II. For every energy, the values are averaged over the six Target cells. Source: [29],[108].

new function describing the electronic recoils component introduces an energy dependent deviation with respect to the mean and standard deviation of the single events

$$\mathcal{M}_\gamma(t) = \mathcal{G}(\Delta\mu_{e-\gamma} \cdot \mu_\gamma(t), \Delta\sigma_{e-\gamma} \cdot \sigma_\gamma(t)) \quad (4.3.5)$$

where  $\Delta\mu_{e-\gamma} = \mu_e/\mu_{\text{gamma}}$  and  $\Delta\sigma_{e-\gamma} = \sigma_e/\sigma_{\text{gamma}}$  are the mean and standard deviation departures from the ones determined from the single events sample. They are energy dependent and obtained from the reactor-off data as a mean over the six Target cells, as shown in figure 4.12. A deviation of  $\sim 15\%$  is present in the 5-6 MeV region, both for the mean and the standard deviation, as expected from the contamination with a proton recoil inducing neutron issued from the  $^{12}\text{C}(n,n'\gamma)^{12}\text{C}$  reactions. The time dependence is taken into account by the anchoring of the mean and standard deviation for the correlated electronic recoils component of the background on the singles events, as it is also the case for the neutrino model from equation 4.3.4.

A second observation made possible by the higher statistics was that the proton recoils component of the correlated background presents a shoulder-like feature<sup>7</sup> at high  $Q_{\text{tail}}/Q_{\text{tot}}$ , which becomes important for energies higher than 3 MeV. This additional component, first observed during the internship that preceded this thesis [108], is again modeled with a Gaussian, but, in order to avoid introducing new parameters into the fit, its parameters are constrained with respect to the main component of the proton recoils population. Thus, the new function describing the proton recoils component has the following form

$$\mathcal{M}_p(t) = \frac{1}{1+a_p} \mathcal{G}(\mu_p^1(t), \sigma_p^1(t)) + \frac{a_p}{1+a_p} \mathcal{G}(m_p \cdot \mu_p^1(t), s_p \cdot \sigma_p^1(t)) \quad (4.3.6)$$

where  $a_p = \mathcal{A}_p^2/\mathcal{A}_p^1$ ,  $m_p = \mu_p^2/\mu_p^1$  and  $s_p = \sigma_p^2/\sigma_p^1$  are the integral, mean and standard deviation ratios between the shoulder component at high  $Q_{\text{tail}}/Q_{\text{tot}}$  and the main component of the proton recoils population, and  $\mathcal{A}_p^1 + \mathcal{A}_p^2 = \mathcal{A}_p$ , the total integral of the proton recoils component appearing in equations 4.3.2 and 4.3.3. They are energy dependent and obtained from the reactor-off data as a mean over the six Target cells, as shown in figure 4.13. At low energy, the two components of the proton recoils population are degenerated ( $m_p \sim s_p \sim 1$ ), thus not shown in the figure, and the simple model using only a Gaussian to describe the proton recoils population is sufficient for the two first energy bins (1.675 MeV and 2.375 MeV).

---

<sup>7</sup>Multiple studies have been performed to assess the origin of this component, but no clear conclusion could be drawn. One hypothesis is that it could be due to multiple low energy neutron interactions, whose characteristic  $Q_{\text{tail}}/Q_{\text{tot}}$  is high, registered during the same event.

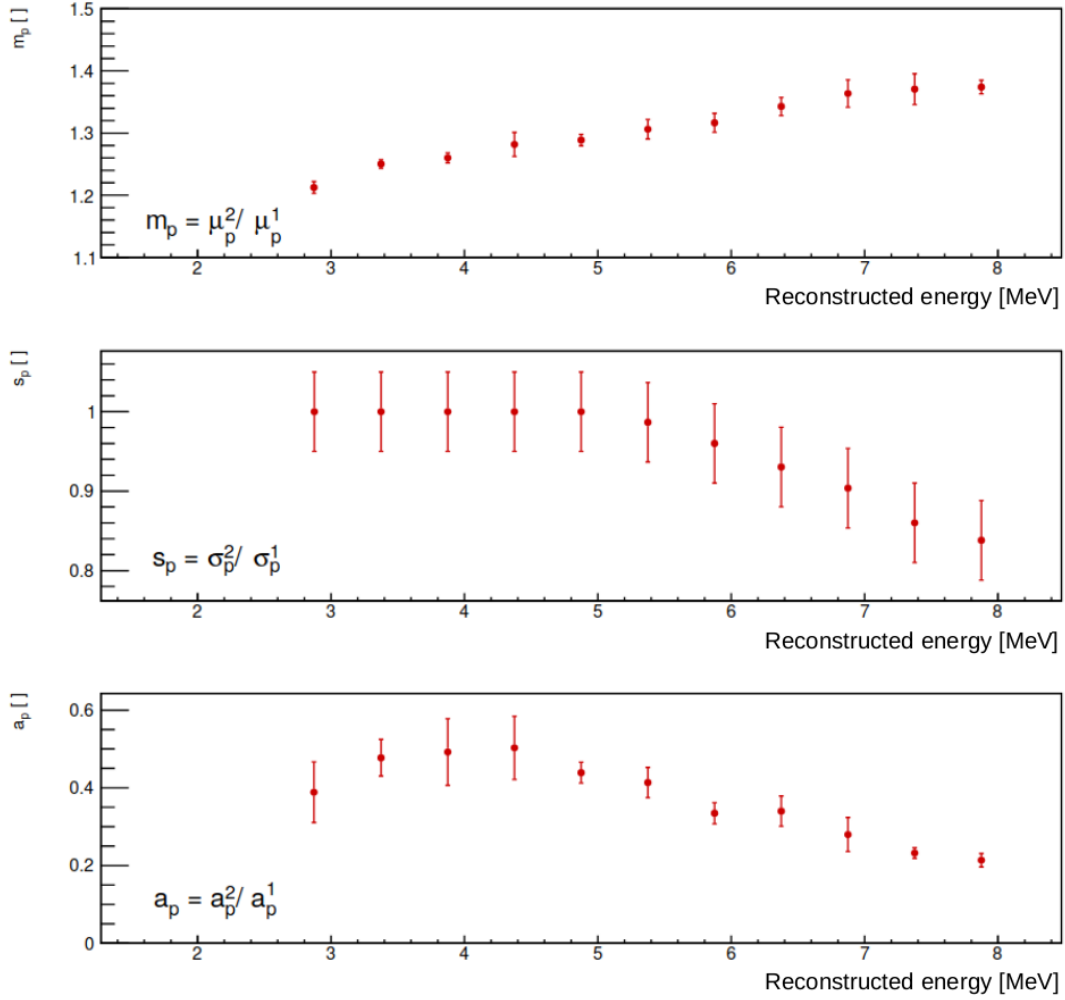


Figure 4.13 – Mean, standard deviation and integral ratios between the shoulder component at high  $Q_{\text{tail}}/Q_{\text{tot}}$  and the main component of the proton recoils population, obtained using data from the reactor-off periods of phase II. For every energy, the values are averaged over the six Target cells. At low energy, the two components of the proton recoils population are degenerated ( $m_p \sim s_p \sim 1$ ) and thus the simple model using only a Gaussian to describe the proton recoils population is sufficient for the two first energy bins (1.675 MeV and 2.375 MeV). The increasing tendency of  $m_p$  is explained by the fact that  $\mu_p^1$  decreases more rapidly than  $\mu_p^2$  over the whole energy range, resulting in an increasing separation of the two components with the energy. Source: [29],[108].

### Fitting procedure

The fitting procedure consists of two steps. Firstly, the reactor-off data is fitted in order to extract the  $\mathcal{A}_\gamma/\mathcal{A}_p$  ratio. Secondly, the extracted ratio is propagated to the model used to fit the reactor-on data and the neutrino rates are extracted.

The  $\mathcal{A}_\gamma/\mathcal{A}_p$  ratio has a specific value for every cell and energy bin but is supposed to be constant over time. This is justified by the compatible correlation between the electronic recoils and the proton recoils rates with the atmospheric pressure, as it was shown in figure 4.7, which proves that the two population rates vary similarly with the pressure. Furthermore, this was confirmed by comparing the  $\mathcal{A}_\gamma/\mathcal{A}_p$  value obtained from the summed PSD distribution of all the reactor-off data from phase I, with the fit by a zeroth-order polynomial of the  $\mathcal{A}_\gamma/\mathcal{A}_p$  values extracted from the division in 14 days bins of the same reactor-off data from phase I, which proved that the two extracted values were compatible within the uncertainties [29].

The accidental coincidences distribution, obtained using the delayed-gates method illustrated in section 4.1.5, and the correlated pairs distribution are fitted simultaneously. We chose not to directly subtract the accidental contribution from the correlated pairs distribution, since the reduced statistics available in each time bin used for the analysis of phase I data could lead to having unphysical negative values for some  $Q_{\text{tail}}/Q_{\text{tot}}$  bins. Thus, the fitting function for the correlated pairs distribution  $f_{\text{corr+acc}}(\text{PSD})$  is the sum of one of the models from equations 4.3.2 or 4.3.3 and the accidental contribution, which is constrained by the fit of the delayed-gates distribution,  $f_{\text{acc}}(\text{PSD})$ . As an example, for the reactor-on fit of a PSD distribution corresponding to a given cell, energy bin and time bin, we have

$$f_{\text{corr+acc}}(q) = P \cdot \left[ [\mathcal{A}_{\text{acc}}] \cdot \mathcal{M}_{\text{acc}}(q) + [\mathcal{A}_p] \cdot \left( \left[ \frac{\mathcal{A}_\gamma}{\mathcal{A}_p} \right] \cdot \mathcal{M}_\gamma(q) + \mathcal{M}_p(q) \right) + [\mathcal{A}_\nu] \cdot \mathcal{M}_\nu(q) \right]$$

$$f_{\text{acc}}(q) = (P/F_{\text{acc}}) \cdot [\mathcal{A}_{\text{acc}}] \cdot \mathcal{M}_{\text{acc}}(q) \quad (4.3.7)$$

where  $q = Q_{\text{tail}}/Q_{\text{tot}}$ ,  $P = T_{\text{eff}} \cdot b$  is a factor that allows the extraction of the relevant parameters (between square brackets) directly in number of events/day, with  $T_{\text{eff}}$  being the effective duration of the considered time bin and  $b$  the width of a  $Q_{\text{tail}}/Q_{\text{tot}}$  interval. The  $F_{\text{acc}}$  factor is needed to normalize the accidental distribution, which, as explained in 4.1.5, is obtained by shifting by 1 ms each valid Prompt event a number of 100 times.

Finally, the minimisation of the negative logarithm of a global likelihood function allows to simultaneously fit the PSD distributions of the accidental coincidences and of the correlated coincidences for the reactor-off and reactor-on data with the model from equation 4.3.7 and thus extract the parameters of interest

$$- \ln(\mathcal{L}_{\text{global}}) = -\ln(\mathcal{L}_{\text{acc}}) - \ln(\mathcal{L}_{\text{corr+acc}}) + \prod_i \frac{(p_i - p_i^0)^2}{2\sigma_i^2} \quad (4.3.8)$$

where  $\ln(\mathcal{L}_{acc})$  is the logarithm of the likelihood of the accidental distribution model and  $\ln(\mathcal{L}_{corr+acc})$  is the logarithm of the likelihood of the correlated distribution model (which includes the accidental coincidences). The third term reflects the implementation of the so called "pull-terms" [109], whose interest is threefold. Firstly, it helps implement external constraints on the fit parameters (for example, the constraints on the deviations of the electronic recoils component Gaussian with respect to the singles, see figure 4.12), while allowing for variations within the uncertainties of these constraints. Secondly, it helps the fit converge, and, thirdly, it propagates the uncertainties of the constraint parameters to the final results of the fit. One should note that we supposed that the constrained parameters follow a normal distribution centered on  $p_i^0$  and with standard deviation  $\sigma_i$ .

A fit example using the Saclay method is illustrated in figure 4.14 for a given cell, energy bin and time bin. The width of the energy bins used in the analysis is 500 keV. To obtain the neutrino rate for a given cell and energy bin, the neutrino rates  $\mathcal{A}_\nu$  obtained in the different time bins are fitted with a zeroth-order polynomial.

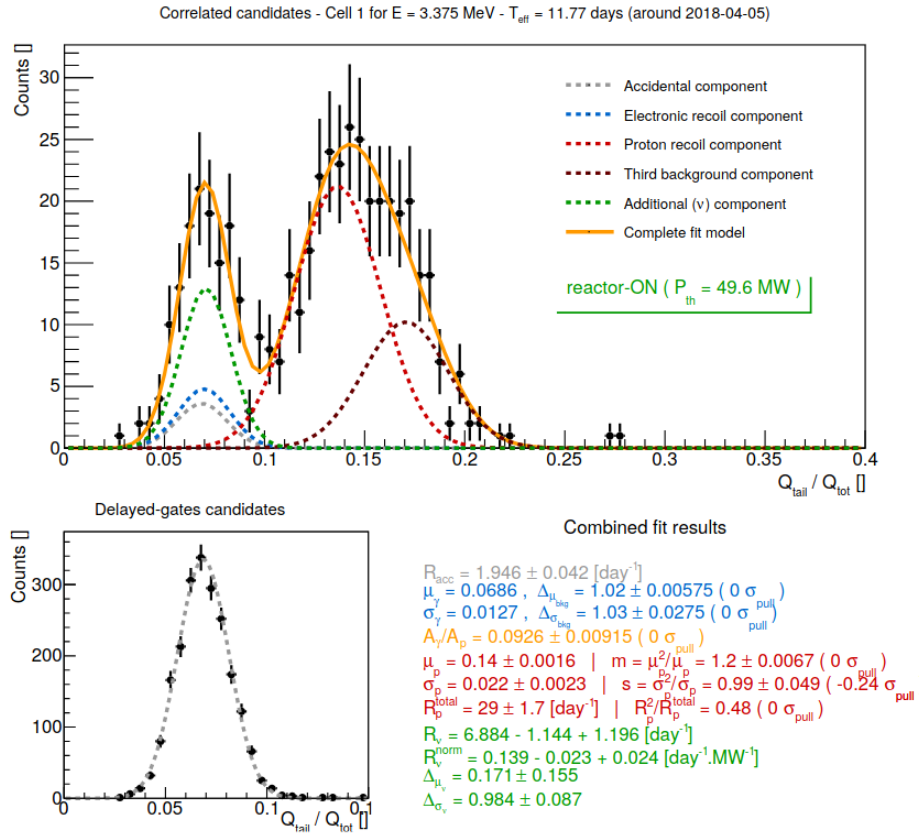


Figure 4.14 – Example of combined fit performed to extract the antineutrino rate for the energy bin centered on 3.375 MeV of cell 1 for a time bin with  $T_{eff} = 11.77$  days, using data from phase II. The five Gaussian components of the complete model (orange) are plotted with dotted lines: neutrino (green), accidental component (grey), electronic recoils component (blue), main proton recoils component (red) and second -shoulder-proton recoils component (burgundy). Source: [29].



### 4.3.2 The LPSC method

The LPSC method made use of the increased statistics of phase II and of the stability of the light leaks after the separating walls between the cells were repaired in order to cumulate together all the data and get rid of the separation in time bins. This was made easier after the PSD dependence on the temperature of the liquid was corrected, as explained in section 4.2.3. The idea of this method is to directly use the form of the PSD distribution of the correlated background measured during the reactor-off periods as a model for the correlated background measured during the reactor-on periods. Again, this is based on the form stability of the PSD distribution of correlated background between reactor-off and reactor-on periods, which was proven reliable in section 4.2.3.

Considering a given cell and energy bin, we denote the PSD distributions of IBD candidates for reactor-off and reactor-on periods by  $OFF_i$  and  $ON_i$ , where  $i$  runs over the  $Q_{\text{tail}}/Q_{\text{tot}}$  bins. The corresponding PSD distributions of accidental coincidences are denoted by  $OFF_i^{\text{acc}}$  and  $ON_i^{\text{acc}}$ .

The accidental coincidences are simply modeled by a set of free parameters running over all the PSD bins, designated by  $m_i^{\text{acc},OFF}$  and  $m_i^{\text{acc},ON}$  and weighted by the correction factors  $f^{\text{acc},OFF}$  and  $f^{\text{acc},ON}$ , that take into account the number of time shifts used in the accidental extraction method (which is similar to the method presented in 4.1.5 and used by the Saclay extraction method, but was developed independently).

The OFF model  $\mathcal{M}_i^{OFF}$  is composed of the sum between a free parameter representing the correlated background  $m_i^{OFF}$  and the weighted free parameter describing the reactor-off accidental coincidences  $m_i^{\text{acc},OFF}$

$$\mathcal{M}_i^{OFF} = m_i^{OFF} + f^{\text{acc},OFF} m_i^{\text{acc},OFF} \quad (4.3.9)$$

Concerning the ON model,  $\mathcal{M}_i^{ON}$ , besides the correlated background parameter  $m_i^{OFF}$  and the accidental coincidences parameter  $m_i^{\text{acc},ON}$ , a Gaussian describing the neutrino component is added:  $\mathcal{M}_i^\nu = \mathcal{A}_\nu \mathcal{G}_i(\mu_\nu, \sigma_\nu)$ , where  $\mathcal{G}_i$  is a normalized Gaussian and  $\mathcal{A}_\nu$  is the rate of antineutrinos. Moreover, to take into account the possible variations of the rates of electronic recoils and proton recoils, composing the correlated background, with the atmospheric pressure and water pool level, a normalization factor  $a$ , that could also compensate potential imperfections of the dead-time correction, is added to the ON model

$$\mathcal{M}_i^{ON} = a m_i^{OFF} + f^{\text{acc},ON} m_i^{\text{acc},ON} + \mathcal{A}_\nu \mathcal{G}_i(\mu_\nu, \sigma_\nu) \quad (4.3.10)$$

Finally, the parameters  $m_i^{\text{acc},OFF}$ ,  $m_i^{\text{acc},ON}$ ,  $m_i^{OFF}$ ,  $a$ ,  $\mu_\nu$ ,  $\sigma_\nu$  and  $\mathcal{A}_\nu$  are fitted by minimizing the following  $\chi^2$  function<sup>8</sup>

<sup>8</sup>In practice, a minimization of the negative logarithm of the likelihood is implemented to take into account the PSD bins with low statistics and a Poisson distribution of the counts is used

$$-\ln(\mathcal{L}) = -\ln(\mathcal{L}(ON_i)) - \ln(\mathcal{L}(OFF_i)) - \ln(\mathcal{L}(ON_i^{\text{acc}})) - \ln(\mathcal{L}(OFF_i^{\text{acc}})) \quad (4.3.11)$$

$$\begin{aligned}
\chi^2 = \sum_i \left( \frac{ON_i - (am_i^{OFF} + f^{acc,ON} m_i^{acc,ON} + \mathcal{A}_\nu \mathcal{G}_i(\mu_\nu, \sigma_\nu))}{\sigma_i^{ON}} \right)^2 \\
+ \left( \frac{OFF_i - (m_i^{OFF} + f^{acc,OFF} m_i^{acc,OFF})}{\sigma_i^{OFF}} \right)^2 \\
+ \left( \frac{OFF_i^{acc} - m_i^{acc,OFF}}{\sigma_i^{acc,OFF}} \right)^2 \\
+ \left( \frac{ON_i^{acc} - m_i^{acc,ON}}{\sigma_i^{acc,ON}} \right)^2
\end{aligned} \tag{4.3.12}$$

which makes apparent the fact that the correlated background model  $m_i^{OFF}$  is the same for the reactor-off and reactor-on PSD distributions. Figure 4.15 shows a fit example.

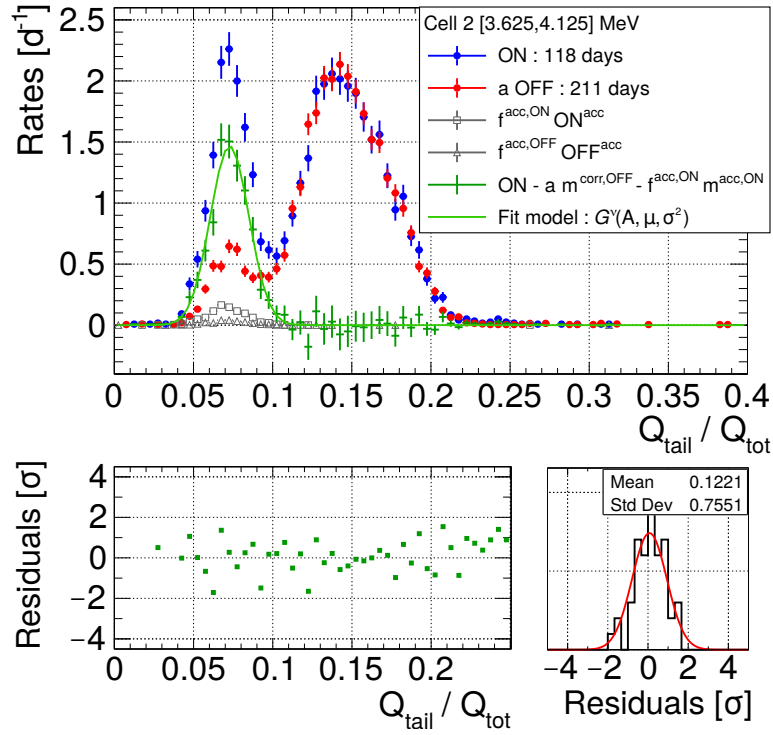


Figure 4.15 – Top: example of fit performed to extract the antineutrino rate for the energy bin centered on 3.875 MeV of cell 2 for the whole reactor-on data of phase II. The correlated background model was constrained using 211 days of reactor-off data. The shown PSD distribution for the correlated background (red) is scaled with the parameter  $a$ . The green points are obtained as a difference between the  $ON_i$  PSD distribution and the sum of the models for the ON accidentals  $f^{acc,ON} m_i^{acc,ON}$  and the OFF distribution  $am_i^{OFF}$ . They are fitted by a Gaussian function  $\mathcal{A}_\nu \mathcal{G}_i(\mu_\nu, \sigma_\nu)$  to extract the antineutrino rate. Bottom: residuals of the fit model  $\mathcal{A}_\nu \mathcal{G}_i(\mu_\nu, \sigma_\nu)$  relative to the uncertainties of each data point. Source: [77].

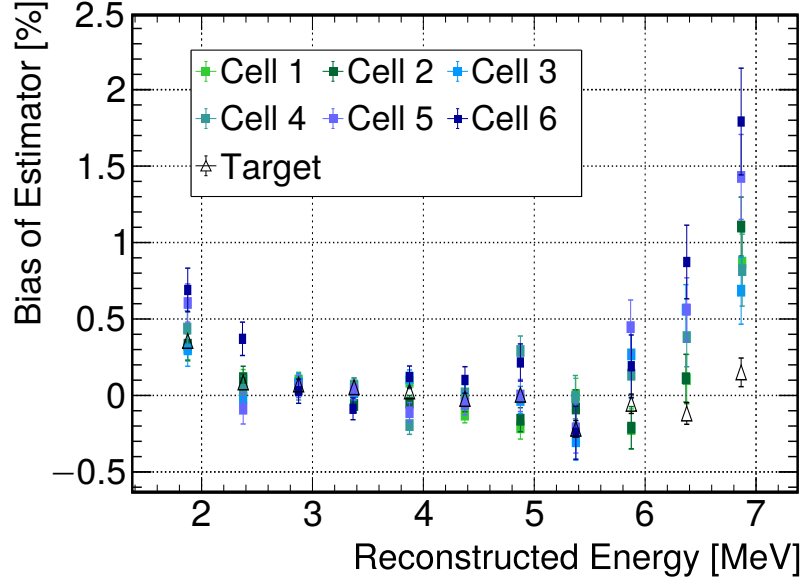


Figure 4.16 – Bias of the likelihood estimator of the antineutrino rates for every cell and energy bin used in the analysis, obtained with statistics characteristic of phase II. Also shown is the bias obtained for the summed spectrum (Target spectrum), for which the PSD distributions of the six cells are summed before the fit. Source: [77].

### Bias of the likelihood estimator

It is known that in the low statistics regime, the maximum likelihood estimator is biased. For the extracted rate of antineutrinos, this bias writes [110]

$$\text{bias}(\mathcal{A}_\nu) \propto \frac{k}{\mathcal{A}_\nu} + \mathcal{O}\left(\frac{1}{\mathcal{A}_\nu^2}\right) \quad (4.3.13)$$

where  $k$  is a constant that depends on the form of the likelihood function. These biases are estimated by performing simulations that reproduce the fitting procedure and include all the relevant experimental conditions (IBD rates, signal-over-background ratios, background shape, etc.). For a given pseudoexperiment, designed to compute the bias for a given cell and energy bin, the bias is defined as

$$b_{c_i, E_j} = \frac{\mathcal{A}_\nu^{\text{fit}} - \mathcal{A}_\nu^{\text{generated}}}{\mathcal{A}_\nu^{\text{generated}}} \quad (4.3.14)$$

where  $\mathcal{A}_\nu^{\text{generated}}$  is the number of generated antineutrinos and  $\mathcal{A}_\nu^{\text{fit}}$  is the number of fitted antineutrinos. A number of 5000 pseudoexperiments are performed for every cell and energy bin, for which the bias  $b_{c_i, E_j}$  value is distributed following a normal law. The mean position of the normal law is then extracted and shown in figure 4.16. It can be seen that the magnitude of the bias is inferior to 1% below 6.5 MeV and it reaches values up to 2% in the last energy bin, where the signal-over-background ratio becomes smaller.

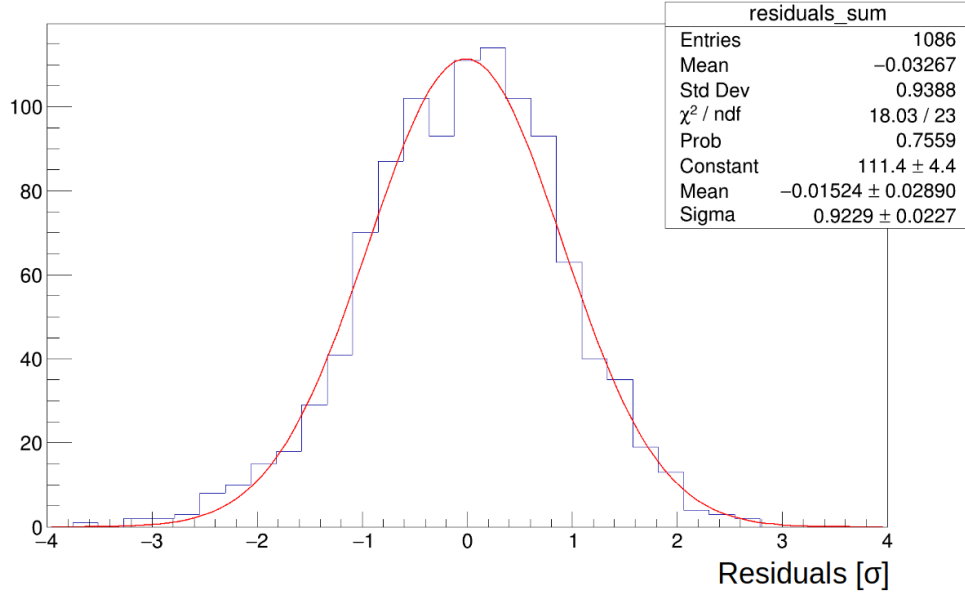


Figure 4.17 – Residuals distribution obtained by summing the residuals distributions for all the cells and energy bins from phase II. In red is shown a Gaussian fit of the residuals distribution.

Finally, this bias is corrected during the extraction of the antineutrino rates.

#### Bias due to the Gaussian model for the antineutrino signal

This section aims to evaluate the bias induced by the Gaussian-form hypothesis on the neutrino signal. In order to do so, we first computed the means of the residuals distributions (see bottom part of figure 4.15) by fitting them with a Gaussian for every cell and energy bin of phase II. Since all the extracted means were compatible with zero, we summed up the residuals distributions for all the cells and energy bins together and we fitted again with a Gaussian to extract the mean and standard deviation, as shown in figure 4.17. We found that the fitted mean of the summed residuals distribution,  $\mu = -0.015 \pm 0.029$ , is compatible with zero, while the fitted standard deviation,  $\sigma = 0.923 \pm 0.023$ , is not compatible with zero. This could point out that the uncertainties on the neutrino histograms are slightly underestimated.

## 4.4 Comparison between the LPSC and Saclay methods

The LPSC method presented in the previous section is the official method used to extract the antineutrino rates. Furthermore, it has also been used to re-analyse the phase I data that was initially analysed using the Saclay method. However, having two distinct

methods allowing to extract the antineutrino rates is useful for performing cross-checks. This section will first present a modified and improved version of the Saclay method, adapted to be compared with the results obtained with the LPSC method for phase II data. Then, the comparison in norm and form between the results obtained with the two methods will be presented and a systematic uncertainty on the total antineutrino rate will be derived. The results presented in this section were an important part of the work done during this thesis.

#### 4.4.1 Modified Saclay method

The Saclay extraction method needs to be adapted in order to make possible its comparison with the LPSC method. Firstly, we need to gather all the phase II data into one reactor-off bin and one reactor-on bin. Secondly, we need to use the same correlated background model for the reactor-off and reactor-on PSD distributions, allowing only for a different normalization parameter. An additional improvement consists in the treatment of the accidental coincidences distributions, which are no longer fitted with a Gaussian fixed on the single events mean and standard deviation. Instead, we use free parameters that allow to independently fit every  $Q_{\text{tail}}/Q_{\text{tot}}$  bin. Finally, the ON and OFF PSD distributions of correlated background and accidental coincidences are fitted simultaneously, thus eliminating the need to first fit the reactor-off data in order to extract the  $\frac{\mathcal{A}_\gamma}{\mathcal{A}_p}$  parameter and then to propagate it to the reactor-on data as a constraint in the fit.

Using the same notations as those used in section 4.3.1 for equation 4.3.7, the fitting functions for the correlated pairs distribution and the accidental distribution for reactor-off and reactor-on data are

$$\begin{aligned}
 f_{\text{corr+acc}}^{\text{OFF}}(q) &= P \cdot \left[ [p_q^{\text{OFF}}] + [\mathcal{A}_p] \cdot \left( \left[ \frac{\mathcal{A}_\gamma}{\mathcal{A}_p} \right] \cdot \mathcal{M}_\gamma(q) + \mathcal{M}_p(q) \right) \right] \\
 f_{\text{acc}}^{\text{OFF}}(q) &= (P/F_{\text{acc}}) \cdot [p_q^{\text{OFF}}] \\
 f_{\text{corr+acc}}^{\text{ON}}(q) &= P \cdot \left[ [p_q^{\text{ON}}] + [\mathcal{A}_p] \cdot \left( \left[ \frac{\mathcal{A}_\gamma}{\mathcal{A}_p} \right] \cdot \mathcal{M}_\gamma(q) + \mathcal{M}_p(q) \right) + [\mathcal{A}_\nu] \cdot \mathcal{M}_\nu(q) \right] \\
 f_{\text{acc}}^{\text{ON}}(q) &= (P/F_{\text{acc}}) \cdot [p_q^{\text{ON}}]
 \end{aligned} \tag{4.4.1}$$

where the free parameters  $[p_q^{\text{OFF}}]$  and  $[p_q^{\text{ON}}]$  have replaced the previously used Gaussian function for the description of the accidental PSD distributions. The corresponding common negative logarithm of likelihood to minimize for the simultaneous fit of the PSD distributions of IBD candidates,  $\text{OFF}_i$  and  $\text{ON}_i$ , and of accidental coincidences,  $\text{OFF}_i^{\text{acc}}$  and  $\text{ON}_i^{\text{acc}}$ , has the following form

$$-ln(\mathcal{L}_{global}) = -ln(\mathcal{L}_{acc}^{OFF}) - ln(\mathcal{L}_{corr+acc}^{OFF}) - ln(\mathcal{L}_{acc}^{ON}) - ln(\mathcal{L}_{corr+acc}^{ON}) + \prod_i \frac{(p_i - p_i^0)^2}{2\sigma_i^2} \quad (4.4.2)$$

where the fact that we simultaneously fit the four PSD distributions is made apparent. We consider that the number of events in each  $Q_{tail}/Q_{tot}$  bin follows a Poisson distribution. Thus, as an example, the likelihood for the PSD distribution of IBD candidates during a reactor-on period is written as

$$\mathcal{L}_{corr+acc}^{ON} = \sum_q e^{-f_{corr+acc}^{ON}(q)} \frac{(f_{corr+acc}^{ON}(q))^{OFFq}}{OFFq!} \quad (4.4.3)$$

where  $q$  runs over the  $Q_{tail}/Q_{tot}$  bins.

In order to compare the Saclay method with the LPSC one, all the Gaussian parameters need to be common between the simultaneously fitted reactor-off and reactor-on fit functions for the PSD distributions of IBD candidates, with the exception of  $[\mathcal{A}_p]$ , the total rate of proton recoils, which is allowed to vary to account for the different environmental conditions. However, before performing the fits in this way, we needed to check the compatibility between the reactor-off and reactor-on Gaussian parameters. To do so, we only imposed two common parameters,  $\frac{A_\gamma}{A_p}$  and  $a_p$  and we checked the relative difference between the fitted means and standard deviations of the different Gaussians for OFF and ON data. We found that for most of the cells and energy bins, the compared values are within one standard deviation between one another, which confirmed that we could perform the simultaneous fit with only  $[\mathcal{A}_p]$  allowed to vary, thus allowing the comparison with LPSC results.

Before going to the comparison itself, we first verified that the PSD distributions of IBD candidates obtained with the two different pair search algorithms for the phase II data were compatible within the uncertainties and that the total acquisition times were compatible at 0.1% level. This guarantees that we are fitting the same PSD distributions and thus the possible differences in the results obtained with the Saclay and LPSC methods only come from the fitting procedure. We also performed several pseudoexperiments in order to estimate the possible bias on the extracted antineutrino rates, which will be presented in the next paragraphs.

### Bias on the extracted neutrino rates

This section aims at estimating the bias on the extracted neutrino rates due to the multi-Gaussian model itself and also due to the PSD peak variation with the height.

First, to estimate the bias on the neutrino rates due to the multi-Gaussian model used to model the different components of the PSD distributions of IBD candidates, we

performed pseudoexperiments with the following principle, illustrated for a given cell and energy bin

1. We draw the number of background events  $N_{bck}$ , the number of accidental events  $N_{acc}$  and the number of antineutrino events  $N_\nu$  for both reactor-off and reactor-on PSD distributions from Gaussians centered on their respective values given by the fit of the phase II data.
2. We generate the PSD distributions of IBD candidates and of accidentals by generating the respective number of events drawn earlier following the different Gaussian fits of the different PSD distributions for a specific cell and energy bin.
3. We fit the obtained PSD distributions in the same way in which we fitted the data in order to extract the antineutrino rate.
4. We perform N pseudoexperiments for each cell and energy bin and compute the relative bias on the extracted number of antineutrinos as

$$b^{rel} = \frac{\overline{N}_\nu^{fit} - \overline{N}_\nu^{gen}}{\overline{N}_\nu^{gen}} \quad (4.4.4)$$

where  $\overline{N}_\nu^{fit}$  is the average of the fitted number of antineutrinos over the N pseudoexperiments and  $\overline{N}_\nu^{gen}$  is the average of the generated number of antineutrinos over the N pseudoexperiments. The relative bias obtained for cell 1 for the statistics of phase II data with 1000 pseudoexperiments performed for each energy bin is shown in figure 4.18. It can be observed that the bias is approximately constant up to the last energy bin used in the analysis (centered on 6.875 MeV), and has a mean value of  $\sim 0.3\%$ . This results in an overestimation of the neutrino rates, that can be corrected for. The behaviour for the other cells is similar to the one shown for cell 1.

Another observed effect was the fact that the PSD distributions obtained for the  $^{54}\text{Mn}$  source placed inside the calibration tubes were not perfectly described by Gaussian functions. The closest one to a Gaussian was found to be the one obtained with the  $^{54}\text{Mn}$  source placed at  $z=45$  cm inside the calibration tube, as expected. However, the bias on the integral of the distribution induced by fitting with a Gaussian was found to be smaller than  $0.4\%$ , with the biggest difference observed for the source placed at  $z=80$  cm.

Moreover, the position of the peak of the PSD distribution was found to vary with the position of the source along the  $z$ -axis, as shown in figure 4.19. This leads us to performing pseudoexperiments in order to assess the possible impact of such a variation on the neutrino rates, considering that we use a multi-Gaussian fit function. The principle of the pseudoexperiments is the same as explained earlier, with the difference that we also vary

1. the mean of the neutrino Gaussian distribution from which we draw the PSD of the neutrino events.

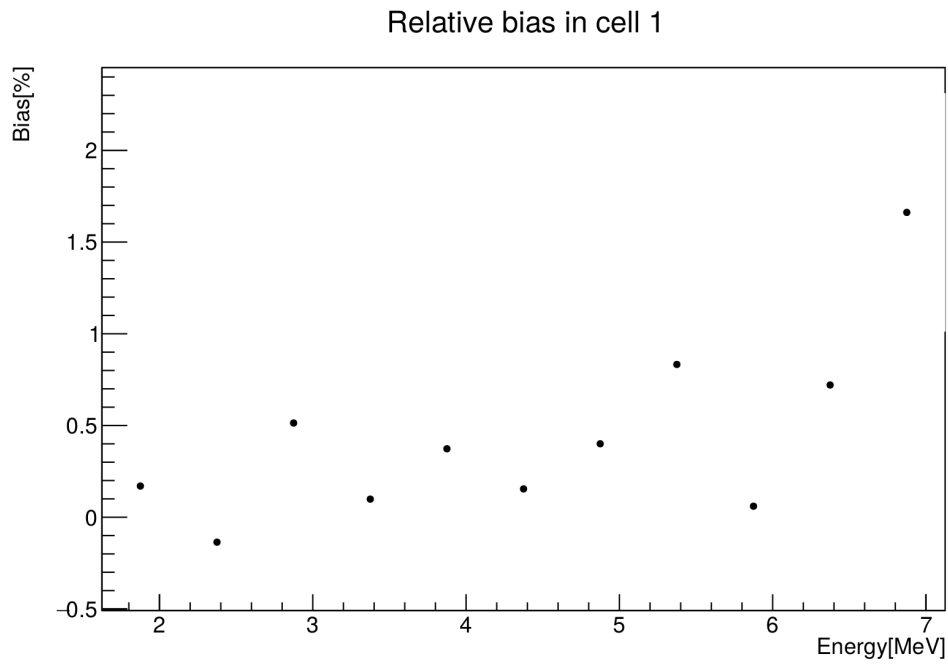


Figure 4.18 – Relative bias on the extracted antineutrino rates found by performing 1000 pseudoexperiments, in which we vary the number of background, accidental and neutrino events around their fitted value, while keeping all the other fitted parameters constant, for each energy bin.

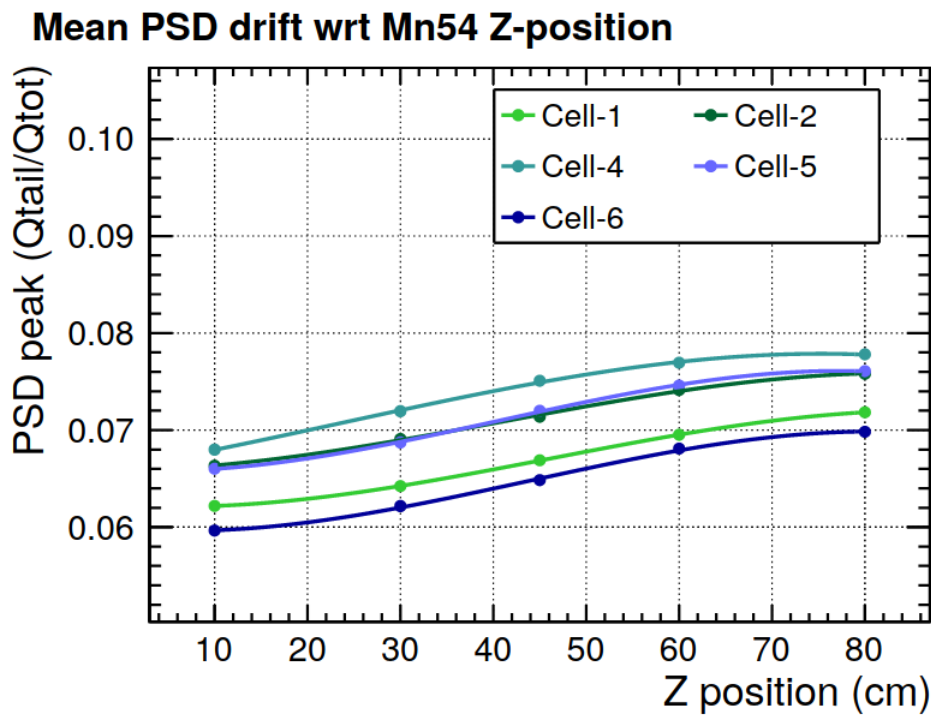


Figure 4.19 – Evolution of the PSD peak position with the position of the  $^{54}\text{Mn}$  source along the z-axis. Source: [92].



2. the mean of the neutrino, electronic recoils and proton recoils Gaussian distributions from which we draw the PSD of the neutrino events.

To vary the mean, we construct a linear model starting from the mean PSD dependence with the  $z$  position for the  $^{54}\text{Mn}$  source (see figure 4.19) and considering that the fitted Gaussian mean given by the fit procedure corresponds to the mean PSD value found when the  $^{54}\text{Mn}$  source is placed at  $z=45$  cm. Then, for a given randomly drawn event (accidental, neutrino or background), we first draw a  $Z$  value representing the  $z$ -axis position of the interaction vertex. Afterwards, we deduce the corresponding mean,  $\mu(z)$ , from the previously defined linear model and finally draw the PSD of the event from the respective Gaussian with mean  $\mu(z)$ . We extended the same procedure for the proton recoils events, supposing that their PSD evolves with  $z$  similarly to the electronic recoil-like PSD of the  $^{54}\text{Mn}$  source.

The biases found by performing 1000 pseudoexperiments for every cell and energy bin and taking into account the  $z$ -dependence of the PSD are shown in figure 4.20, for the two considered scenarios. It can be seen that the bias induced on the neutrino rates is constant and centered on zero below 5 MeV and it becomes more important after 5 MeV. However, since the antineutrino rates expected in the high energy region above 5 MeV are low, the impact of this bias on the total rate is of  $\sim 0.03\%$  when varying only the neutrino mean and of  $\sim 0.05\%$  when varying all the components means. Instead, since the bias is energy dependent, it may have an influence on the shape of the extracted antineutrino spectrum.

All the possible bias sources explored for the Saclay and LPSC methods are found to induce biases which are much smaller than the uncertainty on the neutrino rate due to the limited statistics.

#### 4.4.2 Comparison between the two neutrino extraction methods

After having presented the two different extraction methods and examined their possible biases, we can now compare their respective obtained results. In the first place, we will look at the rates comparison at the level of every energy bin for all the Target cells. We define the relative difference between the rates obtained with the Saclay and LPSC methods as

$$\text{rate difference} = \frac{N_{\nu, \text{Saclay}} - N_{\nu, \text{LPSC}}}{0.5 \cdot (\sigma_{\text{Saclay}} + \sigma_{\text{LPSC}})} \quad (4.4.5)$$

where  $N_{\nu, \text{Saclay}}$  and  $N_{\nu, \text{LPSC}}$  are the neutrino rates obtained with the Saclay and LPSC methods respectively and  $\sigma_{\text{Saclay}}$  and  $\sigma_{\text{LPSC}}$  are the uncertainties on the neutrino rates given by the fit. The uncertainty difference is defined as

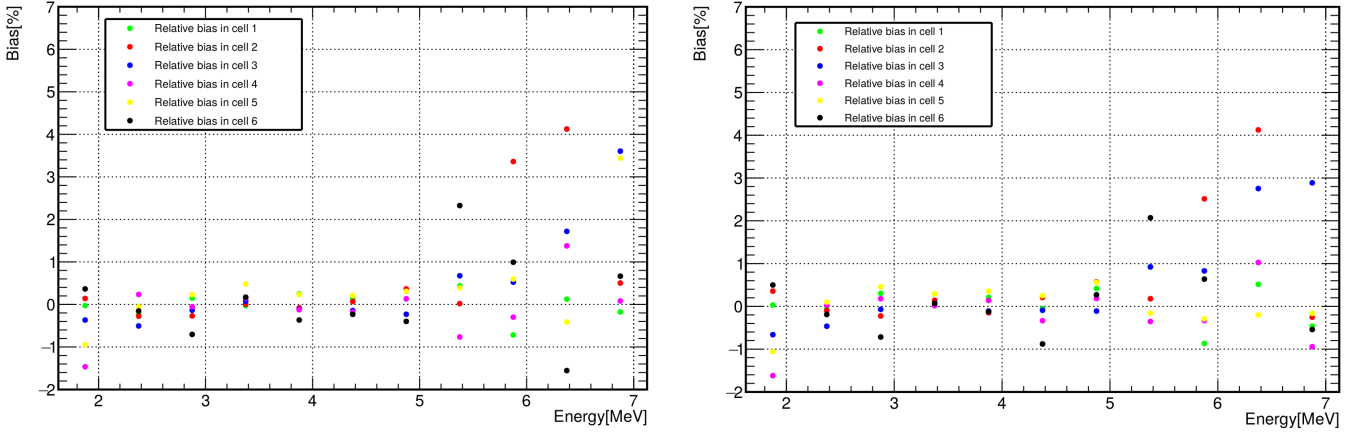


Figure 4.20 – Relative bias on the extracted antineutrino rates found by performing 1000 pseudoexperiments, in which we vary the number of background, accidental and neutrino events around their fitted value and we consider an evolving PSD mean with the interaction vertex along the z-axis. Left: only the mean of the neutrino Gaussian is allowed to vary when generating the PSD distributions. Right: the means of the neutrino, electronic recoils and proton recoils Gaussians are allowed to vary when generating the PSD distributions.

$$\text{uncertainty difference} = \frac{\sigma_{Saclay}}{\sigma_{LPSC}} \quad (4.4.6)$$

The results of the comparison between the two methods are shown in figure 4.21. It can be seen that the Saclay rates are systematically higher than the LPSC rates and that the uncertainties on the neutrino rates are compatible between the two methods.

Concerning the total rate, obtained by summing the rates in every cell for the first 11 energy bins, i.e. for energies in the [1.625,7.125] MeV range, the results obtained with the two methods are

$$\begin{aligned} \mathcal{A}_\nu^{Saclay} &= 367.0 \pm 3.3 \bar{\nu}/day \\ \mathcal{A}_\nu^{LPSC} &= 362.1 \pm 3.3 \bar{\nu}/day \end{aligned} \quad (4.4.7)$$

which is equivalent to a  $1.5 \sigma$  or 1.33% difference in the total rate. One should note that no bias was corrected for when obtaining these results. However, should we correct the biases for each of the two methods, we would obtain a very similar result.

This cross check allowed us to set a systematic uncertainty on the total antineutrino rate, taken to be half of the difference in rate between the two methods, i.e. 0.65%.

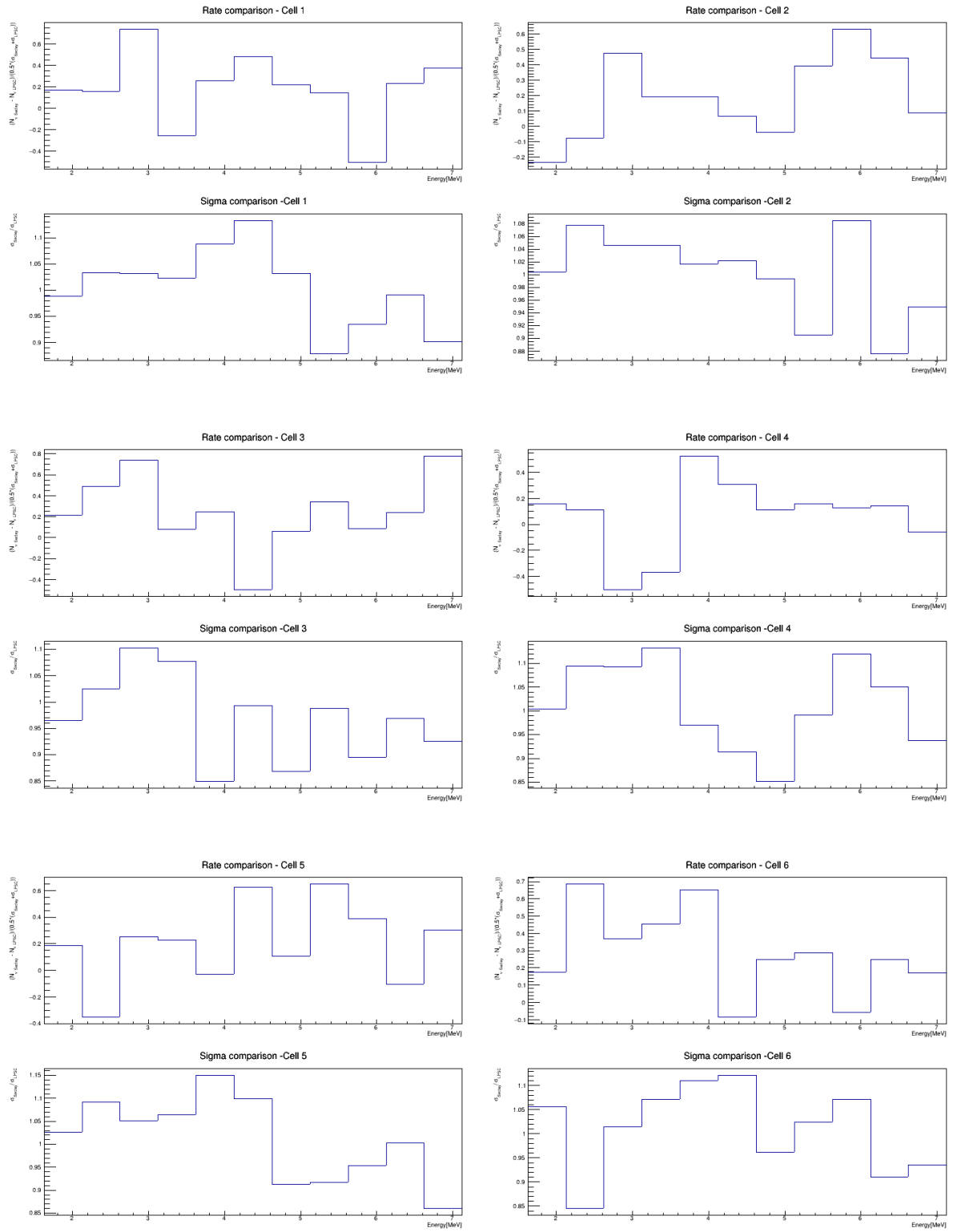


Figure 4.21 – Comparison between the neutrino rates and uncertainties obtained with the two different extraction methods.

## 4.5 Conclusion

This chapter first introduced the cuts used to select the IBD candidates and then discussed the different background sources relevant for the antineutrino extraction. We have seen how the PSD method allows to reject most of the proton recoil inducing events and studied the stability of the background with respect to the environmental conditions. The good shape stability of the background in time allowed us to develop two independent neutrino extraction methods that rely on the PSD distributions of IBD candidates obtained during reactor-off periods as a model of background.

The work presented in this thesis focused on adapting and testing the potential biases of an antineutrino extraction method that makes use of a multi-Gaussian modelization of the reactor-off and reactor-on PSD distributions, in order to render it comparable with the official method employed in the STEREO analysis. The comparison between the two methods allowed us to set a systematic uncertainty of 0.65% on the total antineutrino rate, thus contributing to the accuracy of the measurement.

# Chapter 5

## Stereo results

*"Une théorie ne vaut que ce que valent ses prémisses. Si les prémisses sont erronées, la théorie n'a pas de valeur scientifique réelle. Le seul critère scientifique pour juger de la validité scientifique d'une théorie est en effet sa confrontation avec les données de l'expérience."*

*Maurice Allais*

### Sommaire

---

<b>5.1</b>	<b>Absolute rate . . . . .</b>	<b>144</b>
<b>5.2</b>	<b>Oscillation analysis . . . . .</b>	<b>148</b>
<b>5.3</b>	<b>Unfolded <math>^{235}\text{U}</math> spectrum . . . . .</b>	<b>152</b>
5.3.1	Response matrix . . . . .	152
5.3.2	Systematic uncertainties . . . . .	153
5.3.3	Unfolding procedure . . . . .	155
5.3.4	Unfolded spectrum and bump parameters . . . . .	157
<b>5.4</b>	<b>On the possible origin of the reactor anti-neutrino anomalies</b>	<b>159</b>
5.4.1	The summation method . . . . .	159
5.4.2	An empirical beta strength model . . . . .	162
5.4.3	Comparison with STEREO results . . . . .	167
<b>5.5</b>	<b>Conclusion . . . . .</b>	<b>172</b>

---

This chapter will present the three main results obtained by STEREO, along with an improvement of the summation method aimed at testing if the origin of the reactor antineutrino anomalies comes from an issue with the reference  $^{235}\text{U}$  electron energy spectra. The main goal of STEREO was to test the hypothesis that an oscillation of the reactor  $\bar{\nu}_e$  towards a sterile neutrino could explain the deficit of the absolute measured antineutrino rate with respect to the prediction, i.e. the RAA. The first section will expose the method used to extract the absolute antineutrino rate and how the result obtained by STEREO compares with that of other similar experiments. The oscillation analysis is presented in the second section of the present chapter, along with the exclusion contour in the  $(\Delta m_{14}^2, \sin^2(\theta_{ee}))$  parameter space. The third section is dedicated to the framework applied to obtain the pure  $^{235}\text{U}$  unfolded antineutrino spectrum. This measurement allows to test the presence of the 5 MeV bump in the STEREO data. The last section presents the improved summation method and compares its predictions with the ILL  $^{235}\text{U}$  electron spectrum and with the STEREO antineutrino spectrum.

## 5.1 Absolute rate

The measurement done by STEREO allows to test the previously observed deficit in the total antineutrino reactor flux, namely the RAA, for a quasi pure  $^{235}\text{U}$  spectrum. To test the deficit, one needs to compare the measured absolute antineutrino rate with its expected value. The results presented in this section are based on data acquired during phase II of the data taking, which represents 119 reactor-on days and 211 reactor-off days, amounting for 43400 detected antineutrino events.

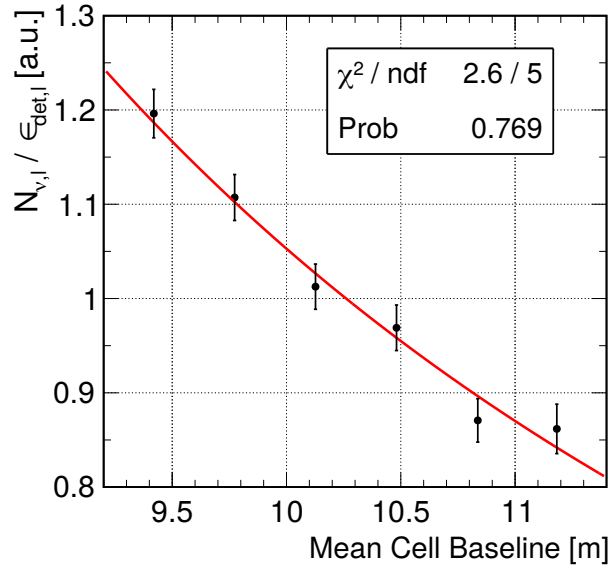


Figure 5.1 – Measured antineutrino rate for each cell with respect to the mean cell baseline. The points are fitted with a  $1/r^2$  model that includes a free normalization, shown in red. The rates are obtained using phase II data. Source: [77].

The number of IBD candidates for each cell is obtained using the extraction method presented in section 4.3.2. Figure 5.1 shows the extracted antineutrino rate, normalized to take into account the detection efficiency  $\epsilon_{det,l}$ , for each cell  $l$  with respect to the average baseline of the cell  $r_l$ . Considering that the antineutrinos are emitted isotropically from the reactor core, we expect that their rate is inversely proportional to the squared distance from their emission point:

$$\frac{N_{\bar{\nu}_e}}{\epsilon_{det,l}} = \frac{N_0}{r_l^2} \quad (5.1.1)$$

where  $N_0$  is a normalization parameter. We found a very good agreement between the antineutrino rates and the fitted function 5.1.1, which is shown in red in figure 5.1.

The predicted number of detected antineutrinos  $N_{\nu}^{\text{pred}}$  can be written as

$$N_{\nu}^{\text{pred}} = N_{\nu}^{\text{emi}} \cdot \tau_{\text{int}} \cdot c_p^{\text{Data/MC}} \cdot \epsilon_d \cdot c_n^{\text{Data/MC}} \quad (5.1.2)$$

where  $N_{\nu}^{\text{emi}}$  is the number of emitted antineutrinos (see equation 1.3.3),  $\tau_{\text{int}}$  is the fraction of interacting antineutrinos,  $c_p^{\text{Data/MC}}$  is the proton number correction (see section 3.1.3),  $\epsilon_d$  is the total detection efficiency and  $c_n^{\text{Data/MC}}$  is the correction of the detection efficiency of the delayed signal (see section 4.1.6). These quantities are tabulated in table 5.1 and their uncertainties will be briefly discussed in the following paragraphs.

The main uncertainties on the predicted emitted antineutrino rate  $N_{\nu}^{\text{emi}}$  come from the measurement of the thermal power  $P_{th}$  of the ILL reactor (1.44%) and from the Huber prediction of the form of the antineutrino spectra of the different beta emitters (2.4%). The uncertainty coming from the correction factors taking into account the time evolution of the fission fraction of  $^{239}\text{Pu}$ , the time evolution of fission fragments activities and the activation of structural elements (0.1%) [77] is found to be negligible with respect to the previously quoted uncertainty on the Huber model.

The fraction of interacting antineutrinos  $\tau_{\text{int}}$  is evaluated by convolving the antineutrino spectra reaching the detector with the IBD interaction cross section, using a Monte Carlo method developed by the collaboration [87] to randomly generate the emission and interaction  $\bar{\nu}_e$  vertices. The uncertainties on its value come from the geometrical solid angle (0.5%), the IBD cross section (0.22%) and the statistical uncertainty of the MC method itself (0.12%).

The detection efficiency  $\epsilon_d$  measures the fraction of antineutrinos interacting in the detector that pass the selection cuts. It is obtained through simulations and it accounts for energy nonlinearities and energy resolution ( $\epsilon_d = 0.2049 \pm 0.0084$ ).

Taking into account all the discussed factors, we obtain a predicted antineutrino rate of  $(383.7 \pm 8.1 [\text{sys}] \pm 9.2 [\text{model}]) \bar{\nu}_e/\text{day}$ , where the experimental and Huber model uncertainties are displayed separately.

Table 5.1 – Summary of all relevant quantities and their corresponding relative uncertainties on the IBD yield. Source: [111]

Quantity	Symbol	Value	Uncertainty/%
Number of $\nu$ /fission	$N_\nu^{[2,8]\text{MeV}}$	1.846	2.40
Huber prediction		1.722	2.40
Correction factors		1.072	0.10
Number of fissions/day		$1.30 \cdot 10^{23}$	1.44
Thermal power	$\langle P_{\text{th}} \rangle$	49.2 MW	1.44
Energy/fission	$\langle E_f \rangle$	203.4 MeV	0.13
Fract. of interacting $\nu$	$\tau_{\text{int}}$	$8.10 \cdot 10^{-21}$	0.56
Solid angle			0.50
IBD cross-section	$\sigma_{\text{IBD}}$		0.22
MC statistics			0.12
Correc. of $p$ -number	$c_p^{\text{Data/MC}}$	0.983	1.00
Detection efficiency	$\epsilon_d$	0.2049	0.54
Selection cuts			0.41
Energy Scale			0.30
MC statistics			0.19
Correc. of delayed effi.	$c_n^{\text{Data/MC}}$	0.9774	0.86
Predicted IBD yield		$383.7 \text{ d}^{-1}$	$2.10 \oplus 2.40$
Observed IBD yield		$363.8 \text{ d}^{-1}$	$0.88 \oplus 1.06$
Statistics			0.88
$\nu$ extrac. method			0.65
Reactor-induced bkg.			0.83
Off-time method			0.14



The measured antineutrino rate, obtained using the method presented in 4.3.2, has a value of  $(363.8 \pm 5.0) \bar{\nu}_e/\text{day}$ . The contribution to the uncertainty due to statistics is of 0.88 %. Other systematic uncertainties come from the discrepancy obtained in this thesis work by comparing the IBD rates obtained with the LPSC (used for the extraction of the absolute rate) and Saclay methods, as illustrated in section 4.4.2 (0.65 %, corresponding to half of the discrepancy), the contribution of a possible reactor-induced background (0.83 %, see section 4.2.3) and a potential bias in the off-time extraction method of accidental coincidences (0.14 %) [77, sec. IX-A].

The ratio between the measured and predicted antineutrino rate is  $(0.948 \pm 0.008 [\text{stat}] \pm 0.023 [\text{sys}] \pm 0.023 [\text{model}])$ , where the first uncertainty is statistical, the second comes from the experimental systematic uncertainties listed in table 5.1, and the third uncertainty is from the Huber model, common to all experiments. A very good agreement with the world average of pure  $^{235}\text{U}$  measurements is found when considering only the two experimental uncertainties [45] as shown in figure 5.2, where the ratio between the measured antineutrino yield and the Huber model prediction is plotted for various experiments. After including the STEREO measurement, the world average is improved from  $(0.950 \pm 0.015)$  to  $(0.950 \pm 0.013)$ , where again only experimental uncertainties were considered.

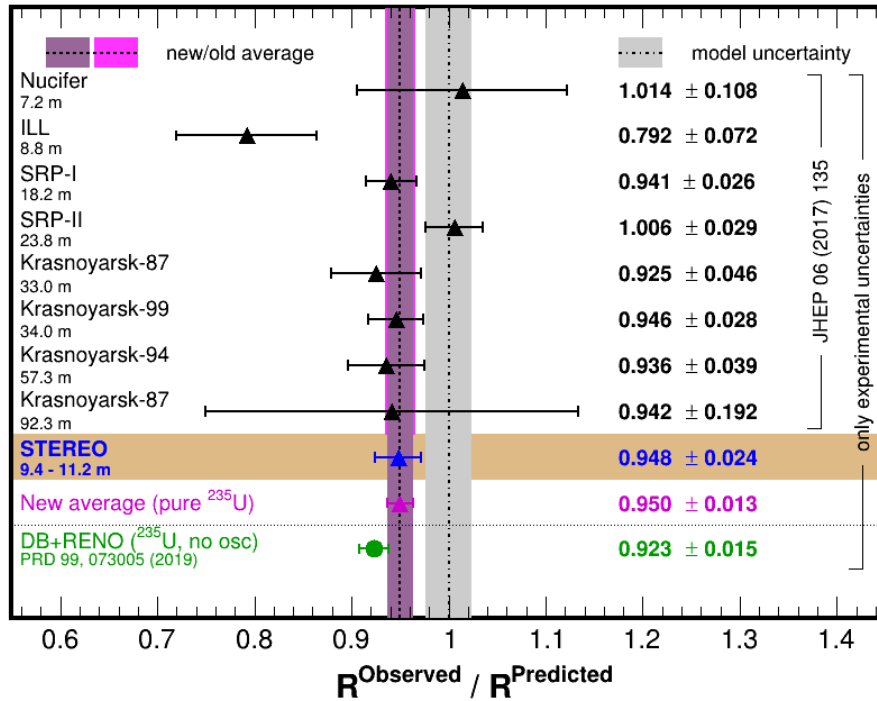


Figure 5.2 – Ratios between measured antineutrino yields and the Huber model predictions of various experiments. The uncertainty bars represent only experimental uncertainties. The common model uncertainty of 2.4 % is shown as a grey band around unity. Values of other experiments are taken from [45, 112]. For Daya Bay and RENO we show only the ratio for the  $^{235}\text{U}$  component. The value is taken from a fit, where isotopic IBD yields of  $^{235}\text{U}$  and  $^{239}\text{Pu}$  are free, while those of  $^{238}\text{U}$  and  $^{241}\text{Pu}$  are constrained to the prediction [112]. Source: [111].

To compare between them the results obtained by different experiments, one needs to determine the IBD cross section per fission, which is an observable that doesn't depend on the detection efficiencies and solid angles specific to each experiment. We use an extrapolated Huber spectrum  $S_H(E_\nu)$  for pure  $^{235}\text{U}$  without corrections for  $^{28}\text{Al}$ ,  $^{56}\text{Mn}$ , and off-equilibrium effects to obtain the predicted IBD cross section per fission

$$\sigma_f^{\text{pred}} = \int_{1.8 \text{ MeV}}^{10.0 \text{ MeV}} S_H(E_\nu) \sigma_{\text{IBD}}(E_\nu) dE_\nu \quad (5.1.3)$$

which yields a value of  $(6.69 \pm 0.15) \cdot 10^{-43} \text{cm}^2/\text{fission}$ , fully consistent with the value found in [57].

The STEREO IBD cross section per fission, obtained by applying our observed to predicted ratio to the predicted value, has a value of  $\sigma_f = (6.34 \pm 0.06 [\text{stat}] \pm 0.15 [\text{sys}] \pm 0.15 [\text{model}]) \cdot 10^{-43} \text{cm}^2/\text{fission}$ , consistent with the value in [112] and the Daya Bay result [46].

The antineutrino rate measured by STEREO is the most precise among all pure  $^{235}\text{U}$  measurements. Moreover, we expect to gain in precision by also analysing the data acquired during phase III, since the statistics will be doubled with respect to the present result.

## 5.2 Oscillation analysis

This section will present the oscillation analysis, which exploits the segmented nature of the STEREO detector in order to explore the possible existence of an eV sterile neutrino that could explain the RAA. The results presented in this section are based on the full STEREO dataset, i.e. on the data acquired during phases I, II and III of the data taking, which represent 334 reactor-on days and 543 reactor-off days.

The main philosophy behind the oscillation analysis is to compare the antineutrino energy spectra for the six Target cells, extracted as explained in section 4.3.2, with their respective expected values (allowing for neutrino oscillations), using a prediction independent method. In practice, a relative comparison between cell spectra is performed using a  $\Delta\chi^2$  formalism, with the  $\chi^2$  defined as

$$\chi^2 = \sum_{l=1}^{N_{\text{cells}}} \sum_{i=1}^{N_{\text{Ebins}}} \left( \frac{A_{l,i} - \phi_i M_{l,i}}{\sigma_{l,i}} \right)^2 + \sum_{l=1}^{N_{\text{cells}}} \left( \frac{\alpha_l^{\text{EscaleU}}}{\sigma_l^{\text{EscaleU}}} \right)^2 + \left( \frac{\alpha^{\text{EscaleC}}}{\sigma^{\text{EscaleC}}} \right)^2 + \sum_{l=1}^{N_{\text{cells}}} \left( \frac{\alpha_l^{\text{NormU}}}{\sigma_l^{\text{NormU}}} \right)^2 \quad (5.2.1)$$

where the  $l$  and  $i$  indices run over all the cells and energy bins,  $A_{l,i}$  are the measured antineutrino rates,  $M_{l,i}$  are the expected antineutrino rates, and  $\vec{\alpha}$  is a set of nuisance

parameters that account for the systematic uncertainties relevant for the oscillation analysis: the cell-to-cell correlated and uncorrelated energy scale uncertainties ( $\sigma^{\text{EscaleC}}$  and  $\sigma_l^{\text{EscaleU}}$ ) and the cell-to-cell uncorrelated normalization uncertainty ( $\sigma_l^{\text{NormU}}$ ). These uncertainties were discussed in section 3.3.3 for the phase II dataset and are summarized in table 5.2 for phases II and III of the data taking. The nuisance parameters  $\vec{\alpha}$  are constrained by their corresponding uncertainties via pull terms. Moreover, the  $\phi_i$  factors, common for all cells, can be regarded as free normalization parameters for each energy bin  $i$ . They wipe off all the absolute rate information per energy bin  $i$  by adjusting the expected antineutrino rates  $M_{l,i}$  across all cells  $l$  to match on average the measured antineutrino rates  $A_{l,i}$ , thus rendering the analysis independent from any spectrum prediction. The expected antineutrino rates  $M_{l,i}$  depend both on the oscillation parameters  $[\sin^2(2\theta_{ee}), \Delta m_{41}^2]$  and on the set of nuisance parameters  $\vec{\alpha}$

$$M_{l,i} \equiv M_{l,i}(\sin^2(2\theta_{ee}), \Delta m_{41}^2, \vec{\alpha}) \\ = \mathcal{M}_{l,i}(\sin^2(2\theta_{ee}), \Delta m_{41}^2) \cdot [1 + \alpha_l^{\text{NormU}} + S_{l,i}^{\text{Escale}} \cdot (\alpha_l^{\text{EscaleU}} + \alpha^{\text{EscaleC}})] \quad (5.2.2)$$

where the dependence of  $\mathcal{M}_{l,i}$  on the oscillation parameters is implemented by applying equation 1.4.2 to each MC event. The  $S_{l,i}$  factors encode the sensitivity of the antineutrino rate to a distortion of the energy scale and are determined from simulations.

The statistical uncertainty  $\sigma_{l,i} = \sigma_{l,i}(\phi_i M_{l,i})$  from equation 5.2.1 depends on the expected antineutrino rates  $\phi_i M_{l,i}$  and is estimated by performing simulations that take into account the signal-to-background ratio, the expected antineutrino and background rate, and the spectral shape. The uncertainty  $\sigma_{l,i}$  cannot be simply approximated by the statistical uncertainty of the data, since we are testing a potential neutrino oscillation by scanning the entire  $[\sin^2(2\theta_{ee}), \Delta m_{41}^2]$  parameter space and, thus, the model can be significantly different from the experimental data, especially for large mixing angles.

Since the performance of the detector has changed between the three data acquisition phases (different Monte Carlo fine tuning, different systematic uncertainties), we treat

Table 5.2 – Systematic uncertainties relevant to the oscillation analysis for phases II and III. Source: [88].

<b>Preliminary</b>	<b>Uncertainty</b>	
<b>Type</b>	<b>Phase-II</b>	<b>Phase-III</b>
<b>Uncorrelated normalization</b>		
• Cell volume	0.83%	0.83%
• Neutron efficiency correction	1.13%	1.13%
<b>Uncorrelated energy scale</b>		
• Mn anchor point	0.2%	0.3%
• Cell-to-cell deviations	1.0%	1.0%
<b>Correlated energy scale</b>		
• Time stability	0.3%	0.3%

phase I, phase II and phase III as three separate experiments. Therefore the  $\chi^2$  function describing simultaneously the data of the three phases can be written as

$$\chi^2_{PI+PII+PIII} = \chi^2(\vec{\mu}, \Phi_i, \vec{\alpha}_{PI}) + \chi^2(\vec{\mu}, \Phi_i, \vec{\alpha}_{PII}) + \chi^2(\vec{\mu}, \Phi_i, \vec{\alpha}_{PIII}) \quad (5.2.3)$$

where  $\vec{\mu} = [\sin^2(2\theta_{ee}), \Delta m_{41}^2]$  are identical for the three phases, the normalization parameters  $\Phi_i$  are common between the three phases, and the nuisance parameters  $\vec{\alpha}$  are different, since the systematic uncertainties evolved.

The no-oscillation hypothesis is tested and the exclusion contours obtained by performing pseudoexperiments in which pseudo-data are generated as fluctuations around the expected nonoscillated values within their uncertainties. For each pseudoexperiment, a  $\Delta\chi^2$  value is computed

$$\Delta\chi^2(\sin^2(2\hat{\theta}_{ee}), \Delta\hat{m}_{41}^2) = \chi^2(\sin^2(2\hat{\theta}_{ee}), \Delta\hat{m}_{41}^2, \hat{\vec{\alpha}}) - \chi^2(\sin^2(2\theta_{ee}), \Delta m_{41}^2, \vec{\alpha}) \quad (5.2.4)$$

where all parameters but  $\sin^2(2\hat{\theta}_{ee})$  and  $\Delta\hat{m}_{41}^2$  are allowed to vary, since they are the parameters of the model that we want to test (for example, they are both equal to zero in the no-oscillation hypothesis).

The no-oscillation hypothesis is tested by comparing the  $\Delta\chi^2$  of the data with the  $\Delta\chi^2$  distribution obtained from  $10^4$  pseudoexperiments. We obtain a p-value of 17%, which means that the no-oscillation hypothesis cannot be rejected.

For the exclusion contours, we first obtain the  $\Delta\chi^2$  distributions for each point in the parameter space  $[\sin^2(2\theta_{ee}), \Delta m_{41}^2]$  by generating  $10^4$  pseudoexperiments. Then, we compute the contours in a two-dimensional frequentist approach by normalising the confidence level of the oscillation-hypothesis to the confidence level of the null-hypothesis, i.e. no-oscillation-hypothesis, (CLs method) [113]. The exclusion contour thus obtained is depicted in figure 5.3. The best fit point of the RAA ( $\Delta m_{41}^2 = 2.3 \text{ eV}^2$ ,  $\sin^2(2\theta_{ee}) = 0.14$ ) is rejected at more than 99.99% confidence level.

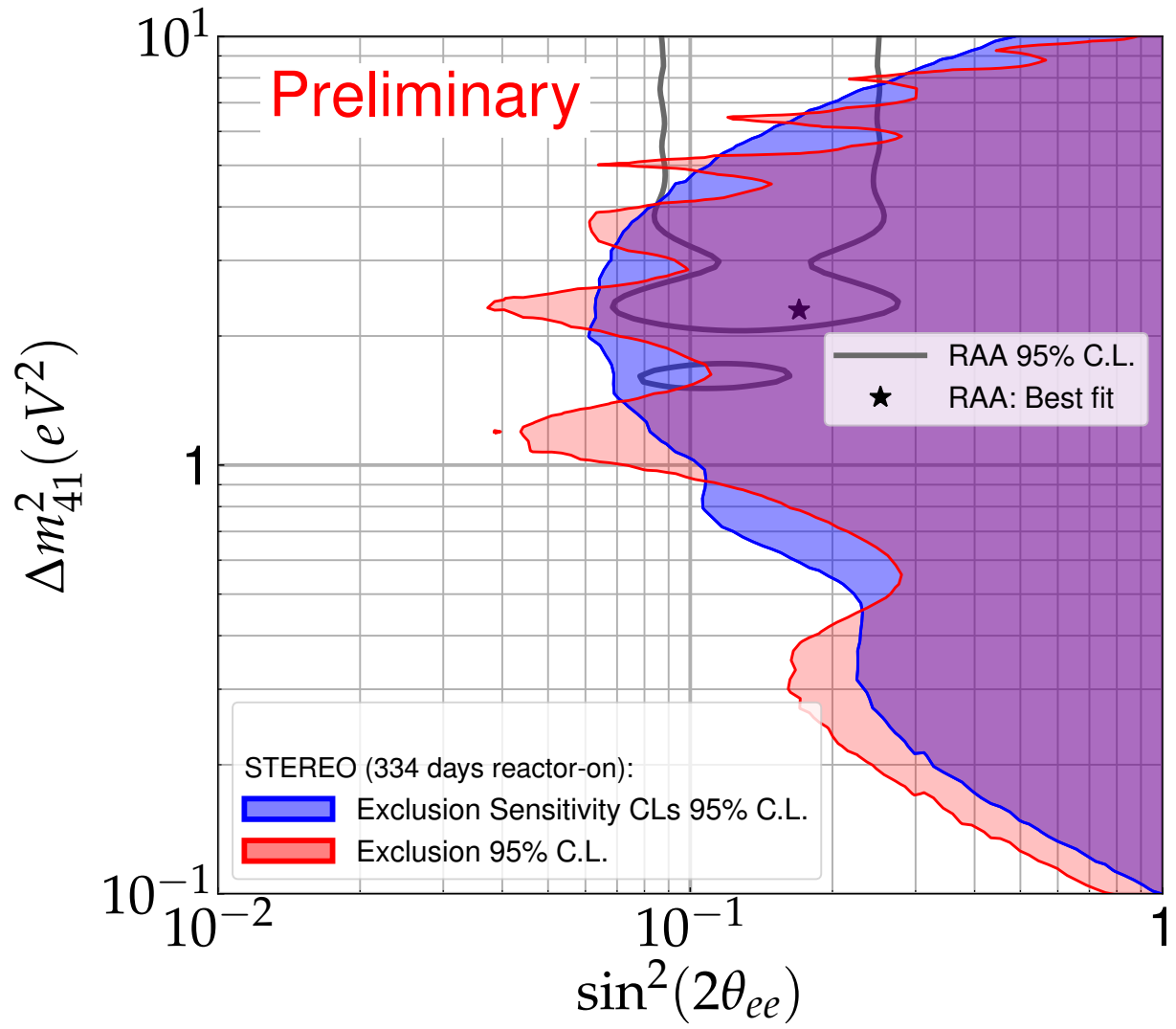


Figure 5.3 – Exclusion contour (red) and exclusion sensitivity contour (blue) at 95% C.L. of phase-I+II+III. Overlaid are the allowed regions of the RAA (grey) and its best-fit point (star) [44]. Source: [88].

### 5.3 Unfolded $^{235}\text{U}$ spectrum

This section will present the method developed by the collaboration to unfold the  $^{235}\text{U}$  antineutrino energy spectrum from the detector response. Since STEREO operates near a Highly Enriched Uranium (HEU) reactor, the contribution from  $^{239}\text{Pu}$  to the shape of the unfolded spectrum is negligible ( $<0.15\%$ ). Furthermore, we will also discuss the significance of the 5 MeV bump in the antineutrino energy space. The results presented in this section are based on data acquired during phases II and III of the data taking, which represent 273 reactor-on days and 519 reactor-off days.

#### 5.3.1 Response matrix

We have seen in section 2.2.1 that the prompt visible energy  $E_{\text{visible}}$  is related to the incident antineutrino energy  $E_{\bar{\nu}_e}$  in the following way

$$\begin{aligned} E_{\bar{\nu}_e} &= E_{\text{visible}} - m_e + \Delta \\ &= E_{\text{visible}} + 0.782\text{MeV} \end{aligned} \quad (5.3.1)$$

where  $\Delta = m(n) - m(p)$  and the kinetic energy of the neutron has been neglected. However, due to various detection effects, such as energy resolution, quenching, energy loss and inefficiencies, equation 5.3.1 cannot be used to obtain directly the antineutrino energy from the prompt visible energy on an event by event basis. Alternatively, one needs to use the detector's response matrix  $R$ , which accounts for all the previously mentioned effects. This matrix encodes the probability that an antineutrino with energy  $E_{\bar{\nu}_e}$  is detected with a prompt visible energy  $E_{\text{visible}}$

$$R_{ij} = P(E_{\text{visible}} \text{ in bin } j | E_{\bar{\nu}_e} \text{ in bin } i) \quad (5.3.2)$$

The response matrix is normalized such that  $\sum_j R_{ij} = e_i$ , where  $e_i < 1$  is the selection efficiency in bin  $i$ , which is smaller than 1 because there is a probability that an antineutrino with energy  $E_{\bar{\nu}_e}$  is rejected by the selection cuts.  $R$  is obtained using STEREO's detector Monte Carlo simulation and is used to obtain the predicted prompt spectrum  $N_j$  from any input IBD spectrum  $\Phi_i^{\text{tot}}$

$$N_j = \sum_i R_{ij} \Phi_i^{\text{tot}} \quad (5.3.3)$$

The energy range used in the antineutrino space is  $E_{\bar{\nu}_e} \in [2.625, 7.125]$  MeV, while the one used in the prompt visible energy space is  $E_{\text{visible}} \in [1.625, 7.125]$  MeV. The shift

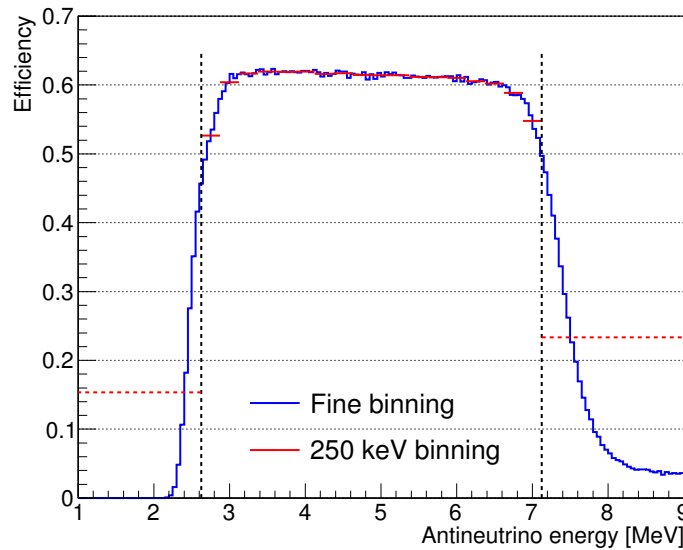


Figure 5.4 – The selection efficiency  $e_i$  as a function of the antineutrino energy  $E_{\bar{\nu}_e}$  for the 250 keV bins is shown in red, while the blue line represents a finer binning. The vertical dotted lines define the analysis range. The larger edge bins are used for regularization purposes only. Source: [114].

in the lower limit is due to the difference between  $E_{\bar{\nu}_e}$  and  $E_{\text{visible}}$ , as seen in equation 5.3.1. The  $E_{\bar{\nu}_e}$  range is divided in 18 bins of 250 keV and corresponds to the region of highest selection efficiency ( $>50\%$ ), as shown in figure 5.4. In addition, edge bins at low and high energy are added for regularization purposes. Finally,  $R$  is a  $22$  ( $E_{\text{visible}}$  bins)  $\times$   $20$  ( $E_{\bar{\nu}_e}$  bins) matrix.

### 5.3.2 Systematic uncertainties

#### Reactor-related background and detector time stability

As discussed in section 4.2.3, a potential reactor-related background is taken into account by correcting the low energy extracted prompt IBD rates, with an 100% energy bin to energy bin uncorrelated uncertainty on the respective corrections. Another uncorrelated uncertainty between the energy bins arises from a slight discrepancy observed in the PSD distributions from reactor-off data far apart in time. Since the extraction of the antineutrino rates is based on the shape stability of the reactor-off PSD distributions, a systematic uncertainty of 2% on the background rates is propagated on the antineutrino rates taking into account the signal-to-background ratio for each energy bin.

### Energy scale

The uncertainties on the energy scale discussed in section 3.3 translate into a distortion of the response matrix, which can be described using a nuisance parameter  $\alpha_{ES}$  that follows a standard normal distribution  $\mathcal{N}(0, 1)$

$$R_{ij}(\alpha_{ES}) = R_{ij}^0 + \alpha_{ES} \delta R_{ij} \quad (5.3.4)$$

where  $R_{ij}^0$  is the undistorted response matrix and the distortion due to energy scale uncertainties,  $\delta R_{ij}$ , is estimated through simulations. Consequently, the distorted prompt prediction is written as

$$N_j(\alpha_{ES}) = \sum_i R_{ij}(\alpha_{ES}) \Phi_i^{tot} \quad (5.3.5)$$

and has full bin-to-bin correlations.

### Selection cuts

The sensitivity of the antineutrino rates to the uncertainties of the selection cuts presented in section 4.1 has been studied within simulations that take into account the existing correlations between cuts. At the Target level, the uncertainties on the antineutrino rates,  $\delta N_j$ , correlated between energy bins, are described using a nuisance parameter  $\alpha_{cuts}$  that follows a standard normal distribution  $\mathcal{N}(0, 1)$  as

$$N_j(\alpha_{Cuts}) = N_j^0 (1 + \alpha_{Cuts} \delta N_j) \quad (5.3.6)$$

with  $N_j^0 = \sum_i R_{ij}^0 \Phi_i^{tot}$  being the undistorted prompt spectrum. The distortion of the response matrix can thus be written as

$$R_{ij}(\alpha_{Cuts}) = R_{ij}^0 (1 + \alpha_{Cuts} \delta N_j) \quad (5.3.7)$$

### Predicted flux corrections

The corrections that need to be applied to the Huber-Mueller spectrum in order to take into account the off-equilibrium effects and the contribution from activated materials, typical for the STEREO site, come with their associated uncertainties of 30% and respectively 5%. Thus, the IBD spectrum induced by such corrections can be written as



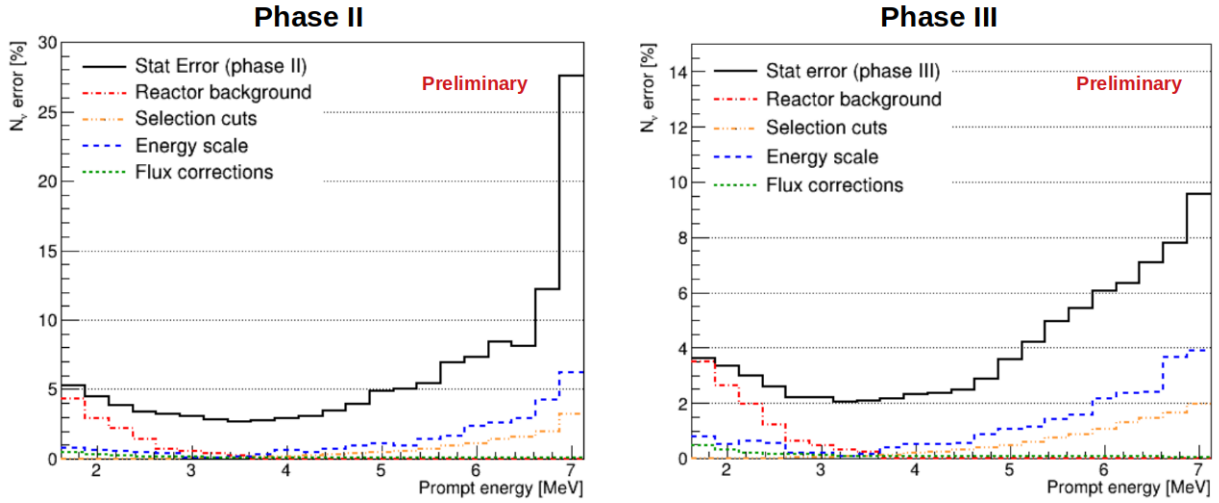


Figure 5.5 – Uncertainties considered for the spectrum shape unfolding. Source: [115].

$$\Phi_i^{\text{corr}}(\alpha_\phi) = \Phi_i^{\text{corr}} + \alpha_\phi \cdot \delta\Phi_i^{\text{corr}} \quad (5.3.8)$$

where  $\alpha_\phi$  is a nuisance parameter that follows a standard normal distribution  $\mathcal{N}(0, 1)$ .

A summary of all the previously discussed systematic uncertainties is shown in figure 5.5 at the Target level as a function of the Prompt energy, for both phase II and III of the data taking. It can be seen that for both phases, statistical uncertainties are dominant across the whole considered energy range.

### 5.3.3 Unfolding procedure

A procedure has been developed in order to obtain the  $^{235}\text{U}$  unfolded antineutrino energy spectrum from the measured prompt visible energy spectrum. The main idea behind this method is to fit the desired unfolded antineutrino energy spectrum convolved with the response matrix of the detector (equation 5.3.2) to the measured antineutrino spectrum. In other words, we convert the desired unfolded antineutrino energy spectrum from the real energy space to the prompt visible energy space, so that we could compare it with the measured antineutrino spectrum, which lies in the latter space. The fit is based on a  $\chi^2$  minimization with nuisance parameters formalism, as detailed in the following paragraphs.

The desired  $^{235}\text{U}$  unfolded antineutrino energy spectrum  $\Phi_i(\vec{\lambda})$  is modelled with 20 weights  $\lambda_i$  that describe the deviation to a prior. In our case, the prior is the Huber-Mueller spectrum  $\Phi^{HM}$  and thus  $\Phi_i(\vec{\lambda})$  writes

$$\Phi_i(\vec{\lambda}) = \lambda_i \Phi_i^{HM}. \quad (5.3.9)$$

Since we want to obtain the unfolded antineutrino energy spectrum corresponding to  $^{235}\text{U}$ , we need to account for the reactor-related flux corrections  $\Phi_i^{\text{corr}}(\alpha_\Phi)$  (off-equilibrium effects, structural activation, see section 5.3.2) before convolving the desired  $^{235}\text{U}$  unfolded antineutrino energy spectrum with the response matrix in view of comparing it with the measured antineutrino spectrum. Consequently, the total spectrum to be convolved writes

$$\Phi_i^{\text{tot}}(\vec{\lambda}; \alpha_\Phi) = \Phi_i(\vec{\lambda}) + \Phi_i^{\text{corr}}(\alpha_\Phi) \quad (5.3.10)$$

and yields the following prediction in the prompt visible energy space

$$N_j(\vec{\lambda}; \vec{\alpha}) = \sum_i R_{ij}(\alpha_{ES}, \alpha_{cuts}) \Phi_i^{\text{tot}}(\vec{\lambda}; \alpha_\Phi), \quad (5.3.11)$$

where  $\vec{\alpha} = (\alpha_\phi, \alpha_{ES}, \alpha_{cuts})$  is the set of nuisance parameters following standard normal distributions described in section 5.3.2. To obtain the best-fit  $^{235}\text{U}$  unfolded antineutrino spectrum  $\hat{\Phi}$ , i.e. the best-fit value  $\hat{\lambda}_i$  of  $\lambda_i$  parameters, one has to minimize the following  $\chi^2$

$$\chi^2(\vec{\lambda}; \vec{\alpha}) = \sum_i \left( \frac{N_j(\vec{\lambda}; \vec{\alpha}) - D_j}{\sigma_j} \right)^2 + \alpha_{ES}^2 + \alpha_{cuts}^2 + \alpha_\Phi^2 + \mathcal{R}_1(\vec{\lambda}) \quad (5.3.12)$$

where  $D_j$  is the data spectrum in prompt visible energy space and  $\sigma_j$  is the statistical uncertainty that takes into account the reactor background and time evolution systematics presented in section 5.3.2. The pull terms  $\alpha_{ES}^2$ ,  $\alpha_{cuts}^2$  and  $\alpha_\Phi^2$  constrain the variations of the nuisance parameters and  $\mathcal{R}_1(\vec{\lambda})$  is a regularization term, which ensures the smoothness of the fitted  $^{235}\text{U}$  antineutrino spectrum with respect to the reference Huber-Mueller spectrum shape. Its expression is

$$\mathcal{R}_1(\vec{\lambda}) = r \sum_{i=1}^{19} (\lambda_{i+1} - \lambda_i)^2. \quad (5.3.13)$$

where  $r > 0$  is the regularization strength, tuned to achieve negligible dependence on the shape of the reference Huber-Mueller spectrum  $\Phi^{HM}$  chosen as a prior (see details in section 7 from [114]). In practice, the optimal value of  $r$  is found to be around 50.

The covariance matrix  $V_\Phi$  of the unfolded spectrum is computed numerically by unfolding thousands of pseudo-data spectra, obtained by fluctuating the prompt prediction within the experimental uncertainties.

### 5.3.4 Unfolded spectrum and bump parameters

Before combining the data from phase II and phase III at the Target level to obtain the  $^{235}\text{U}$  unfolded spectrum, we have checked the compatibility between their respective prompt visible energy antineutrino spectra. To compare the spectra of the two phases, we performed a  $\chi^2$  test and we found a value of  $\chi^2/\text{ndf} = 17.9/21$  when taking into account both statistical and systematic uncertainties. This proves that the two spectra are compatible and allows us to combine them in order to obtain the jointly unfolded  $^{235}\text{U}$  spectrum. To do so, a generalized  $\chi^2$ , similar to that from equation 5.3.12, which takes into account the contribution from both phases, as well as the correlated uncertainties between them, has been minimized.

The unfolded spectrum thus obtained is shown in figure 5.7. It gives an agreement of  $\chi^2/\text{ndf} = 40.5/17$  (p-value  $\sim 10^{-3}$ ) against the Huber-Mueller prediction.

By adding to the Huber-Mueller prediction a Gaussian distortion, with three additional parameters to be fitted, the minimization of the following  $\chi^2$

$$\chi^2(A, \mu, \sigma, \alpha) = [\Phi - \Phi_{HM}(\alpha + \text{Gaus}(A, \mu, \sigma))]^T V_{\Phi}^{-1} [\Phi - \Phi_{HM}(\alpha + \text{Gaus}(A, \mu, \sigma))] \quad (5.3.14)$$

leads to an agreement of  $\chi^2/\text{ndf} = 11.6/14$  (p-value  $\sim 0.63$ ), with the following best-fit parameters for the Gaussian

$$\begin{aligned} A &= 0.107 \pm 0.021 \\ \mu &= 5.39 \pm 0.13 \text{ MeV} \\ \sigma &= 0.585 \pm 0.157 \text{ MeV} \end{aligned} \quad (5.3.15)$$

This confirms the previously observed excess of events in the 5-6 MeV region with respect to the Huber-Mueller prediction for a pure  $^{235}\text{U}$  antineutrino spectrum. The same conclusion can be drawn with the up-to-date summation model which completes the ENSDF database with all the existing TAGS measurements to correct for the *Pandemonium* effect, and uses the Gross theory spectra from JENDL to complete for unknown transitions (see [116] for more details). As seen in figure 5.7, the ratio between the summation model and the Huber-Mueller is closed to one, except above 5.5 MeV, where a small deviation of few percent is observed.

Finally, a joint analysis between STEREO and PROSPECT [117] was performed, which combined phase II data from STEREO with the whole dataset of PROSPECT, and confirmed the presence of the bump. However, since the uncertainties on the jointly unfolded STEREO-PROSPECT  $^{235}\text{U}$  antineutrino spectrum are bigger than the ones for the STEREO only phase II-phase III spectrum presented in this section, the former results won't be presented here.

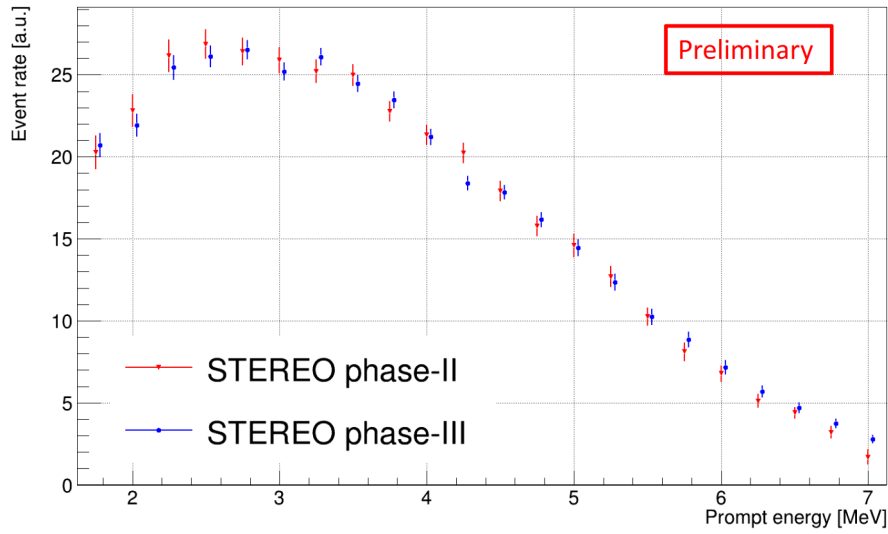


Figure 5.6 – Comparison between the antineutrino spectra in prompt energy for data collected in phases II and III of the data taking. Source: [88].

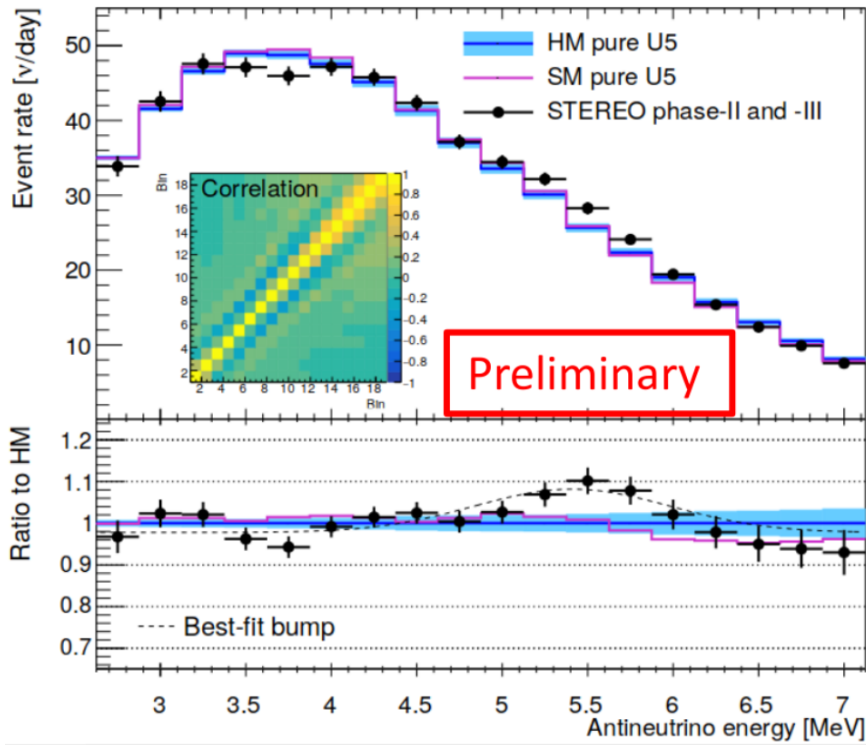


Figure 5.7 – Top: unfolded  $^{235}\text{U}$  antineutrino spectrum along with Huber-Mueller (HM) and summation model (SM) [116] predictions, obtained from the combination of phase II and phase III data. The correlation matrix of the unfolded spectrum is also displayed. Bottom: ratio between the unfolded  $^{235}\text{U}$  antineutrino spectrum and the Huber-Mueller prediction. The ratio between the summation model (SM) and the Huber-Mueller (HM) predictions is also shown in magenta. Source: [88].

## 5.4 On the possible origin of the reactor anti-neutrino anomalies

The results of STEREO confirm the norm and shape reactor antineutrino anomalies when compared to the Huber-Mueller prediction and reject the hypothesis of the existence of a sterile neutrino at the eV mass scale compatible with the RAA allowed region. As introduced in section 1.3, the Huber and Mueller predictions are made using the conversion method of electron energy spectra measured at ILL. This method allows to predict the antineutrino energy spectra with low uncertainties (the experimental uncertainties on the electron energy spectra dominate), but propagates any biases in the measurement, such as the normalisation of the data or any distortion of the electromagnetic spectrometer response.

In this section we present an improvement of the summation method, presented in section 1.3, aimed to test the hypothesis that the origin of the anomalies resides in the reference  $^{235}\text{U}$  electron energy spectrum, as suggested by the recent experimental evidences presented in section 1.4.2. The main improvement proposed in this work is the introduction of a beta-decay strength model able to correct for the *Pandemonium* effect in the nuclear databases and to generate beta-transitions for nuclei with unknown transitions.

### 5.4.1 The summation method

The summation method was already introduced in section 1.3. It is based on equation 1.3.2 reported here

$$\phi_{\bar{\nu}_e}(E_\nu, t) = \sum_f A_f(t) S_f(E_\nu) \quad (5.4.1)$$

where the  $f$  index runs over all the beta-emitters (fission fragments and activated structural elements), the time-dependent term  $A_f(t)$  is the beta-activity of one beta-emitter and the energy dependent term  $S_f(E_\nu)$  is the corresponding antineutrino energy spectrum. The same equation is valid for electrons.

The activities depend on the time evolution of the fission rates during the irradiation or the reactor functioning. For this study, we used the FISPACT-II code [118] to calculate the time-evolution of each fragment activity. The code solves the Bateman equations for the evolution of the number of atoms  $N_f(t)$  of isotope  $f$

$$\frac{dN_f}{dt} = Y_f - (\lambda_f + \sigma_a \phi_n(t)) N_f(t) + \sum_{i \neq f} \lambda_{i \rightarrow f} N_i(t) \quad (5.4.2)$$

where  $Y_f$  is the independent fission yield taken from the JEFF3.3 nuclear data library [119],  $\lambda_f$ ,  $\lambda_{i \rightarrow f}$  and  $\sigma_a$  are, respectively, the decay rate of isotope  $f$ , the decay rate of isotope  $i$  to isotope  $f$  and the neutron absorption cross section. All these nuclear data are also taken from JEFF3.3. The neutron flux  $\phi_n(t)$  was calculated with MCNP for realistic configurations of the ILL experiment for the electron measurement and for the STEREO experiment [77]. The independent fission yields for the  $^{235}\text{U}$  and  $^{239}\text{Pu}$  isotopes are quite well known.

To calculate the energy spectrum for each isotope we used the BESTIOLE code [120],[33], updated in a recent thesis work [121]. The code uses nuclear structure information, such as level energies, spins and parities of the initial and final states, to first calculate the electron and antineutrino energy spectra for each beta-branch and then sum up these spectra weighted with their branching ratios in order to get the full spectrum corresponding to the isotope. The computation for each branch is based on the Fermi theory of beta-decay for point-like nucleons and takes into account nucleon and nuclear form factors and radiative correction factors.

The electron/antineutrino energy spectrum for an isotope (Z,A) writes

$$S_f(E) = \sum_b BR_f^b \times S_f^b(Z, A, E_0^b, E) \quad (5.4.3)$$

where the  $b$  index runs over the different beta branches of the given isotope,  $E$  stands for the kinetic energy of the electron or antineutrino and  $E_0^b$  is the energy available in the transition, i.e. the end-point.

In the Fermi theory, the transition rate between the initial and final states results from the combination of hadronic and leptonic currents. With a very good approximation, the hadronic current can be factorised and the electron energy spectrum writes [33]

$$S_f^b(Z, A, E_0^b, E_e) = K_f^b \mathcal{F}(Z, A, E_e) C_f^b(Z, E_e) p_e E_e (E_e - E_0^b)^2 (1 + \delta_f^b(Z, A, E_e)) \quad (5.4.4)$$

where  $K_f^b$  is a normalization factor,  $p_e$  is the electron momentum and  $\mathcal{F}(Z, A, E_e)$  is the Fermi function which corrects for the deceleration of the electron in the Coulomb field created by the positive charges of the daughter nucleus. The Fermi function is calculated for a point-like charge and the correction term  $\delta_f^b(Z, A, E_e) = \delta_{FS} + \delta_{rad} + \delta_{WM}$  is added to account for the finite size of the nucleus ( $\delta_{FS}$ ), the weak current induced by the interference of the magnetic moment distribution of the vector current with the spin distribution of the axial current ( $\delta_{WM}$ ) and the exchange of real and virtual photons for the fermion with the nucleus ( $\delta_{rad}$ ).

The shape factor  $C_f^b(Z, E_e)$  contains the nuclear transition-matrix elements and the energy dependence of the wave functions for the electron and the antineutrino. It depends on the change of spin and parity between the initial and final states, which defines the type of transition (allowed, first forbidden, second forbidden, etc.). For allowed transitions (no parity change and  $\Delta J = 0, 1$ ) the shape factor is constant and is absorbed in the

normalization factor. For first-forbidden unique transitions (parity change and  $\Delta J = 2$ ), only one matrix element contributes and the shape factor could be reduced to a polynomial function of the electron momentum. In the BESTIOLE version used in this work, only allowed and unique  $n^{th}$ -forbidden transitions are treated.

The antineutrino energy spectrum is obtained from Equation 5.4.4 by applying the closure relation:  $E_0^b = E_e + E_\nu$ . Thus, it is clear that when applying the summation method, both electron and antineutrino energy spectra are computed on the same basis and the *Pandemonium* effect or missing nuclear data should affect both spectra in the same way.

The ENSDF beta-decay nuclear structure database (2020 release) [31], denoted as ENSDF-2020 in the following, was used to get the inputs (end-point, spin-parity, branching ratios) for the BESTIOLE calculations. ENSDF-2020 covers 93% (67%) of the fission fragments, amounting to 96.5% (97%) of the fission fragment activities for  $^{235}\text{U}$  after 12h (30 days) of irradiation in the HFR at ILL. As shown in figure 5.8, missing nuclei in ENSDF-2020 have  $Q_\beta$  values higher than 5 MeV, with most of them being above 7 MeV. To generate beta-transitions for these missing nuclei in ENSDF-2020 we used the NUBASE2016 [122] mass data table for computing the  $Q_\beta$  values. NUBASE-2016 covers almost 100% (99.86%) of the fission products contained within the JEFF3.3 database.

One should note that in a reactor, not only  $\beta^-$  reactions occur, but also  $\beta^+$  or internal

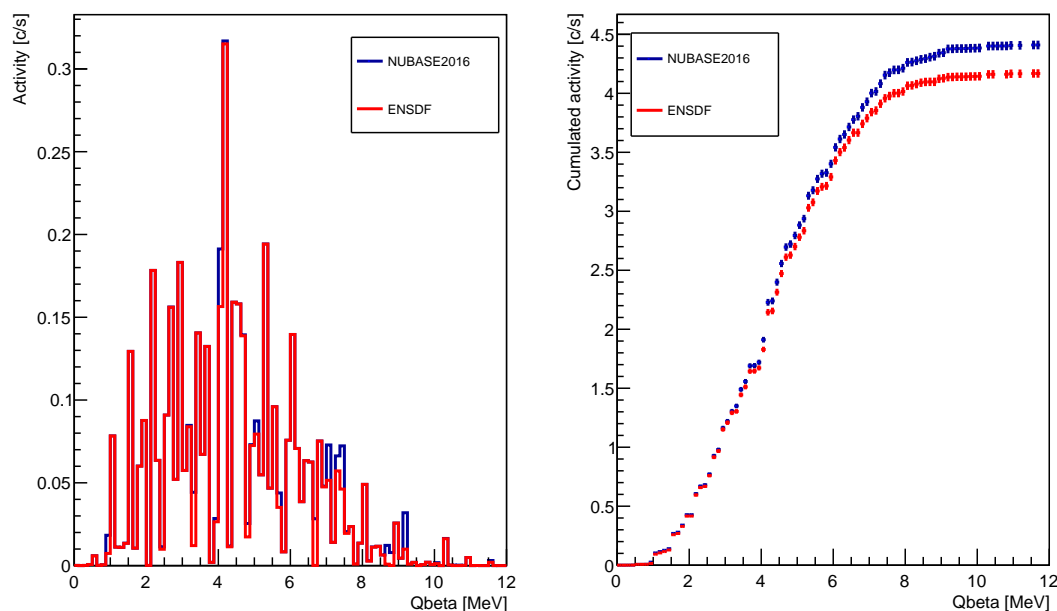


Figure 5.8 – Distribution of fission fragment activities (left) and their cumulative (right) as a function of their  $Q_\beta$  values, for the fission of  $^{235}\text{U}$  for 12h of irradiation, calculated with FIPSACT-II and JEFF3.3, when the fission fragments are present in the ENSDF-2020 and NUBASE2016 databases.

transitions for isomeric states. We have evaluated that non- $\beta^-$  activity amounts to 2.4% (4.2%) of the total fission fragment activity for  $^{235}\text{U}$  after 12h (30 days) of irradiation in the HFR at ILL. This number has to be taken into account when using cumulative fission yields to estimate reactor antineutrino energy spectra.

### 5.4.2 An empirical beta strength model

To generate transitions for missing or unknown transitions, and thus correct for the *Pan-demonium* effect and complete the existing data, a model to calculate the beta-transition strength function for each nucleus is needed. The beta strength function  $S_\beta(E)$  is the reduced transition probability to individual daughter states. It can be extracted from beta-decay measurements or calculated using models.

Sophisticated microscopic nuclear models could be used to calculate the beta strength, as for example the pnQRPA on top of HFB calculations, as in [123]. Nonetheless, such an approach is very time-consuming and its implementation is out of the scope of this thesis work. We have instead chosen an empirical approach, based on the study of the beta strength distributions extracted from the experimental data.

#### Study of the beta-decay strength structure

The  $\beta^-$ -decay is a charge exchange reaction occurring as an isospin transformation: a neutron transforms into a proton with low momentum transfer, creating a neutron-hole and an additional proton. Such a transformation is known to produce a very narrow resonance (the Isobar Analogue State or IAS) for Fermi type transitions in which the spin is not modified ( $\Delta J = 0$ ), and a giant resonance for Gamow-Teller type transitions ( $\Delta J > 0$ ) due to the spin-isospin interaction, in all nuclei with excess of neutrons. Since a charge is created in the transformation, these two resonances are located around the Coulomb energy difference between the two isobars. For fission fragments, the Coulomb energy difference ranges between 9 and 15 MeV, which is out of the beta-decay energy window for most of the fission fragments. Nevertheless, the Gamow-Teller resonance is wide and its tail enters in the beta-decay window. This is the reason why we consider only Gamow-Teller type transitions in the following.

The Gamow-Teller beta strength can be extracted from the intensity  $I(E_j)$  of the beta feeding to the state  $j$  of the daughter nucleus by

$$B_{GT}(E_j)\lambda^2 = \frac{K}{f(Z, Q_\beta - E_j)T_{1/2}} I(E_j) \quad (5.4.5)$$

where  $K = 6143.6(17)$  [124],  $\lambda = g_A/g_V = -1.270(3)$  [125], and  $T_{1/2}$  is the half-life of the isotope.



The phase-space factor is calculated as:

$$f(Z, Q_\beta - E_j) = \int_0^{Q_\beta - E_j} \mathcal{F}(Z, A, E_j) \sqrt{E(E + 2m_e c^2)} E(E_j - E) dE \quad (5.4.6)$$

where  $\mathcal{F}(Z, A, E_j)$  is the Fermi function, as in equation 5.4.4.

In figure 5.9 are shown four examples of beta-decay strengths extracted from the high resolution ENSDF-2020 (in red) and low resolution TAGS (in blue) data using equation 5.4.5. The complete extracted set of beta strengths from all TAGS data is shown in the Appendices. For comparison, we have added, for each fragment, the level density curve calculated by Hartree Fock Bogolyubov (HFB) technique plus combinatorial nuclear level densities deformations based on the BSk14 Skyrme force from RIPL3 [126]. Curves are not corrected to match the tabulated recommended spacings of s-wave neutron resonances  $\langle D_0 \rangle$  and the cumulative number of low-lying levels.

The Gamow-Teller beta-decay strength clearly exhibits an universal feature as a function of the excitation energy: a discrete region, up to about 2-3 MeV, and above, an increase in the density of transitions with a resonance structure more visible in the low-

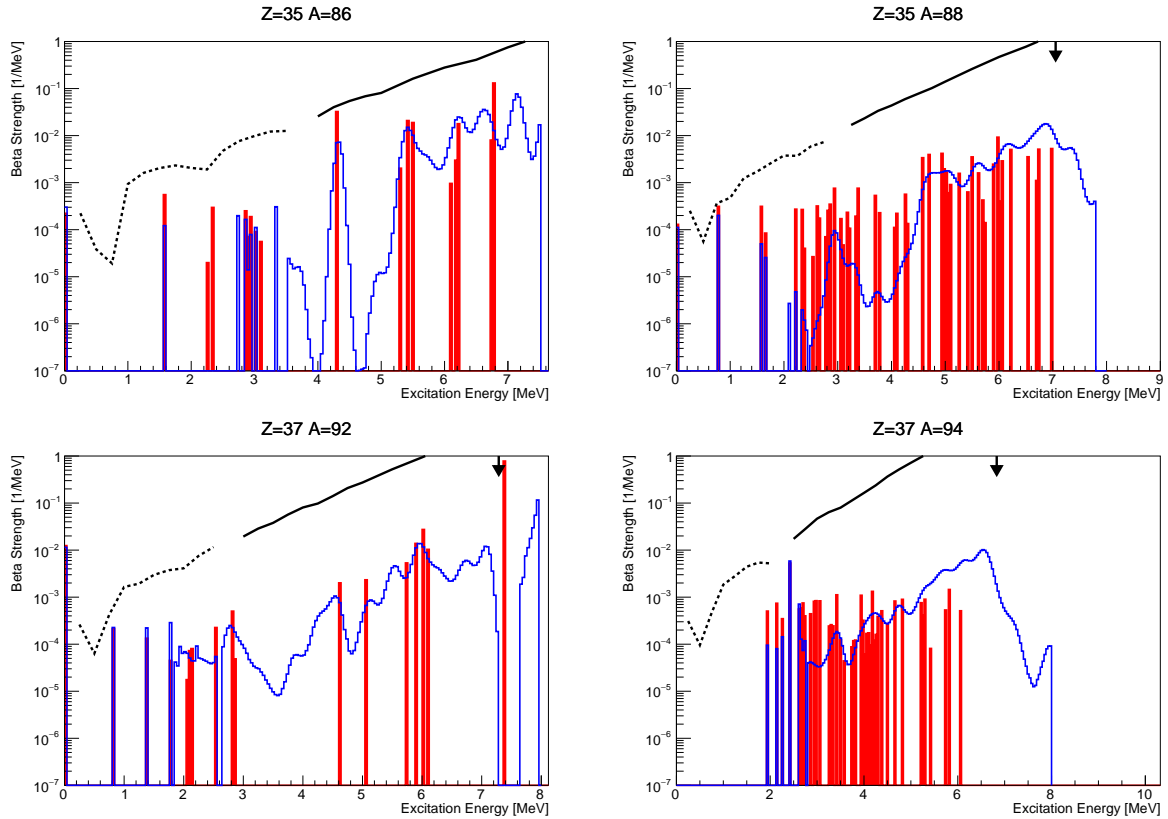


Figure 5.9 – Example of beta-decay strengths extracted from the analysis of ENSDF-2020 (in red) and TAGS data (in blue) for  $^{86}\text{Br}$  [127],  $^{88}\text{Br}$ ,  $^{94}\text{Rb}$  [34] and  $^{92}\text{Rb}$  [128]. The black arrows indicate the neutron separation energy ( $S_n$ ). The black lines are the scaled ( $\times 10^{-11}$ ) HFB level densities. The separation between dashed and continuous lines correspond to the energy cutoff for the model (see text).

resolution TAGS data. These resonances are known as pygmy resonances. Moreover the beta-decay strengths seem to follow the general trends of HFB level densities. As already stated, it is out of the scope of this thesis work to try to predict the exact positions and intensities of the resonances. But, by studying their statistical properties, we have deduced a model able to reproduce their global features.

We have studied the average spacing between two consecutive resonances and the width of the resonances in the TAGS data. We have developed an algorithm to search and identify peaks in an automatic way for all the available TAGS data [129, 130, 131, 132, 127, 128, 34]. The peak search method is based on a scan of the relative variations of three consecutive points. Points are considered as consecutive when their distance is lower than a prior width of the resonances. As the width increases with the excitation energy, this method allows to include discrete transitions to low energy levels in the scan and to adapt the distance between two consecutive points in order to be the most sensitive to the width of the resonance.

With this simple peak search method, the number of resonances, their excitation energy position and their width can be extracted. Unfortunately, it does not allow to fully resolve close resonances (when the distance between them is lower than their width), but these missing resonances should not change too much the overall conclusions.

In figures 5.10 and 5.11 are shown the results concerning the energy spacing between two consecutive resonances and the widths as a function of the excitation energy. The energy spacings are distributed up to 1.2 MeV with a mean value of 340 keV and a standard

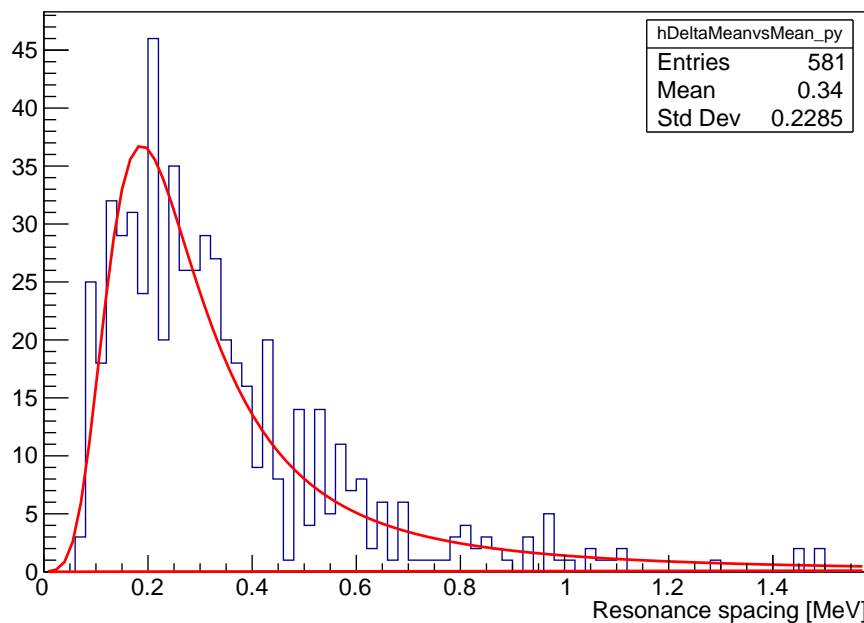


Figure 5.10 – Energy spacing between two consecutive resonances extracted from the analysis of TAGS data. The red curve is a Landau distribution fitted on the data.

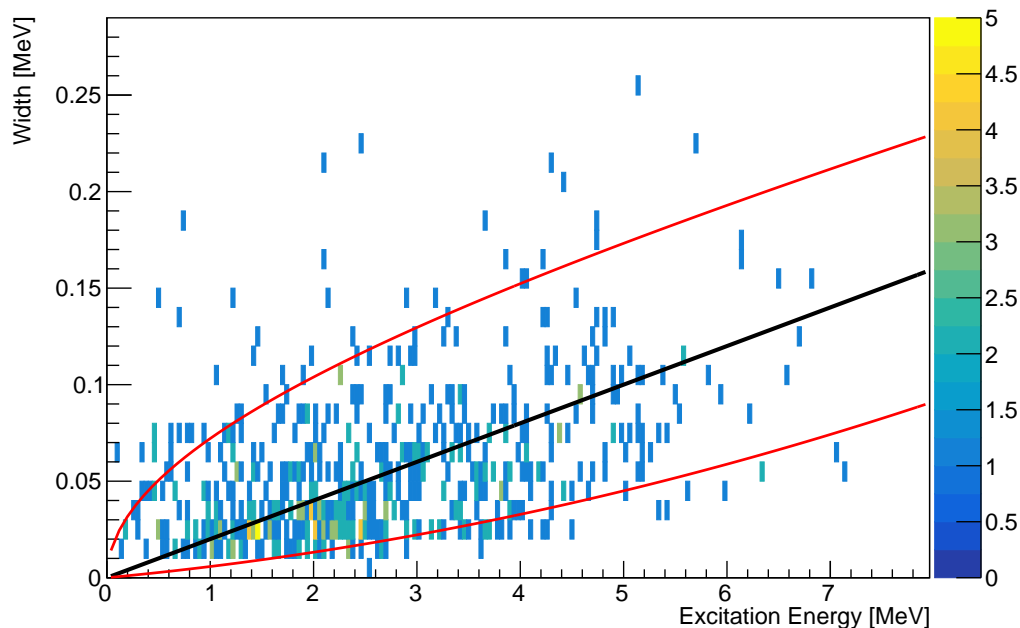


Figure 5.11 – Width distribution of resonances extracted from the analysis of TAGS data. The curves define the mean (black) and limits (red) used in the model.

deviation of 220 keV. No clear dependence with the excitation energy was observed. The widths are distributed up to about 150 keV with a mean of about 50 keV at 2 MeV and 100 keV at 6 MeV of excitation energy.

### Modelisation of the low-energy beta-transitions

The beta strength model is based on the observed structure of the beta strengths extracted from the TAGS data and has the following features

- a discrete domain at low excitation energy.
- a continuous domain at higher excitation energy, with Gaussian-shaped resonances.
- a general trend that follows nuclear level densities.

In our model, the two energy domains are separated by a cutoff energy  $E_{cut}$ , defined for each isotope on the basis of HFB nuclear level densities. The chosen criterion imposes that the HFB density have to be higher than 100 levels/MeV. As shown in figure 5.9, this criterion allows for a separation between the two domains in the 2-3 MeV region.

In the model, the discrete transitions and pygmy resonances' properties (energy, amplitude and width for the resonances) are treated as random variables. Their probability density distribution is defined by the observed level spacing distribution (figure 5.10) for

the energies, the width distribution as a function of the excitation energy (figure 5.11) for the widths, and the HFB level densities from RIPL3 for the amplitudes.

As seen in figure 5.12, the HFB densities are significantly bigger than the measured ones for most of the nuclei. This is the reason why the authors of [126] introduced corrections to match the tabulated recommended spacings of s-wave neutron resonances  $\langle D_0 \rangle$  and the cumulative number of low-lying levels, when data exists. Since we develop a global approach, aiming to work even when no data exists, we introduce a quenching function to reduce the HFB density

$$\rho(E^*) = e^{-\alpha\sqrt{E^*}} \rho_{HFB}(E^*) \quad (5.4.7)$$

where  $\alpha$  is the only free parameter of the model. The effect on the cumulative nuclear level density is shown in figure 5.12 for  $\alpha = 0.6$ , where a better agreement with ENSDF-2020 data is observed in the low excitation energy range. Above 2-3 MeV, a systematic deviation between experimental and calculated cumulative level densities is observed, showing that levels are probably missing in the high resolution experiments (ENSDF-2020) and confirming that the *Pandemonium* effect probably affects most of the nuclei.

Following this argument, we decided to systematically generate the resonances region (above 2-3 MeV) with the model. The discrete region is generated with the model only when no data are available in ENSDF-2020, ENSDF-2020 data being used otherwise. Resonances are constructed by an iterative procedure starting at  $E_{cut}$  energy. Then, the energy distance between two resonances is chosen randomly from the Landau distribution fitted on the measured resonance spacing (see figure 5.10). The width of each resonance is randomly determined using the mean and the limits of each width distribution as a function of the excitation energy (see figure 5.11).

When existing, the discrete beta-transitions from ENSDF-2020 data are used. In that way, the low-lying state information on the beta strength structure is conserved. We make the assumption that the relative intensities between the known beta-transitions are correct, with only the summation of the intensities being wrong due to missing transitions (*Pandemonium* effect).

As the beta-decay strength is generated randomly, several strengths (realizations) are generated for each isotope and an average strength function is extracted. This allows to determine an uncertainty on the model as the standard deviation of all the realizations.

## Model validation

The model was tested by comparing the electron energy spectra generated with BESTI-OLE using the ENSDF-2020 model-corrected data and TAGS data as an input. The propagation of the model's uncertainties, due to the random character of the resonances, was obtained by generating several beta-decay realizations for each isotope. For each

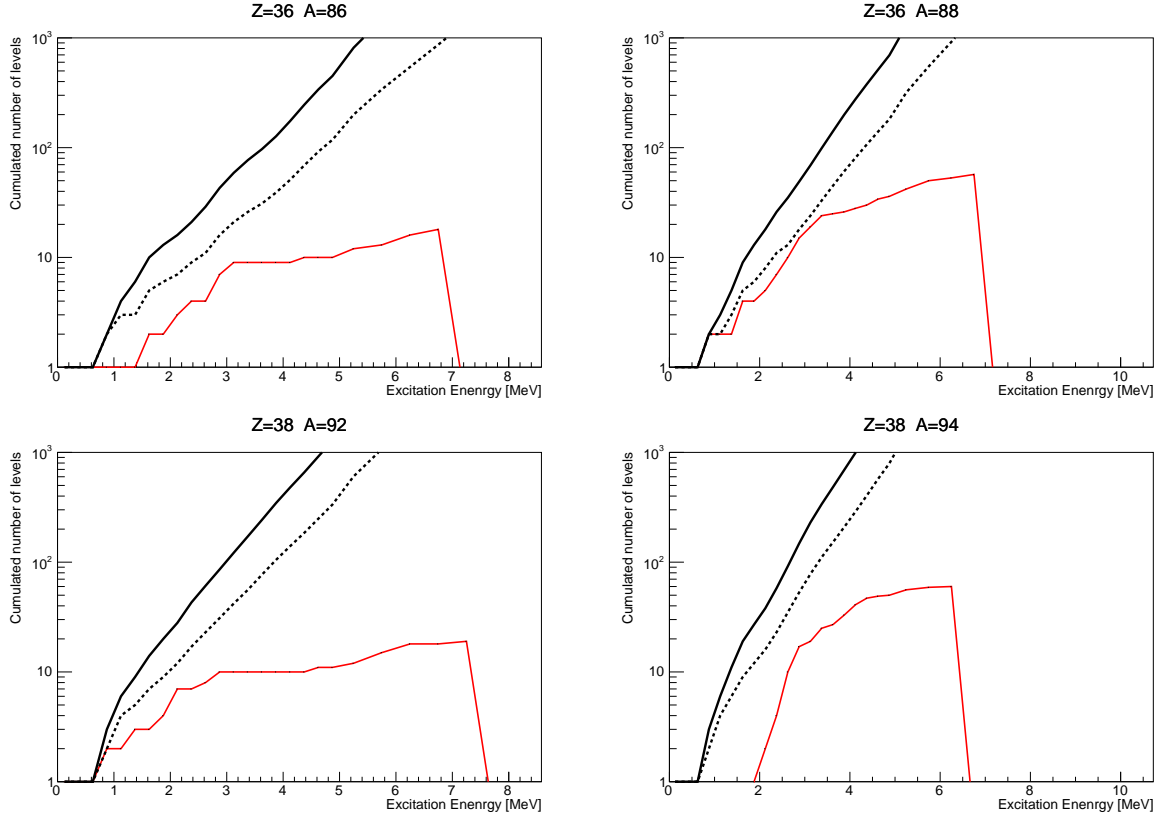


Figure 5.12 – Cumulative nuclear level densities extracted from ENSDF-2020 (red) and compared with HFB (continuous black lines) and the quenched HFB level densities (dashed black lines) with  $\alpha = 0.6$ , as explained in the text, for the daughter isotopes of those from figure 5.9.

realization, a database was generated and an electron spectrum calculated. Results are shown in figure 5.13 for four selected isotopes and in the Appendices for all TAGS data [129, 130, 131, 132, 127, 128, 34] for  $\alpha = 0.6$ . From a general point of view, the ENSDF-2020 model-corrected spectra are not fully compatible with all the TAGS spectra, but there is an overall good agreement at the shape level, showing that the model could correct the *Pandemonium* effect by tuning the  $\alpha$  parameter.

### 5.4.3 Comparison with STEREO results

The new database generated with the beta strength model was used to calculate the antineutrino and electron energy spectra for  $^{235}\text{U}$  after 12 hours of irradiation in the ILL reactor. The time-evolution of the fission fragments was calculated using the FISPACT-II code, with JEFF3.3 as an input for the independent fission yields.

As a first step, we performed a relative comparison between our model and the Huber-Mueller model antineutrino spectra, for different  $\alpha$  values. The results of this comparison are shown in figure 5.14, together with the scaled STEREO ratio to Huber-Mueller. It

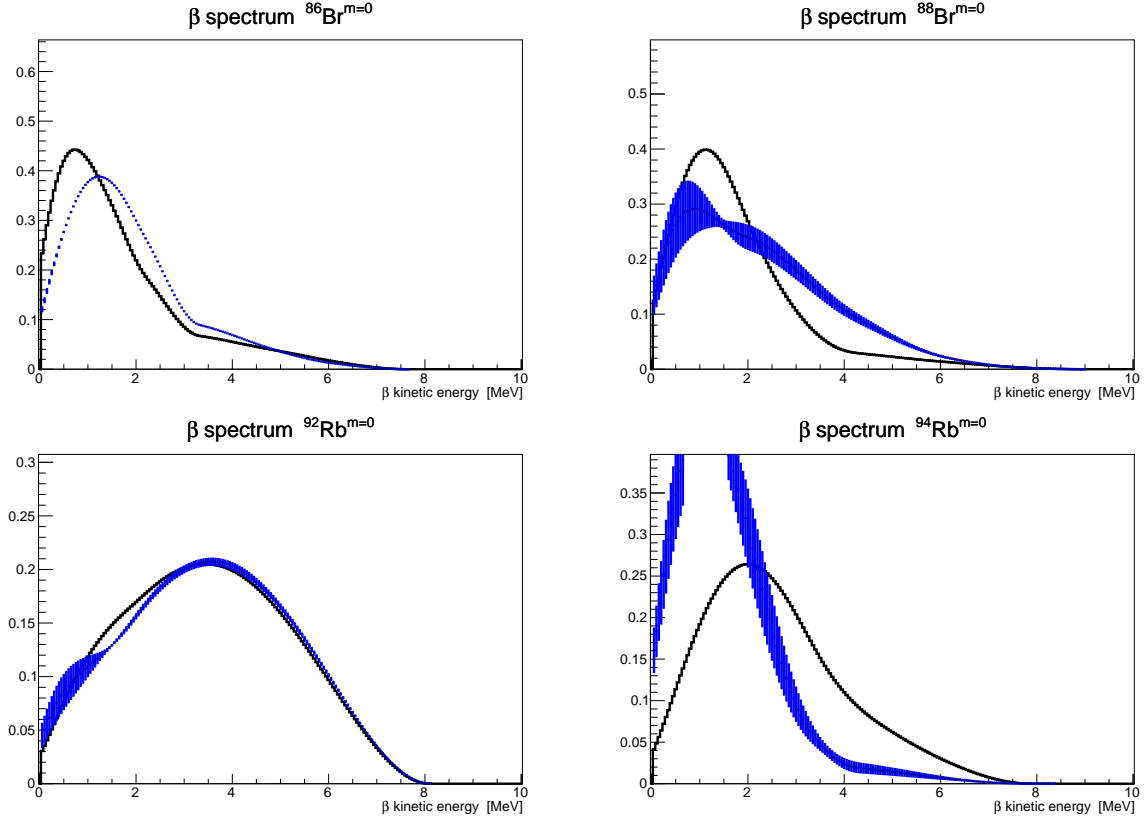


Figure 5.13 – Comparison between the electron energy spectra computed with BESTIOLE using ENSDF-2020 model-corrected data (blue) and TAGS data (black) for the same isotopes as those from figure 5.9. The HFB level densities are quenched with  $\alpha = 0.6$ .

clearly appears that the model for  $\alpha \sim 0.6$  is able to reproduce the deviation of the STEREO data to Huber-Mueller and absorb the shape anomaly.

We have also compared our model to the unfolded antineutrino energy spectrum measured by STEREO (Phase II + III), for  $\alpha = 0.6$ . As the unfolded STEREO spectrum is not yet normalized per fission, we normalized the model on the data as done in figure 5.7. The result is shown in figure 5.15 and indicates a very good agreement between the model and STEREO data. One should note that this result is very preliminary, since the correct procedure, which consists in taking into account the bin-to-bin correlations introduced by the regularization procedure of the unfolding process (see section 5.3), was not applied here.

Finally, when corrected from the *Pandemonium* effect and the missing nuclei in ENSDF-2020, the summation method gives access to the absolute antineutrino yield and the IBD cross section per fission defined in equation 5.1.3. Table 5.3 summarizes the IBD cross section per fission calculated with our model for different  $\alpha$  values and compared with Huber-Mueller. The best agreement is found for an  $\alpha$  value in the range of  $[0.5-0.6]$ , as expected from the previous discussion.

The advantage of the summation method is that it allows us to generate the antineu-

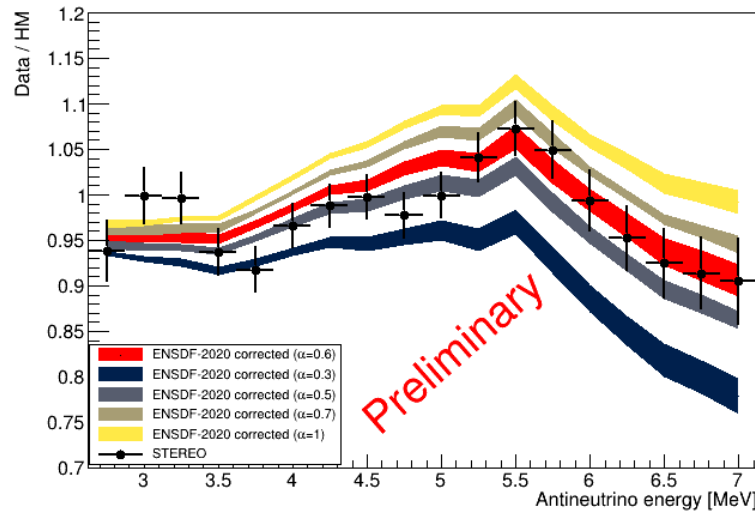


Figure 5.14 – Ratio of the antineutrino energy spectrum calculated with our model, for different  $\alpha$  values, and the Huber-Mueller one. As a comparison, the STEREO (phase II + III) ratio to Huber-Mueller is also plotted. This latter ratio is scaled by the 0.948 factor found in phase II (see section 5.1). The width of the lines indicate the standard deviation of the model due to the random process used to generate the beta-decay strengths.

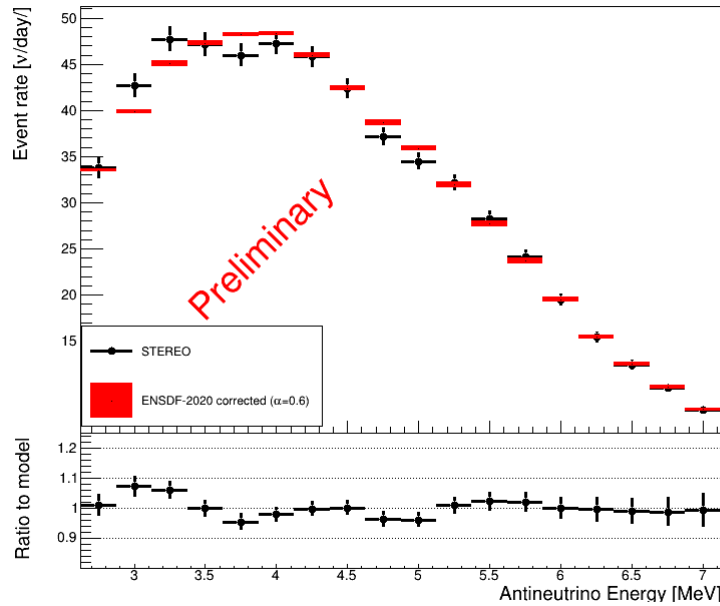


Figure 5.15 – Top: unfolded antineutrino energy spectrum measured by STEREO along with that predicted by our model ( $\alpha = 0.6$ ). The model is normalized to the data. Bottom: ratio of the Stereo data to our model. No uncertainty from our model is propagated, nor any bin-to-bin correlation introduced by the regularization process.

Data	IBD cross section ( $10^{-43}$ cm <sup>2</sup> /fission)	Number of electrons per fission in the [2-8] MeV range
$\alpha = 0$	5.67	1.038
0.3	6.16	1.098
0.5	6.41	1.123
0.6	6.55	1.140
0.7	6.69	1.154
1	7.02	1.188
Huber-Mueller	$6.69 \pm 0.15$	$1.197 \pm 0.022$

Table 5.3 – IBD cross section per fission and number of electrons per fission calculated with the model for different  $\alpha$  values.

trino and electron energy spectra on the same basis. Thus, we can perform the previous comparisons on the electron side as well. Table 5.3 summarizes the integrated number of electrons per fission in the [2-8] MeV range for different  $\alpha$  values. These results clearly point out towards a norm disagreement between the two models, which amounts to a value ranging between 0.938 and 0.952 for  $\alpha$  ranging in [0.5-0.6]. These values are compatible with the RAA and could explain its origin as a normalisation issue of the original electron energy spectra measured at ILL after 12h of irradiation [37], used as a reference for the Huber-Mueller model.

The comparisons of the model with the electron energy spectra are shown in figures 5.16 and 5.17 for  $^{235}\text{U}$ . There is a clear disagreement between our model, for all  $\alpha$  values, and the Huber-Mueller one. If we ignore the deviations above 7 MeV, which are due to some nuclei with high  $Q_\beta$  and intense transitions to the low-lying levels that cannot be reproduced in our statistical model, the antineutrino shape anomaly is now transformed into an electron shape anomaly. As observed in figure 5.17, such a deviation cannot be contained within the envelope defined by the systematic uncertainty associated to the  $^{235}\text{U}$  measurement [37]. This 90% C.L. uncertainty band was determined from the uncertainties and dispersion of the (n,e-) calibration reactions used to calibrate the electromagnetic spectrometer efficiency.

Further studies, out of the scope of this work, have to be pursued in order to improve the model, to test its compatibility with data, and to conclude on the origin of the anomalies.



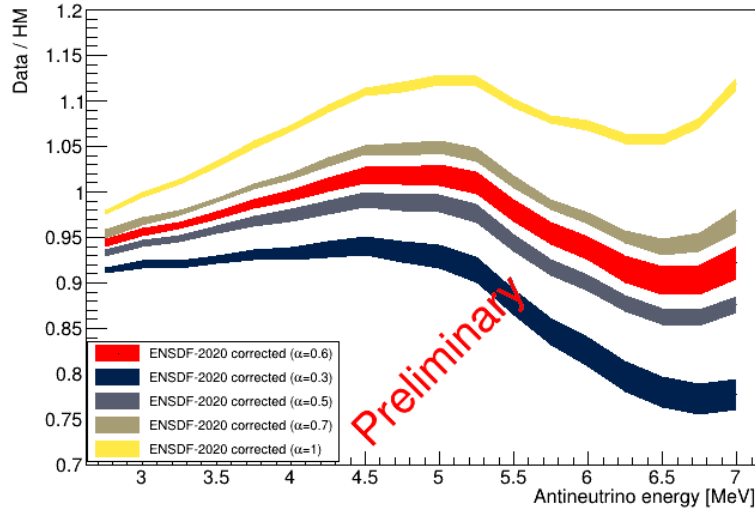


Figure 5.16 – Ratio of the electron energy spectrum calculated with our model, with different  $\alpha$  values, to the Huber-Mueller model for  $^{235}\text{U}$ . The width of the lines indicate the standard deviation of the model due to the random process used to generate the beta-decay strengths.

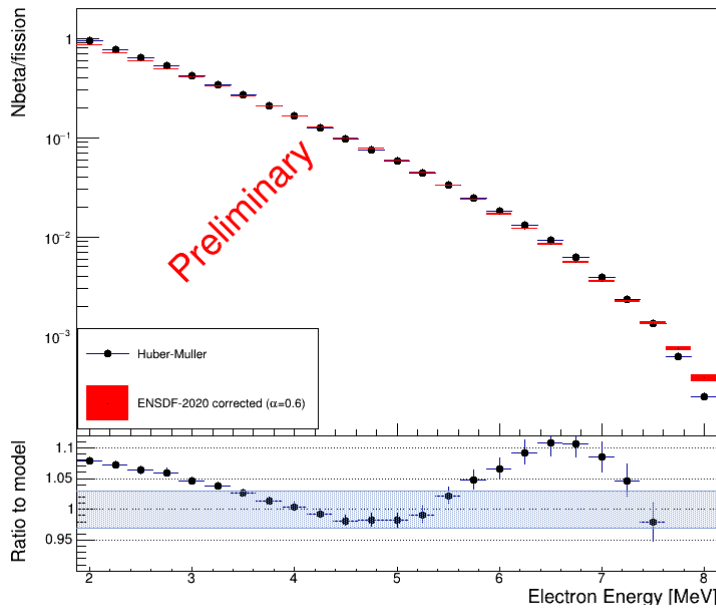


Figure 5.17 – Top:  $^{235}\text{U}$  Huber-Mueller electron energy spectrum along with that predicted by our model ( $\alpha = 0.6$ ). Bottom: ratio between Huber-Mueller and our model. The shaded band indicates the 90% C.L. systematic uncertainty associated to the Schreckenbach et al. data [37]. No uncertainty from our model is propagated.

## 5.5 Conclusion

The analysis of the STEREO data validates the  $\sim 6\%$  deficit observed in the total rate of reactor antineutrinos with respect to the predicted value, allows to reject the RAA best fit point at  $>99.99\%$  confidence level, and provides the most accurate pure  $^{235}\text{U}$   $\bar{\nu}_e$  spectrum, which features the previously observed  $\sim 5$  MeV bump.

We have developed a new prediction model based on the summation approach to test the origin of the anomalies. The model integrates a purely phenomenological beta-decay strength model to account for transitions towards highly excited daughter states (pygmy resonances) and generate transitions for nuclei with unknown transitions. The beta strength model follows the nuclear level densities and pygmy resonances are generated randomly based on a statistical study of the TAGS data.

Using this new prediction, we have shown that we are able to reproduce the antineutrino energy spectrum measured by STEREO. In this context, we have highlighted some deviations in the electron energy spectra with respect to the ILL electron spectra, which may point out that the origin of the anomaly resides in the normalisation of the original electron energy spectra measured at ILL.

Further studies are needed to conclude with certainty, but such an approach could help shed some light on the origin of the anomalies.

# Chapter 6

## NUCLEUS experiment

*"Whether you take the doughnut hole as a blank space or as an entity unto itself is a purely metaphysical question and does not affect the taste of the doughnut one bit."*

*Haruki Murakami*

### Sommaire

---

6.1	Experimental site . . . . .	174
6.2	Expected background . . . . .	175
6.3	Target detector and shielding . . . . .	175
6.4	Prototype design and performance . . . . .	178
6.5	Conclusion . . . . .	183

---

The NUCLEUS experiment is designed to measure the nuclear recoils induced by the coherent scattering of reactor antineutrinos off the nuclei of the cryogenic detectors employed as a target. It will be installed between the two 4.25 GW<sub>th</sub> reactor cores of the Chooz nuclear power plant, at a location where the expected antineutrino flux reaches  $10^{12} \bar{\nu}_e/(s \cdot cm^2)$ . The two main requirements to measure CE $\nu$ NS of reactor antineutrinos are a very low detection threshold and a fast time response, such that the detector could be operated in above-ground conditions.

The first section of this chapter will describe the experimental site, while the second one will treat the expected background at the detector's location. The next section provides a description of the detector and the shielding used to mitigate the environmental background. The last section presents the Muon Veto prototype that was built and tested at CEA Saclay, in the construction of which I also participated.

## 6.1 Experimental site

The NUCLEUS experiment will be placed in a 24 m<sup>2</sup> room situated in the basement of a five-story office building between the two nuclear reactors of the Chooz nuclear power plant, as illustrated in figure 6.1. This location will be referred to as the "Very Near Site" (VNS). The two distances separating the VNS from the reactor cores are of 72 m and 102 m. The mean shielding provided by the office building is of  $\sim 3$  m.w.e, justifying the need of sophisticated background rejection techniques. The two 4.25 GW<sub>th</sub> reactors emit a flux of  $\sim 16 \cdot 10^{20} \bar{\nu}_e/s$ , from which  $10^{12} \bar{\nu}_e/(s \cdot cm^2)$  reach the VNS.

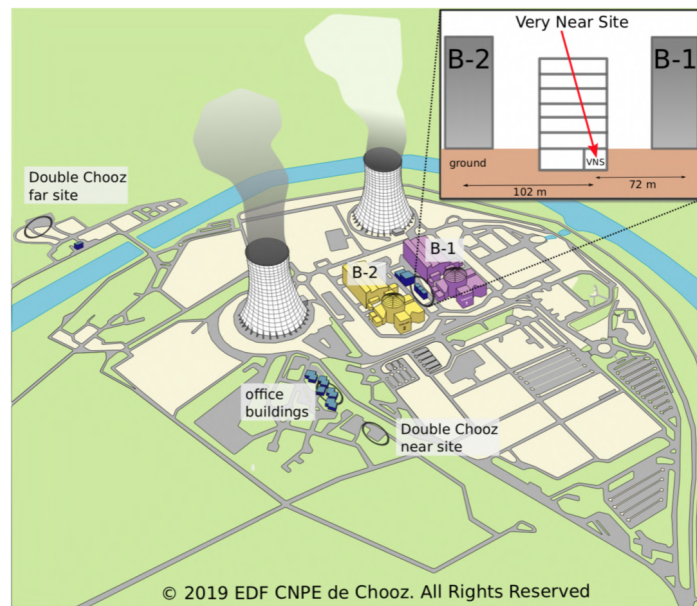


Figure 6.1 – Scheme of the Chooz nuclear power plant illustrating the placement of the NUCLEUS detector relative to the two nuclear reactors. Source: [133].

## 6.2 Expected background

The NUCLEUS experiment benefits from the high antineutrino flux coming from the two Chooz reactors. However, since it is placed in above-ground conditions, it has a very limited protection from the environmental background. It has been shown that the neutron background coming from the reactor core is negligible [133]. Thus, the relevant background sources, classified into external, internal and cosmic-ray induced background, will be briefly discussed in the following paragraphs

### External and internal background

This source of background is mainly made up of gamma-rays coming from the  $\alpha$ - and  $\beta$ -decaying nuclides present in the decay chains of  $^{232}\text{Th}$ ,  $^{238}\text{U}$ ,  $^{235}\text{U}$  and  $^{40}\text{K}$ , which are found in the materials surrounding the experiment, and of ambient neutrons created in nuclear ( $\alpha, n$ ) reactions. We classify as internal background any particle that is produced following the decay of an unstable nuclide found inside the target detector. This type of events can be reduced by using highly pure materials for the target crystal growth.

### Cosmic-ray induced background

This source of background is mainly made up of muons and neutrons, as already discussed in chapter 2 for STEREO. Neutrons, either atmospheric or produced by muon-induced spallation, are a particularly dangerous background, since they produce the same experimental signature (a nuclear recoil) as the searched  $\text{CE}\nu\text{NS}$  events<sup>1</sup>. A measurement campaign performed in 2018 [133] quantified the muon and neutron flux reduction at the experimental site compared to the surface. It was shown that the neutron flux is attenuated by a factor of  $(8.1 \pm 0.4)$ , while the muon flux is attenuated by a factor of  $(1.41 \pm 0.02)$ . It is worth noting that muons can also represent a dangerous background. They can either decay in the proximity of the target detector and give rise to an electron or a positron or be absorbed by a  $^{12}\text{C}$  nucleus and create an excited  $^{12}\text{B}$  that  $\beta$ -decays afterwards with a mean lifetime of  $\sim 20$  ms (see the discussion about the  $^{12}\text{B}$  beta spectrum from section 3.3.3).

## 6.3 Target detector and shielding

The NUCLEUS detector is composed of three calorimetric systems operating at a temperature of  $\sim 10$  mK, obtained using a dry dilution refrigerator. The target detector is encapsulated into a cryogenic inner and outer veto, which operate as anticoincidence

---

<sup>1</sup>More precisely, neutrons with an energy of the order of a few keV can produce similar nuclei recoils as the ones expected for the antineutrinos.

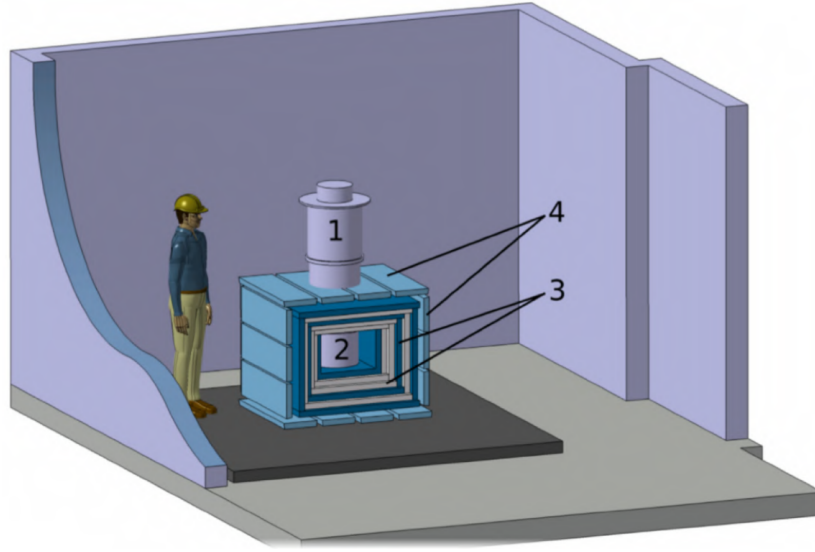


Figure 6.2 – Depiction of the main components of the NUCLEUS experiment: 1) the dry dilution refrigerator, 2) the experimental volume containing the target and the inner and outer veto, 3) the external passive shielding, 4) the active Muon Veto. Source: [133].

detectors in order to suppress the background. Moreover, the experimental volume is surrounded by passive and active shielding in order to further mitigate the background. A schematic drawing of the NUCLEUS setup is shown in figure 6.2. The first phase of the experiment, called NUCLEUS-10g, aims at using a detector with a 10 g  $\text{CE}\nu\text{NS}$  target, while later phases that aim at increasing the target mass to 1 kg are foreseen. While NUCLEUS-10g could measure the  $\text{CE}\nu\text{NS}$  cross section with a  $\sim 10\%$  accuracy within few years of measurement time, NUCLEUS-1kg could reach a percent-level precision in the same time period [133].

### Target detector

The target detector is composed of an array of cryogenic calorimeters with a mass of  $\sim 1$  g, made of the crystalline materials  $\text{CaWO}_4$  and  $\text{Al}_2\text{O}_3$ , illustrated in figure 6.3 together with the cryogenic inner and outer veto. The crystals are operated at a temperature of  $\sim 10$  mK, where their heat capacity  $C$  is very small. In these conditions, a particle scattering inside the detector, which deposits an energy  $\Delta E$ , can induce a temperature rise  $\Delta T = \Delta E/C$  big enough to be read using thin-film tungsten transition edge sensors (TES). Using a  $(5 \times 5 \times 5)$  mm<sup>3</sup> cubic crystal prototype detector, an unequalled threshold of  $E_{th} = (19.7 \pm 0.9)$  eV was reached [134], which is one order of magnitude lower than that of previous experiments. The fact that NUCLEUS uses two targets,  $\text{CaWO}_4$  and  $\text{Al}_2\text{O}_3$ , allows for an in-situ background characterization. While the  $\text{CE}\nu\text{NS}$  scattering rate is strongly enhanced for  $\text{CaWO}_4$  (since the cross section is proportional to  $N^2$ , see equation 1.5.1), we expect that fast neutrons induce comparable signals in both crystals due to scattering on  $O$  nuclei. Another advantage of the multi-target detector is that it can reject background events that produce coincident signals in several detectors, since  $\text{CE}\nu\text{NS}$  events are expected to undergo a single scattering.

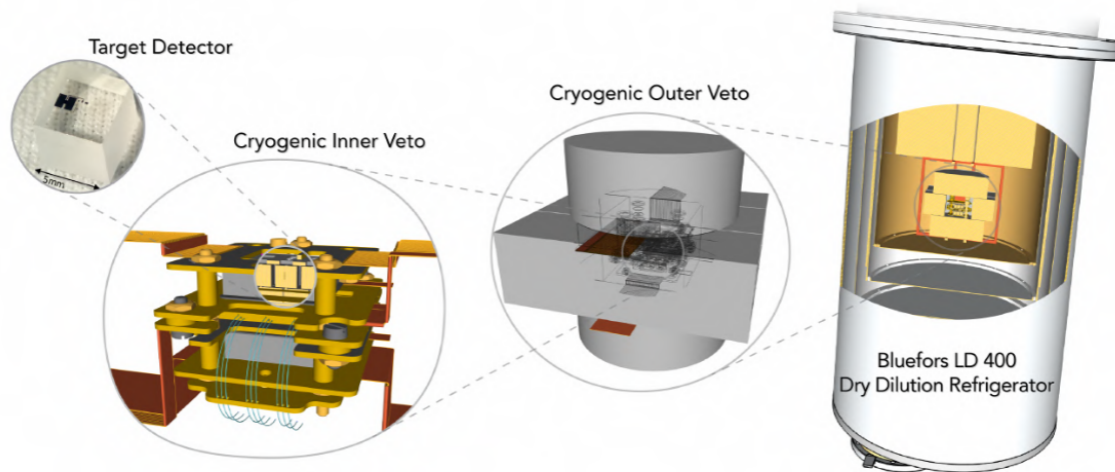


Figure 6.3 – Illustration of the NUCLEUS experimental volume (first picture from the right) with detailed zoom-in on its sub-components. One of the cryogenic calorimeters of the target detector is shown in the first picture from the left. An active inner veto provides an almost  $4\pi$  coverage of the target detector and helps reducing the  $\alpha$  and  $\beta$  surface contaminations (shown on the second picture from the left). Both the target and the inner veto are encapsulated by the outer veto, which is responsible for suppressing ambient  $\gamma$  and neutron backgrounds (third picture from the left). Source: [135].

### Passive shielding

Since NUCLEUS aims to achieve a background rate of  $10^2$  counts/(keV·kg·day) in the sub-keV region of interest, a layered external passive shielding will surround the experimental volume. Its main scope is to reduce the muon-induced backgrounds, of which the secondary neutrons are the most dangerous. The inner layer of the passive shielding is made out of borated polyethylene and its role is to moderate and absorb neutrons, while the outer layer is made out of lead, which highly reduces the gamma-ray background. A thickness of 5 cm is envisaged for the lead layer in order to keep at a minimum the number of neutrons created by muon-induced spallation inside the lead.

### The Muon Veto

In addition to the passive shielding discussed previously, a Muon Veto is needed to actively reject the cosmic muons. With a cosmic muon rate at the earth's surface of  $\sim 100$  Hz/m<sup>2</sup>, the expected flux of muons passing through the experimental setup is of  $\sim 700$  Hz. However, the fast rise-time of the cryogenic detectors used in NUCLEUS, which governs the overall detector dead time, indicates that detector dead times of only  $\sim 1$ -2% can be obtained.

To reach the required background rate of  $10^2$  counts/(keV·kg·day) in the sub-keV region of interest, we estimate that a very high muon detection efficiency of more than 99% is needed. To achieve this number, we need to be able to efficiently distinguish between gammas and muons and to obtain a nearly complete solid angle coverage of the NUCLEUS target detector and passive shielding. Since the amplitude of the signal produced by a traversing muon in a plastic scintillator is proportional to the energy deposited within it, the discrimination power between gammas and muons increases with the thickness of the plastic scintillator. Another important requirement that needs to be satisfied by the Muon Veto is a high uniformity of the light yield over its whole volume. The NUCLEUS Muon Veto will consist of 24 single organic plastic scintillator panels, arranged to form a cube around the target detector and the passive shielding, with a thickness of 5 cm each, and encapsulated in light-tight stainless steel boxes with a thickness of 1 mm.

A Muon Veto prototype has been designed and tested at CEA Saclay with the goal to prove that the requirements of NUCLEUS can be met. The details about the design and performance of the prototype, in the construction of which I also participated, will be presented in section 6.4. The next chapter will present a set of simulations aimed at studying the efficiency of the full Muon Veto for different experimental configurations, which represent the main participation of the present thesis to the NUCLEUS collaboration.

## 6.4 Prototype design and performance

### Muon Veto prototype: design and test stand

A muon deposits  $\sim 2$  MeV/cm when traversing a polyvinyltoluene (PVT)-based plastic scintillator. Taking into account that the gamma rays coming from the natural radioactivity have a maximal energy of 2.6 MeV (from  $^{208}\text{Tl}$ ), we chose to use a 5 cm thick plastic scintillator (BC-408 from Saint-Gobain [136]) for the prototype tested at CEA Saclay.

The scintillation light produced in the plastic scintillator is partly absorbed by wavelength shifting fibers (BC-91A from Saint-Gobain [137]) installed in shallow grooves that run along the length of the Muon Veto panel prototype. Inside the fibers, the light is re-emitted at a longer wavelength and transmitted by total internal reflection towards a SiPM module (PE3325-WB-TIA-SP from KETEK [138]) that is installed at the end of the fibers. The wavelength shifting fibers were chosen such that their absorption spectrum matches the transmission spectrum of the plastic scintillator, and their re-emission spectrum matches the range of high photo detection efficiency of the SiPM. A picture of the plastic scintillator with the fibers and SiPM installed, taken during its assembly, can be seen on the left hand side of figure 6.4.

Several fiber configurations were tested during the R&D of the NUCLEUS Muon Veto prototype. The two most relevant configurations are shown in the right hand side of figure 6.4



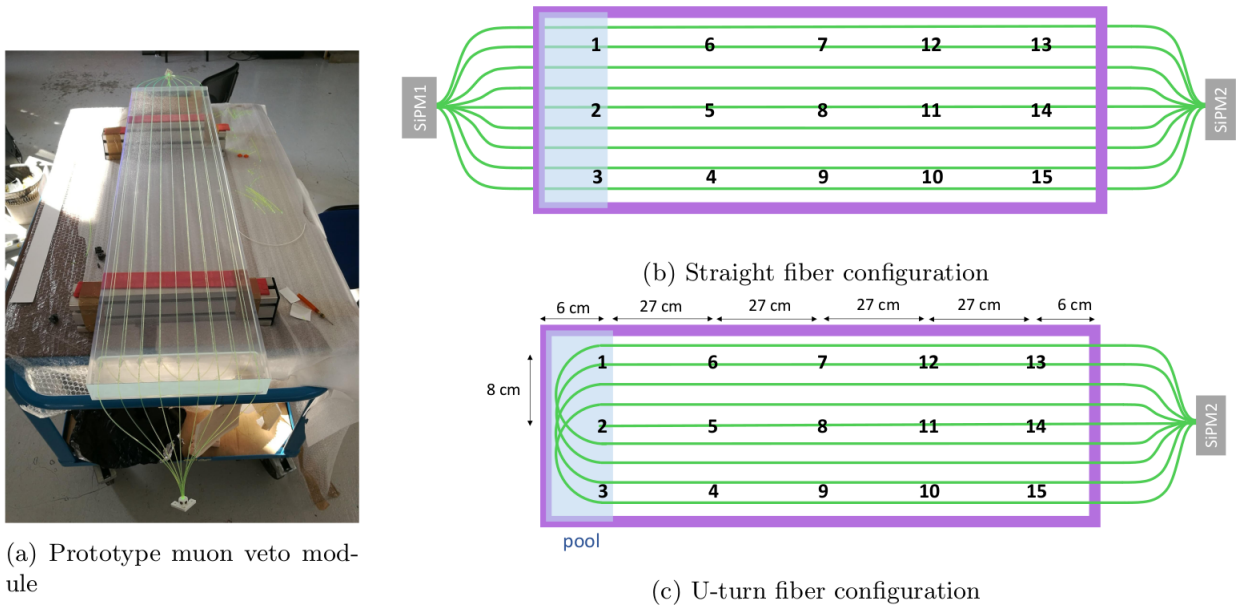


Figure 6.4 – (a) Picture of the prototype panel showing the side with the straight fiber configuration. The schemes of the straight and U-turn fiber configurations are shown in (b) and (c). Source: [139].

1. **The straight fiber configuration:** the nine fibers are positioned in straight lines and are read at both ends by SiPMs.
2. **The U-turn fiber configuration:** four fibers describe a U-turn on one side of the plastic scintillator and re-enter the groove with a radius of 6 cm, while a straight fifth fiber is placed in the middle groove; in this configuration, the fibers are read only at one end.

The prototype plastic scintillator that was developed at CEA Saclay features the straight fiber configuration on one side, and the U-turn configuration on the other side. Finally, it is covered with diffusive foil to increase the light collection and enclosed in an Aluminum light-tight box.

While the straight fiber configuration is expected to be the most efficient in terms of light collection, it has two disadvantages: it needs a second SiPM and it implies additional un-instrumented volume inside the Aluminum box. The U-turn fiber configuration solves the two shortcomings of the straight fiber configuration, but, in this case, one expects that light might be lost due to attenuation (the fibers are significantly longer in this configuration) and the bending of the fibers.

A dedicated test stand, shown in figure 6.5, was built to characterize the performance of the prototype. The prototype (middle panel) is placed between two 1.6 m-long plastic scintillator panels, denoted top and bottom panel, which are each coupled to a PMT. A triple coincidence between the three panels allows to select muon events passing through the prototype. Moreover, a triple coincidence between a small plastic scintillator with

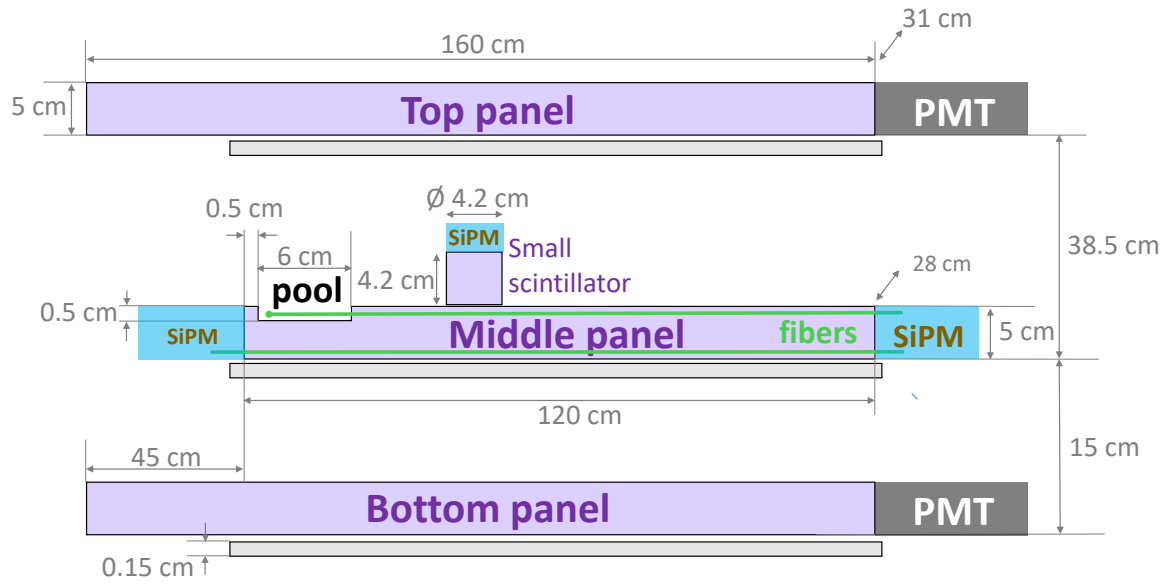


Figure 6.5 – Muon veto test stand. The middle panel is the prototype built at CEA Saclay. The blue area on the middle panel delimits the non-instrumented part of the Aluminum box where the SiPM modules are placed. Source: [139].

a diameter of 4.2 cm and 4.2 cm height, read-out with a SiPM, the prototype, and the bottom panel, allows to select muons passing through a defined volume of the prototype.

### SiPM calibration

In order to monitor the stability of the SiPM performance and to be able to compare the different fiber configurations, one needs to calibrate the SiPM. The goal of the calibration is to convert the measured charges of the integrated SiPM signals into a number of detected photons (NPE).

Inside a SiPM, the absorption of a photon can give rise to a macroscopic current flow. The amount of charge created by a detected photon depends on the applied overvoltage<sup>2</sup> and is measured by the gain. In our case, we used the large dark count rate of the SiPM to determine the gain. In fact, at an overvoltage of 5 V, we expect a rate of  $\sim 1$  MHz thermally excited electrons that can produce measurable currents in the SiPM. The signal produced by these electrons is identical to the one produced by the electrons extracted following a photon absorption, and can be used to extract the gain of the SiPM. Finally, the gain is extracted by fitting the charge spectrum of dark counts, shown on the left hand side of figure 6.6, with a model similar to the one from [140], to which an exponential

<sup>2</sup>The overvoltage is defined as the difference between the applied bias voltage and the breakdown voltage, which is the bias voltage above which the absorption of a photon can be converted into a macroscopic current flow by the SiPM. For the SiPM used for the Muon Veto prototype, the breakdown voltage lies between 24 V and 25 V at 21° [138].

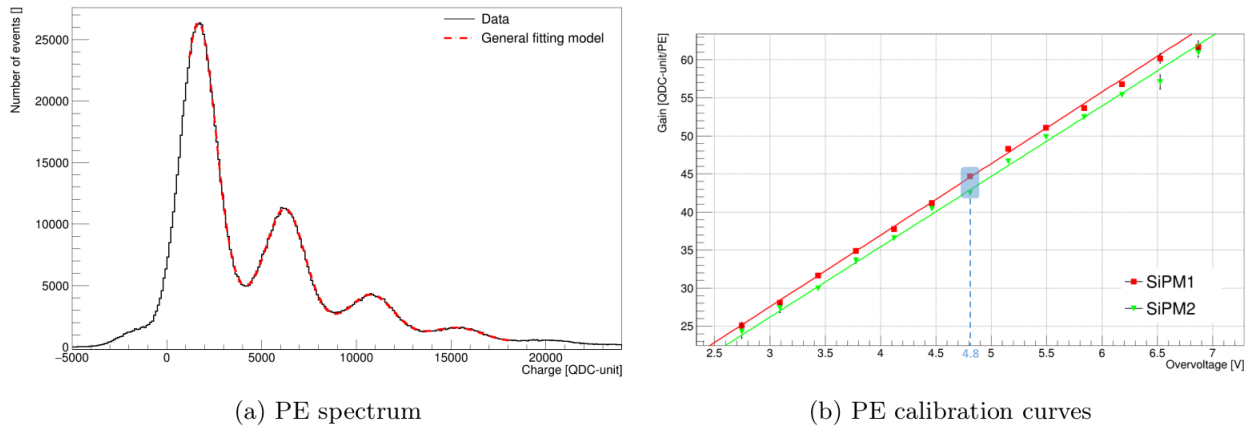


Figure 6.6 – (a) Charge spectrum of dark counts measured at an overvoltage of 4.8 V, where the peaks corresponding to one, two, three and four photo-electrons are visible. (b) Gain calibration curves of the two SiPMs as a function of the overvoltage. Source: [139].

background is added. The gain as a function of the overvoltage, for the two SiPMs used for the prototype, is shown on the right hand side of figure 6.6. As expected, it increases linearly with the overvoltage and thus allows us to convert the charge spectra into NPE spectra.

### Prototype performance

Figure 6.7 shows the muon+background (obtained by triggering on events in the prototype panel itself that surpass a certain threshold) and muon (obtained by triggering on coincidences between the top, middle and bottom panels) spectra for the straight fiber configuration. Looking at the muon+background spectrum, we observe three features

- a gamma background which increases abruptly when approaching the threshold.
- a Landau-like distribution populated by muon events, whose most probable value corresponds to vertical muons passing through the 5 cm thickness of the scintillator.
- a well defined plateau separating the two previous populations.

In the following we will discuss the light yield and the muon identification efficiency for the two studied fiber configurations. The light yield (LY) is defined as the number of photo-electrons (NPE) generated for an energy deposit of 1 MeV. It is determined as the ratio between the position of the muon peak in NPE and the expected position of the muon peak in MeV (determined by a dedicated GEANT4 Monte Carlo simulation [141] of the full test stand), and is shown in the first column of table 6.1 for the two studied fiber configurations. The muon identification efficiency is defined as the fraction of selected muons (red line from figure 6.7 for the straight fiber configuration) that are

above a threshold of 5 MeV (blue vertical line from figure 6.7), which is well above the highest gamma energy coming from natural radioactivity (2.6 MeV), and is shown in the second column of table 6.1 for the two studied fiber configurations. While the light yield is significantly bigger for the straight fiber configuration, it can be seen that the muon identification efficiency is similar for the two configurations, but smaller than the required 99% efficiency. However, in the case of the full Muon Veto, which will cover almost entirely the experimental setup, most of the muons pass through multiple plastic scintillator panels, thus increasing the overall muon tagging efficiency to values  $>99\%$ , as will be proved in the next chapter.

Configuration	LY [NPE/MeV]	$\epsilon$ [%]
Straight fiber	$47.47 \pm 0.02$	$97.15 \pm 0.01$
U-turn configuration	$32.13 \pm 0.02$	$96.36 \pm 0.01$

Table 6.1 – Light yield (LY) and muon identification efficiency  $\epsilon$  for a threshold of 5 MeV for the two studied fiber configurations.

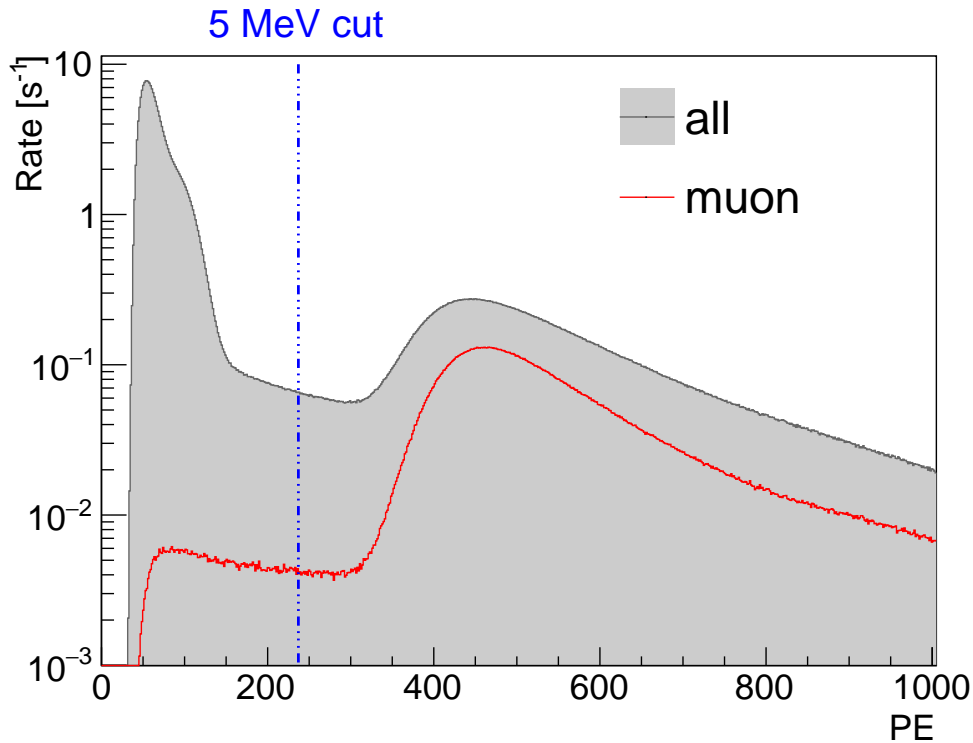


Figure 6.7 – The full spectrum (grey area) and muon spectrum (red line) for the straight fiber configuration (obtained as the calibrated sum of the two SiPMs). Source: [139].

## 6.5 Conclusion

This chapter presented the NUCLEUS experiment and emphasized the need of a highly efficient Muon Veto to reject the expected muon-induced background. In addition to that, we have also presented a Muon Veto prototype designed and built at CEA Saclay and discussed its performance. The prototype studies shown that we can accurately discriminate the muons from the gamma background, with an accuracy of 96-97%, depending on the fiber configuration that is used. The next chapter, representing the main contribution of this thesis to the NUCLEUS experiment, will be dedicated to a set of geometrical muon track simulations aimed at estimating the overall efficiency of the full Muon Veto and optimizing its geometrical configuration.



# Chapter 7

## Muon tracks simulations

*"Il ne faut pas uniquement intégrer. Il faut aussi désintégrer. C'est ça la vie.  
C'est ça la philosophie. C'est ça la science. C'est ça le progrès, la civilisation."*

*Eugène Ionesco*

### Sommaire

---

<b>7.1</b>	<b>Simulation framework . . . . .</b>	<b>186</b>
7.1.1	Geometry . . . . .	186
7.1.2	Simulation algorithm . . . . .	190
7.1.3	Energy loss implementation . . . . .	192
<b>7.2</b>	<b>Observables of interest: efficiency &amp; stopping muons . . . . .</b>	<b>198</b>
7.2.1	Efficiency . . . . .	198
7.2.2	Normalization of the simulation . . . . .	204
7.2.3	Veto muon rate . . . . .	205
7.2.4	Stopping muons . . . . .	207
<b>7.3</b>	<b>Sensitivity studies . . . . .</b>	<b>208</b>
7.3.1	Cryogenic Muon Veto . . . . .	208
7.3.2	Hollow Cylindrical Muon Veto . . . . .	209
7.3.3	Further improvements of the geometry of the Muon Veto . . . . .	211
<b>7.4</b>	<b>Conclusion . . . . .</b>	<b>213</b>

---

The muon tracks simulations were developed to assess the performances of the Muon Veto in terms of rejection efficiency and to test different geometrical configurations meant to optimize its design.

Initially, the simulations were of a purely geometrical nature and were performed using the TGeometry package of ROOT. The advantage of the TGeometry package is that it runs independently to any tracking Monte Carlo engine and it is thus not constraint by physics considerations. The muons were generated using an energy-independent generator that only takes into account their angular distribution. However, as the simulation was also used to estimate the rejection efficiency of the Muon Veto in experimental conditions of energy threshold, realistic muon energy spectra and energy loss calculations were later implemented in the simulation.

The first section of this chapter is dedicated to the simulation framework: the geometry and the simulation algorithm will be presented. The second section will define the observables of interest, the efficiency and the number of stopping muons, and will discuss their values for the default geometrical configuration of the Muon Veto. Finally, in the last section we will explore different improvements that can be brought to the geometry of the Muon Veto and discuss their impact on the observables of interest.

## 7.1 Simulation framework

### 7.1.1 Geometry

We present here the default geometry based on the technical drawings of the individual NUCLEUS components. Later on we will explore slight modifications of the default geometry and evaluate their impact on the observables of interest: the efficiency and the rate of stopping muons. Within the TGeometry framework, the basic bricks for constructing the geometry are called volumes. The volumes represent the un-positioned pieces of the geometry to be built and they possess well defined properties, such as a medium, a shape and dimensions. They are placed one inside another and thus create an in-depth hierarchy. Hence, there needs to be a "mother" volume that contains all the other volumes and which is denoted as the "world". The positioned volumes are called nodes and they reference both a volume and a transformation which serves to position the volume inside the hierarchy of volumes.

The Muon Veto (see figure 7.1) is composed of 6 sides that will be denoted as: Top, Bottom, Front, Rear, Side A and Side B panels. Each of the 6 sides is composed of 4 individual plastic scintillator panels. The 16 individual panels contained in the Front, Rear and Side panels have a parallelepipedic shape (see figure 7.2) while the 8 individual panels contained in the Top and Bottom panels have a trapezoidal shape (see figure 7.3). Such a shape was chosen for the Top and Bottom panels in order to minimize the number of muons that would pass through the gap between the individual plastic scintillator panels and thus would not be tagged by the Muon Veto if we used parallelepipedic shaped



panels. Another thing to be noticed in figures 7.2 and 7.3 is the fact that the gap between the individual plastic scintillator panels is smaller in the case of the Bottom panel (the same applies for the Top panel) than in the case of the Side panels (the same applies for the Front and Rear panels). This is because all the individual plastic scintillator panels that compose the Top and Bottom panels are placed in a single stainless steel box, while the individual plastic scintillator panels that compose the Side, Front and Rear panels are each placed inside a single stainless steel box. Moreover, the Top panel presents a circular hole through which the cryogenic arm that will hold the bolometer is supposed to enter (see figure 7.4). We expect that the presence of such a hole would decrease the overall efficiency of the Muon Veto. In order to limit the effect of the hole on the overall efficiency, a plastic scintillator cylinder, which will be denoted as a Cryogenic Muon Veto, is placed inside the cryogenic arm at the level of the Top panel. The impact of the Cryogenic Muon Veto and of its misalignment with respect to the Top panel will be evaluated in section 7.3.

For the muon tracks simulations, two shielding types have been implemented (see figure 7.1): a lead shielding, composed of an exterior lead shielding and a cylinder of lead inside the cryogenic arm, and a polyethylene shielding, composed of an exterior polyethylene shielding and a cylinder of polyethylene inside the cryogenic arm. These shielding volumes are important in the muon energy deposition calculation, whose goal is to compute the number of stopping muons inside the different volumes composing the Muon Veto and inside the shielding. Moreover, the lead shielding will also be used to give a realistic definition of the efficiency, as it will be explained in section 7.2. A list of the Muon Veto and of the shielding volumes of the default geometry, as well as their "daughters" (copies in the table) can be found in Table 7.1, along with their relevant dimensions.

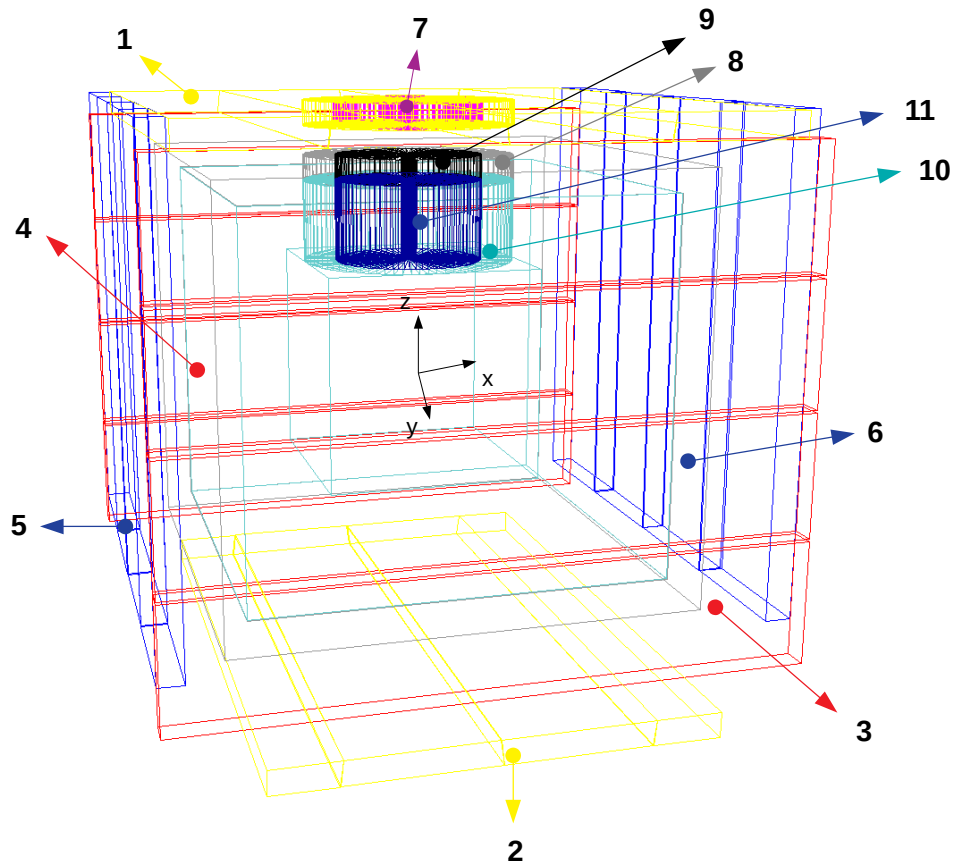


Figure 7.1 – The default geometry used for the muon tracks simulations is composed of plastic scintillator panels and lead and polyethylene inner and outer shielding. A bigger volume, with a cubic shape, denoted the "world", contains all the other volumes of the geometry. The "world" volume is not plotted here. Legend: 1) Top Muon Veto Panel, 2) Bottom Muon Veto Panel, 3) Front Muon Veto Panel, 4) Rear Muon Veto Panel, 5) Side Muon Veto Panel A, 6) Side Muon Veto Panel B, 7) Cryogenic Muon Veto (Inner Active Shielding), 8) Lead Outer Passive Shielding, 9) Lead Inner Passive Shielding, 10) Polyethylene Outer Passive Shielding, 11) Polyethylene Inner Passive Shielding.



Figure 7.2 – View of the individual plastic scintillator parallelepipedic panels composing the Side panels (a similar panel shape is used for the Front and Rear panels).



Figure 7.3 – View of the individual plastic scintillator trapezoidal panels composing the Bottom panel (a similar panel shape is used for the Top panel).

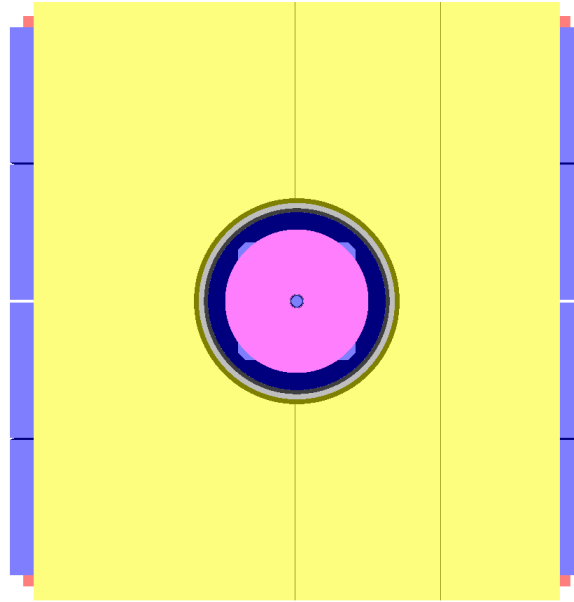


Figure 7.4 – Top view of the Muon Veto. The hole through which the cryogenic arm will enter is apparent. The cryogenic Muon Veto is depicted in purple.

Table 7.1 – List of the default geometry volumes along with the number of associated copies. In the case where a volume doesn't have copies, the shape of the respective volume is put between parentheses in the Muon Veto volumes column. The individual plastic scintillator panels have either a parallelepipedic or a trapezoidal shape. The dimensions are given in the (x×y×z) format only for the Muon Veto panels. For the shielding volumes, we only give the relevant dimensions.

Muon Veto volumes	Copies	Dimensions [cm]
Top Muon Veto Panel	4	24.9(25.55)×125×5
Bottom Muon Veto Panel	4	30.28(28.96)×125×5
Front Muon Veto Panel	4	120×5×24.125
Rear Muon Veto Panel	4	120×5×24.125
Side Muon Veto Panel A	4	5×28.25×96
Side Muon Veto Panel B	4	5×28.25×96
Cryogenic Muon Veto (Inner Active Shielding)(cylinder)	-	$R_{max} = 15 \quad dz = 5$
Lead Outer Passive Shielding (hollow cube with hole)	-	$width = 5$
Lead Inner Passive Shielding(cylinder)	-	$R_{max} = 15 \quad dz = 5$
Polyethylene Outer Passive Shielding (hollow cube with hole)	-	$width = 20.25 \times 20 \times 16.5$
Polyethylene Inner Passive Shielding(cylinder)	-	$R_{max} = 15 \quad dz = 16.5$

### 7.1.2 Simulation algorithm

This section will explain the functioning of the muon tracks simulation code and will present the observables that are registered for a simulated experiment. Muons are generated and tracked until they exit the "world". For each muon event or track, several observables are registered in a tree structure.

The first step of the muon tracks simulation code is the generation of muons. The philosophy behind the muon generation code is based on the Choozerent library that was implemented in Geant4 by the NUCLEUS collaboration. The muons are randomly generated on planes tangent to a demi-sphere of a given radius centered on the Muon Veto, such that the whole volume of the Muon Veto is populated by muons of a given direction defined by the polar and azimuthal angles  $\theta$  and  $\phi$ , as it can be seen in figure 7.6. The plane's point of tangency coordinates,  $\theta$  and  $\phi$ , are drawn in a  $\cos^2\theta$  and a uniform distribution respectively, such that the muons' directionality replicates the realistic behaviour of atmospheric muons, as illustrated in figure 7.5.

After being generated, the muon propagates in a straight line until it exits the "world", at which point a new muon will be generated and tracked. The muon propagation is done in steps. At each step, the distance between the current position of the muon and the frontier of the next volume found on the muon's direction is computed. Then, the muon's position is updated and it becomes

$$\vec{r}_{i+1} = \vec{r}_i + \vec{d}_{i,i+1}$$

where  $\vec{r}_i$  represents the current position of the muon,  $\vec{r}_{i+1}$  represents the position of the muon after performing the step and the distance  $\vec{d}_{i,i+1}$  is the sum of the distance between the current position of the muon and the frontier of the next volume found on the muon's direction, and a small  $\epsilon$  factor, which ensures that the muon's new position,  $\vec{r}_{i+1}$ , is well inside the next volume encountered on its trajectory.

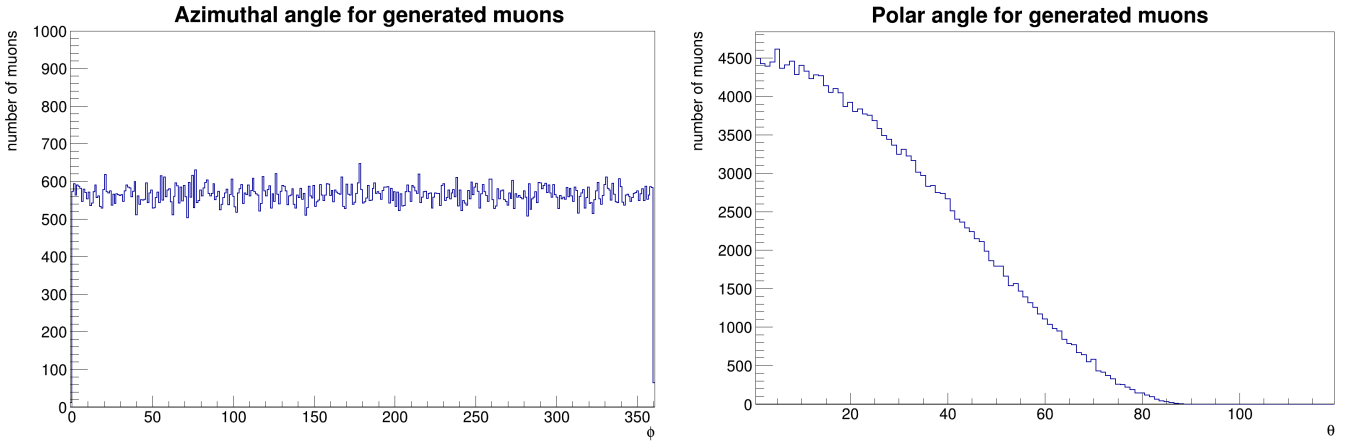


Figure 7.5 – Azimuthal and polar angle distributions for the generated muons.

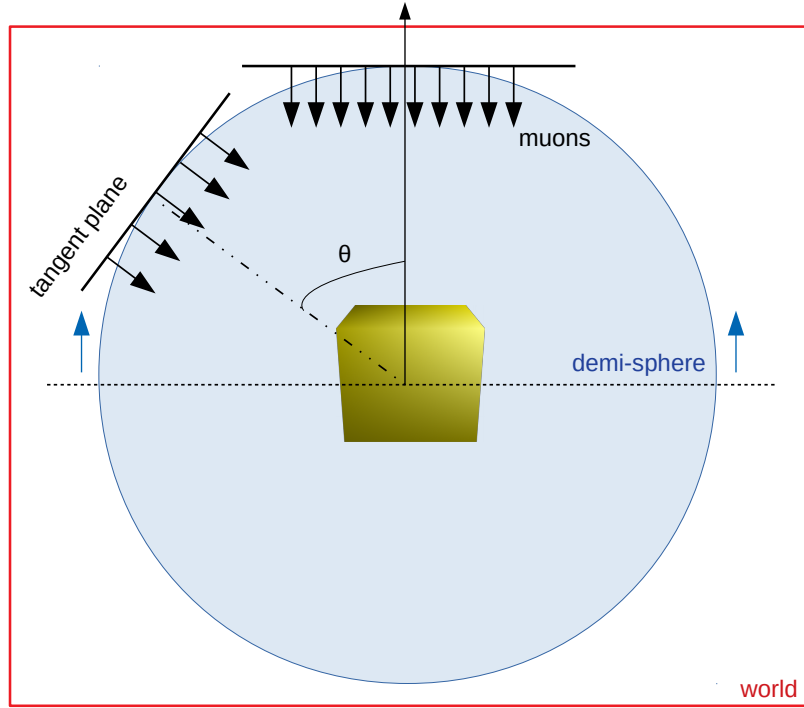


Figure 7.6 – 2D scheme illustrating the functioning of the muon generator used within the muon tracks simulations. The density of arrows representing muons in the figure is proportional to the  $\cos^2\theta$  distribution for illustration purposes.

The step approach propagation of the muons allows us to store information about the "state" of the muon at every step, i.e. in every volume. For a given muon event we store the track length in every traversed volume, as well as the material from which the traversed volume is made of, which will be useful later when computing the energy loss of the muons in every volume (see section 7.1.3). A plot of the total track length inside the Muon Veto can be found in figure 7.7. It can be seen that the total track length distribution has a structure that is particular to the geometrical arrangement of the Muon Veto's plastic scintillator panels. The mean total track length is of 17.4 cm. For example, the 1<sup>st</sup> peak in figure 7.7, which is situated around 5 cm, is populated mostly by muons that traverse the thickness of one plastic scintillator (which is equal to 5 cm, see table 7.1). Another interesting example is the peak number 4, situated around 96 cm, which is populated by muons traversing vertically one of the individual vertical plastic scintillator panels composing the Side panels. Most of these muons also have a Muon Veto multiplicity equal to 1. The majority of the muons enter the detector through the Top Panel and exit through the Bottom panel, thus traversing  $\sim 10$  cm of plastic scintillator, as it can be seen by looking at the 2<sup>nd</sup> peak in figure 7.7.

Moreover, boolean variables were defined, which store information about the different traversed media by the muon track. These boolean variables will be useful when computing the efficiency of the Muon Veto, as it will be explained in section 7.2. Another stored observable is the multiplicity for every medium, which tells us how many times a given

medium was traversed by the muon track. It can be observed in figure 7.8 that about 80% of the muon tracks traverse at least two plastic scintillator panels and thus have an increased probability to be tagged. The maximal Muon Veto multiplicity is equal to 8 and it can be attained for muons entering the Muon Veto at the level of the intersection between two plastic scintillator panels of the Top panel, then traversing the 4 plastic scintillator panels of the Front or Rear panels and exiting at the level of the intersection between two plastic scintillator panels of the Bottom panel.

### 7.1.3 Energy loss implementation

The goal of the Muon Energy Loss Script is to use the results of the purely geometrical muon tracks simulations in order to estimate the muons' energy deposition inside the volumes composing the Muon Veto and the shielding. In order to do this, the information about the track length of the simulated muons through every traversed volume, as well as the material of every traversed volume will be used. Knowing the energy deposition inside every volume will allow us to compute the number of stopping muons inside the Muon Veto and inside the shielding and thus to have a more realistic estimation of the Muon Veto efficiency.

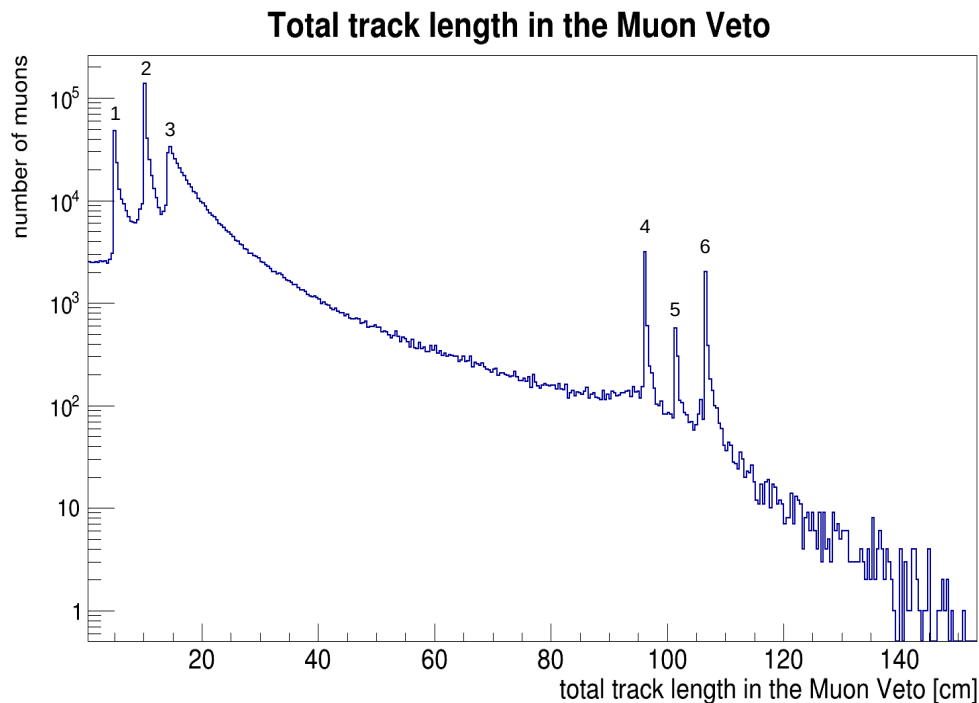


Figure 7.7 – Total track length in the Muon Veto. Several peaks can be distinguished in the plot. The numbers above the peaks are used to identify them in the text.

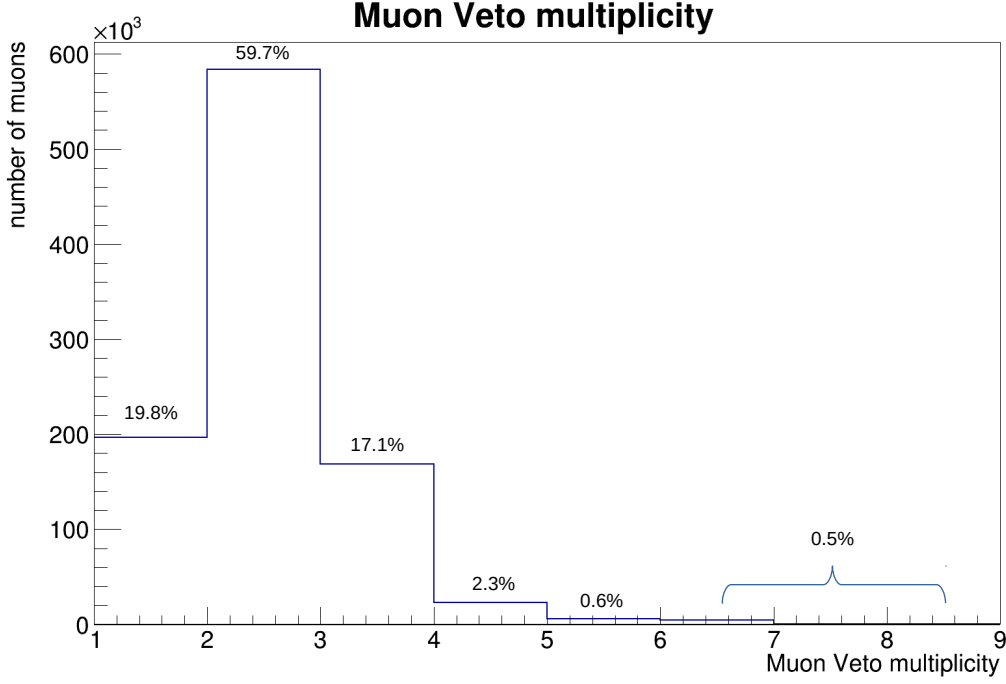


Figure 7.8 – Muon Veto multiplicity, i.e number of plastic scintillator panels traversed by the muon track. The percentage of the total simulated muon tracks for every given multiplicity is marked on the plot.

The first step of the Muon Energy Loss Script is to assign to each muon track an energy drawn from a realistic energy spectrum. In order to define this realistic energy spectrum we have used the absolute vertical flux of atmospheric muons at the sea level in the momentum range 0.6-400 GeV/c, measured by the BESS-TeV Spectrometer [142], which we fitted with a theoretical energy distribution of atmospheric muons at the sea level [143]. The fit function that was used follows a power law in energy  $E^{-n}$ , slightly modified in the low and high energy regions

$$\Phi(E) = \Phi_0 N (E_0 + E)^{-n} \left(1 + \frac{E}{\epsilon}\right)^{-1} \quad (7.1.1)$$

where  $\Phi_0$  is the vertical muon flux integrated over energy,  $N$  is a normalization factor,  $E_0$  is a parameter which accounts for energy loss due to both the hadronic as well as the electromagnetic interactions with air molecules of the atmosphere and  $\epsilon$  is a parameter that modifies the flux in the high energy part and that should account for the finite lifetime of pions and kaons.

Figure 7.9 shows the atmospheric muon energy spectrum superposed with the fitted function from equation 7.1.1. The muons' energies are drawn from the fitted function in the energy range [0.1,20] GeV. We have chosen this range because the probability for a

muon to have an energy bigger than 20 GeV is negligible. One should note that even though the experimental spectrum begins at 0.6 GeV, we extrapolate the fitted spectrum down to 0.1 GeV when drawing the energy of the muons.

Several approximations have been made concerning the muon energy spectrum from which we draw the energy of the muons. Firstly, we have used an experimental spectrum of vertical muons, while the muons in our code are generated on planes tangent to a demi-sphere, as explained in section 7.1.2. Experimentally, the muon spectra for  $\theta > 0$  are shifted towards higher energies with respect to the muon spectrum for  $\theta = 0$  and thus our approximation means that we attribute on average smaller energy values for muons with  $\theta > 0$ . This means that we may overestimate the number of stopping muons inside the Muon Veto and inside the shielding. However, this overestimation does not represent a problem for us since the energy loss study presented in this chapter is a means of estimating the number of stopping muons for different geometrical arrangements and thus, it is the relative changes in the number of stopping muons in which we are the most interested. Moreover, an overestimation in the number of stopping muons is equivalent with an underestimation of the efficiency. Thus, a validation of the experimental setup in these conditions will allow us to be conservative with respect to the results expected in the real conditions of the data taking.

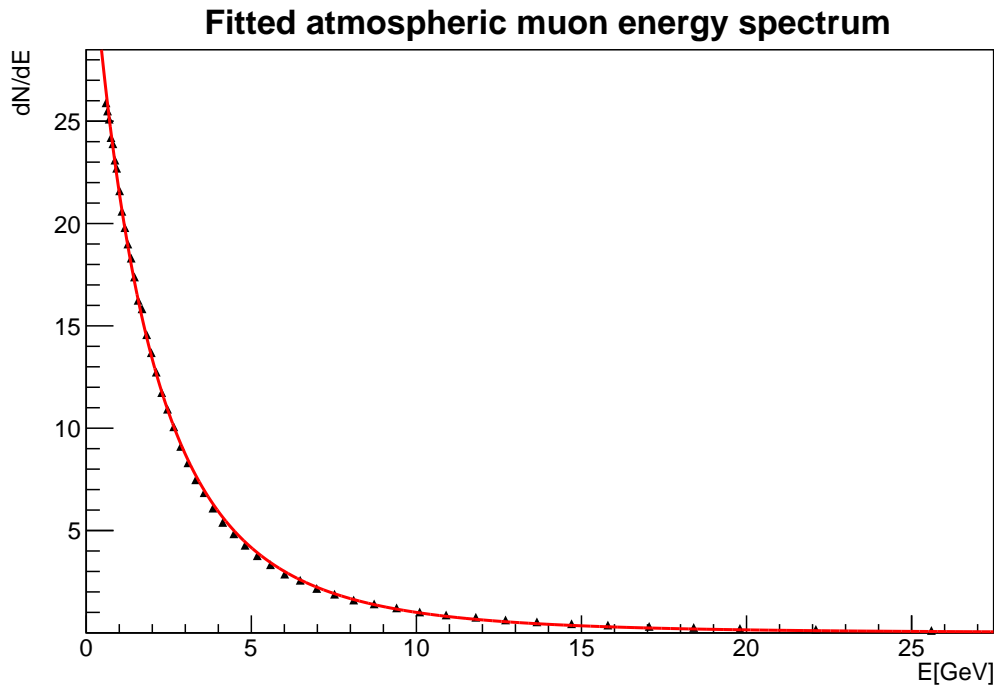


Figure 7.9 – Fitted experimental atmospheric muon energy spectrum used for assigning energies to the muon tracks. The experimental data [142] are shown with black triangles while the fitted function is plotted in red. One could observe the good agreement between the experimental data and the fitted function in the displayed energy region. The energies attributed to the muon tracks are drawn from the [0.1,20] GeV range of the fitted spectrum.



After attributing an energy to the muon track we are able to compute the deposited energy in every volume. The computation is done by steps, in the sense that we divide the total track length in steps of equal length  $dx=0.01$  cm. In order to compute the energy deposited in a volume of a given material for a length equal to the step length we use the Bethe-Bloch formula [144] for relativistic charged particles<sup>1</sup>

$$\left\langle -\frac{dE}{dx} \right\rangle = K z^2 \frac{Z}{A} \frac{1}{\beta^2} \left[ \frac{1}{2} \ln \frac{2m_e c^2 \beta^2 \gamma^2 W_{max}}{I^2} - \beta^2 \right] \quad (7.1.2)$$

where  $z$  is the charge of the incident particle,  $\beta$  is the velocity of the incident particle,  $Z$  is the charge number of the medium,  $A$  is the atomic mass of the medium and  $\gamma$  is the Lorentz factor.  $W_{max}$  denotes the maximum energy transfer in a single collision and  $I$  is the mean excitation energy of the medium. In order to determine  $I$  for the different materials composing the Muon Veto and its shielding we have used an interpolation method applied on the experimental curve of  $I(Z)$  found in [144].

Equation 7.1.2 describes the mean rate of energy loss in the region  $0.1 < \beta\gamma < 1000$  for intermediate- $Z$  materials with an accuracy of a few percent. One should note that equation 7.1.2 represents the mass stopping power and its units are  $\text{MeV} \cdot \text{g}^{-1} \cdot \text{cm}^2$ . In order to obtain the linear stopping power in  $\text{MeV} \cdot \text{cm}^{-1}$  one has to multiply equation 7.1.2 by the density of the medium in which the particle is depositing energy,  $\rho$ , measured in  $\text{g} \cdot \text{cm}^{-3}$ . It is the linear stopping power that we then multiply by the step length  $dx=0.01$  cm at each step in order to compute the mean energy loss per step. A muon that loses all its kinetic energy inside our defined geometry is denoted as a stopping muon.

In our defined geometry there are 3 different material types: Polyvinyltoluene for the plastic scintillator panels, Lead and Polyethylene for the shielding. Table 7.2 summarizes the material properties relevant to the energy deposition computation.

After having computed the mean energy loss in every traversed volume for a muon we want to compute the "real" deposited energy and its equivalent in NPE (number of photoelectrons) for the plastic scintillator panels.

Table 7.2 – Material properties that are used when computing the mean energy loss with the Bethe-Bloch formula 7.1.2. For the composite materials, the mean value of  $Z$  and  $A$  is given in the table.

Material	Atomic composition	Density [ $\text{gcm}^{-3}$ ]	$\langle Z \rangle$	$\langle A \rangle$	$I$ [eV]
Lead	Pb	11.35	82	207.2	818.82
Polyethylene	$[C_2H_4]_n$	0.92	5.28	10.43	62.10
Polyvinyltoluene	$[CH_2CH(C_6H_4CH_3)]_n$	10.023	5.58	11.08	70.94

<sup>1</sup>One could note that we do not include the density-effect correction in  $\delta(\beta\gamma)$  in the equation that we are using. This effect becomes important at high energies and is negligible for the range of energies that we are using in our simulation.

To do that we define an effective model that allows us to convert the deposited energy computed with the Bethe-Bloch equation into a number of photoelectrons (NPE) detected by the SiPMs. This model has two parameters: the width  $w$  of the Landau distribution that characterizes the distribution of deposited energies centered on the mean deposited energy given by the Bethe-Bloch equation, and a conversion factor  $c$  (NPE/MeV) that transforms the value in MeV in a number of photoelectrons (NPE). Finally, the NPE value given by the Landau distribution is convolved with a Gaussian distribution in order to take into account the photoelectron statistical fluctuations.

There are two parameters that need to be fine tuned to obtain the NPE spectra in the plastic scintillator panels, the conversion factor  $c$  and the width of the Landau function  $w$ . In order to do so we perform the muon tracks simulation for the prototype setup geometry shown in figure 6.5 and then we compute the NPE spectrum inside the middle plastic scintillator panel, which is the prototype detector that we are testing. We consider only muons that pass through the bottom plastic scintillator shown in figure 6.5 and through the small SiPM placed at the center of the middle plastic scintillator, i.e. in position 8 shown in figure 6.4. We then compare this simulated NPE spectrum with the experimental NPE spectrum obtained in the same configuration (coincidence between the bottom plastic scintillator panel with the small SiPM placed in position 8) and fine tune the parameters  $c$  and  $w$  such that the simulated NPE spectrum matches at best the experimental NPE spectrum. Figure 7.10 shows such a comparison between the experimental and simulated NPE spectra in the case in which the prototype plastic scintillator is read at both ends and the summed signal is converted into NPE. It can be seen that the simulation can reproduce well the experimental spectrum in the peak region after fine tuning the  $c$  and  $w$  parameters of the Landau function. However, the simulation does not reproduce well either the small plateau found at low NPE or the queue of the experimental spectrum. The excess in the data at high NPE could be due to cosmic showers or to multiple muons traversing the detector simultaneously, while the excess at low NPE could come from events other than muons.

After the fine tuning of the  $c$  and  $w$  parameters, we can obtain the simulated NPE spectra in every plastic scintillator volume. Having access to the NPE spectra for every plastic scintillator panel will also allow us to apply a realistic detection threshold, inspired by the experimental spectra, on the number of NPE and thus estimate the efficiency more realistically.

Figure 7.11 shows the simulated NPE spectra obtained using the Landau  $c$  and  $w$  fine-tuned parameters deduced from the comparison between the experimental NPE spectrum and the simulated NPE spectrum for a coincidence between the small SiPM and the bottom PM. It can be seen that, for the bottom panels, shown in green and yellow in figure 7.11, the NPE spectrum is similar to the one obtained for the prototype and shown in figure 7.10. This is because the bottom panels are positioned similarly with the prototype plastic scintillator with respect to the muon flux. Furthermore, the position of the muon peak for the vertical side plastic scintillator panel and for the horizontal front plastic scintillator panel is shifted towards higher NPE values. This is explained by the orientation of these plastic scintillator panels with respect to the muon flux. If the mean track length for the bottom plastic scintillator panels is of about 5.7cm, the mean track

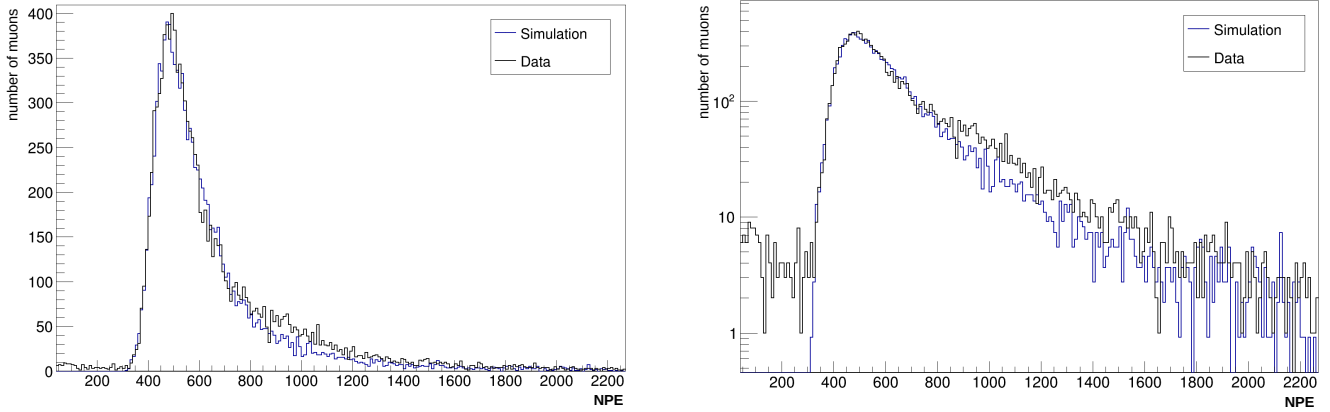


Figure 7.10 – Comparison between the simulated and experimental NPE spectra in the case in which the prototype plastic scintillator is read at both ends and we convert the summed signal into NPE. The right plot is in log Y scale. The simulation reproduces well the main region of the muon peak but does not reproduce the small plateau found at low NPE or the queue of the experimental spectrum.

length for the side and front plastic scintillator panels is higher and thus the deposited energy and consequently the corresponding NPE are higher. This also translates into a wider distribution, with a bigger proportion of events in its queue. Moreover, it can be observed that for the horizontal front plastic scintillator panel there are two visible peaks. The events forming the first peak are coming from vertical muons that traverse the plastic scintillator panel in the  $z$  direction while the events forming the second peak are coming from muons that traverse the panel in the  $x$  direction (see figure 7.1 for the coordinate system).

We summarize here the steps of the energy deposition script for a single event (muon track)

1. Retrieve the track lengths through every traversed volume as well as the material of every traversed volume from the output file of the muon tracks simulation.
2. Attribute an energy drawn from a realistic atmospheric muon spectrum to the muon track.
3. Compute the deposited energy in every traversed volume using the Bethe-Bloch formula. If the muon deposits all its kinetic energy before exiting the experimental setup it is tagged as a stopping muon.
4. Convert the deposited energy in NPE and then convolve this value with a Landau and a Gaussian function; when a muon traverses a plastic scintillator panel, fill the histogram corresponding to the traversed volume with the NPE value obtained earlier. At the end we will have the NPE spectra corresponding to every plastic scintillator volume.

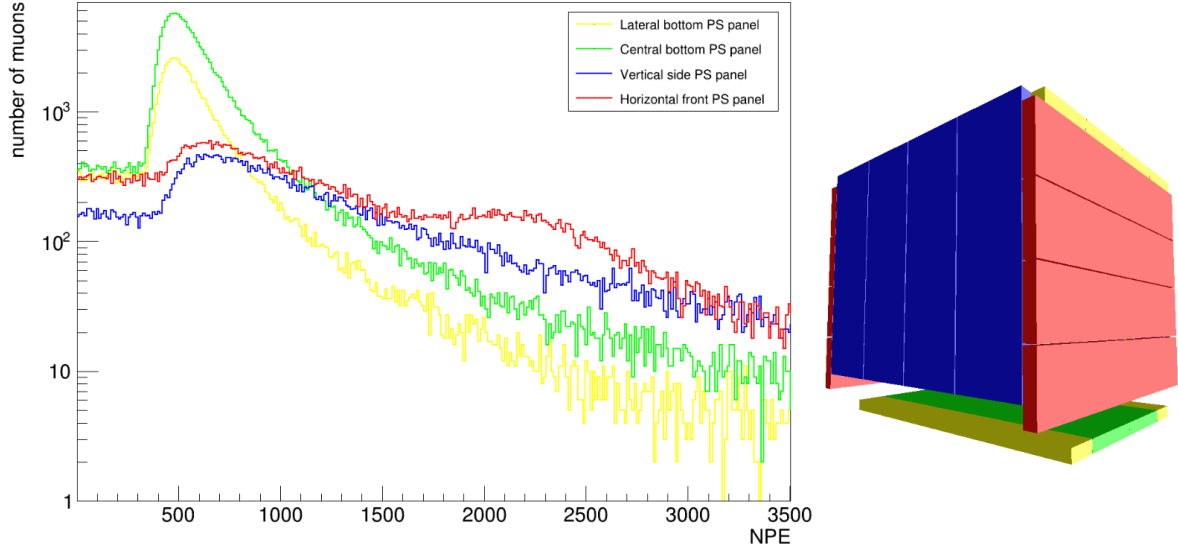


Figure 7.11 – NPE spectra inside the different panels composing the Muon Veto; PS stands for plastic scintillator. It can be seen that the position of the muon peak for the vertical side plastic scintillator panel and for the horizontal front plastic scintillator panel is shifted towards higher NPE values with respect to the position of the muon peak for the bottom plastic scintillator panels.

## 7.2 Observables of interest: efficiency & stopping muons

In this section we will present the definition of the two observables of interest: the efficiency and the rate of stopping muons and show the results of the simulation for the default Muon Veto geometry. All the results that will be presented subsequently are derived from simulations of  $2 \cdot 10^6$  muon tracks, from which about  $10^6$  pass through the experimental setup.

### 7.2.1 Efficiency

The muon tracks simulation allows us to compute the efficiency of the Muon Veto. We will present here two different definitions for the efficiency, one that relies only on the physical volumes of the defined geometry and another one that relies on the definition of an additional "fictitious volume". The fictitious volume is defined as a volume that tightly encloses the whole Muon Veto setup. It is called fictitious because it does not exist in reality. It has two purposes: firstly, as we said earlier, it will be used in one definition of the efficiency; secondly, only the information about the muons that pass through the fictitious volume will be written to the output file, thus reducing its final size.

The efficiency defined via the fictitious volume will be denoted by  $\epsilon_{fictitious}$  and has the following definition

$$\epsilon_{fictitious} = \frac{\text{number of muons traversing the scintillator volumes}}{\text{number of muons traversing the fictitious volume}} \quad (7.2.1)$$

This definition of the efficiency is sensitive to all the muons that enter the fictitious volume but are not seen by the Muon Veto, i.e they do not pass through any of the plastic scintillator panels. We obtain  $\epsilon_{fictitious} = 99.21\%$  for the default geometry configuration. There are two main types of muons that can traverse the fictitious volume containing the Muon Veto geometry without passing through any plastic scintillator panel, as shown in figure 7.12, where we have plotted the intersection points between the muon tracks and the traversed volumes

1. Muons that pass through one of the corners of the fictitious volume, region which is not covered by plastic scintillator panels. These muons do not pass the Muon Veto "barrier" and thus do not have a harmful potential of creating background events that could mimic the neutrino-nucleus scattering signal expected by NUCLEUS. The only way in which they could be harmful would be to create neutrons by spallation reactions inside the concrete underneath the detector. We expect that there is a very small probability that these created neutrons reach the bolometer exactly in the energy region in which the signal is expected. However, this type of effects exceeds the scope of the current study and would be better explored by performing Geant4 complete simulations.
2. Muons that enter the experimental setup either through the circular top hole or through the gaps between the plastic scintillators forming the Top Panel and exit either through the bottom corners not covered by plastic scintillators or through the gaps between the plastic scintillators forming the Bottom Panel. However, since the plastic scintillators forming the Top and Bottom panels have a trapezoidal form and the gap between them is of only 1 mm, it is highly improbable for muons to traverse the Top and Bottom panels undetected. This leaves us with a majority of muons that enter through the circular hole in the Top Panel and exit through one of the 4 bottom corners not covered by plastic scintillator panels. These muons represent the most dangerous muon background source for NUCLEUS, since they can either decay<sup>2</sup> inside the shielding close to the bolometer and give rise to an  $e^-$  or a  $e^+$  or be captured<sup>3</sup> by a  $^{12}\text{C}$  nucleus and create an excited  $^{12}\text{B}^*$  that will then beta decay with a mean lifetime of about 20 ms, which is much longer than the foreseen veto gate ( $\sim 50\mu\text{s}$ ).

The second definition of the efficiency, which will be denoted by  $\epsilon_{physical}$ , takes into account only the potentially harmful muons for the experiment, namely the ones that penetrate the lead or polyethylene shielding and get close to the bolometer. This definition is based only on the physical volumes of the Muon Veto and gives us information about

---

<sup>2</sup> $\mu^\pm \rightarrow e^\pm + \nu_e + \nu_\mu$   
<sup>3</sup> $\mu^- + ^{12}\text{C} \rightarrow ^{12}\text{B}^* \rightarrow ^{12}\text{C} + e^- + \bar{\nu}_e$

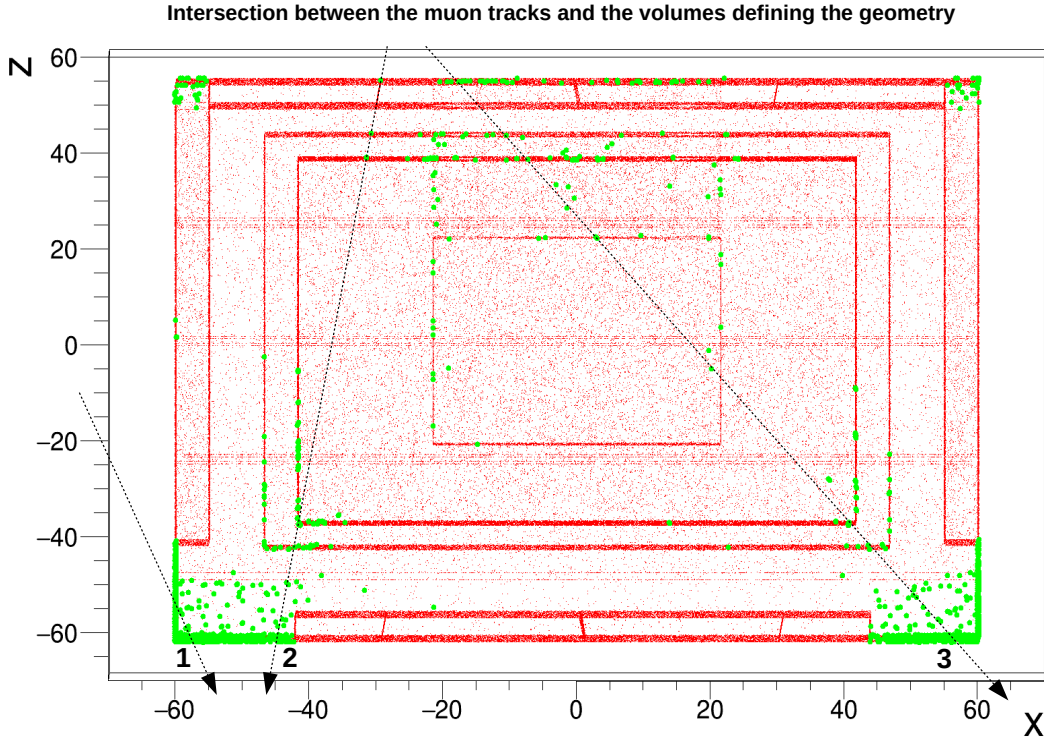


Figure 7.12 – Front view of the intersection points between the muon tracks and the traversed volumes. In red are depicted the muons that traverse at least one plastic scintillator panel and in green are depicted the muons that enter the fictitious volume surrounding the Muon Veto but do not pass through any plastic scintillator panel. Three particular examples are marked with arrows on the plot: 1) a muon that passes through a bottom corner of the fictitious volume and then exits the fictitious volume without passing through any plastic scintillator panel; 2) the rare case of a muon entering through the gap between the Top plastic scintillator panels and exiting through one of the bottom corners not covered by plastic scintillator panels; 3) a muon entering through the circular hole in the Top Panel and exiting through one of the bottom corners not covered by plastic scintillator panels.

the number of muons that passed through the Lead shielding<sup>4</sup> but were not seen by the plastic scintillator panels, i.e they did not traverse any plastic scintillator volume

$$\epsilon_{physical} = \frac{\text{number of muons traversing the scintillator volumes AND the Lead}}{\text{number of muons traversing the Lead}} \quad (7.2.2)$$

We expect  $\epsilon_{physical}$  to have a bigger value than  $\epsilon_{fictitious}$  since we are no longer taking into account the muons that were traversing the fictitious volume at the Top and Bottom

<sup>4</sup>We chose to use the Lead shielding in this definition because it is the closest physical volume to the plastic scintillator panels.

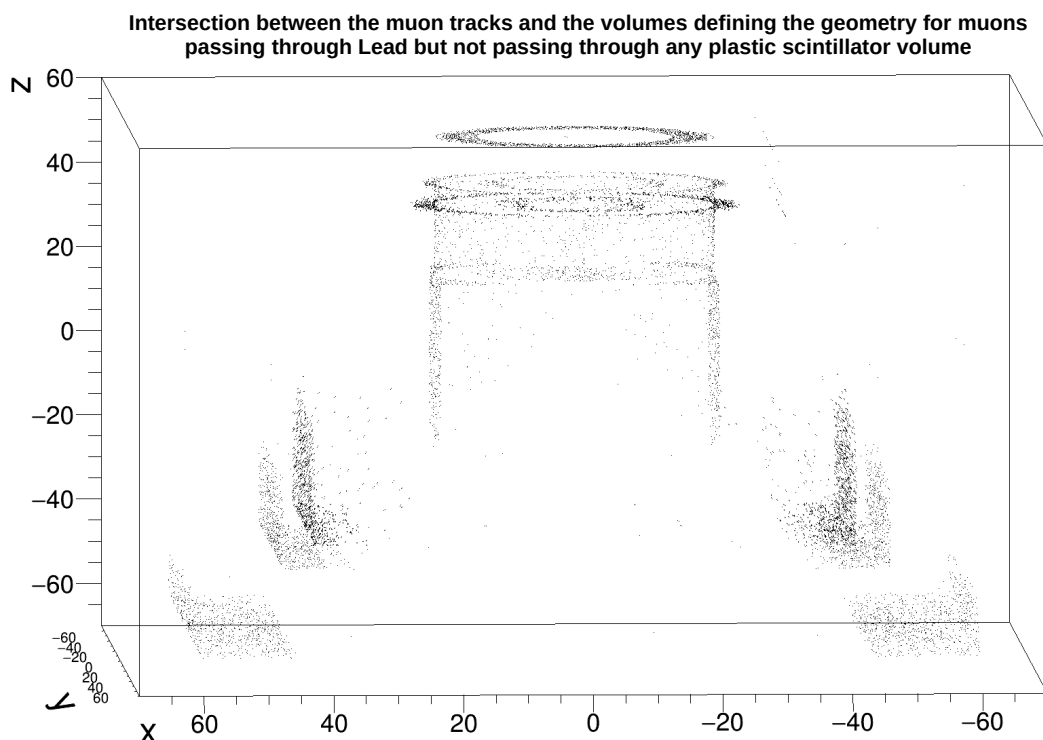


Figure 7.13 – View of the intersection points between the muon tracks and the traversed volumes for muons that passed through the Lead but didn't pass through any plastic scintillator volume. The top circular ring representing the intersection between the muon tracks and the fictitious volume reflects the fact that most of the muons that pass through the lead and are not seen by the Muon Veto enter the experimental setup through the hole in the Top Panel and exit through one of the side bottom corners.

corners (see figure 7.12). Indeed, we obtain  $\epsilon_{physical} = 99.60\%$  for the default geometry configuration. This means that  $\sim 0.4\%$  of the muons pass through the Lead and are not seen by the Muon Veto. The majority of these muons enter the experimental setup through the Top Panel circular hole and exit through one of the side bottom corners, as seen in figure 7.13.

### Uncertainty on the efficiency estimation

In order to estimate the statistical uncertainty on the computed efficiency values for the default geometry of the Muon Veto we have repeated 20 times the muon tracks simulation, with  $2 \cdot 10^6$  events for each simulation, and computed the mean value and standard deviation for both  $\epsilon_{fictitious}$  and  $\epsilon_{physical}$ :

- $\bar{\epsilon}_{fictitious} = 96.18 \pm 0.02$
- $\bar{\epsilon}_{physical} = 99.61 \pm 0.01$

Such an uncertainty estimation is important to be able to say if the difference in efficiency is more likely due to the change in the geometrical configuration rather than a fluctuation due to the limited number of simulated events, namely  $2 \cdot 10^6$  in our case, when comparing two different geometrical configurations of the Muon Veto. Finally, we can conclude that the used MC statistics is high enough to look for sub-% variations of the efficiency.

### Realistic efficiency and threshold

The numbers presented earlier for the two efficiency definitions,  $\epsilon_{fictitious} = 96.21\%$  and  $\epsilon_{physical} = 99.60\%$ , are ideals, since they do not take into account any detection threshold of the plastic scintillators themselves. In fact, besides the muon signal, the plastic scintillators also detect background particles coming from the environmental natural radioactivity. Most of the background is represented by neutral particles with energies of about  $\sim 1$  MeV. Since the maximal gamma energy from the natural radioactivity is of 2.6 MeV ( $^{208}Tl$ ), we can clearly separate the background from the muon events, which are centered on  $\sim 10$  MeV. In order to optimize the dead time of the experiment we would like to minimize the number of times in which we are tagging on background events.

Figure 6.7 shows a muon spectrum obtained by asking for a coincidence between the top and bottom PM signals of the prototype setup shown in figure 6.5. It can be seen that there is roughly a factor of 2 between the center of the background plateau and the muon peak position. Since the width of the plastic scintillator used as a prototype to measure muon energy deposits is of 5 cm and since most of the muons traversing the plastic scintillator are almost vertical, we can deduce that the center of the background plateau corresponds to muons whose track length is of  $\sim 2.5$  cm. These considerations allow us to apply a threshold on the muons' track lengths in our simulations in order to have a more precise estimate of the efficiency. Consequently, we can impose that a muon's track length is of at least 2.5 cm in at least one of the traversed plastic scintillator panels for it to be considered as detected by the Muon Veto.

Another improvement of the efficiency precision is to take into account the energy deposition inside the Muon Veto plastic scintillator panels and inside the Lead and Polyethylene shielding, as explained in section 7.1.3. In order to do so, we converted the deposited energy spectra in every plastic scintillator panel into NPE spectra and we have imposed a threshold at half the value of the muon peak for an event to be registered as detected, instead of imposing the 2.5 cm threshold on the track length. Taking into account the energy deposition should decrease the efficiency further since we are now considering the muons that stop before being detected by the Muon Veto. For example, a muon entering the experimental setup through the Top Panel circular hole and exiting through the Bottom Panel would be considered as detected in the purely geometrical simulations. However,



if, after the energy deposition considerations, this muon stops inside the shielding before reaching the Bottom Panel, it will no longer be considered as detected.

The evolution of the efficiency for the default geometry and taking into account all the previous considerations can be found in table 7.3.

It can be seen in table 7.3 that the physical efficiency,  $\epsilon_{physical}$  decreases from 99.6% in the purely geometrical simulations to 99.2% when taking into account the energy deposition and imposing a threshold of 2.5 cm on the track length through the plastic scintillator panels. If, instead of imposing the threshold on the track length through the plastic scintillator panels, we impose a threshold on the corresponding NPE value, namely we ask that the NPE value corresponding to the track length be bigger than half the value of the muon peak from figure 7.10, we obtain an efficiency value of 99.11%<sup>5</sup>. However, it should be noted that this is a strict threshold, since it is applied in the middle of the background plateau. If we applied a threshold value that eliminates all the events below the beginning of the background plateau, the efficiency value would be closer to the one obtained by applying the 2.5 cm threshold on the track length through the plastic scintillator panels.

Table 7.3 – Efficiency values for its two definitions, the one using the fictitious volume and the physical one, both for the purely geometrical simulations and for the realistic case in which we compute the energy deposition using the Bethe-Bloch formula and we estimate the number of stopping muons. For the realistic case we also show the efficiency values when applying a threshold either on the track length of the muon inside the plastic scintillators or on the corresponding value in NPE.

	geometric	realistic	realistic (2.5 cm)	realistic (NPE)
$\epsilon_{fictitious}$	96.21%	96.11%	94.54%	94.41%
$\epsilon_{physical}$	99.60%	99.44%	99.20%	99.11%

### Efficiency dependence on the threshold

We have performed a sensitivity study in order to assess the dependence of the efficiency on the applied threshold. For that, we have considered two ways of applying the threshold

1. We ask that the full path length of the muon through the plastic scintillator panels is bigger than the threshold.

---

<sup>5</sup>One should note that we deduced the threshold in NPE by fine-tuning the Landau parameters on the NPE sum of the straight double-sided readout. However, not all the plastic scintillator panels will be read at both ends in the final design of the Muon Veto. Moreover, the value of the muon peak will depend on the spatial orientation of the plastic scintillator panels. For example, for the side vertical panels, the mean track length for muons is bigger than for one of the top panels and thus the position of the muon peak in NPE will be higher. That is why we chose to apply a stringent threshold in the middle of the background plateau computed for a top panel like configuration. In this way, we are sure that we eliminate most of the background events for the other panels as well.

2. We ask that the path length through at least one plastic scintillator panel is bigger than the threshold<sup>6</sup>.

Figure 7.14 shows the evolution of the efficiency with the applied threshold for the two definitions of the efficiency. Firstly, it can be seen that if we want to impose a more strict threshold, say of 3 cm,  $\epsilon_{fictitious}$  would only decrease by 0.2% with respect to the case in which we apply the 2.5 cm threshold, while  $\epsilon_{physical}$  would only decrease by 0.1% with respect to the case in which we apply the 2.5 cm threshold. Secondly, it can be seen that for a threshold  $\in [0, 2.5]$  cm the difference between the two ways of applying the threshold is negligible. This justifies the fact that we use a threshold applied on the full path length for all the results that will be shown in the following sections.

Finally, this study shows that we can always put the threshold in a region of the plateau such that we reject most of the gamma background while maintaining a high and quasi-constant muon detection efficiency.

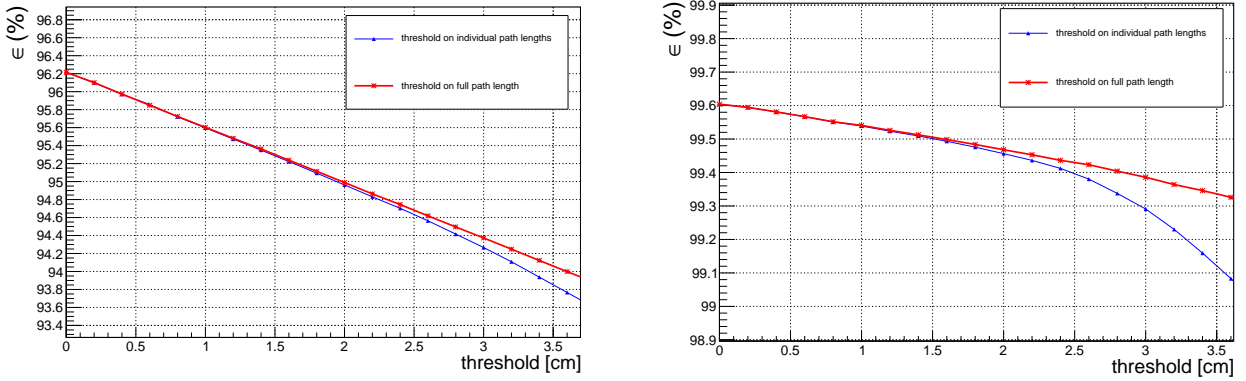


Figure 7.14 – Evolution of the efficiency with the threshold. Left:  $\epsilon_{fictitious}$ ; Right:  $\epsilon_{physical}$ .

## 7.2.2 Normalization of the simulation

In order to compute the rate of stopping muons inside the Muon Veto and the shielding we need to determine the real time equivalent to our muon tracks simulations. In other words, we want to know what is the real time equivalent, which will be denoted as  $t_{MC}$  for a given number  $N$  of simulated muons. Once we know this value we will compute the different muon rates by dividing the number of muons of interest by the real time equivalent  $t_{MC}$ .

In order to compute the real time equivalent to our muon tracks simulations we performed several simulations of  $N=10^5$  muon events generated on a plane of surface  $a^2$

<sup>6</sup>This is the more natural way of imposing the threshold, since we consider the panels individually. However, figure 7.14 shows that for a threshold smaller or equal to 2.5 cm there is no significant difference concerning the efficiency values between the two ways of imposing the threshold.

tangent to a demi-sphere and counted how many of these muons pass through a unit length width square of surface  $d^2$  placed at the origin of the coordinate system, as seen in figure 7.15. Then we can obtain  $t_{MC}$  as the ratio between the number of events that passed through the square of surface  $d^2$  and the real expected flux of muons through the square of surface  $d^2$ .

The flux of muons at surface is equal to [145]

$$\Phi_{surface} = 70 \text{ sr}^{-1} \text{ m}^{-2} \text{ s}^{-1} \quad (7.2.3)$$

Taking into account the attenuation factor for the muon flux  $att=1.41$  for the room in which the NUCLEUS detector will be placed, we can write the expected flux through the square of surface  $d^2$  as

$$\Phi_{expected} = \frac{\Phi_{surface}}{att} 2\pi d^2 \quad (7.2.4)$$

For a simulation with a given number of muons  $N$ , we can then obtain the real time equivalent of the simulation  $t_{MC}$  as

$$t_{MC}(N) = \frac{\text{number of muons passing through } d^2}{\Phi_{expected}} \quad (7.2.5)$$

The real time equivalent of a simulation  $t_{MC}$  should be constant when varying  $d$  provided that  $d < a$ , since the muons generated on the plane of surface  $a^2$  are exploring all the surface of the unit length width square of surface  $d^2$ . Figure 7.16 shows the evolution of the real time equivalent of the simulation  $t_{MC}$  as a function of  $d$  with  $a$  fixed to a value of 2 cm. It can be observed that  $t_{MC}$  is constant while  $d < a$  and then it decreases, as expected, since for  $d > a$  the muons generated on the plane of surface  $a^2$  do not explore all the surface  $d^2$ . From all simulations with  $d < a$  we obtain  $\langle t_{MC} \rangle = 72.5 \pm 1 \text{ s}$ , which means that  $10^5$  simulated muons correspond to 72.5 s of integrated real muon flux. Having determined the  $t_{MC}$  for  $10^5$  muons we can now extrapolate this in order to determine the  $t_{MC}$  for any number of simulated muons and thus be able to compute the rate of muons passing through the Muon Veto, as well as the rate of stopping muons.

### 7.2.3 Veto muon rate

Having determined the real time equivalent of the muon tracks simulations, we can now compute the rate of muons passing through the Muon Veto as:

$$\Phi_{veto} = \frac{\text{number of muons passing through the Muon Veto}}{\text{real time equivalent of the simulation}} \quad (7.2.6)$$

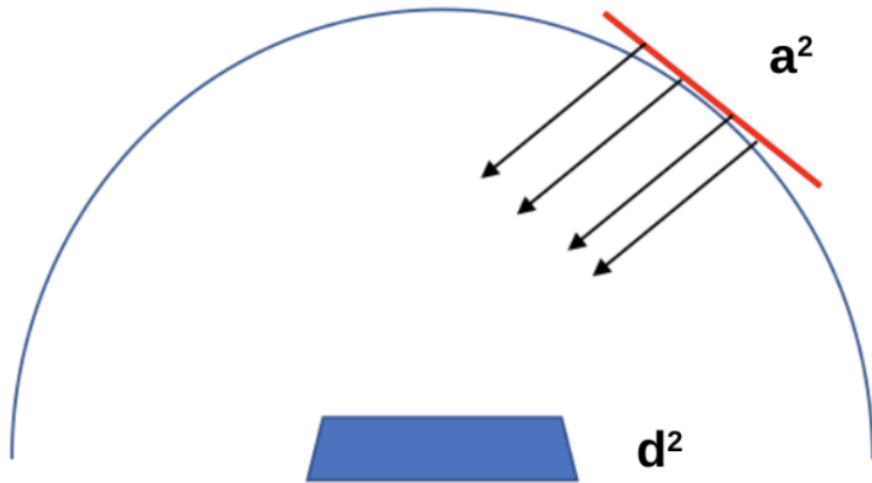


Figure 7.15 – Scheme illustrating the simulation configuration that was used to estimate the real time equivalent to our muon tracks simulations,  $t_{MC}$ . The muons are generated on a plane of surface  $a^2$  tangent to a demi-sphere and we count the number of muons that pass through the unit length width square of variable surface  $d^2$ .

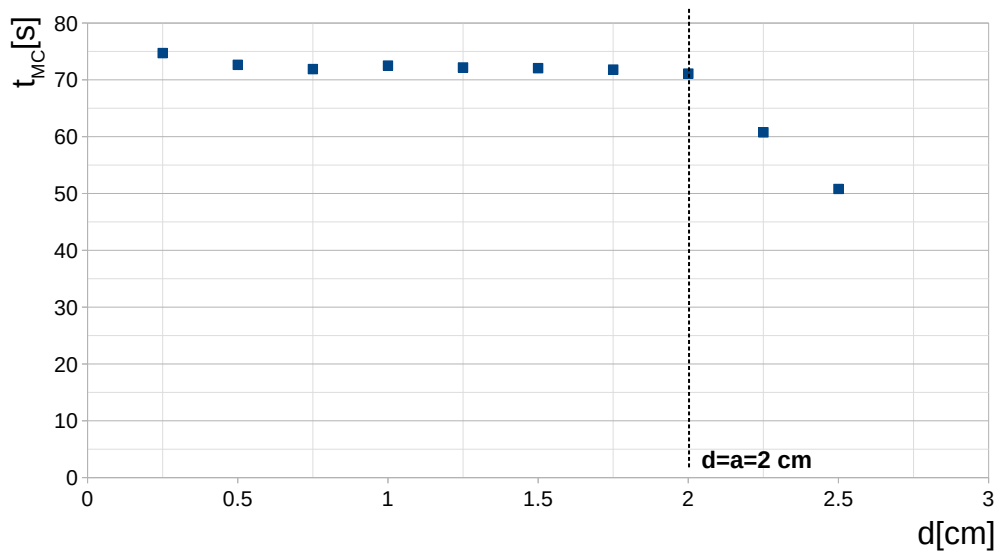


Figure 7.16 – Evolution of the real time equivalent of the simulation  $t_{MC}$  with the length of the unit length width square  $d$ , for a fixed value of  $a$ . As expected,  $t_{MC}$  stays constant for  $d < a$ .

The veto muon rates for a simulation of  $2 \cdot 10^6$  events are found in table 7.4. It can be seen that taking into account the stopping muons does not have an important impact on the veto muon rate. However, if in addition to taking into account the stopping muons, we impose a 2.5 cm threshold on the muons' path lengths through the plastic scintillator panels, the veto muon rate decreases by  $\sim 1.7\%$

Table 7.4 – Veto muon rate in 3 different scenarios:  $\Phi_{\text{geometric}}$  counts the number of muon tracks that pass through the Muon Veto,  $\Phi_{\text{realistic}}$  takes into account the energy deposition inside the veto and the shielding, i.e. the fact that some of the muons will stop inside the experimental setup,  $\Phi_{\text{realistic}}(2.5\text{cm})$  takes into account a 2.5 cm threshold on the muons path lengths through the plastic scintillator panels in addition to considering the stopping muons.

	geometric	realistic	realistic (2.5 cm)
$\Phi_{\text{veto}} [\text{s}^{-1}]$	677.2	676.5	665.4

### 7.2.4 Stopping muons

A stopping muon is defined as a muon that deposits all its energy inside the Muon Veto or inside the polyethylene or lead shielding. Table 7.5 shows the total rate of stopping muons and the rate of stopping muons inside the Muon Veto and inside the shielding, both for muons that are detected by the Muon Veto and for muons that are not detected<sup>7</sup> by the Muon Veto. Moreover the rates of stopping muons are given both for the case in which no threshold is applied on the muons' path lengths and for the case when we apply a 2.5 cm threshold on the muons' path lengths.

Table 7.5 – Table showing the rates of detected and not detected stopping muons in the different volumes composing the Muon Veto and the shielding.

	full setup	PS	Pb	PE
$\Phi^{\text{total}} [\text{s}^{-1}]$	46	3.5(7.66%)	30.2(65.6%)	12.3(26.8%)
$\Phi^{\text{not detected}} [\text{s}^{-1}]$	0.89	0	0.56(63%)	0.33(37%)
$\Phi^{\text{not detected}} (2.5\text{cm}) [\text{s}^{-1}]$	1.25	0.038(3.08%)	0.76(60.3%)	0.46(36.6%)

From table 7.5 we can deduce that 2.7% of the total stopping muons are not detected by the Muon Veto when we apply a 2.5 cm threshold on the muons' path lengths in order to consider them as detected. Of these,  $\sim 60.3\%$  stop inside the Lead and  $\sim 36.6\%$  stop inside the Polyethylene. The most dangerous muons for the NUCLEUS experiment are those who stop inside the Polyethylene since it is the closest shielding to the bolometer inside which the coherent neutrino-nucleus scattering events are to be detected. The stopping muons can give rise to electrons and positrons which can then create gamma rays through Bremsstrahlung. These gammas can represent an important source of background for the experiment.

---

<sup>7</sup>By a not detected muon we mean a muon that doesn't pass through any plastic scintillator panel. When we apply the 2.5 cm threshold on the muon's path length, by a non detected muon we mean a muon whose path length through the plastic scintillator panels is smaller than 2.5 cm.

## 7.3 Sensitivity studies

This section presents several sensitivity studies performed to evaluate how different geometrical changes impact the efficiency of the Muon Veto and the rate of stopping muons. The three following topics will be addressed:

1. The impact of the presence of the Cryogenic Muon Veto and of its placement on the efficiency of the Muon Veto and on the rate of stopping muons.
2. The impact of an envisaged Hollow Cylindrical Muon Veto that would surround the circular top hole on the efficiency of the Muon Veto and on the rate of stopping muons and the necessity of such a veto.
3. The impact of having longer vertical side plastic scintillator panels (which means that they are read at the top side using a U-turn fiber configuration) and larger bottom plastic scintillator panels on the efficiency of the Muon Veto and on the rate of stopping muons.

### 7.3.1 Cryogenic Muon Veto

Firstly, this section treats the impact of the presence of the Cryogenic Muon Veto on the efficiency of the Muon Veto and on the rate of stopping muons in order to assess the necessity of such a Muon Veto. Secondly, we investigate the impact of the vertical placement of the cryogenic Muon Veto inside the cryostat on the observables of interest. Figure 7.17 shows that there is a gap of 6 cm between the mixing chamber of the NUCLEUS cryostat and the upper edge of the lead passive shielding.

We performed simulations for the following positions of the cryogenic Muon Veto:  $z=0$  cm (the cryogenic Muon Veto is aligned with the Top Panel of the Outer Muon Veto),  $z=-2$  cm,  $z=-4$  cm and  $z=-6$  cm. The efficiency values for these different configurations, as well as for the configuration in which the Cryogenic Muon Veto is absent, can be found in table 7.6. It can be seen that in the absence of the Cryogenic Muon Veto, the realistic efficiency with an applied threshold of 2.5 cm on the muons path lengths,  $\epsilon_{\text{physical,realistic}}(2.5\text{cm})$ , has a value of 98.34 %. The installation of the Cryogenic Muon Veto increases  $\epsilon_{\text{physical,realistic}}(2.5\text{cm})$  by  $\sim 0.85\%$ . Moreover, the results in table 7.6 show that the efficiency remains stable withing the uncertainty when varying the vertical placement of the Cryogenic Muon Veto, thus making us choose the  $z=0$  cm position as the one that will be used in the final design of the Muon Veto.

The results concerning the rates of stopping muons are summarized in table 7.9. It can be seen that without the Cryogenic Muon Veto, about  $\sim 5.8\%$  of the total number of stopping muons are not detected, from which  $\sim 55\%$  stop in the Lead and  $\sim 42\%$  stop in the Polyethylene. Comparing these numbers with the ones that we obtain with the Cryogenic Muon Veto installed (see section 7.2.4), we see that the presence of the

Cryogenic Muon Veto reduces the number of not detected stopping muons by a factor of  $\sim 2$ .

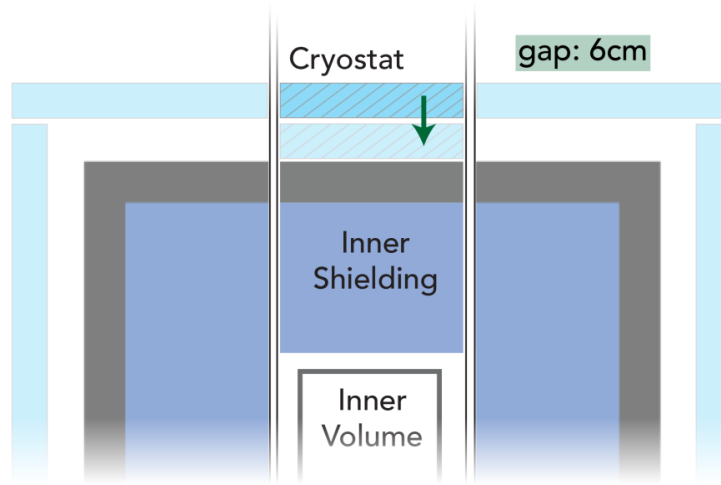


Figure 7.17 – Section of the NUCLEUS experimental setup illustrating the available region for the Cryogenic Muon Veto. The configuration where the Cryogenic Muon Veto is aligned with the Top Panel of the Muon Veto is considered as the default position and is labeled as the  $z=0$  cm position. Source: [135].

Table 7.6 – Impact of the Cryogenic Muon Veto on the efficiency.

	$\epsilon_{\text{fictitious,geometric}}$	$\epsilon_{\text{physical,geometric}}$	$\epsilon_{\text{physical,realistic}}$	$\epsilon_{\text{physical,realistic}}(2.5\text{cm})$
<b>No Cryogenic Muon Veto</b>				
	95.89 %	99.07 %	98.58 %	98.34 %
<b>Cryogenic Muon Veto</b>				
$z=0$ cm	96.21 %	99.60 %	99.44 %	99.20 %
$z=-2$ cm	96.20 %	99.61 %	99.44 %	99.21 %
$z=-4$ cm	96.23 %	99.63 %	99.47 %	99.23 %
$z=-6$ cm	96.20 %	99.60 %	99.43 %	99.21 %

### 7.3.2 Hollow Cylindrical Muon Veto

In the previous section we have seen that the presence of the Cryogenic Muon Veto has a significant impact on the overall efficiency of the Muon Veto and on the number of not detected stopping muons. However, even with the Cryogenic Muon Veto installed, a rate

of not detected stopping muons of  $\sim 1.25 \text{ s}^{-1}$  still remains, which can cause problems if these muons are stopped in one of the shielding materials, since they could create secondary particles that may represent a harmful background in the region of interest of NUCLEUS. Most of the not detected muons enter the experimental setup through the circular hole of 6.5 cm width that is present at the level of the Top Panel of the Muon Veto.

In order to minimize the impact of the circular hole, we propose to test the impact of an additional Hollow Cylindrical Muon Veto placed on the top of the Muon Veto and surrounding the cryostat vessel tightly, as seen in figure 7.18. The role of this additional Muon Veto is to restrain the range of the angle of incidence at which the muons entering the experimental setup remain undetected. The proposed thickness of the Hollow Cylindrical Muon Veto is of 5 cm, equal to the thickness of the plastic scintillator panels. Concerning the height, we have tested 3 different configurations:  $h=10 \text{ cm}$ ,  $h=20 \text{ cm}$  and  $h=30 \text{ cm}$ . We expect that the bigger the height is, the bigger the number of previously undetected stopping muons will be detected.

The results of the efficiency analysis for the geometrical configuration that contains the proposed Hollow Cylindrical Muon Veto are summarized in table 7.7. It can be seen that there is an increase in the efficiency of  $\sim 0.23\%$  for a Hollow Cylindrical Muon Veto with a height of 10 cm and of  $\sim 0.38\%$  for a Hollow Cylindrical Muon Veto with a height of 30 cm, with respect to the configuration without the Hollow Cylindrical Muon Veto.

Concerning the rate of stopping muons, it can be seen in table 7.9 that the proportion of stopping muons that are not detected by the Muon Veto decreases from  $\sim 2.7\%$  in the default configuration of the experimental setup, to  $\sim 1.5\%$  with the additional Hollow Cylindrical Muon Veto with a height of  $h=30 \text{ cm}$ .

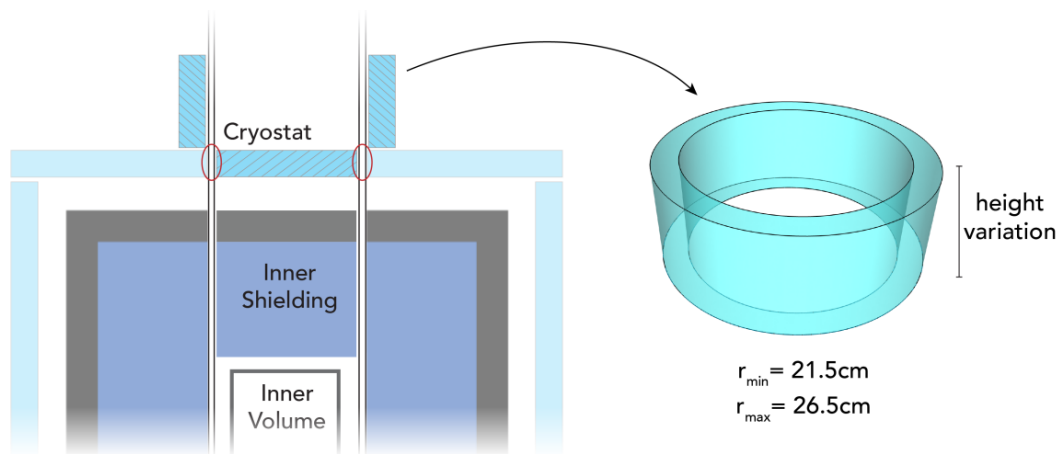


Figure 7.18 – Section of the NUCLEUS experimental setup illustrating the proposed additional Hollow Cylindrical Muon Veto. This optional component sits on top of the Muon Veto and encloses the NUCLEUS cryostat vessel tightly. Source: [135].



Table 7.7 – Efficiency values showing the impact of the proposed Hollow Cylindrical Muon Veto on the efficiency.

	$\epsilon_{\text{physical,geometric}}$	$\epsilon_{\text{physical,realistic}}$	$\epsilon_{\text{physical,realistic}}(2.5\text{cm})$
<b>No Hollow Cylindrical Muon Veto</b>			
	99.60 %	99.44 %	99.20 %
<b>Additional Hollow Cylindrical Muon Veto</b>			
z=10 cm	99.73 %	99.60 %	99.43 %
z=20 cm	99.77 %	99.68 %	99.54 %
z=30 cm	99.79 %	99.70 %	99.58 %

### 7.3.3 Further improvements of the geometry of the Muon Veto

This section treats two proposed modifications with respect to the default geometrical configuration of the Muon Veto

1. The increase of the length of the side vertical panels by 20 cm (in blue in figure 7.19) in order to reach the level of the bottom panels. In the default geometrical configuration, the side vertical scintillator panels were supposed to be read by SiPMs at both ends, i.e. using a straight fiber configuration. However, if we read the side vertical panels only at the top end with a SiPM, i.e. we use a U-turn fiber configuration, we can fill the bottom end, which was previously used to read the fibers, with plastic scintillator. We expect that this will have an impact on the muons that were entering the experimental setup through the top circular hole and were exiting through the side bottom gap, without being detected by the Muon Veto, in the sense that it will reduce their number.
2. The increase of the width of the Bottom Panel by 10 cm. It can be seen on the right hand side of figure 7.19 that in the default geometrical configuration of the Muon Veto, there is still some unused space between the end of the Bottom Panel of plastic scintillators and the rails that will be holding the NUCLEUS experiment. We expect again that by increasing the width of the Bottom Panel we will detect a fraction of the previously undetected muons that were entering the experimental setup through the top circular hole and were exiting through the side bottom gap.

The results of the efficiency analysis for the geometrical configurations proposed in this section are summarized in table 7.8. The increase in  $\epsilon_{\text{fictitious,geometric}}$  from 96.2 % in the default geometrical configuration to 99.06 % in the configuration with longer vertical side panels confirms that the loss in efficiency observed for the fictitious definition of the efficiency was mainly due to muons passing at an angle through the bottom side gap. Moreover, we observe an increase in  $\epsilon_{\text{physical,realistic}}(2.5\text{cm})$  of the same order of magnitude, around  $\sim 0.2\%$ , for the 2 geometrical changes discussed above. If we combine

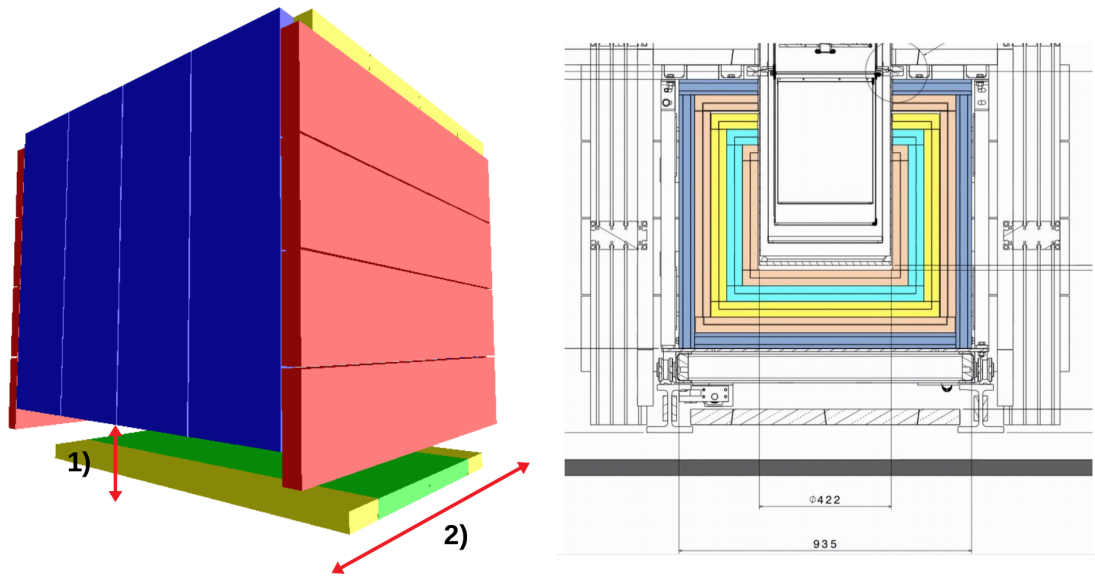


Figure 7.19 – **Left:** Scheme of the Muon Veto illustrating the two geometrical changes that are explored in this section: 1) the increase in length by 20 cm of the side vertical plastic scintillator panels; 2) the increase in width by 10 cm of the Bottom Panel of plastic scintillators.

**Right:** Scheme of the NUCLEUS experiment illustrating the space between the end of the Bottom Panel of plastic scintillators and the rails that will be holding the experiment.

Table 7.8 – Efficiency values showing the impact of the two proposed geometrical changes on the efficiency (see text).

$\epsilon_{\text{fictitious,geometric}}$	$\epsilon_{\text{physical,geometric}}$	$\epsilon_{\text{physical,realistic}}$	$\epsilon_{\text{physical,realistic}}(2.5\text{cm})$
<b>Longer vertical side panel +20 cm</b>			
99.06 %	99.76 %	99.57 %	99.37 %
<b>Larger Bottom Panel +10 cm</b>			
96.68 %	99.73 %	99.56 %	99.34 %
<b>Combined effect</b>			
99.27 %	99.89 %	99.70 %	99.54 %

the 2 geometrical changes we obtain an efficiency  $\epsilon_{\text{physical,realistic}}(2.5\text{cm})$  of 99.54%, similar to the one obtained when adding the Hollow Cylindrical Muon Veto.

Concerning the rate of stopping muons, it can be seen in table 7.9 that for both geometrical changes (and for their combination) the proportion of stopping muons that are not detected by the Muon Veto after applying the 2.5 cm threshold is similar to the one obtained for the default configuration of the experimental setup and has a value of  $\sim 1.25 \text{ s}^{-1}$ . This is due to the fact that most of the not detected stopping muons enter the experimental setup through the top circular hole and stop mostly inside the lead or

the polyethylene.

## 7.4 Conclusion

This chapter presented the muon tracks simulations developed during this thesis to estimate the overall efficiency of the full Muon Veto and to optimize its geometrical configuration.

We have shown that the installation of a Cryogenic Muon Veto increases the efficiency of the Muon Veto and reduces the number of non detected stopping muons by a factor of  $\sim 2$ . Moreover, GEANT4 simulations performed within the NUCLEUS collaboration confirmed the usefulness of the Hollow Cylindrical Muon Veto in increasing the overall Muon Veto efficiency and shown that it is a crucial element, needed to reach the required signal-to-background ratio.

The final experimental configuration of the NUCLEUS Muon Veto will also take into account the two changes proposed and studied in section 7.3.3: the increase of the length of the side vertical panels by 20 cm (U-turn fiber configuration) and the increase of the width of the Bottom Panel by 10 cm. The estimated realistic efficiency for this final configuration is of  $\sim 99.54\%$  and the estimated rate of not detected stopping muons is of  $\sim 1.25 \text{ s}^{-1}$ , thus meeting NUCLEUS requirements. The construction of the Muon Veto panels is scheduled for 2022.

$\phi_{veto}$	$\phi^{total}$	$\phi^{total}(PS)$	$\phi^{total}(Pb)$	$\phi^{total}(PE)$	$\phi^{ND}$	$\phi^{ND}(PS)$	$\phi^{ND}(Pb)$	$\phi^{ND}(PE)$
No Cryogenic Muon Veto								
673.1	45.8	3.4	30.0	12.4	2.68	0.071	1.47	1.14
Cryogenic Muon Veto								
z=0 cm	676.5	46.0	3.5	30.2	12.3	1.25	0.0386	0.757
z=-2 cm	676.5	45.7	3.5	29.9	12.2	1.21	0.0359	0.726
z=-4 cm	677.1	45.5	3.4	29.9	12.2	1.18	0.051	0.728
z=-6 cm	676.1	45.9	3.4	30.2	12.3	1.23	0.0359	0.746
Additional Hollow Cylindrical Muon Veto								
h=10 cm (z=0 cm)	678.1	45.8	3.4	30.3	12.2	0.913	0.0317	0.536
h=20 cm (z=0 cm)	677.8	45.9	3.4	30.5	12.1	0.755	0.0255	0.437
h=30 cm (z=0 cm)	679.3	46.3	3.5	30.6	12.3	0.681	0.0193	0.399
Longer vertical side panel +20 cm								
696.0	46.1	3.8	30.2	12.2	1.24	0.0393	0.770	0.430
Larger Bottom Panel +10 cm								
680.2	45.9	3.5	30.2	12.3	1.22	0.0503	0.714	0.457
Combined effect								
698.0	46.5	4.0	30.3	12.2	1.25	0.0421	0.750	0.455

Table 7.9 – Simulated muon fluxes through the NUCLEUS experiment, together with the number of stopping muons. The values in the table are based on the energy deposition of the muons inside the plastic scintillator volumes with applied track-length threshold of 2.5cm and are given in units of muons / seconds. The chosen abbreviations of the listed parameters refer to the following physical quantities:  $\phi_{veto}$  denotes the muon flux through plastic scintillator volumes,  $\phi^{total}$  the flux of muons stopping inside the experimental arrangement and  $\phi^{ND}$  the flux of muons, which stop inside the experimental arrangement and are not detected by any plastic scintillator volume. The indices  $PS$ ,  $Pb$  and  $PE$  specify in which of the materials the muons stop.

# Conclusion

*"Ainsi cette science qui devait tout m'apprendre finit dans l'hypothèse, cette lucidité sombre dans la métaphore, cette incertitude se résout en œuvre d'art. Qu'avais-je besoin de tant d'effort ? Les lignes douces de ces collines et la main du soir sur ce cœur agité m'en apprennent bien plus. Je suis revenu à mon commencement. Je comprends que, si je puis par la science saisir les phénomènes et les énumérer, je ne puis pour autant appréhender le monde."*

Le mythe de Sisyphe, *Albert Camus*

The questions raised by the reactor antineutrino anomalies observed at the short baseline experiments have not yet been answered. Even though the origin of the RAA is not yet known, the hypothesis of a sterile neutrino explaining it is less and less probable. The Very Short Baseline reactor experiments, among which is STEREO, have already rejected most of the parameter space favoured by the best fit of the RAA. Moreover, the results from commercial reactor experiments seem to point out towards a  $^{235}\text{U}$  normalization problem in the antineutrino flux prediction.

The precision of the STEREO analysis depends on a good understanding and control of the energy scale. In this context, this thesis focused on the fine tuning of the optical parameters of the Monte Carlo simulation. To do so, we used the raw charge calibration spectra of a  $^{24}\text{Na}$  source, whose 3-peak structure provides us with accurate information about the light leaks between the detector's cells. The goal of the fine tuning was to reach a good agreement between the data and simulated raw charge spectra both in the gamma-peaks region and in the light leaks region. Finally, a sub-percent agreement was reached, with the simulation reproducing accurately the top-bottom asymmetries observed in the data. This is crucial for the energy reconstruction method, which can only correct the remaining discrepancies between data and simulation at the first order, and leads to a stable and well-controlled energy scale.

Another important aspect dealt with in this thesis was the extraction of the antineutrino rates. The first contribution was to adapt an existing method in order to analyse the data of a whole phase at once, so that we could cross-check the results obtained with the official antineutrino extraction method. Several studies proved that the biases of the method due to the PSD time evolution are negligible with respect to the statistical uncertainty on the antineutrino rates. Finally, the comparison between this newly adapted method and the official method allowed us to set a systematic uncertainty of 0.65% on the total antineutrino rate, thus contributing to the accuracy of the measurement.

The analysis of the STEREO data validates the  $\sim 6\%$  deficit observed in the total rate of reactor antineutrinos with respect to the predicted value, rejects the RAA best fit point at  $>99.99\%$  confidence level, thus disproving the hypothesis that a  $\sim 1$  eV sterile neutrino could explain the observed deficit, and provides the most accurate pure  $^{235}\text{U}$   $\bar{\nu}_e$  spectrum.

We have proposed a way to improve the summation method prediction by calculating realistic beta-decay strengths for all the fission fragments on a phenomenological and stochastic basis. We have shown that within this simple approach, we are able to reproduce the antineutrino energy spectrum measured by STEREO without observing any residual norm or shape anomaly. This observation suggests that the possible origin of the anomalies may come from the  $^{235}\text{U}$  electron energy spectra measured at ILL.

Further improvements are needed to conclude on the origin of the reactor antineutrino anomalies. On the prediction side, the model proposed here has to be tested on larger observables and improved to agree with all the existing data at the isotope level (electron energy spectra, beta-decay intensities, neutron emission probabilities). More accurate microscopic calculations of the beta strengths and nuclear level densities could be included in the model and further TAGS experiments are needed to better constrain the model. This would lead to a very accurate reactor antineutrino prediction model that could be used by all the reactor neutrino experiments. On the experimental side, with the availability of more and more accurate reactor antineutrino measurements, the same level of accuracy has to be reached for the electron spectra, and new measurements would be needed for both fissioning and individual selected isotopes.

The NUCLEUS experiment is aimed at measuring  $\text{CE}\nu\text{NS}$  induced by reactor antineutrinos, thus probing nuclear-recoil energies down to 20 eV. Since it is an above-ground experiment, NUCLEUS needs sophisticated background rejection techniques. This work presented the development of a Muon Veto prototype and proved that it meets the efficiency-related requirements of NUCLEUS. The main NUCLEUS-related aspect treated in this thesis was represented by a series of geometrical simulations of the full NUCLEUS Muon Veto. Within this work, we explored several configurations of the Muon Veto and we have selected the optimal one in view of its upcoming construction. Moreover, we have shown that the overall Muon Veto efficiency for the final configuration is expected to be  $>99\%$ , which satisfies the cosmic background rejection power needed by NUCLEUS.

The assembly and validation tests of NUCLEUS are scheduled for 2022 in Munich, while its installation at Chooz and the first physics runs are expected to take place in 2023. The goal of the first phase, NUCLEUS-10g, is to observe  $\text{CE}\nu\text{NS}$  interactions for reactor antineutrinos and, even though the expected statistics is low ( $\sim 150$  detected events/year), to measure the  $\text{CE}\nu\text{NS}$  cross section with a  $\sim 10\text{-}20\%$  accuracy and put to test the Standard Model's predictions.

# Appendices





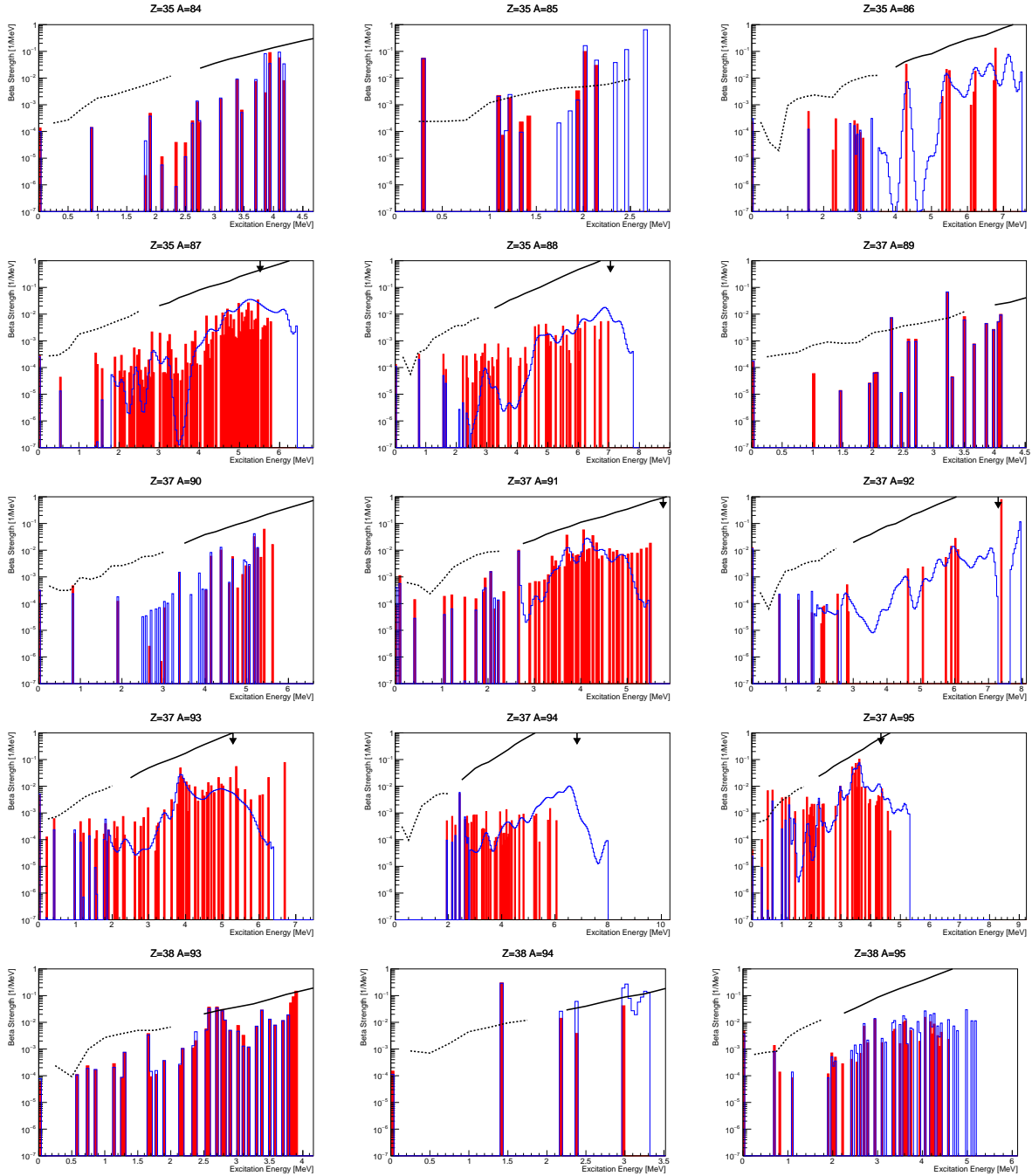


Figure 20 – Beta-decay strengths extracted from TAGS data (blue) and ENSDF-2020 data (red). The energy range corresponds to the mass difference between the two isotopes, i.e. the  $Q_\beta$  value. The arrow indicates the neutron separation energy ( $S_n$ ). The thick full and dashed lines are the HFB level densities scaled by  $10^{-11}$ . The limit between the dashed and the thick lines indicates when the level density reaches 100 levels/MeV.

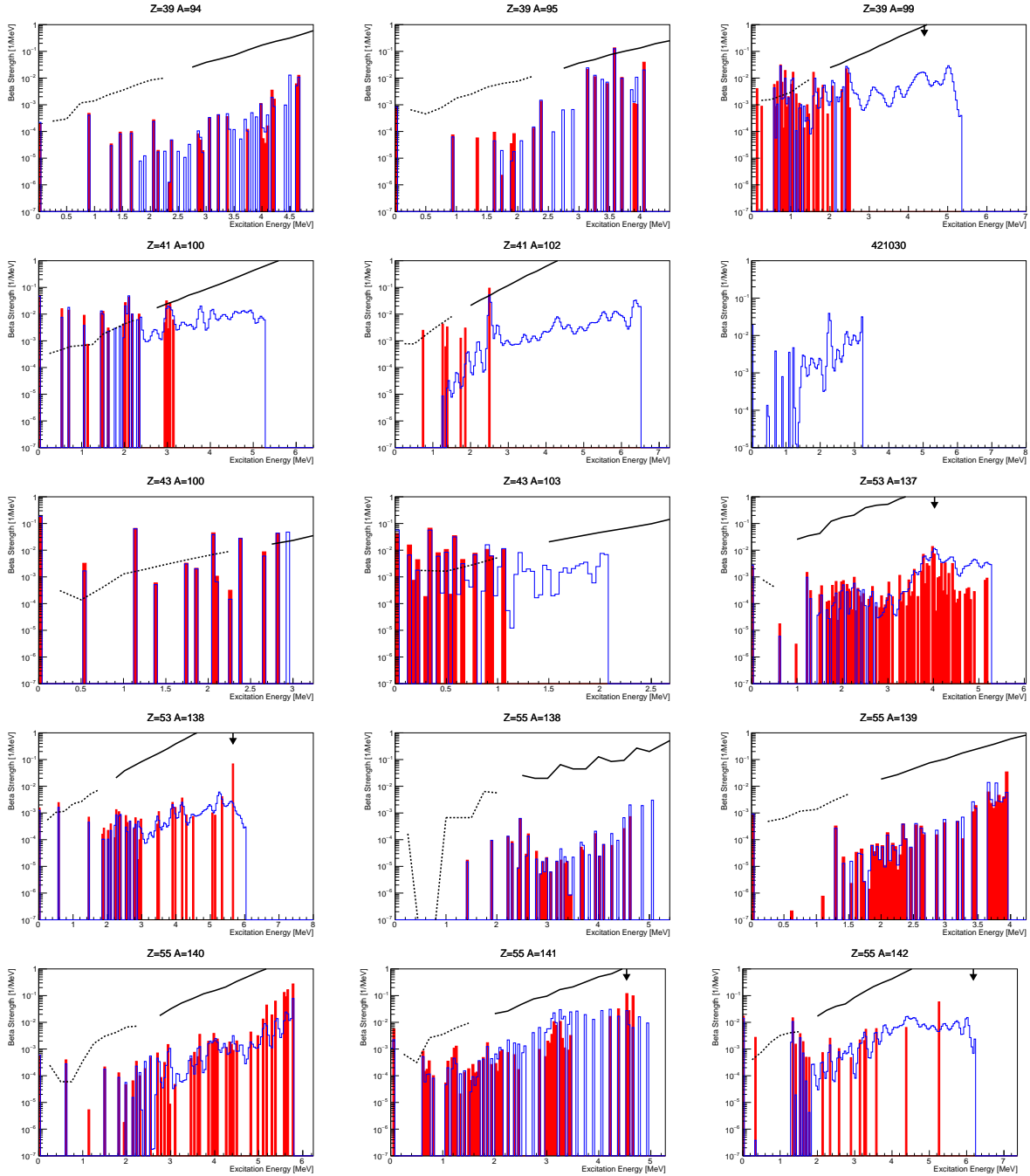


Figure 21 – Beta-decay strengths extracted from TAGS data (blue) and ENSDF-2020 data (red). The energy range corresponds to the mass difference between the two isotopes, i.e. the  $Q_\beta$  value. The arrow indicates the neutron separation energy ( $S_n$ ). The thick full and dashed lines are the HFB level densities scaled by  $10^{-11}$ . The limit between the dashed and the thick lines indicates when the level density reaches 100 levels/MeV.

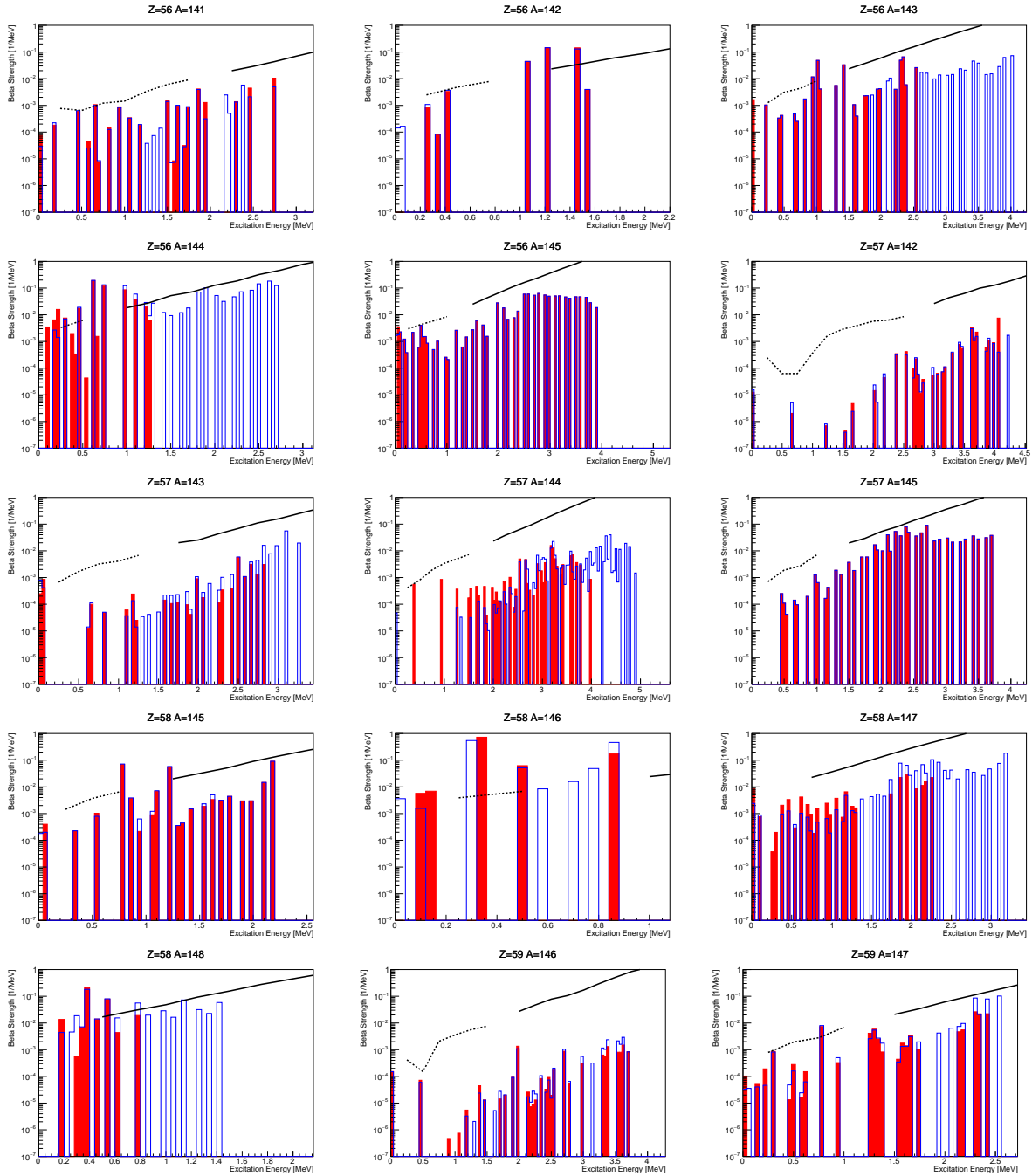


Figure 22 – Beta strength extracted from TAGS data (in blue) and ENSDF data (in red). The energy range corresponds to the mass difference between the two isotopes, i.e. the  $Q_\beta$  value. The arrow indicates the neutron separation energy ( $S_n$ ). The thin black line indicates the limit for an intensity equal to one. The Thick full and dashed lines are the HFB level density scaled by  $e-11$ , the limit between the dashed and the thick line indicates when the level density reaches 100 levels/MeV.

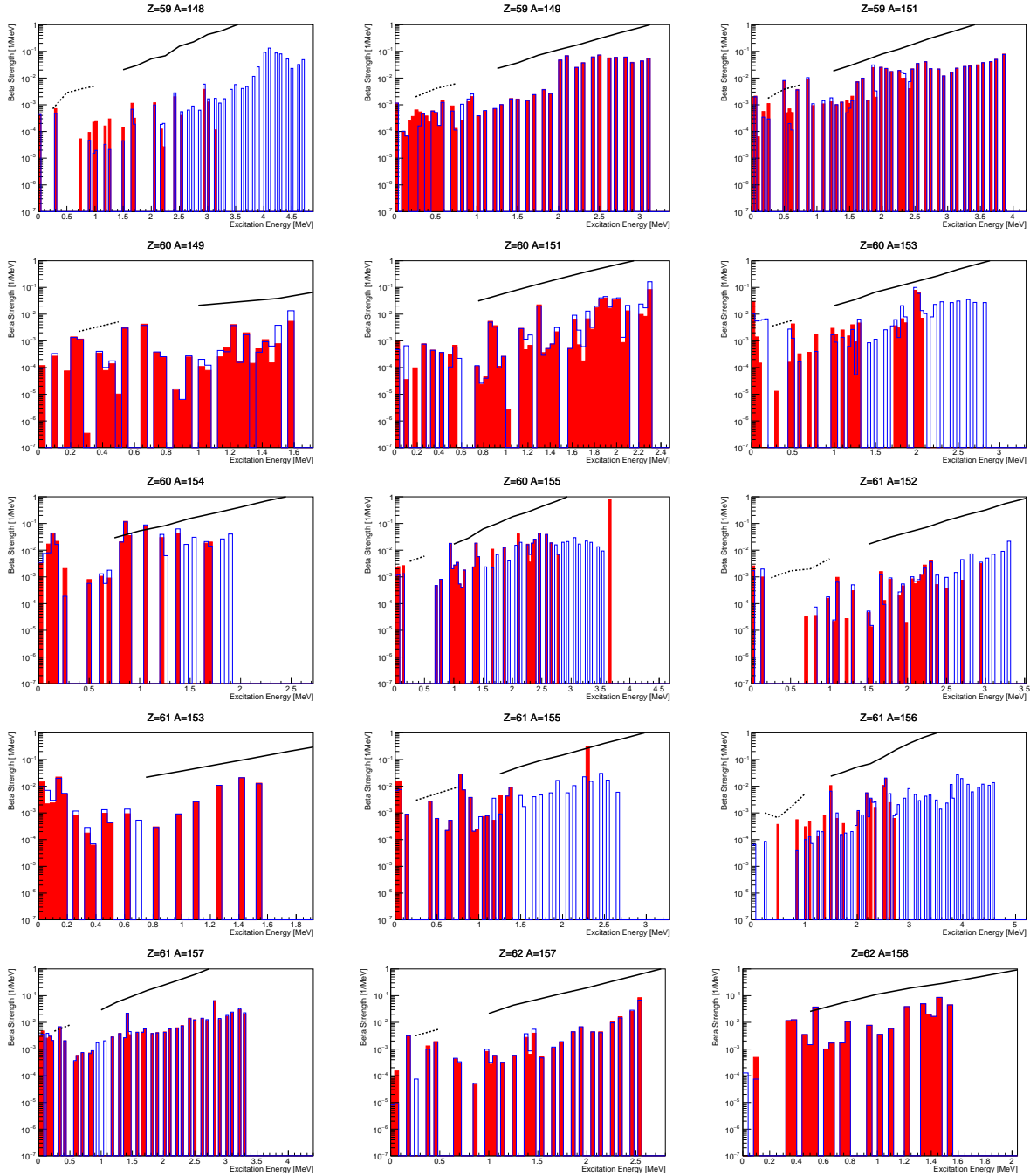


Figure 23 – Beta-decay strengths extracted from TAGS data (blue) and ENSDF-2020 data (red). The energy range corresponds to the mass difference between the two isotopes, i.e. the  $Q_\beta$  value. The arrow indicates the neutron separation energy ( $S_n$ ). The thick full and dashed lines are the HFB level densities scaled by  $10^{-11}$ . The limit between the dashed and the thick lines indicates when the level density reaches 100 levels/MeV.

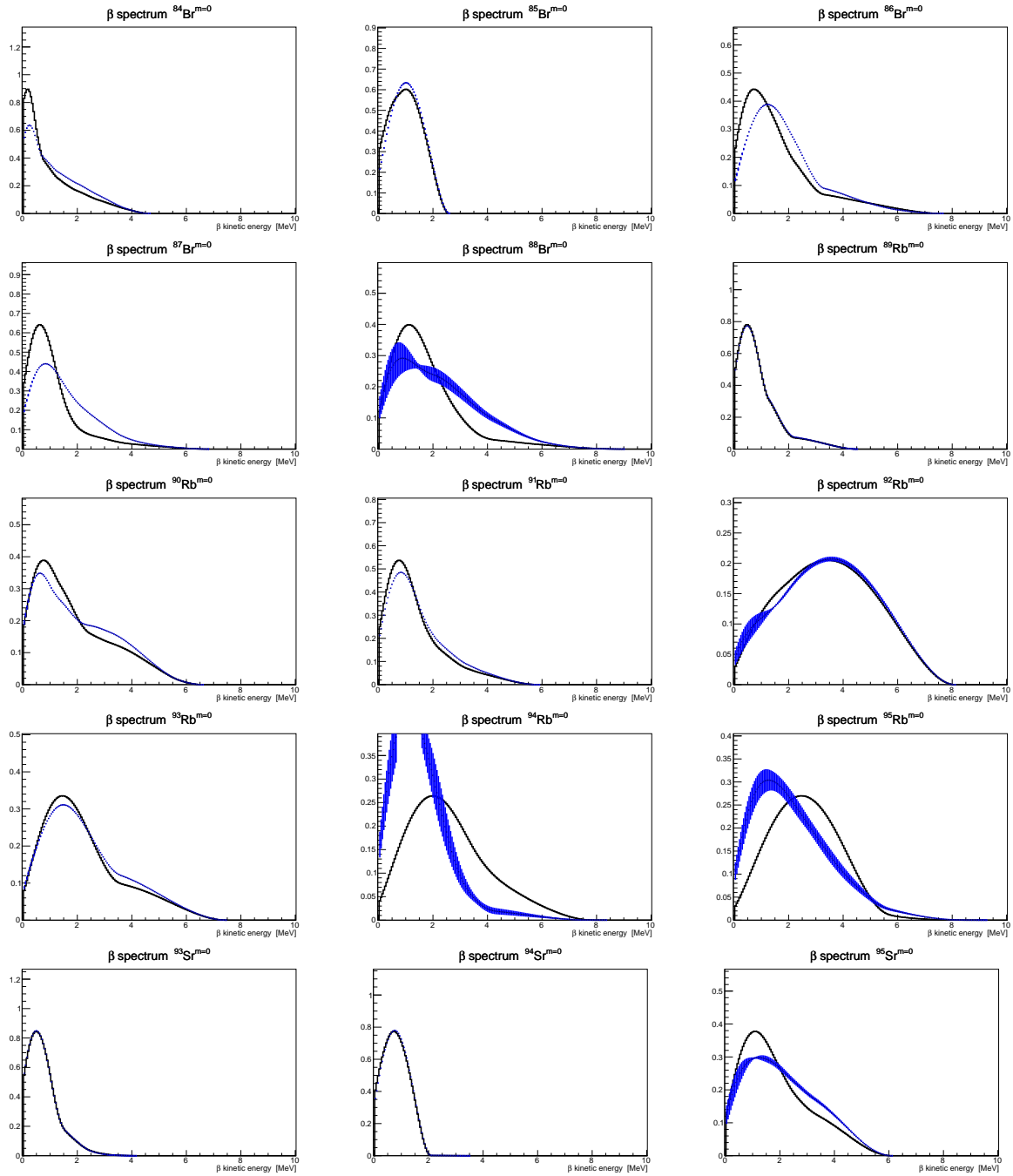


Figure 24 – Electron energy spectra generated with the model (the blue area indicates the  $1\sigma$  uncertainty) compared with the ones generated using TAGS data (black line).

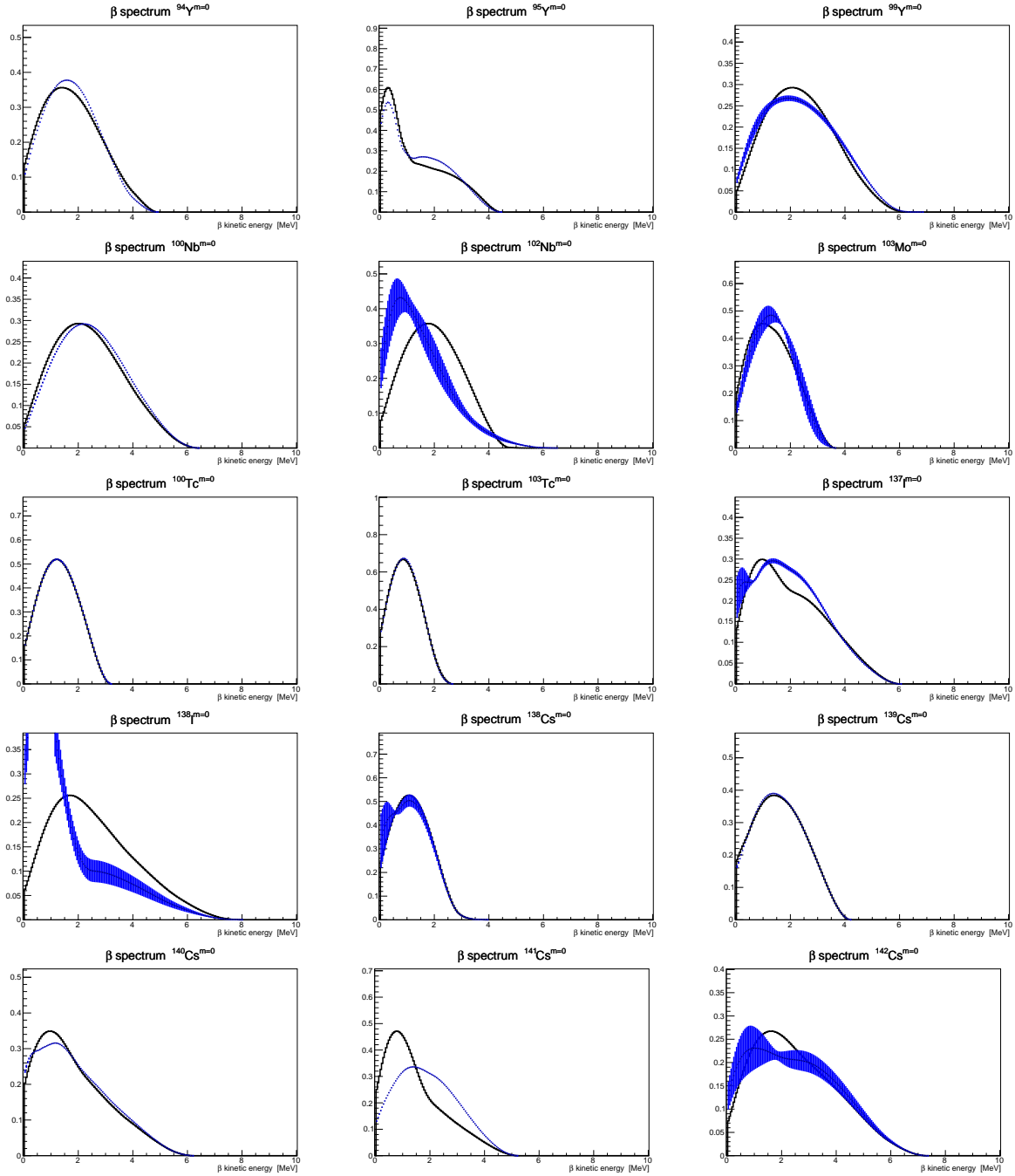


Figure 25 – Electron energy spectra generated with the model (the blue area indicates the  $1\sigma$  uncertainty) compared with the ones generated using TAGS data (black line).

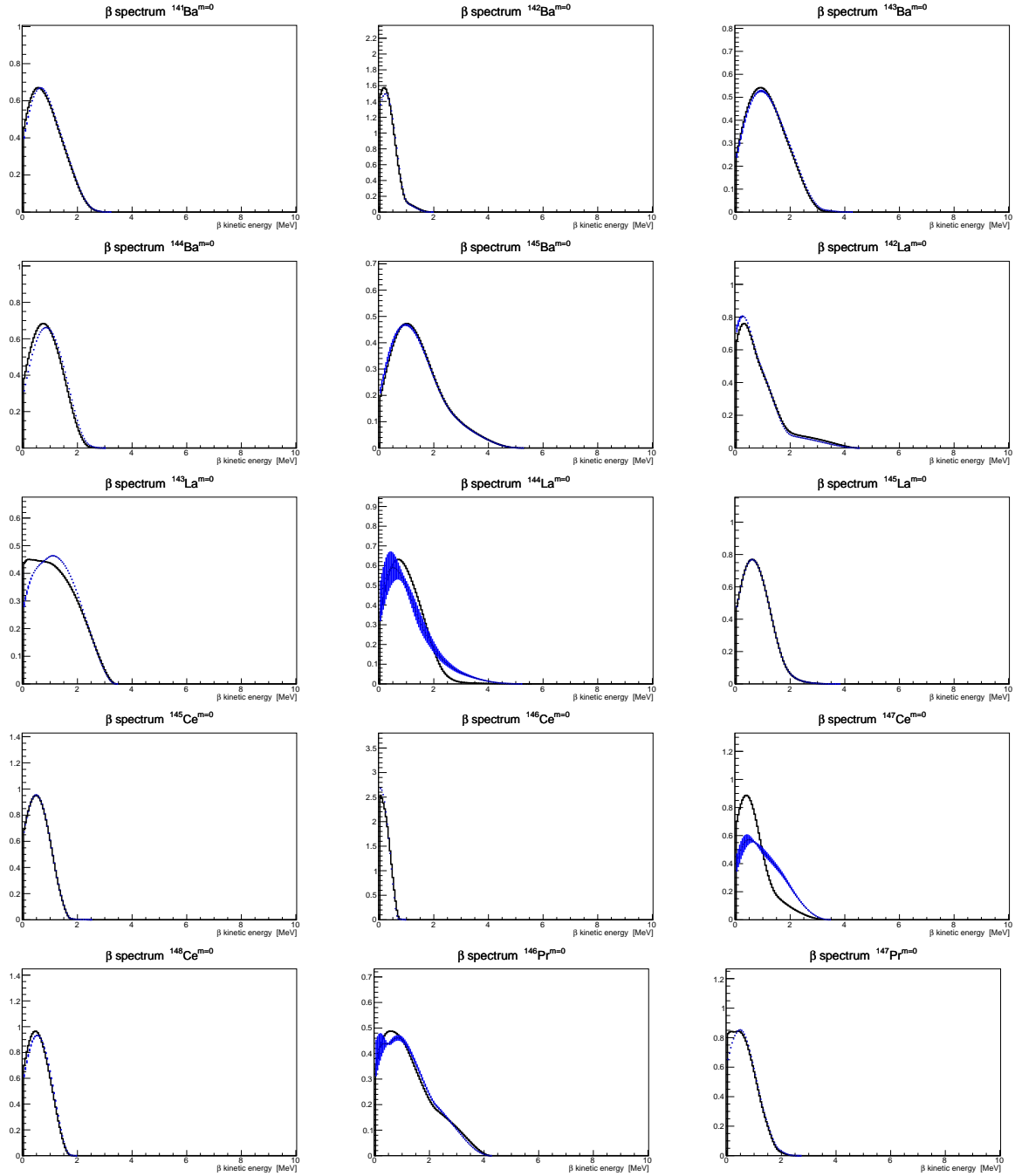


Figure 26 – Electron energy spectra generated with the model (the blue area indicates the  $1\sigma$  uncertainty) compared with the ones generated using TAGS data (black line).

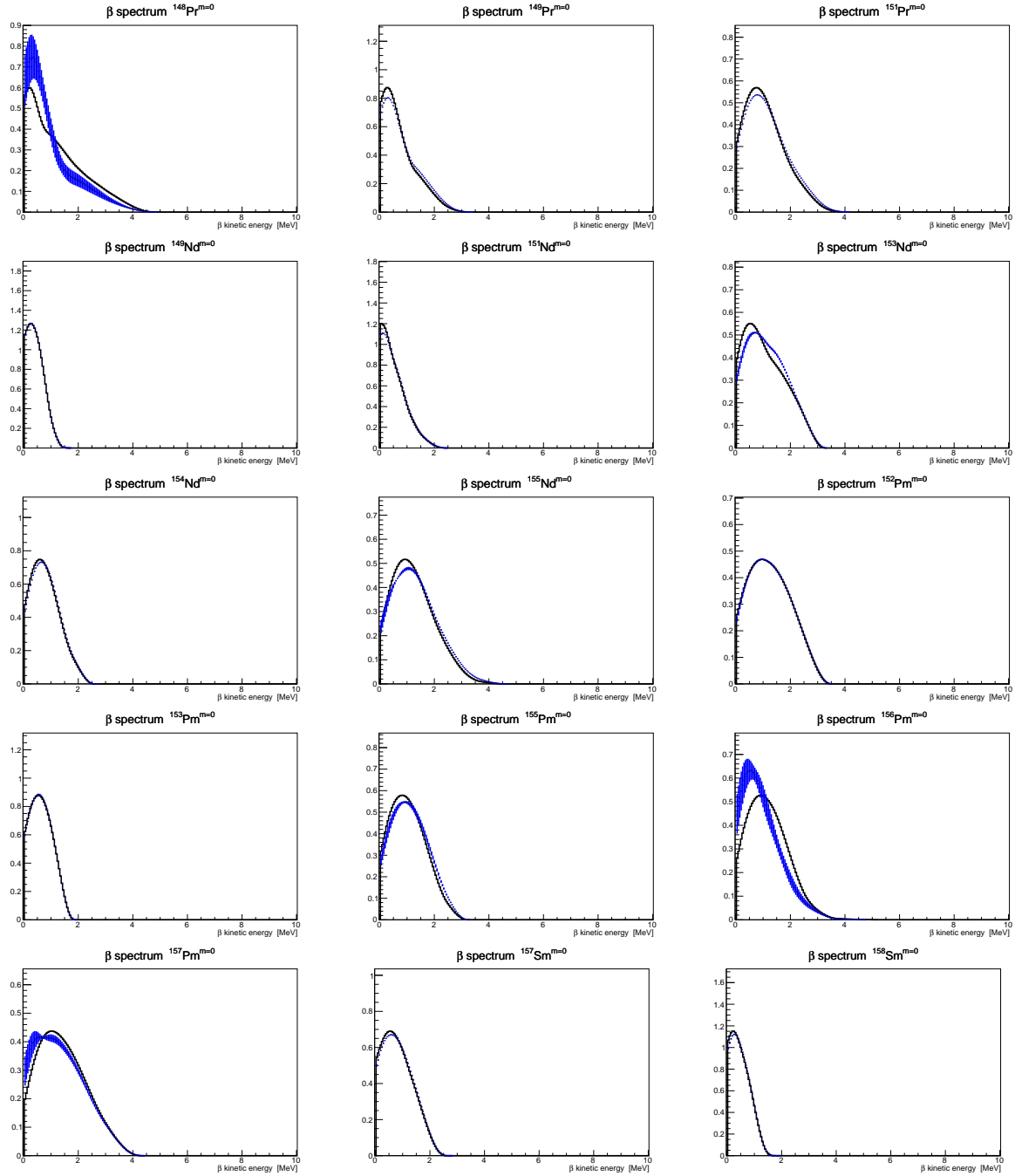


Figure 27 – Electron energy spectra generated with the model (the blue area indicates the  $1\sigma$  uncertainty) compared with the ones generated using TAGS data (black line).



# Résumé en français

La présente thèse porte sur l'étude des neutrinos de réacteur dans le cadre de deux expériences : STEREO, qui vise à tester l'existence d'un hypothétique neutrino stérile, et NUCLEUS, qui vise à détecter la diffusion élastique cohérente entre neutrinos et noyaux ( $\text{CE}\nu\text{NS}$ ).

Le neutrino est une particule très légère, sans charge électrique, qui n'interagit que par le biais de la force faible. Il existe trois saveurs de neutrino,  $\nu_e$ ,  $\nu_\mu$  et  $\nu_\tau$ , associées aux trois leptons chargés du modèle standard, l'électron, le muon et le tau. L'une des propriétés les plus fascinantes des neutrinos est qu'ils peuvent changer de saveur au cours de leur propagation. Cela est dû au fait que les états de saveur, dans lesquels les neutrinos sont créés, ne coïncident pas avec les états de masse, qui sont responsables de leur propagation. La matrice de mélange qui décrit la relation entre les états de saveur et de masse,  $U_{PMNS}$ , est paramétrée à l'aide de trois angles de mélange et d'une phase, si l'on considère que les neutrinos sont des particules de Dirac.

La probabilité qu'un neutrino initialement créé dans un état de saveur  $\alpha$  soit détecté dans un état de saveur  $\beta$  peut s'écrire comme suit

$$P(\nu_\alpha \rightarrow \nu_\beta; L) = \delta_{\alpha\beta} - 4 \sum_{i>j} \text{Re}(U_{\alpha i} U_{\beta i}^* U_{\alpha j}^* U_{\beta j}) \sin^2 \left( \frac{\Delta m_{ji}^2 L}{4E} \right) \\ + 2 \sum_{i>j} \text{Im}(U_{\alpha i} U_{\beta i}^* U_{\alpha j}^* U_{\beta j}) \sin \left( \frac{\Delta m_{ji}^2 L}{2E} \right)$$

où  $L$  est la distance entre le site de création du neutrino et l'endroit où il est détecté,  $E$  est l'énergie du neutrino,  $U_{\alpha i}$  sont les éléments de la matrice PMNS et  $\Delta m_{ji}^2$  sont les différences de masse au carré entre les différents états de masse du neutrino. Les éléments de la matrice  $U$  contenant les angles de mélange déterminent l'amplitude de la probabilité et les différences de masse au carré déterminent sa fréquence.

À ce jour, tous les angles de mélange et les différences de masse au carré sont bien déterminés. Cependant, plusieurs questions brûlantes concernant le neutrino demeurent : l'échelle de masse absolue et la hiérarchie des masses des neutrinos, la nature du neutrino, Dirac ou Majorana, et l'existence potentielle d'un état supplémentaire de neutrino stérile qui n'interagit que par la gravitation, qui sera également abordée par STEREO.

Le premier sujet abordé dans cette thèse est lié aux anomalies des antineutrinos de réacteur. La première anomalie, appelée RAA, se manifeste par une différence de 6% entre les taux d'antineutrinos mesurés et prédits par des expériences situées sur des lignes de

base courtes entre 10 et 100 mètres. La deuxième anomalie, appelée l'anomalie en forme, met en évidence un excès d'événements dans la région de 5 MeV, appelée bosse à 5 MeV, et a été observée par plusieurs expériences menées à proximité de réacteurs commerciaux. Une explication possible de la RAA pourrait être fournie par l'introduction d'un neutrino stérile vers lequel une partie des antineutrinos du réacteur oscillerait. Une autre explication possible pourrait venir du côté des prédictions. En effet, la prédiction de référence Huber-Mueller utilise une méthode de conversion pour obtenir les spectres d'antineutrinos à partir des spectres d'électrons mesurés à l'ILL dans les années 80. Ceci implique que tout problème avec le spectre d'électrons mesuré à l'ILL se propagerait directement sur le spectre antineutrino. Ces deux anomalies seront traitées dans le contexte de STEREO pour un spectre  $^{235}\text{U}$  quasiment pur.

Le deuxième sujet abordé dans cette thèse concerne la détection de la diffusion élastique cohérente entre neutrinos et noyaux induite par des antineutrinos de réacteur. Ce type d'interaction, dans lequel le neutrino interagit avec le noyau atomique dans son ensemble par l'échange d'un boson Z, domine aux énergies de neutrino inférieures à 50 MeV. Ce type d'interaction a été observé pour la première fois par COHERENT en 2017 en utilisant des neutrinos d'accélérateur avec des énergies allant jusqu'à 50 MeV. NUCLEUS vise à détecter  $\text{CE}\nu\text{NS}$  induite par des antineutrinos de réacteur, qui ont des énergies de quelques MeV. L'avantage d'utiliser des neutrinos de réacteur vient de leur flux élevé, qui permet de réaliser un test précis de la prédiction du modèle standard sur la section efficace de  $\text{CE}\nu\text{NS}$ .

Après avoir introduit les sujets traités dans cette thèse au chapitre 1, l'expérience STEREO est décrite au chapitre 2. STEREO vise à tester l'hypothèse selon laquelle une oscillation vers un neutrino stérile de masse  $\sim 1 \text{ eV}/c^2$  pourrait expliquer la RAA. C'est pourquoi il utilise un détecteur segmenté, rempli d'un scintillateur liquide dopé au Gadolinium (Gd), placé à  $\sim 10 \text{ m}$  du cœur quasi pur en  $^{235}\text{U}$  du réacteur de recherche de l'ILL à Grenoble, pour détecter les antineutrinos par la réaction de désintégration bêta inverse (IBD):  $\bar{\nu}_e + p \rightarrow e^+ + n$ . Le principe de détection est basé sur l'identification des produits de la réaction IBD corrélés dans le temps. L'événement prompt est représenté par le positron, qui dépose son énergie presque instantanément et porte également l'information sur l'énergie du neutrino. L'événement retardé est représenté par la capture du neutron sur un noyau de Gd, qui a lieu  $\sim 18 \mu\text{s}$  après l'événement prompt, et donne lieu à une cascade de rayons gamma d'une énergie totale de  $\sim 8 \text{ MeV}$ . Une comparaison relative indépendante de la prédiction entre les spectres mesurés dans les différentes cellules du détecteur est réalisée afin de tester l'apparition d'un modèle d'oscillation.

STEREO a commencé à acquérir des données en 2016 et il a été démantelé à la fin de 2020. La prise de données était structurée en cycles de 50 jours avec le réacteur allumé, entrecoupée de longues périodes d'arrêt du réacteur. Les périodes d'arrêt du réacteur ont été cruciales pour la caractérisation du bruit de fond et ont eu un impact important sur la précision de l'extraction des neutrinos. Au total, STEREO a enregistré des données pendant trois phases distinctes et a totalisé près de 400 jours de données avec le réacteur allumé, ce qui équivaut à environ 157 000 neutrinos détectés.

Les travaux relatifs à STEREO réalisés dans le cadre de cette thèse se concentrent

sur deux aspects de l'analyse STEREO : le réglage fin de la simulation Monte Carlo du détecteur et l'extraction du signal  $\bar{\nu}_e$  à l'aide d'une modélisation des distributions de PSD (Pulse Shape Discrimination) du réacteur éteint et du réacteur allumé.

La précision de l'analyse STEREO dépend d'une bonne compréhension et du contrôle précis de l'échelle en énergie. Dans ce contexte, cette thèse s'est concentrée sur le réglage fin des paramètres optiques de la simulation Monte Carlo, qui est présenté dans le chapitre 3 avec son impact sur l'échelle en énergie. Pour ce faire, nous avons utilisé les spectres de calibration en charge brute d'une source de  $^{24}\text{Na}$ , dont la structure à 3 pics nous fournit des informations précises sur les fuites de lumière entre les cellules du détecteur. L'objectif du réglage fin était d'atteindre un bon accord entre les données et la simulation au niveau des spectres en charge brute à la fois dans la région des pics gamma et dans la région des fuites de lumière. Finalement, un accord inférieur à un pour cent a été atteint, la simulation reproduisant avec précision les asymétries haut-bas observées dans les données. Cela s'est avéré crucial pour la méthode de reconstruction de l'énergie, qui ne peut corriger les divergences restantes entre les données et la simulation qu'au premier ordre, et conduit à une échelle en énergie stable et bien contrôlée.

Un autre aspect important traité dans cette thèse a été l'extraction des taux d'antineutrinos. Les travaux sur l'extraction du signal  $\bar{\nu}_e$ , ainsi que les coupures utilisées pour sélectionner les candidats IBD et la caractérisation du bruit de fond pour STEREO sont présentés au chapitre 4. La première contribution a été d'adapter une méthode existante afin d'analyser les données d'une phase entière en une seule fois et de pouvoir vérifier les résultats obtenus avec la méthode officielle d'extraction des antineutrinos. Plusieurs études ont prouvé que les biais de la méthode dus à l'évolution temporelle de la PSD sont négligeables par rapport à l'incertitude statistique sur les taux d'antineutrinos. Enfin, la comparaison entre cette méthode nouvellement adaptée et la méthode officielle nous a permis de fixer une incertitude systématique de 0,65% sur le taux total d'antineutrinos, contribuant ainsi à la précision de la mesure.

Les résultats de l'expérience STEREO, ainsi qu'une amélioration de la prédiction développée dans ce travail pour tester l'origine des anomalies sont présentés dans le chapitre 5. L'analyse des données STEREO valide le déficit de 6 % observé dans le taux total d'antineutrinos de réacteur par rapport à la valeur prédite (Figure 1 à gauche), rejette le point de meilleur ajustement de la RAA avec un niveau de confiance de 99,99 %, réfutant ainsi l'hypothèse selon laquelle un neutrino stérile de 1 eV pourrait expliquer le déficit observé (Figure 1 à droite), et fournit le spectre le plus précis de  $^{235}\text{U}$  pur, déconvolué de tout effet lié au réacteur ou au détecteur, confirmant la présence de la bosse à 5 MeV (Figure 2 à gauche). Le chapitre 5 propose également un moyen d'améliorer la prédiction de la méthode de sommation en calculant des distributions de forces de désintégration bêta réalistes pour tous les fragments de fission sur une base phénoménologique et stochastique. Le modèle développé corrige la base de données nucléaires ENSDF de l'effet Pandemonium et complète la fonction de force bêta pour les isotopes qui ont des transitions manquantes. Nous avons montré qu'avec cette approche simple, nous sommes capables de reproduire le spectre d'énergie des antineutrinos mesuré par STEREO sans observer d'anomalie résiduelle en norme ou en forme (Figure 2 à droite). Cette observation suggère que l'origine possible de ces anomalies pourrait provenir des spectres en

énergie des électrons  $^{235}\text{U}$  mesurés à l'ILL.

D'autres améliorations sont nécessaires pour conclure sur l'origine des anomalies des antineutrinos des réacteurs. Du côté des prédictions, le modèle proposé dans cette thèse doit être testé sur des observables plus étendus et amélioré pour être en accord avec toutes les données existantes au niveau des isotopes individuels (spectres d'énergie des électrons, intensités de désintégration bêta, probabilités d'émission des neutrons). Des calculs microscopiques plus précis des forces bêta et des densités de niveaux nucléaires pourraient être inclus dans le modèle et d'autres expériences TAGS sont nécessaires pour mieux contraindre le modèle. Cela conduirait à un modèle de prédiction des antineutrinos des réacteurs très précis qui pourrait être utilisé par toutes les expériences sur les neutrinos des réacteurs. Du côté expérimental, avec la disponibilité de mesures de plus en plus précises des antineutrinos de réacteur, le même niveau de précision doit être atteint pour les spectres d'électrons, et de nouvelles mesures seraient nécessaires pour la fission et les isotopes individuels sélectionnés.

Les travaux relatifs à NUCLEUS effectués dans cette thèse sont centrés sur la construction d'un veto à muons avec une étude basée sur la simulation visant à estimer son efficacité et à trouver sa configuration optimale, présentée au chapitre 7. L'expérience NUCLEUS, ainsi que la description du prototype de veto à muons testé dans ce travail, sont présentées au chapitre 6.

L'expérience NUCLEUS vise à mesurer  $\text{CE}\nu\text{NS}$  induite par des antineutrinos de réacteur, sondant ainsi des énergies de recul nucléaire jusqu'à 20 eV. Comme il s'agit d'une expérience en surface, NUCLEUS a besoin de techniques sophistiquées de rejet du bruit de fond. Ce travail présente le développement d'un prototype de veto à muons et prouve qu'il répond aux exigences d'efficacité de NUCLEUS. Le principal aspect lié à NUCLEUS traité dans cette thèse est représenté par une série de simulations géométriques du veto à muons complet de NUCLEUS. Dans le cadre de ce travail, nous avons exploré plusieurs configurations du veto à muons et nous avons sélectionné la configuration optimale en vue de sa construction prochaine. De plus, nous avons montré que l'efficacité globale du veto à muons pour la configuration finale devrait être  $>99\%$ , ce qui satisfait les contraintes en termes de rejet du bruit de fond cosmologique requises par NUCLEUS.

Les tests d'assemblage et de validation de NUCLEUS sont prévus pour 2022 à Munich, tandis que son installation à Chooz et les premiers essais de physique devraient avoir lieu en 2023. L'objectif de la première phase, NUCLEUS-10g, est d'observer les interactions  $\text{CE}\nu\text{NS}$  pour les antineutrinos de réacteur et, même si la statistique attendue est faible ( $\sim 150$  événements détectés/an), de mesurer la section efficace  $\text{CE}\nu\text{NS}$  avec une précision de  $\sim 10\text{-}20\%$  et de mettre à l'épreuve les prédictions du modèle standard.

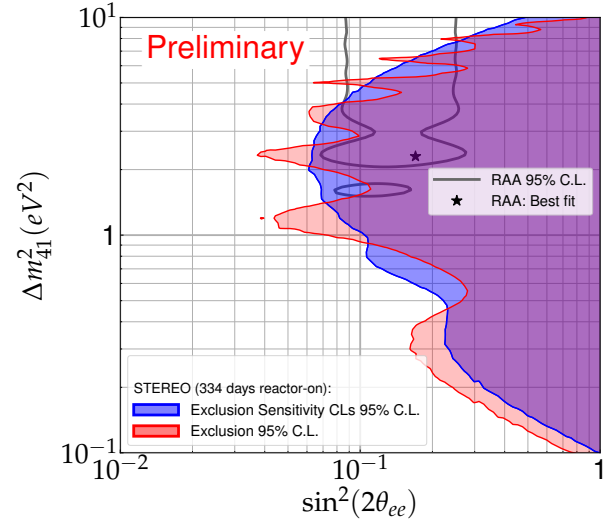
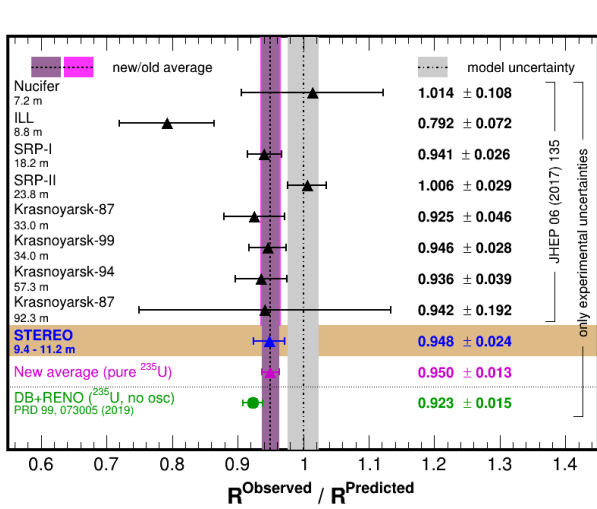


Figure 1 - Gauche: Rapports entre les taux d'antineutrinos mesurés et les prédictions du modèle de Huber pour plusieurs expériences incluant STEREO. Droite: Contour d'exclusion (rouge) et contour de sensibilité (bleu) à 95 % C.L. pour phase-I+II+III. Les régions autorisées de la RAA (gris) et son point de meilleur ajustement (étoile) sont superposés.

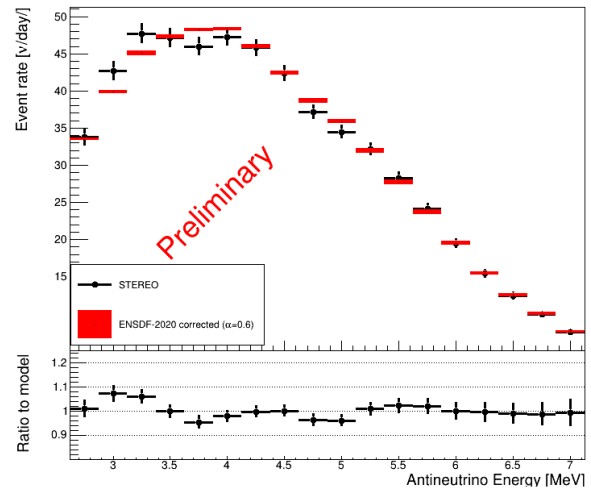
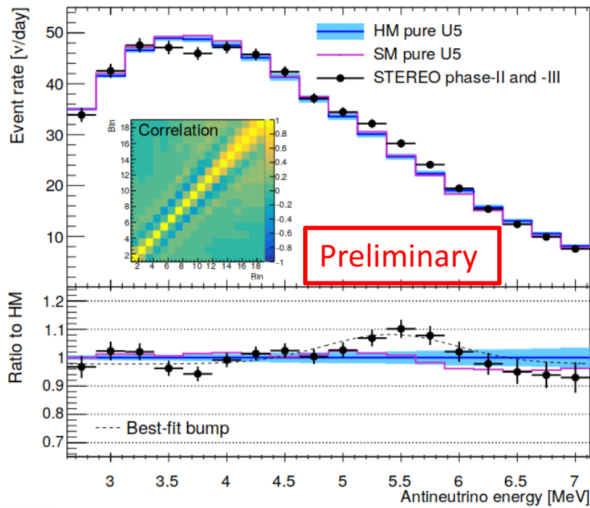


Figure 2 - Gauche: Spectre en énergie pur  $^{235}\text{U}$  extrait des données STEREO comparé à la prédiction de Huber-Mueller et le rapport entre les deux. Droite: Spectre en énergie pur  $^{235}\text{U}$  extrait des données STEREO comparé au spectre prédit par le modèle développé dans cette thèse et le rapport entre les deux.



# Bibliography

- [1] J Chadwick. Intensitätsverteilung im magnetischen Spectrum der  $\beta$ -Strahlen von radium B + C. *Verhandl. Dtsc. Phys. Ges.*, 16:383, 1914.
- [2] N. Bohr, H.A. Kramers, and J.C. Slater. Lxxvi. the quantum theory of radiation. *The London, Edinburgh, and Dublin Philosophical Magazine and Journal of Science*, 47(281):785–802, 1924.
- [3] H. Geiger W. Bothe. Über das wesen des comptoneffekts; ein experimenteller beitrage zur theorie der strahlung. *Z. Physik* 32, 639–663 (1925).
- [4] Wolfgang Pauli, Charles P Enz, and Karl von Meyenn. *Writings on physics and philosophy*. Springer, 1994.
- [5] Chadwick James. The existence of a neutron. *R. Soc. Lond. A*136692–708.
- [6] E. Fermi. An attempt of a theory of beta radiation. 1. *Z. Phys.*, 88:161–177, 1934.
- [7] C. L. Cowan, F. Reines, F. B. Harrison, H. W. Kruse, and A. D. McGuire. Detection of the free neutrino: a confirmation. *Science*, 124(3212):103–104, 1956.
- [8] Frederick Reines and Clyde L. Cowan. The neutrino. *Nature*, 178:446–449, 1956.
- [9] G. Danby, J-M. Gaillard, K. Goulianos, L. M. Lederman, N. Mistry, M. Schwartz, and J. Steinberger. Observation of high-energy neutrino reactions and the existence of two kinds of neutrinos. *Phys. Rev. Lett.*, 9:36–44, Jul 1962.
- [10] K. Kodama et al. Observation of Tau Neutrino Interactions. *Physics Letters B*, 504:218–224, 2001.
- [11] S Turck-Chièze. The standard solar model and beyond. *Journal of Physics: Conference Series*, 665:012078, jan 2016.
- [12] [http://www.sns.ias.edu/\\$\sim\\$jnb/](http://www.sns.ias.edu/$\sim$jnb/).
- [13] Bruce T. Cleveland, Timothy Daily, Jr. Raymond Davis, James R. Distel, Kenneth Lande, C. K. Lee, Paul S. Wildenhain, and Jack Ullman. Measurement of the solar electron neutrino flux with the homestake chlorine detector. *The Astrophysical Journal*, 496(1):505–526, mar 1998.
- [14] K. Hirata, T. Kajita, M. Koshiba, and all. Observation of a neutrino burst from the supernova sn1987a. *Phys. Rev. Lett.*, 58:1490–1493, Apr 1987.
- [15] Raymond Davis, Don S. Harmer, and Kenneth C. Hoffman. Search for neutrinos from the sun. *Phys. Rev. Lett.*, 20:1205–1209, May 1968.
- [16] K. S Hirata et al. Observation of  $^8\text{B}$  solar neutrinos in the kamiokande-2 detector. *Phys. Rev. Lett.*, 63:16–19, Jul 1989.
- [17] Christopher W. Walter. The super-kamiokande experiment. *Neutrino Oscillations*, page 19–43, Mar 2008.
- [18] Vladimir N Gavrin. The russian-american gallium experiment SAGE. *Physics-Uspekhi*, 54(9):941–949, sep 2011.
- [19] D. Vignaud. The gallex solar neutrino experiment. *Nuclear Physics B - Proceedings Supplements*, 60(3):20–29, 1998.
- [20] Y. Fukuda et al. Evidence for oscillation of atmospheric neutrinos. *Phys. Rev. Lett.*, 81:1562–1567, 1998.

- [21] J. Boger, R.L. Hahn, J.K. Rowley, Carter, et al. The sudbury neutrino observatory. *Nuclear Instruments and Methods in Physics Research Section A: Accelerators, Spectrometers, Detectors and Associated Equipment*, 449(1-2):172–207, Jul 2000.
- [22] Q. R. Ahmad et al. Direct evidence for neutrino flavor transformation from neutral current interactions in the Sudbury Neutrino Observatory. *Phys. Rev. Lett.*, 89:011301, 2002.
- [23] G. Alimonti, C. Arpesella, H. Back, M. Balata, D. Bartolomei, A. de Bellefon, G. Bellini, J. Benziger, A. Bevilacqua, D. Bondi, and et al. The borexino detector at the laboratori nazionali del gran sasso. *Nuclear Instruments and Methods in Physics Research Section A: Accelerators, Spectrometers, Detectors and Associated Equipment*, 600(3):568–593, Mar 2009.
- [24] A. Yu. Smirnov. The msw effect and matter effects in neutrino oscillations. *Physica Scripta*, T121:57–64, Jan 2005.
- [25] D. Franco et al. Solar neutrino results from Borexino. *Nucl. Phys. B Proc. Suppl.*, 237-238:104–106, 2013.
- [26] Ivan Esteban, M. C. Gonzalez-Garcia, Michele Maltoni, Ivan Martinez-Soler, and Thomas Schwetz. Updated fit to three neutrino mixing: exploring the accelerator-reactor complementarity. *Journal of High Energy Physics*, 2017(1), Jan 2017.
- [27] K. Abe, R. Akutsu, A. Ali, C. Alt, C. Andreopoulos, L. Anthony, M. Antonova, S. Aoki, A. Ariga, and et al. Constraint on the matter–antimatter symmetry-violating phase in neutrino oscillations. *Nature*, 580(7803):339–344, Apr 2020.
- [28] National Nuclear Data Center.
- [29] Aurelie Bonhomme. *Anomalie des antineutrinos de réacteurs : recherche d’un état stérile avec l’expérience STEREO*. Thèse de doctorat dirigée par Letourneau, alain physique paris-saclay september 2018, Université Paris-Saclay, September 2018.
- [30] Feng Peng An et al. Improved Measurement of the Reactor Antineutrino Flux and Spectrum at Daya Bay. *Chin. Phys. C*, 41(1):013002, 2017.
- [31] <https://www.nndc.bnl.gov/ensdf/>.
- [32] J.C. Hardy, L.C. Carraz, B. Jonson, and P.G. Hansen. The essential decay of pandemonium: A demonstration of errors in complex beta-decay schemes. *Physics Letters B*, 71(2):307–310, 1977.
- [33] Th. A. Mueller, D. Lhuillier, M. Fallot, A. Letourneau, S. Cormon, M. Fechner, L. Giot, T. Lasserre, J. Martino, G. Mention, and et al. Improved predictions of reactor antineutrino spectra. *Physical Review C*, 83(5), May 2011.
- [34] E. Valencia and all. Total absorption  $\gamma$ -ray spectroscopy of the  $\beta$ -delayed neutron emitters  $^{87}\text{Br}$ ,  $^{88}\text{Br}$ , and  $^{94}\text{Rb}$ . *Phys. Rev. C*, 95:024320, Feb 2017.
- [35] W. Mampe, K. Schreckenbach, P. Jeuch, B.P.K. Maier, F. Braumandl, J. Larysz, and T. von Egidy. The double focusing iron-core electron-spectrometer “bill” for high resolution (n, e) measurements at the high flux reactor in grenoble. *Nuclear Instruments and Methods*, 154(1):127–149, 1978.
- [36] K. Schreckenbach, H. R. Faust, F. von Feilitzsch, A. A. Hahn, K. Hawerkamp, and J. L. Vuilleumier. Absolute measurement of the beta spectrum from  $^{235}\text{U}$  fission as a basis for reactor antineutrino experiments. *Phys. Lett. B*, 99:251–256, 1981.
- [37] K. Schreckenbach, G. Colvin, W. Gelletly, and F. Von Feilitzsch. Determination of the antineutrino spectrum from  $^{235}\text{U}$  thermal neutron fission products up to 9.5 mev. *Physics Letters B*, 160(4):325–330, 1985.
- [38] F. von Feilitzsch, A.A. Hahn, and K. Schreckenbach. Experimental beta-spectra from  $^{239}\text{Pu}$  and  $^{235}\text{U}$  thermal neutron fission products and their correlated antineutrino spectra. *Physics Letters B*, 118(1):162–166, 1982.



- [39] A. A. Hahn, K. Schreckenbach, G. Colvin, B. Krusche, W. Gelletly, and F. Von Feilitzsch. Anti-neutrino Spectra From  $^{241}\text{Pu}$  and  $^{239}\text{Pu}$  Thermal Neutron Fission Products. *Phys. Lett. B*, 218:365–368, 1989.
- [40] D. Lhuillier. Reactor flux calculations. *nuclear Physics B - Proceedings Supplements*, 235-236 :11–16, 2013.
- [41] O. Tengblad et al. Nucl. phys. a503, 136 (1989).
- [42] Patrick Huber. Determination of antineutrino spectra from nuclear reactors. *Physical Review C*, 84(2), Aug 2011.
- [43] Ashwani Rajan and Shantanu Desai. A meta-analysis of neutron lifetime measurements. *Progress of Theoretical and Experimental Physics*, 2020(1), 01 2020. 013C01.
- [44] G. Mention, M. Fechner, Th. Lasserre, Th. A. Mueller, D. Lhuillier, M. Cribier, and A. Letourneau. Reactor antineutrino anomaly. *Physical Review D*, 83(7), Apr 2011.
- [45] S. Gariazzo, C. Giunti, M. Laveder, and Y. F. Li. Updated global 3+1 analysis of short-baseline neutrino oscillations. *Journal of High Energy Physics*, 2017(6), Jun 2017.
- [46] Y. Abe et al. Improved measurements of the neutrino mixing angle  $\theta_{13}$  with the Double Chooz detector. *JHEP*, 10:086, 2014. [Erratum: JHEP 02, 074 (2015)].
- [47] Y.J. Ko, B.R. Kim, J.Y. Kim, B.Y. Han, C.H. Jang, E.J. Jeon, K.K. Joo, H.J. Kim, H.S. Kim, Y.D. Kim, and et al. Sterile neutrino search at the neos experiment. *Physical Review Letters*, 118(12), Mar 2017.
- [48] S.H. Seo, W.Q. Choi, H. Seo, J.H. Choi, Y. Choi, H.I. Jang, J.S. Jang, K.K. Joo, B.R. Kim, H.S. Kim, and et al. Spectral measurement of the electron antineutrino oscillation amplitude and frequency using 500 live days of reno data. *Physical Review D*, 98(1), Jul 2018.
- [49] B. Achkar et al. Comparison of anti-neutrino reactor spectrum models with the Bugey-3 measurements. *Phys. Lett. B*, 374:243–248, 1996.
- [50] G. Mention et al. Reactor antineutrino shoulder explained by energy scale nonlinearities? *Phys. Lett. B*, 773:307 – 312, 2017.
- [51] H. de Kerret et al. Double Chooz  $\theta_{13}$  measurement via total neutron capture detection. *Nature Phys.*, 16(5):558–564, 2020.
- [52] C. Buck, A.P. Collin, J. Haser, and M. Lindner. Investigating the spectral anomaly with different reactor antineutrino experiments. *Physics Letters B*, 765:159–162, Feb 2017.
- [53] S. Schael et al. Precision electroweak measurements on the  $Z$  resonance. *Phys. Rept.*, 427:257–454, 2006.
- [54] F.P. An, A.B. Balantekin, H.R. Band, M. Bishai, S. Blyth, D. Cao, G.F. Cao, J. Cao, W.R. Cen, Y.L. Chan, and et al. Improved search for a light sterile neutrino with the full configuration of the daya bay experiment. *Physical Review Letters*, 117(15), Oct 2016.
- [55] T. Abrahão, H. Almazan, J. C. dos Anjos, S. Appel, J. C. Barriere, I. Bekman, T. J. C. Bezerra, L. Bezrukov, E. Blucher, T. Brugière, and et al. Search for signatures of sterile neutrinos with double chooz. *The European Physical Journal C*, 81(8), Aug 2021.
- [56] J. H. Choi and all. Search for sub-ev sterile neutrinos at reno. *Phys. Rev. Lett.*, 125:191801, Nov 2020.
- [57] F.P. An, A.B. Balantekin, H.R. Band, M. Bishai, S. Blyth, D. Cao, G.F. Cao, J. Cao, Y.L. Chan, J.F. Chang, and et al. Evolution of the reactor antineutrino flux and spectrum at daya bay. *Physical Review Letters*, 118(25), Jun 2017.
- [58] G. Bak and all. Fuel-composition dependent reactor antineutrino yield at reno. *Phys. Rev. Lett.*, 122:232501, Jun 2019.
- [59] V. Kopeikin, M. Skorokhvatov, and O. Titov. Reevaluating reactor antineutrino spectra with new measurements of the ratio between  $^{235}\text{u}$  and  $^{239}\text{pu}$   $\beta$  spectra, 2021.

- [60] N. Allemandou et al. The STEREO experiment. *Journal of Instrumentation*, 13(07):P07009–P07009, jul 2018.
- [61] J. Ashenfelter, A.B. Balantekin, C. Baldenegro, H.R. Band, C.D. Bass, D.E. Bergeron, D. Berish, L.J. Bignell, N.S. Bowden, J. Boyle, and et al. The prospect reactor antineutrino experiment. *Nuclear Instruments and Methods in Physics Research Section A: Accelerators, Spectrometers, Detectors and Associated Equipment*, 922:287–309, Apr 2019.
- [62] Y. Abreu, Y. Amhis, L. Arnold, G. Ban, W. Beaumont, M. Bongrand, D. Boursette, J.M. Buhour, B.C. Castle, K. Clark, and et al. A novel segmented-scintillator antineutrino detector. *Journal of Instrumentation*, 12(04):P04024–P04024, Apr 2017.
- [63] I. Alekseev, V. Belov, V. Brudanin, M. Danilov, V. Egorov, D. Filosofov, M. Fomina, Z. Hons, S. Kazartsev, A. Kobayakin, and et al. Search for sterile neutrinos at the danss experiment. *Physics Letters B*, 787:56–63, Dec 2018.
- [64] A. P. Serebrov et al. NEUTRINO4 experiment: preparations for search for sterile neutrino at 100 MW Reactor SM-3 at 6-12 Meters. 5 2012.
- [65] Stefan Schoppmann. Status of anomalies and sterile neutrino searches at nuclear reactors. *Universe*, 7(10):360, Sep 2021.
- [66] Mikhail Danilov. New results from the danss experiment, 2020.
- [67] M. Andriamirado, A.B. Balantekin, H.R. Band, C.D. Bass, D.E. Bergeron, D. Berish, N.S. Bowden, J.P. Brodsky, C.D. Bryan, T. Classen, and et al. Improved short-baseline neutrino oscillation search and energy spectrum measurement with the prospect experiment at hfir. *Physical Review D*, 103(3), Feb 2021.
- [68] Y. Abreu and all. SoLid: a short baseline reactor neutrino experiment. *Journal of Instrumentation*, 16(02):P02025–P02025, feb 2021.
- [69] A. P. Serebrov and all. Search for sterile neutrinos with the neutrino-4 experiment and measurement results. *Phys. Rev. D*, 104:032003, Aug 2021.
- [70] S. Gariazzo, P.F. de Salas, and S. Pastor. Thermalisation of sterile neutrinos in the early universe in the 31 scheme with full mixing matrix. *Journal of Cosmology and Astroparticle Physics*, 2019(07):014–014, jul 2019.
- [71] Sebastian Böser, Christian Buck, Carlo Giunti, Julien Lesgourgues, Livia Ludhova, Susanne Mertens, Anne Schukraft, and Michael Wurm. Status of light sterile neutrino searches. *Progress in Particle and Nuclear Physics*, 111:103736, Mar 2020.
- [72] M. Andriamirado and all. Note on arXiv:2005.05301, 'Preparation of the Neutrino-4 experiment on search for sterile neutrino and the obtained results of measurements'. working paper or preprint, September 2020.
- [73] Pilar Coloma, Patrick Huber, and Thomas Schwetz-Mangold. Statistical interpretation of sterile neutrino oscillation searches at reactors. *The European Physical Journal C*, 81, 01 2021.
- [74] Manfred Lindner, Werner Rodejohann, and Xun-Jie Xu. Coherent neutrino-nucleus scattering and new neutrino interactions. *Journal of High Energy Physics*, 2017(3), Mar 2017.
- [75] D. Akimov et al. Observation of coherent elastic neutrino-nucleus scattering. *Science*, 357(6356):1123–1126, Aug 2017.
- [76] D. Akimov, J.B. Albert, P. An, C. Awe, P.S. Barbeau, B. Becker, V. Belov, I. Bernardi, M.A. Blackston, L. Blokland, and et al. First measurement of coherent elastic neutrino-nucleus scattering on argon. *Physical Review Letters*, 126(1), Jan 2021.
- [77] H. Almazán et al. Improved sterile neutrino constraints from the stereo experiment with 179 days of reactor-on data. *Physical Review D*, 102(5), Sep 2020.
- [78] Charles-Elie Fillon. Détermination de la puissance du réacteur de l'ILL pour la prédiction du flux de neutrinos. Internship report, CEA Paris Saclay, July 2017. Rapport de stage.

- [79] E. Mossou et al. Thermal neutron diffractometer for single-crystal and fibre diffraction D19, 2019.
- [80] M. Enderle et al. Thermal neutron three-axis spectrometer with polarization analysis IN20, 2019.
- [81] F. Kandzia. *Search for a sterile neutrino with the STEREO experiment: shielding optimisation and energy calibration*. PhD thesis, Université Grenoble Alpes, December 2017.
- [82] Alessandro Strumia and Francesco Vissani. Precise quasielastic neutrino/nucleon cross-section. *Physics Letters B*, 564(1-2):42–54, Jul 2003.
- [83] Birks John Betteley. *The theory and practice of scintillation counting*. International series of monographs on electronics and instrumentation. Pergamon Press, Oxford London Edinburgh [etc, 1964.
- [84] Michael F. Weber, Carl A. Stover, Larry R. Gilbert, Timothy J. Nevitt, and Andrew J. Ouderkirk. Giant birefringent optics in multilayer polymer mirrors. *Science*, 287(5462):2451–2456, 2000.
- [85] C. Buck, B. Gramlich, M. Lindner, C. Roca, and S. Schoppmann. Production and properties of the liquid scintillators used in the stereo reactor neutrino experiment. *Journal of Instrumentation*, 14(01):P01027–P01027, Jan 2019.
- [86] O. Bourrion, J.L. Bouly, J. Bouvier, G. Bosson, V. Helaine, J. Lamblin, C. Li, F. Montanet, J.S. Real, T. Salagnac, and et al. Trigger and readout electronics for the stereo experiment. *Journal of Instrumentation*, 11(02):C02078–C02078, Feb 2016.
- [87] Thomas Salagnac. *Recherche d’un neutrino stérile avec l’expérience STEREO : développement de l’électronique et identification des neutrinos*. Theses, Université Grenoble Alpes, October 2017.
- [88] Mathieu Vialat. Results of the stereo experiment. PANIC conference, 2021.
- [89] S. Agostinelli et al. GEANT4—a simulation toolkit. *Nucl. Instrum. Meth. A*, 506:250–303, 2003.
- [90] Horton-Smith G. Glg4sim. <http://neutrino.phys.ksu.edu/~GLG4sim/>. 2015.
- [91] J. Verbeke C. Hagmann, D. Lange and D. Wright. Cosmic-ray shower library(cry)(2012). <http://nuclear.llnl.gov/simulation/>.
- [92] Adrien Blanchet. *Recherche du neutrino stérile auprès du réacteur de l’ILL : expérience Stereo*. Theses, Université Paris-Saclay, October 2019.
- [93] Wei Wang, Qian Sen, Jingkai Xia, Zhe Ning, Yaping Cheng, Meiyu Qi, Y. Heng, Zongyuan Wang, Xiangyang Li, Skyler Liu, and X. Lei. Performance of the 8-in. r5912 photomultiplier tube with super biakali photocathode. *Journal of Instrumentation*, 10:T08001–T08001, 08 2015.
- [94] C. Buck, B. Gramlich, and S. Wagner. Light propagation and fluorescence quantum yields in liquid scintillators. *Journal of Instrumentation*, 10(09):P09007–P09007, Sep 2015.
- [95] M.F. Weber (private communication).
- [96] Maxime Pequignot. *Les expériences Nucifer et Stéréo : étude des antineutrinos de réacteurs à courte distance*. PhD thesis, 2015. Thèse de doctorat dirigée par Lhuillier, David Physique Paris 11 2015.
- [97] J B Birks. Scintillations from organic crystals: Specific fluorescence and relative response to different radiations. *Proceedings of the Physical Society. Section A*, 64(10):874–877, oct 1951.
- [98] G. T. Reynolds, D. B. Scarl, R. A. Swanson, J. R. Waters, and R. A. Zdanis. Muon capture on carbon. *Phys. Rev.*, 129:1790–1794, Feb 1963.
- [99] Jonathan Gaffiot. *Étude des neutrinos de réacteur : mise en place et caractérisation du détecteur Nucifer*. Theses, Université Paris Sud - Paris XI, November 2012.

- [100] H. Almazán. *Evaluation of the neutron detection efficiency in the STEREO reactor neutrino experiment*. PhD thesis, Ruperto-Carola-University, Heidelberg, 2020.
- [101] A. Asghar Mowlavi and R. Koochi-Fayegh. Determination of 4.438mev  $\gamma$ -ray to neutron emission ratio from a  $^{241}\text{Am}$ - $^9\text{Be}$  neutron source. *Applied Radiation and Isotopes*, 60(6):959 – 962, 2004.
- [102] O. Litaize, O. Serot, and L. Berge. Fission modelling with fifrelin. *Eur. Phys. J. A*, 51(12):177, Dec 2015.
- [103] H. Almazán et al. Data from: Improved STEREO simulation with a new gamma ray spectrum of excited gadolinium isotopes using FIFRELIN. *Zenodo*, 2653786, May 2019.
- [104] M.T. Subbotin. On the law of frequency of error. *Matematicheskii Sbornik*, 31(2):296 – 301, 1923.
- [105] William R Leo. *Techniques for nuclear and particle physics experiments: a how-to approach; 2nd ed.* Springer, Berlin, 1994.
- [106] Laura Bernard. *Recherche d’un neutrino stérile avec l’expérience STEREO : détermination des spectres neutrinos et caractérisation du bruit de fond*. PhD thesis, 2019. Thèse de doctorat dirigée par Real, Jean Sébastien Physique subatomique et astroparticules Université Grenoble Alpes (ComUE) 2019.
- [107] H. Almazán et al. Sterile neutrino constraints from the stereo experiment with 66 days of reactor-on data. *Phys. Rev. Lett.*, 121:161801, Oct 2018.
- [108] Vladimir Savu. Reactor antineutrino anomaly: analysis of the stereo experiment. Master’s thesis, CEA Saclay, 2018.
- [109] Till Moritz Karbach and Maximilian Schlupp. Constraints on yield parameters in extended maximum likelihood fits, 2012.
- [110] R. M. Loynes. On cox and snell’s general definition of residuals. *Journal of the Royal Statistical Society. Series B (Methodological)*, 31(1):103–106, 1969.
- [111] H. Almazán, L. Bernard, A. Blanchet, A. Bonhomme, C. Buck, P. del Amo Sanchez, I. El Atmani, J. Haser, L. Labit, J. Lamblin, and et al. Accurate measurement of the electron antineutrino yield of  $^{235}\text{U}$  fissions from the stereo experiment with 119 days of reactor-on data. *Physical Review Letters*, 125(20), Nov 2020.
- [112] C. Giunti, Y.F. Li, B.R. Littlejohn, and P.T. Surukuchi. Diagnosing the reactor antineutrino anomaly with global antineutrino flux data. *Physical Review D*, 99(7):073005, Apr 2019.
- [113] A.L. Read. Presentation of search results: the CLs technique. *Journal of Physics G: Nuclear and Particle Physics*, 28(10):2693–2704, sep 2002.
- [114] H Almazán et al. First antineutrino energy spectrum from  $^{235}\text{U}$  fissions with the stereo detector at ill. *Journal of Physics G: Nuclear and Particle Physics*, 48(7):075107, May 2021.
- [115] Loic Labit. Latest results of the stereo experiment. TAUP conference, 2021.
- [116] Magali Estienne, Muriel Fallot, A. Algora, J. Briz-Monago, V.M. Bui, S. Cormon, W. Gelletly, Lydie Giot, V. Guadilla, D. Jordan, L. Le Meur, Amanda Porta, S. Rice, B. Rubio, J.L. Tañ, E. Valencia, and A.-A. Zakari-Issoufou. Updated Summation Model: An Improved Agreement with the Daya Bay Antineutrino Fluxes. *Phys.Rev.Lett.*, 123(2):022502, 2019.
- [117] H. Almazán et al. Joint measurement of the  $^{235}\text{U}$  antineutrino spectrum by prospect and stereo, 2021.
- [118] <https://fispact.ukaea.uk/>.
- [119] <https://www.oecd-nea.org/dbdata/jeff/jeff33/index.html>.

- [120] Thomas Mueller. *Expérience double Chooz : simulation des spectres antineutrinos issus de réacteurs*. PhD thesis, 2010. Thèse de doctorat dirigée par Lhuillier, David Physique. Physique des neutrinos Paris 11 2010.
- [121] Lorenzo Périssé. *Amélioration de la prédiction des spectres de neutrino réacteur*. PhD thesis, 2021. Thèse de doctorat dirigée par Mougeot, Xavier.
- [122] [http://amdc.in2p3.fr/web/nubase\\_en.html](http://amdc.in2p3.fr/web/nubase_en.html).
- [123] Marco Martini, S Goriely, and S Péru. Gamow-teller strength and beta-decay rate within the self-consistent deformed pnqrpa. *Journal of Physics: Conference Series*, 665:012057, 01 2016.
- [124] J. C. Hardy and I. S. Towner. Superalowed  $0^+ \rightarrow 0^+$  nuclear  $\beta$  decays: A new survey with precision tests of the conserved vector current hypothesis and the standard model. *Phys. Rev. C*, 79:055502, May 2009.
- [125] J. C. Hardy and I. S. Towner. Probing the standard model with superallowed nuclear beta decay. *Nuclear Physics News*, 16(4):11–17, 2006.
- [126] S. Goriely, S. Hilaire, and A. J. Koning. Improved microscopic nuclear level densities within the hartree-fock-bogoliubov plus combinatorial method. *Phys. Rev. C*, 78:064307, Dec 2008.
- [127] S. Rice and all. Total absorption spectroscopy study of the  $\beta$  decay of  $^{86}\text{Br}$  and  $^{91}\text{Rb}$ . *Phys. Rev. C*, 96:014320, Jul 2017.
- [128] A.-A. Zakari-Issoufou, M. Fallot, A. Porta, and all. Total absorption spectroscopy study of  $^{92}\text{Rb}$  decay: A major contributor to reactor antineutrino spectrum shape. *Phys. Rev. Lett.*, 115:102503, Sep 2015.
- [129] R.C. Greenwood, R.G. Helmer, M.H. Putnam, and K.D. Watts. Measurement of  $\beta$ -decay intensity distributions of several fission-product isotopes using a total absorption  $\gamma$ -ray spectrometer. *Nuclear Instruments and Methods in Physics Research Section A: Accelerators, Spectrometers, Detectors and Associated Equipment*, 390(1):95–154, 1997.
- [130] D. Jordan et al. Total absorption study of the  $\beta$  decay of  $^{102,104,105}\text{Tc}$ . *Phys. Rev. C*, 87:044318, Apr 2013.
- [131] V. Guadilla et al. Experimental study of  $^{100}\text{Tc}$   $\beta$  decay with total absorption  $\gamma$ -ray spectroscopy. *Phys. Rev. C*, 96:014319, Jul 2017.
- [132] V. Guadilla et al. Large impact of the decay of niobium isomers on the reactor  $\bar{\nu}_e$  summation calculations. *Phys. Rev. Lett.*, 122:042502, Jan 2019.
- [133] G. Angloher and all. Exploring cevns with nucleus at the chooz nuclear power plant, 2019.
- [134] R. Strauss, J. Rothe, G. Angloher, A. Bento, A. Gütlein, D. Hauff, H. Kluck, M. Mancuso, L. Oberauer, F. Petricca, and et al. The  $\nu$ -cleus experiment: a gram-scale fiducial-volume cryogenic detector for the first detection of coherent neutrino–nucleus scattering. *The European Physical Journal C*, 77(8), Jul 2017.
- [135] Andreas Erhart. Development of an organic plastic scintillator based muon veto operating at sub-kelvin temperatures for the nucleus experiment. Master’s thesis, Technical University of Munchen, 2021.
- [136] Saint Gobain Crystals. BC-408. <https://www.crystals.saint-gobain.com/products/bc-408-bc-412-bc-416>, 2021.
- [137] Saint Gobain Crystals. BC-91A. <https://www.crystals.saint-gobain.com/products/scintillating-fiber>, 2021.
- [138] KETEK. SiPM TIA Module. <https://www.ketek.net/store/products/pe3315-wb-tia-sp/>, 2021.
- [139] V. Wagner, A. Erhart R. Rogly, V. Savu, C. Goupy, D. Lhuillier, M. Vivier, L. Klinkenberg, et al. Development of a compact muon veto for the nucleus experiment. [article in preparation].

- [140] V. Chmill, E. Garutti, R. Klanner, M. Nitschke, and J. Schwandt. On the characterisation of SiPMs from pulse-height spectra. *Nucl. Instrum. Meth. A*, 854:70–81, 2017.
- [141] C. Goupy, R. Rogly, and V.Savu. Nucleus muon veto technical note. CEA Saclay.
- [142] Sadakazu Haino et al. Measurements of primary and atmospheric cosmic - ray spectra with the BESS-TeV spectrometer. *Phys. Lett. B*, 594:35–46, 2004.
- [143] Prashant Shukla and Sundaresh Sankrith. Energy and angular distributions of atmospheric muons at the earth, 2018.
- [144] C. Patrignani et al. Particle Data Group. *Chinese Physics C*, 40(100001), 2016.
- [145] M. P. De Pascale and all. Absolute spectrum and charge ratio of cosmic ray muons in the energy region from 0.2 gev to 100 gev at 600 m above sea level. *Journal of Geophysical Research: Space Physics*, 98(A3):3501–3507, 1993.



**Titre:** Étude des neutrinos de réacteur : expériences STEREO et NUCLEUS

**Mots clés:** neutrino stérile, décroissance bêta, rayonnement cosmique, veto muon, diffusion cohérente

**Résumé:** La présente thèse de doctorat porte sur la physique des neutrinos de réacteur, étudiée dans le cadre de deux expériences : STEREO et NUCLEUS. L'expérience STEREO vise à tester l'hypothèse selon laquelle une oscillation vers un neutrino stérile de masse  $\sim 1 \text{ eV}/c^2$  pourrait expliquer l'anomalie des antineutrinos de réacteurs (RAA). Elle utilise un détecteur segmenté, placé à  $\sim 10 \text{ m}$  du réacteur de recherche quasiment pur en  $^{235}\text{U}$  de l'ILL, pour détecter des antineutrinos par la réaction de désintégration bêta inverse (IBD). Le travail de thèse se concentre principalement sur deux aspects de l'analyse STEREO : le réglage fin de la simulation Monte Carlo du détecteur et l'extraction du signal  $\bar{\nu}_e$  à l'aide d'une modélisation des distributions de PSD (Pulse Shape Discrimination) obtenues avec le réacteur éteint et allumé. Le réglage fin de la simulation a conduit à un accord inférieur à un pour cent entre les données et la simulation au niveau de la charge brute, ce qui permet une meilleure maîtrise de l'échelle en énergie, tandis que le travail sur l'extraction du signal  $\bar{\nu}_e$  a permis de mettre une incertitude systématique sur le taux absolu d'antineutrinos mesuré, conduisant à la mesure la plus précise à ce

jour. L'analyse de l'ensemble des données STEREO valide le déficit de  $\sim 6\%$  du taux total d'antineutrinos de réacteur par rapport à la valeur prédite, rejette le meilleur ajustement de la RAA à  $>99,99\%$  de niveau de confiance et fournit le plus précis spectre  $\bar{\nu}_e$  de pur  $^{235}\text{U}$ . Une amélioration de la prédiction est également proposée dans ce travail de thèse, permettant de reproduire le spectre antineutrino mesuré et d'explorer l'origine des anomalies. L'expérience NUCLEUS est placée entre les deux cœurs de la centrale nucléaire de Chooz et vise à mesurer les reculs nucléaires induits par la diffusion cohérente des antineutrinos du réacteur sur les noyaux d'un détecteur cryogénique ( $\text{CE}\nu\text{NS}$ ). Les principaux défis de l'expérience sont l'obtention d'un seuil de détection très bas, d'une réponse temporelle suffisamment rapide et d'un bon contrôle du bruit de fond, de sorte que le détecteur puisse être exploité dans des conditions de surface. Les travaux menés au cours de cette thèse ont porté sur la construction d'un prototype de veto muon et sur des simulations géométriques du veto muon complet de NUCLEUS, visant à estimer son efficacité et à trouver la meilleure configuration.

**Title:** Reactor neutrino studies : STEREO and NUCLEUS experiments

**Keywords:** sterile neutrino, beta-decay, cosmic rays, muon veto, coherent scattering

**Abstract:** The present doctoral thesis focuses on the physics of reactor neutrinos, studied in the context of two experiments: STEREO and NUCLEUS. STEREO is aimed at testing the hypothesis that an oscillation towards a sterile neutrino with a mass of  $\sim 1 \text{ eV}/c^2$  could explain the reactor antineutrino anomaly (RAA). It uses a segmented detector, placed at  $\sim 10 \text{ m}$  from the virtually pure  $^{235}\text{U}$  research reactor from ILL, to detect antineutrinos through the inverse beta decay (IBD) reaction. This thesis mainly focuses on two aspects of the STEREO analysis: the fine-tuning of the Monte Carlo simulation of the detector and the extraction of the  $\bar{\nu}_e$  signal using a modelization of the reactor-off and reactor-on Pulse Shape Discrimination (PSD) distributions. The simulation fine-tuning led to a sub-percent agreement between data and simulation at the brute charge level, which allows for a better control of the energy scale, while the work on the  $\bar{\nu}_e$  signal extraction allowed to put a systematic uncertainty on the absolute measured rate of antineutrinos, which led to the most accurate measurement to date. The analysis of

the whole STEREO dataset validates the  $\sim 6\%$  deficit observed in the total rate of reactor antineutrinos with respect to the predicted value, allows to reject the RAA best fit point at  $>99,99\%$  confidence level, and provides the most accurate pure  $^{235}\text{U}$   $\bar{\nu}_e$  spectrum. An improvement of the prediction is also proposed in this thesis, allowing to reproduce the measured antineutrino spectrum and to explore the origin of the anomalies. The NUCLEUS experiment is placed between the two reactor cores of the Chooz nuclear power plant and is aimed at measuring the nuclear recoils induced by the coherent scattering of reactor antineutrinos off the nuclei of a cryogenic detector ( $\text{CE}\nu\text{NS}$ ). The main challenges of the experiment are to obtain a very low detection threshold, a sufficiently fast time response, and a good background control, so that the detector could be operated in above-ground conditions. The work carried out during this thesis centered on the construction of a muon veto prototype and on geometrical simulations of the full NUCLEUS muon veto, aimed at estimating its efficiency and finding its optimal configuration.